THE DISSERTATION COMMITTEE FOR ANDREW CHARLES WALKER CERTIFIES THAT

THIS IS THE APPROVED VERSION OF THE FOLLOWING DISSERTATION:

A COMPREHENSIVE NUMERICAL MODEL OF IO'S CHEMICALLY-REACTING SUBLIMATION-DRIVEN ATMOSPHERE AND ITS INTERACTION WITH THE JOVIAN PLASMA TORUS

Committee:

David Goldstein, Co-Supervisor

Philip Varghese, Co-Supervisor

Laurence Trafton

Laxminarayan Raja

John Spencer

Robert Johnson

A COMPREHENSIVE NUMERICAL MODEL OF IO'S CHEMICALLY-REACTING SUBLIMATION-DRIVEN ATMOSPHERE AND ITS INTERACTION WITH THE JOVIAN PLASMA TORUS

BY

ANDREW CHARLES WALKER, B.S.

DISSERTATION

Presented to the Faculty of the Graduate School of

The University of Texas at Austin

in Partial Fulfillment

of the Requirements

for the Degree of

DOCTOR OF PHILOSOPHY

THE UNIVERSITY OF TEXAS AT AUSTIN

MAY 2012

DEDICATION

Dedicated to my parents, Richard and Crystal, and my wife, Kim.

ACKNOWLEDGEMENTS

First, I would like to thank my advisors, Dr. David Goldstein and Dr. Philip Varghese, for their helpful guidance and support throughout my graduate research. Dr. Laurence Trafton has also been very helpful with his expertise in astronomy and planetary science which he gladly shared at our weekly meetings.

I thank my past and present colleagues for the helpful discussions and comfortable atmosphere they have provided over the years. Past colleagues (since graduated), Bénédicte Stewart and Chris Moore were responsible for my introduction to DSMC. Both were always willing to help me when I was lost in the code. I would also like to thank my friends James Strand and Aaron Morris for their friendship throughout graduate school. I would also like to acknowledge other colleagues who have been helpful in my research: Billy McDoniel, Kelly Stephani, Parvathy Prem, Seng Yeoh, and John Tencer.

For over half of my graduate career, I have been married to my wife, Kim. I must thank her for the constant love and reassurance she has given me. I also thank my parents, Richard and Crystal, for their constant support.

I would also like to thank the Texas Advanced Computing Center for the copious number of hours that they allowed me to use for the large parallel simulations discussed herein. I also extend thanks to the NASA Planetary Atmospheres and Outer Planets Research programs for their funding to support this research.

A COMPREHENSIVE NUMERICAL MODEL OF IO'S CHEMICALLY-REACTING SUBLIMATION-DRIVEN ATMOSPHERE AND ITS INTERACTION WITH THE JOVIAN PLASMA TORUS

Publication No._____

Andrew Charles Walker, Ph. D.

The University of Texas at Austin, 2012

Co-supervisors: David B. Goldstein and Philip L. Varghese

Io has one of the most dynamic atmospheres in the solar system due in part to an orbital resonance with Europa and Ganymede that causes intense tidal heating and volcanism. The volcanism serves to create a myriad of volcanic plumes across Io's surface that sustain temporally varying local atmospheres. The plumes primarily eject sulfur dioxide (SO_2) that condenses on Io's surface during the relatively cold night. During the day, insolation warms the surface to temperatures where a global partially collisional atmosphere can be sustained by sublimation from SO_2 surface frosts. Both the volcanic and sublimation atmospheres serve as the source for the Jovian plasma torus which flows past Io at ~57 km/s. The high energy ions and electrons in the Jovian plasma torus interact with Io's atmosphere causing atmospheric heating, chemical reactions, as well as

altering the circumplanetary winds. Energetic ions which impact the surface can sputter material and create a partially collisional atmosphere. Simulations suggest that energetic ions from the Jovian plasma cannot penetrate to the surface when the atmospheric column density is greater than 10^{15} cm^{-2}. These three mechanisms for atmospheric support (volcanic, sublimation, and sputtering) all play a role in supporting Io's atmosphere but their relative contributions remain unclear.

In the present work, the Direct Simulation Monte Carlo (DSMC) method is used to simulate the interaction of Io's atmosphere with the Jovian plasma torus and the results are compared to observations. These comparisons help constrain the relative contributions of atmospheric support as well as highlight the most important physics in Io's atmosphere. These rarefied gas dynamics simulations improve upon earlier models by using a three-dimensional domain encompassing the entire planet computed in parallel. The effects of plasma heating, planetary rotation, inhomogeneous surface frost, molecular residence time of SO_2 on the exposed non-frost surface, and surface temperature distribution are investigated. Circumplanetary flow is predicted to develop from the warm dayside toward the cooler nightside. Io's rotation leads to a highly asymmetric frost surface temperature distribution (due to the frost's high thermal inertia) which results in circumplanetary flow that is not axi-symmetric about the subsolar point. The non-equilibrium thermal structure of the atmosphere, specifically vibrational and rotational temperatures, is also examined. Plasma heating is found to significantly inflate the atmosphere on both the dayside and nightside. The plasma energy flux causes high temperatures at high altitudes, but plasma energy depletion through

the dense gas column above the warmest frost permits gas temperatures cooler than the surface at low altitudes. A frost map (Douté *et al.*, 2001) is used to control the sublimated flux of SO_2 which can result in inhomogeneous column densities that vary by nearly a factor of four for the same surface temperature. A short residence time for SO_2 molecules on the non-frost component is found to smooth lateral atmospheric inhomogeneities caused by variations in the surface frost distribution, creating an atmosphere that looks nearly identical to one with uniform frost coverage. A longer residence time is found to agree better with mid-infrared observations (Spencer *et al.*, 2005) and reproduce the observed anti-Jovian/sub-Jovian column density asymmetry. The computed peak dayside column density for Io agrees with those suggested by Lyman-α observations (Feaga *et al.*, 2009) assuming a surface frost temperature of 115 K. On the other hand, the peak dayside column density at 120 K is a factor of five larger and is higher than the upper range of observations (Jessup *et al.*, 2004; Spencer *et al*., 2005).

The results of the original DSMC simulations of Io's atmosphere show that the most important and sensitive parameter is the SO_2 surface frost temperature. To improve upon the original surface temperature model, we constrain Io's surface thermal distribution by a parametric study of its thermophysical properties. Io's surface thermal distribution is represented by three thermal units: sulfur dioxide (SO_2) frosts/ices, non-frosts (probably sulfur allotropes and/or pyroclastic dusts), and hot spots. The hot spots included in the thermal model are static high temperature surfaces with areas and temperatures based on Keck infrared observations. Elsewhere, over frosts and non-frosts, the

thermal model solves the one-dimensional heat conduction equation in depth into Io's surface and includes the effects of eclipse by Jupiter, radiation from Jupiter, and latent heat of sublimation and condensation. The best fit parameters for the SO_2 frost and non-frost units are found by using a least-squares method and fitting to observations of the Hubble Space Telescope's Space Telescope Imaging Spectrograph (HST STIS) mid- to near-UV reflectance spectra and Galileo photo-polarimeter (PPR) brightness temperature. The thermophysical parameters are the frost Bond albedo, α_F, and thermal inertia, Γ_F, as well as the non-frost surface Bond albedo, α_{NF}, and thermal inertia, Γ_{NF}. The best fit parameters are found to be $\alpha_F \approx 0.55 \pm 0.02$ and $\Gamma_F \approx 200 \pm 50$ J m^{-2} K^{-1} s$^{-1/2}$ for the SO_2 frost surface and $\alpha_{NF} \approx 0.49 \pm 0.02$ and $\Gamma_{NF} \approx 20 \pm 10$ J m^{-2} K^{-1} s$^{-1/2}$ for the non-frost surface.

These surface thermophysical parameters are then used as boundary conditions in global atmospheric simulations of Io's sublimation-driven atmosphere using DSMC. The DSMC simulations show that the sub-Jovian hemisphere is significantly affected by the daily solar eclipse. The SO_2 surface frost temperature is found to drop ~5 K during eclipse but the column density falls by a factor of 20 compared to the pre-eclipse column due to the exponential dependence of the SO_2 vapor pressure on the SO_2 surface frost temperature. Supersonic winds exist prior to eclipse but become subsonic during eclipse because the collapse of the atmosphere significantly decreases the day-to-night pressure gradient that drives the winds. Prior to eclipse, the supersonic winds condense on and near the cold nightside and form a highly non-equilibrium oblique shock near the dawn terminator. In eclipse, no shock exists since the gas is subsonic and the shock only reestablishes itself an hour or more after egress

from eclipse. Furthermore, the excess gas that condenses on the non-frost surface during eclipse leads to an enhancement of the atmosphere near dawn. The dawn atmospheric enhancement drives winds that oppose those that are driven away from the peak pressure region above the warmest area of the SO_2 frost surface. These opposing winds meet and are collisional enough to form stagnation point flow. The simulations are compared to Lyman-α observations in an attempt to explain the asymmetry between the dayside atmospheres of the anti-Jovian and sub-Jovian hemispheres. A composite "average dayside atmosphere" is formed from a collisionless simulation of Io's atmosphere throughout an entire orbit. The composite "average dayside" atmosphere without the effect of global winds indicates that the sub-Jovian hemisphere should have lower average column densities than the anti-Jovian hemisphere (with the strongest effect at the sub-Jovian point) due entirely to the diurnally averaged effect of eclipse.

Lastly, a particle description of the plasma is coupled with the sophisticated surface thermal model and a final set of global DSMC atmospheric simulations are performed. The particle description of energetic ions from the Jovian plasma torus allows for momentum transfer from the ions to the neutral atmosphere. Also, the energetic ions (or solar photons) can dissociate the neutral atmosphere and cause sputtering of SO_2 on the surface. SO_2 remains the dominant dayside species (>90%) despite being dissociated by ions and photons to form O, O_2, S, and SO. SO_2 remains the dominant atmospheric species on the nightside between dusk and midnight due to sputtering of SO_2 surface frosts by energetic ions as well as the high thermal inertia of SO_2 frosts that cause the surface temperature to cool slowly and thus sublime a thicker SO_2 atmosphere. O_2

becomes the dominant atmospheric species above coldest areas of the surface because it is non-condensable at Io's surface temperatures and other species are sticking to the surface. SO and O are present in similar gas fractions because they are created together via the same ion and photo-dissociation reactions. Sulfur column densities are the lowest throughout the atmosphere because S is created slowly via direct dissociation of SO_2; it is instead created primarily through dissociation of SO.

The momentum transfer from the plasma is found to have substantial effect on the global wind patterns. The interaction between the plasma pressure and day-to-night pressure gradient is highly dependent on Io's subsolar longitude. Similar to previous simulations, the westward winds reach higher Mach numbers and wind speeds than the eastward winds. This is because the westward winds are accelerated by a larger day-to-night pressure gradient due to the very cold surface temperatures that exist prior to dawn. Eastward equatorial winds on the nightside are accelerated by the plasma pressure and condense out near the dawn terminator after traveling ~3/4 of the circumference of Io. O_2 is pushed to the nightside by the circumplanetary winds where it builds-up until it reaches an equilibrium column density. On the nightside, O_2 is destroyed by ion dissociation. On the nightside, a shear layer develops between the equatorial eastward winds and stagnant non-condensable species at mid-latitudes. This shear layer generates lateral vorticity which is especially visible in O_2 streamlines. Large cyclones develop in the northern and southern hemispheres and are most apparent in the O_2 wind patterns because other species condense out on the nightside.

Table of Contents

LIST OF TABLES

LIST OF FIGURES

CHAPTER 1: INTRODUCTION

1.1 MOTIVATION

The predominant mechanism for supporting the observed atmosphere on Io has long been a subject of debate. The three mechanisms originally proposed were volcanic plumes, sublimation from SO_2 surface frosts, and sputtering from SO_2 surface frosts. Io is the most volcanically active body in the solar system due to an orbital resonance with Ganymede and Europa which causes strong tidal heating. The volcanic plumes have been observed to create temporally varying local atmospheres that consist primarily of SO_2 gas. The SO_2 gas ejected from the volcanic plumes condenses onto the surface during the night when the surface cools and forms optically thick frosts. In the presence of insolation, these SO_2 frosts warm and begin to sublimate a partially collisional atmosphere over the dayside. Lastly, energetic ions from the Jovian plasma torus can impact SO_2 surface frosts and sputter off SO_2 gas and other species. Cheng and Johnson (1989) give a detailed review of sputtering models and also show that sputtering is a minor process in support of the dayside atmosphere since it can only produce an atmosphere limited to $10^{15} – 10^{16}$ cm^{-2} and recent observations show that large portions of the dayside exceed those limits. Therefore, sputtering is a secondary mechanism of atmospheric support except possibly near the poles and on the nightside (away from active volcanic plumes) where the vapor pressure of SO_2 is very low.

Observations over the last 20 or more years have conflicted over the dominant process with a roughly 50/50 split between those observations that support a sublimation-driven atmosphere and those that support a volcanically-driven atmosphere. See Spencer *et al*. (2005) for a detailed review of these conflicting

observations. Recently, data on the disk-averaged spectra of the ν_2 band of SO_2 collected by Tsang *et al*. (2012) as a function of heliocentric distance have given strong evidence that there is a seasonal variation in the atmosphere that supports a sublimation-driven model; however, model fits to the observed data show that a substantial volcanic column is also needed.

The lack of polar caps on Io is also puzzling because the circumplanetary winds will transport SO_2 toward the poles. One would expect the SO_2 gas to condense on the cold poles and eventually build-up to form thick observable polar caps; however, observations show that Io lacks polar caps and that the frost fraction is quite low near the poles (McEwen *et al*., 1988; Carlson *et al*., 1997; Douté *et al*., 2001; Laver and de Pater, 2008; 2009). Ingersoll *et al*. (1985) put forward two alternative explanations for the lack of polar caps. In their gas dynamic calculations, they found that SO_2 condensed out before reaching the poles and therefore the flux to the poles was negligibly small ($<10^{11}$ cm^{-2}). They also hypothesized that sputtering by energetic ions could also keep the poles barren of SO_2 frost. These are still the two leading hypotheses to explain the lack of polar caps on Io; however, Ingersoll *et al*.'s simulations were continuum and also vertically integrated. Our global 3D simulations of Io's atmosphere can provide a more rigorous examination of whether these two mechanisms are truly the cause of the barren poles of Io.

Lastly, observations over the past 15 years have indicated an asymmetry between the sub-Jovian and anti-Jovian hemispheres. The asymmetry is present not only in the atmospheric column densities (Strobel and Wolven, 2001; Feaga *et al*., 2009) but also in the observed SO_2 frost fraction (Douté *et al*., 2001). Both asymmetries have been correlated with the distribution of volcanic plumes on Io's surface but there may be other mechanisms by which this asymmetry can be generated. By including dynamic effects such as eclipse into the global DSMC

atmospheric simulations (Chapter 6), we can determine whether such effects might contribute to the observed asymmetry.

1.2 OBJECTIVES

In this work, we hope to further constrain the concentration of gas from sublimation and volcanism by comparing global atmospheric DSMC simulations of Io's atmosphere with various observations. Not only can these atmospheric simulations shed light on the relative contributions from sublimation and volcanism, but they may help us better understand other unexplained phenomena on Io such as the observed prograde wind at eastern elongation (Moullet *et al*., 2008) or the striking drop-off in dayside column density at ±45° latitude (Feaga *et al*., 2009). Other unexplained observations such as the sub-Jovian/anti-Jovian asymmetry in both column density (Strobel and Wolven, 2001; Feaga *et al*., 2009) and SO_2 frost fraction (Douté *et al*., 2001) or the lack of polar caps despite supersonic circumplanetary winds (McEwen *et al*., 1988; Carlson *et al*., 1997; Douté *et al*., 2001; Laver and de Pater, 2008; 2009) can be understood better using our global atmospheric simulations.

To properly model Io's sublimation atmosphere requires the inclusion of a sophisticated surface model and a particle description of the plasma. The sophisticated surface model includes a surface temperature model which solves the 1D heat conduction problem within the solid and accounts for the effects of thermal inertia, latent heats of sublimation and condensation, eclipse by Jupiter, and radiation from Jupiter. The surface model also accounts for the observed variation of SO_2 surface frosts over Io's surface (Douté *et al*., 2001) and the likely sticking and residence time of SO_2 gas molecules on a non-frost surface (Sandford and Allamandola, 1993). The particle description of the plasma creates sources for the daughter species of SO_2 by chemical reactions, enables sputtering from SO_2 surface

frosts, and alters circumplanetary winds by transfer of momentum from the plasma to the atmosphere.

1.3 OVERVIEW

Chapter 2 reviews much of the pertinent literature concerning Io's atmosphere, surface properties, and the Jovian plasma torus. It is broken down into early (historical), atmospheric, and surface observations, and concludes by summarizing computational studies of Io. In Chapter 3, the DSMC method is briefly summarized along with the various physical models that have been incorporated in order to simulate Io's atmosphere. Chapter 4 reviews the results of early global atmospheric DSMC simulations which used a relatively crude surface temperature model. This chapter focuses on the structure and variations of macroscopic properties such as number density, column density, temperature (translational, rotational, and vibrational), and Mach number. In Chapter 5, a parametric study that uses a more sophisticated surface temperature model to constrain Io's surface thermophysical properties is summarized. The updated surface solves the 1D heat conduction equation to obtain the temperature as a function of depth into Io's surface and includes the effects of thermal inertia, eclipse by Jupiter, radiation from Jupiter, and the latent heats of sublimation and condensation. Chapter 6 utilizes the best fit parameters determined by the parametric study in global atmospheric DSMC simulations. The atmospheric results are compared to observations and the original simulations discussed from Chapter 4. In Chapter 7, the global atmospheric DSMC simulations are further updated by incorporating both the sophisticated surface temperature model used in Chapter 6 as well as a particle description for ions and electrons from the Jovian plasma torus. The particle description of plasma heating allows for the ions and electrons to interact with Io's atmosphere realistically, cause atmospheric heating, chemical reactions, as well as alter the circumplanetary winds

due to the plasma pressure. In Chapter 8, the overarching conclusions from each chapter are summarized.

CHAPTER 2: LITERATURE REVIEW

2.1 EARLY OBSERVATIONS

In 1964, Binder and Cruikshank reported post-eclipse brightening when observing Io (Binder and Cruikshank, 1964) and attributed the anomalous brightening to a frost deposit or a haze layer caused by the surface temperature drop during eclipse. But the existence of an atmosphere remained in question due to the conflicting results of other observations in search of post-eclipse brightening (O'Leary and Veverka, 1971; Franz and Millis, 1971; Cruikshank and Murphy, 1973). In 1973, Pioneer 10 detected and probed Io's ionosphere through radio occultation providing proof of an atmosphere on Io. Kliore *et al.* (1975) modeled the Pioneer data to estimate a surface pressure between 1 to 10 nbar near the terminator. It was not until 1979 that the primary dayside species, sulfur dioxide, was detected by the Voyager IR spectrometer (IRIS) (Pearl *et al.*, 1979). Lellouch *et al.* (1992) later reinterpreted the same IRIS data but included non-local thermodynamic equilibrium (non-LTE) effects to infer surface pressures in the 5 to 40 nbar range. The UV spectral observations of Ballester *et al.* (1990) are best fit by a cool gas with large spatial extent, supporting a sublimated atmosphere. However, millimeter–wave observations of the 222 GHz rotational line of SO_2 (Lellouch *et al.*, 1990) are best fit by a warm gas with limited extent and are argued to be best matched by volcanic models (Lellouch *et al.*, 1992).

As illustrated by the conflicting observations of Ballester *et al.* (1990) and Lellouch *et al.* (1990), there are two important mechanisms on Io which could produce a substantial atmosphere: volcanic activity and sublimation from surface

frost. No observations have shown conclusively which mechanism is the dominant producer of Io's atmosphere. Spencer *et al.* (2005) give a detailed review and discussion of the various observations supporting either volcanic or sublimated atmospheres.

2.2 ATMOSPHERIC OBSERVATIONS

The local dayside SO_2 vertical column abundance varies between ~5×10^{15} cm^{-2} and 6×10^{17} cm^{-2}. These variations are likely due to actual variations in the column density due to the insolation, surface frosts, volcanoes, and lava lakes as well as the different measurement techniques and data analysis methods used. Estimates of the dayside vertical column densities fall into two categories: spatially unresolved, disk-integrated values and spatially resolved values.

UV Hubble Space Telescope (HST) disk-integrated observations made in 1992 utilizing the Faint Object Spectrograph (FOS) predict column densities of $6-10\times10^{15}$ cm^{-2} (Ballester *et al*., 1994) and 4×10^{16} cm^{-2} (Clarke *et al*., 1994) for uniform atmospheric distributions. Ballester *et al*. (1994) also fit their spectra to localized atmospheric models with column densities of $10^{16}-3\times10^{17}$ cm^{-2}. Jessup *et al*. (2002) analyzed additional HST/FOS observations made in 1994 and 1996 and fit the data with a two component model: an extended component at 110−350 K with column densities of $10^{15}-10^{16}$ cm^{-2} and a confined component at 105−115 K with column densities of ~$2.0\times10^{16}-2.0\times10^{17}$ cm^{-2}. Trafton *et al*. (1996) inferred disk-averaged column densities of 5.0×10^{15} cm^{-2} and 7.0×10^{15} cm^{-2} for the leading and trailing hemispheres, respectively, from UV spectra observed with the Goddard High Resolution Spectrograph (GHRS) on HST. Disk-averaged observations at millimeter wavelengths (Lellouch *et al*., 1992) made with the IRAM (Institut de Radio-Astronomie Millimétrique) radiotelescope are best fit by local column densities of ~10^{17} cm^{-2} and temperatures >600 K. Spencer *et al*. (2005) obtained disk-integrated

mid-infrared spectra at the NASA Infrared Telescope which yielded inferred equatorial column densities of 1.5×10^{17} cm^{-2} near 180º W and 1.5×10^{16} cm^{-2} near 300º W. These results are discussed in detail in later in this section as a key constraining observation.

Observations that spatially resolve Io have been performed. The first successful spatially resolved observation of Io's atmosphere was performed in 1996 (McGrath *et al*., 2000) with HST/FOS. The UV observations reported spatial inhomogeneity in column densities between 3 separate locations: the Pele volcano, the Ra volcano, and a control region centered at 45º S and 300º W. The column densities at these locations were inferred to be 3.25×10^{16} cm^{-2}, 1.5×10^{16} cm^{-2}, and 7×10^{15} cm^{-2}, respectively. A 1998 observation made by the Galileo Ultraviolet Spectrometer with marginal disk resolution, and spectral resolution inadequate to resolve the 10 Å wide SO_2 absorption bands, yielded an inferred SO_2 abundance near 4×10^{17} cm^{-2} covering ~25% of the observed region and a local abundance as high as 1×10^{19} cm^{-2} (Hendrix *et al.*, 1999). However, these high values are uncertain because they depend on assumptions about the reflectivity of Io's surface materials. HST observations utilizing the Space Telescope Imaging Spectrograph (STIS) in the Lyman-α (Roesler *et al*., 1999; Feldman *et al*., 2000) yield column densities of ~10^{16} cm^{-2}. Feaga *et al*. (2009) further analyzed the HST/STIS images; their results are discussed in detail in later in this section as a key constraining observation for our atmospheric model.

Jessup *et al*. (2004) used HST/STIS mid- to near-UV observations to obtain spatially resolved column densities that generally vary between 10^{16}–10^{17} cm^{-2} and peak near the equator at 1.25×10^{17} cm^{-2} with an additional 5×10^{16} cm^{-2} column near Prometheus. These inferred column densities are consistent with vapor pressure equilibrium (with a peak temperature of ~117 K) for latitudes <30º or solar zenith angles <40º (see Figure 2.1). Beyond these latitudes and solar zenith angles, the

inferred atmospheric column densities do not follow vapor pressure equilibrium. Jessup *et al*. give several explanations for the divergence from vapor pressure equilibrium: enhancement by dynamical flow, warm areas that inhibit condensation, and/or SO_2 plumes. Moullet *et al*. (2008) obtained the first disk-resolved millimeter observations using the IRAM Plateau de Bure Interferometer and inferred that the atmosphere covers ~80% of the leading side and ~60% of the trailing side. They also found a limb-to-limb velocity difference of 330 ± 100 m/s which is at odds with the models of Ingersoll (1985; 1989) that predict uniform flow away from the subsolar point for uniform frost coverage. Moullet *et al*. hypothesize that the limb-to-limb velocity difference could be due to a plume near the limb or geographical variations in the surface pressure due to either thermal inertia or surface frosts.

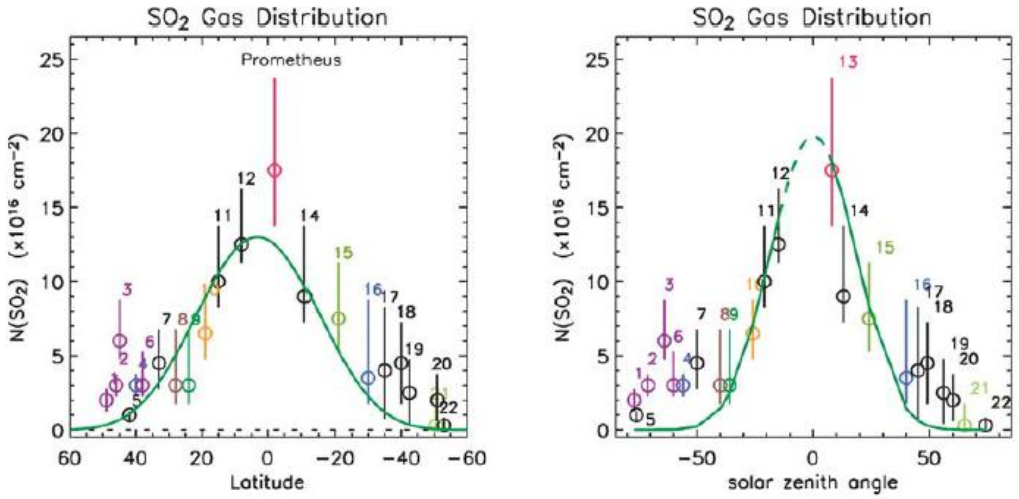

Figure 2.1: Inferred column densities as a function of latitude and solar zenith at 22 locations on Io's anti-Jovian hemisphere from HST-STIS observations of mid- to near-UV spectra. Both (left) and (right) are fit well by vapor pressure equilibrium (VPE) except at high latitudes and/or solar zenith angles where the observations overshoot VPE. (*From Jessup et al. (2004), courtesy of Elsevier*).

Spencer *et al.* (2005) obtained disk-averaged data from emission in the SO_2 ν_2 vibrational band at 19.3 μm at the NASA Infrared Telescope Facility on Mauna Kea in Nov. 2001, Dec. 2002, and Jan. 2004 (see Figure 2.2). They modeled the vertical

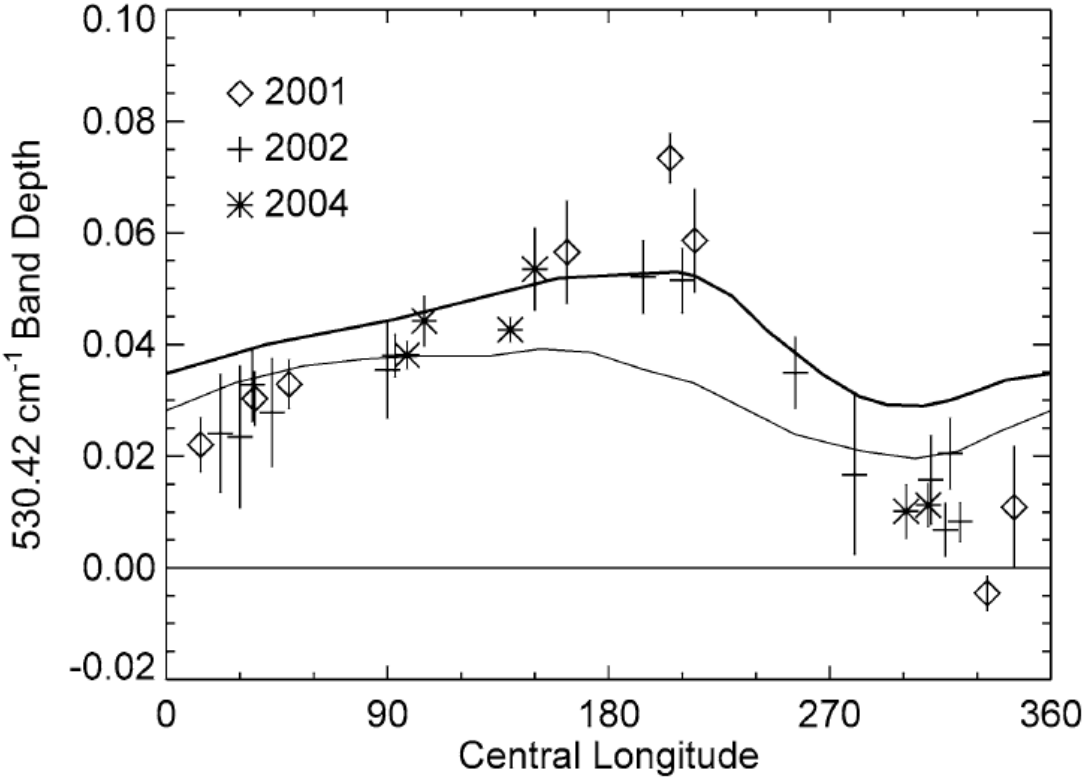

Figure 2.2: The 19.3 μm SO_2 ν_2 disk-averaged band depth as a function of central longitude between observed between 2001 and 2004. The anti-Jovian hemisphere has higher disk-averaged band depths than the sub-Jovian hemisphere which, under certain assumptions, correlates with higher column densities on the anti-Jovian hemisphere in agreement with Lyman-α observations (Feldman *et al*., 2000; Strobel and Wolven, 2001; Feaga *et al*., 2009). (*From Spencer et al. (2009), courtesy of Elsevier*).

thermal structure of the atmosphere with the most important production and loss processes assuming non-LTE by simultaneously solving the statistical equilibrium equation of state and the radiative transfer equation. Their surface temperature model was compared to data from the Galileo PPR (Rathbun *et al.,* 2004) and empirically weighted to increase the temperature near the subsolar point and decrease the temperature near the limb. Spencer *et al.* (2005) found that there are ambiguities in interpreting the IR spectra because an increase in density can lead to both higher and lower absorption strength depending on the vertical thermal structure present in the model atmosphere. An atmosphere with a modified latitudinal dependence (i.e.

hydrostatic column densities everywhere except between absolute latitudes of 32º and 50º, where the column density is held fixed at the 32º latitude value) was found to be the best fit to the observations. As discussed earlier, the inferred column densities were 1.5×10^{17} cm^{-2} near 180º W and 1.5×10^{16} cm^{-2} near 300º W.

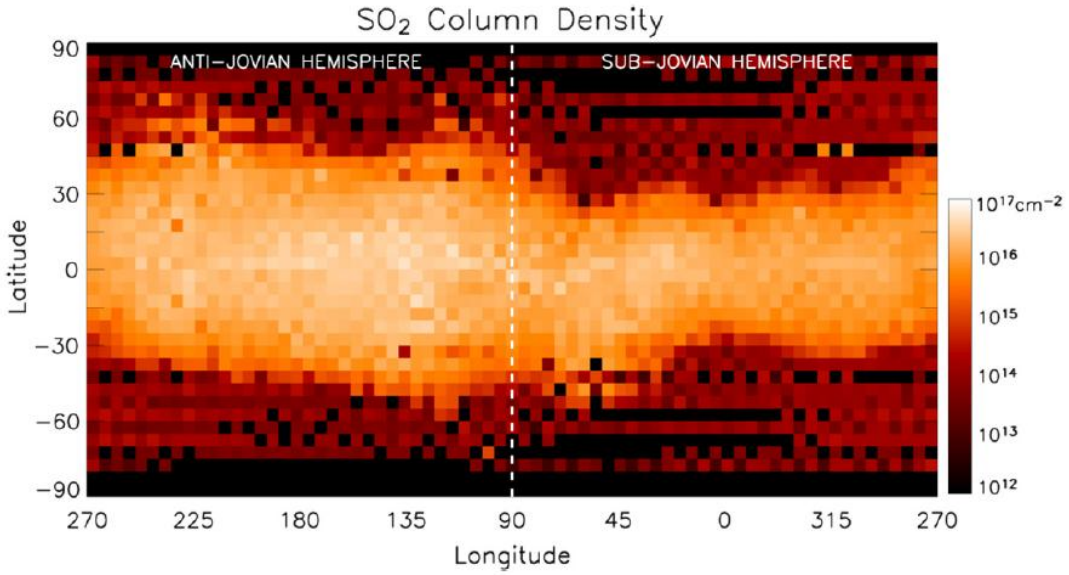

Figure 2.3: The average dayside column density compiled from an extensive set of Lyman-α observations. Note the higher magnitude and larger latitudinal extent of the anti-Jovian hemisphere in comparison to the sub-Jovian hemisphere. (*From Feaga et al. (2009), courtesy of Elsevier*).

Feaga *et al.* (2009) obtained Lyman-α spectroscopic data with HST. At 1216 Å, SO_2 is a continuum absorber with a large absorption cross-section, meaning that solar Lyman-α radiation will be attenuated by Io's column of SO_2. The attenuation enables the derivation of the SO_2 atmosphere's spatial extent and column density. These derived vertical column densities were found to have small absolute temporal variation, except in specific locations usually around known volcanic centers. Feaga *et al.* (2009) also created a spatially smoothed global map of the SO_2 distribution from the individual images across all observed orbital longitudes by averaging the vertical column density at points where the images overlapped (see

Figure 2.3). The global map shows a distinct asymmetry between the abundance of SO_2 on the sub-Jovian and anti-Jovian hemispheres. The peak vertical column density was determined to be 5.0×10^{16} cm^{-2} on the anti-Jovian hemisphere, 4.2×10^{16} cm^{-2} at the anti-Jovian point, and 1.5×10^{16} cm^{-2} at the sub-Jovian point. The column densities at high latitudes above 45º were suggested to be below 1×10^{14} cm^{-2}. The anti-Jovian hemisphere's peak vertical column density does not lie at the anti-Jovian point possibly due to volcanic activity since the peak occurs (at 140º W along the equator) near Prometheus.

2.3 SURFACE OBSERVATIONS

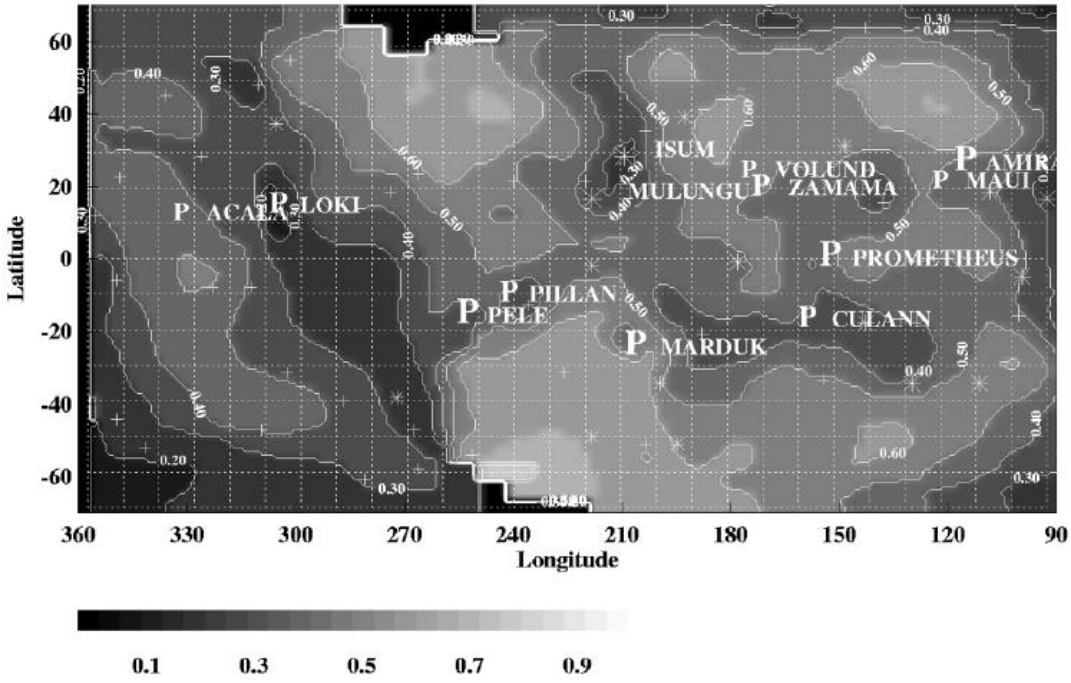

Figure 2.4: SO_2 frost fraction over nearly three quarters of Io's surface inferred from Galileo NIMS observations. (*From Douté et al. (2001), courtesy of Elsevier*).

The SO_2 surface frost abundance has been mapped by McEwen *et al.* (1988) based on Voyager multispectral mosaics, Carlson *et al.* (1997) with the Galileo near-infrared mapping spectrometer (NIMS) data, Douté *et al*. (2001) with hyperspectral

data cubes from Galileo NIMS, and others (Nash *et al.*, 1980; Nelson *et al.*, 1980; Howell *et al.*, 1984; Sartoretti *et al.*, 1994; Geissler *et al.*, 1999). McEwen *et al.* (1988) found that SO_2 frost is concentrated near the equator and is relatively deficient near Pele-type volcanoes and near the polar regions in stark contrast to the results of Douté *et al.* (2001). Carlson *et al.* (1997) found frost nearly everywhere with localized concentrations of thicker deposits the inferred locations of which vary with observation wavelength. At 3.35 μm, the frost abundance appears largely equatorial; however, there are polar deposits seen at both 2.79 μm and 3.78 μm.

The distribution of SO_2 frost on Io's surface should be closely linked with the surface temperature and the column density if the atmosphere is driven by sublimation. Douté *et al.* (2001) investigated the abundance of SO_2 frost by analyzing images acquired by the Galileo NIMS instrument. By assuming that the deposits of SO_2 frost are optically thick and geographically mixed, they found the SO_2 frost distribution over about three quarters of Io's surface (while the remaining quarter of the surface was not observed; see Figure 2.4). They found that frost is omnipresent over Io's surface but is concentrated within several large areas centered at medium latitudes which show a longitudinal correlation with the distribution of plumes at lower latitudes (Douté *et al.*, 2001). Although there are no data from 0º W to approximately 60º W longitude, the sub-Jovian longitudes between 270º W and 360º W show a lower average frost abundance than the anti-Jovian hemisphere, which could relate to the anti-Jovian hemisphere having a higher atmospheric vertical column density.

More recently, Laver and de Pater (2008, 2009) have mapped the equivalent widths of two SO_2 frost absorption bands at 1.98 and 2.13 μm using the OH Suppressing Infra-Red Integral field Spectrometer (OSIRIS) on the W.M. Keck II telescope. In their 2008 paper, they found that the frost abundance (based on the equivalent widths) correlated more closely with the maps of McEwen *et al*. (1988)

than those of Douté *et al*. (2001). They tentatively proposed that the differences between the maps may be due to the mapping of different grain sizes. In Laver and de Pater's most recent work (2009), they expanded upon their previous work by mapping both the trailing and leading hemispheres in the same two SO_2 frost absorption bands and by converting their equivalent widths into SO_2 frost abundance. The increased coverage allowed additional comparison to the SO_2 frost maps of Carlson *et al.* (1997). The Laver and de Pater (2009) frost maps are very similar to those of McEwen *et al.* (1988) and two of the Carlson *et al.* (1997) maps (derived from 2.79 μm and 3.35 μm bands of SO_2) all of which found large regions of SO_2 frost near the equator; however, they disagree with a third Carlson *et al.* (1997) frost map (derived from the 3.77 μm band of SO_2) and the frost map created by Douté *et al*. (2001). Laver and de Pater (2009) again theorize that the disparity in the frost maps is due to the different grain sizes that are probed with the different spectral bands. They suggest that the weak SO_2 frost absorption bands (1.98 μm and 2.12 μm) are more sensitive to the older frost regions with larger grain sizes due to grain growth over time; they are not able to probe the fine grains that may exist at higher latitudes. Douté *et al*. (2001) used a broad spectral region to map the SO_2 frosts and therefore were able to detect the fine grained frosts at higher latitudes. We have chosen to use the Douté *et al.* (2001) data in our simulations because they provide the most comprehensive map of Io's SO_2 frost distribution and appear to include the fine-grain polar deposits.

Simonelli *et al*. (2001) used two sets of Galileo images taken with red, green, and violet filters to construct bolometric Bond albedo maps of Io's surface. The bolometric Bond albedo is the true energy balance albedo and is dependent on all wavelengths. Despite their observations being taken only over specific wavelength regimes, they were taken near the maximum of the solar spectrum which increases the

validity of the bolometric Bond albedo maps generated. Simonelli *et al*. (2001) found that the global mean bolometric Bond albedo was ~0.52.

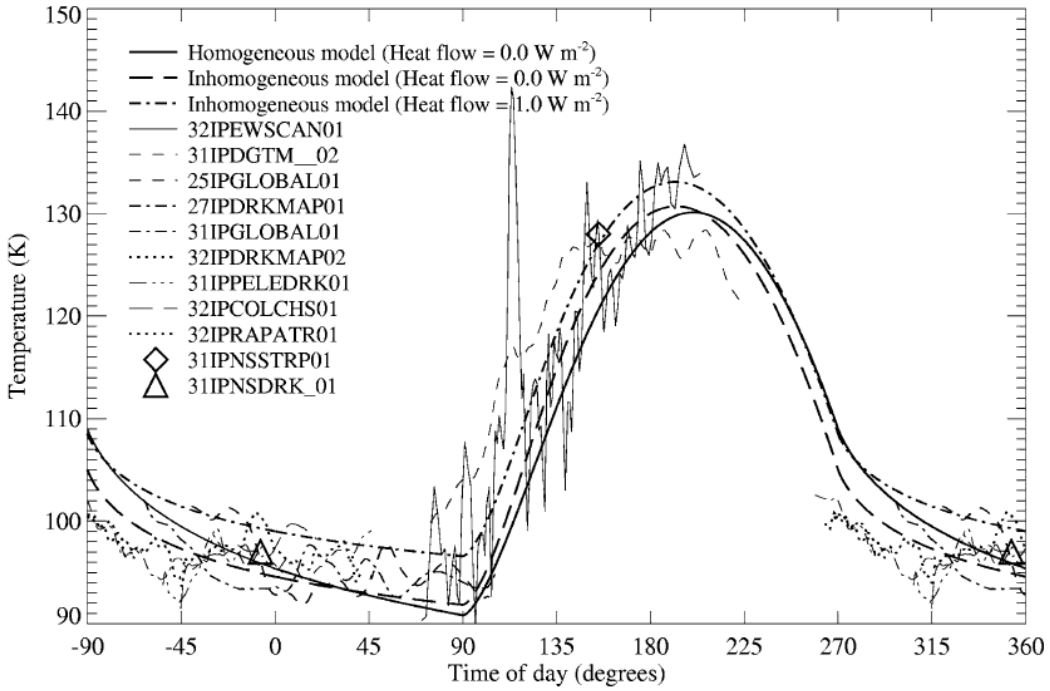

Figure 2.5: The near equatorial diurnal variation of the surface brightness temperature observed by the Galileo PPR. The observations are fit by three separate surface temperature models which vary the thermal inertia, albedo, and heat flow to the surface. (*From Rathbun et al. (2004), courtesy of Elsevier*).

There are numerous observations and thermal models of Io's surface which can help constrain the surface thermophysical parameters. Sinton and Kaminski (1988) observed Io in eclipse at several infrared wavelengths. To fit their data adequately they found that Io's surface must be composed of two different albedo regimes (light and dark) and that the thermal inertia of the bright component was nearly 10 times that of the dark component. In their best fit two-albedo case having a dark component homogeneous in depth and a bright component inhomogeneous in depth (e.g. a thin layer of bright material over another material of differing thermal parameters), the albedos and thermal inertias were $\alpha_F = 0.475$ and

$\Gamma_F = 56.65$ J m^{-2} K^{-1} s$^{-1/2}$ for the high albedo (bright) component and $\alpha_{NF} = 0.103$ and $\Gamma_{NF} = 5.17$ J m^{-2} K^{-1} s$^{-1/2}$ for the low albedo (dark) component. Veeder *et al*. (1994) analyzed over 10 years of infrared observations (1983 – 1993) of Io and constrained the global heat flow to be more than 2.5 W m^{-2} with the majority coming from large warm (>200 K) volcanic regions. They fit the observational data with a thermal model comprising three units: an equilibrium unit (zero thermal inertia, $\alpha_{NF} = 0.29$, ~20% areal coverage), a reservoir unit (infinite thermal inertia, $\alpha_F = 0.58$–0.70, ~80% areal coverage), and thermal anomalies (hot spots and thermal inertia anomalies).

Our modeled diurnal surface temperature variation is compared to data recorded by the Galileo spacecraft's PPR and NIMS instruments between 1999 and 2002 (Rathbun *et al.* 2004). The NIMS instrument measured emission from hot spots with temperatures greater than 200 K, while the PPR was able to probe the cooler temperatures of the passive background. The present simulations are compared to the temperatures derived from the PPR data because we are interested in the passive background temperature of SO_2 surface frosts and non-frosts. Rathbun *et al*. (2004) observed the radiated flux and converted these measurements to brightness temperature (for single wavelength observations) or effective temperature (for open filter observations). The brightness temperature is defined as the temperature of a blackbody emitting an observed power at the observed wavelength whereas the effective temperature is defined as the temperature of a blackbody emitting an observed power at all wavelengths. To follow the convention of Rathbun *et al*. (2004), the calibrated temperatures will be referred to as "brightness temperatures" whether or not they are actual brightness temperatures or effective temperatures. See Table 1 of their paper for the filter used for each observation. At 27 μm, the dayside brightness temperature distribution showed the expected pattern with the temperature peaking near the subsolar point. Non-volcanic anomalies were present in the

temperature distribution which could be attributed to variations in the thermal inertia of the surface. On the nightside, the brightness temperature is dominated by the presence of hot spots. The passive background nightside temperature was ~95 K both near the poles and equator, suggesting little drop-off with latitude. They constrained the global heat flow to between 2.0–2.5 W m^{-2} and also attempted to fit the surface thermal distribution with a two-component thermal model (see Figure 2.5). The low-latitude diurnal variation is well matched by two components with the following thermophysical parameters: unit one ($\alpha_F = 0.70$, $\Gamma_F = 100$ J m^{-2} K^{-1} $s^{-1/2}$, 50% areal coverage) and unit two ($\alpha_{NF} = 0.34$, $\Gamma_{NF} = 40$ J m^{-2} K^{-1} $s^{-1/2}$, 50% areal coverage).

Thermophysical Parameters				**Reference**
Bond Albedo		Thermal Inertia		
α_F	α_{NF}	Γ_F	Γ_{NF}	
0.475	0.103	56.65	5.17	Sinton and Kaminksi (1988)
0.58-0.70	0.29	∞	0	Veeder *et al*. (1994)
0.75	N/A	25-100	N/A	Kerton *et al*. (1996)
0.7	0.34	100	40	Rathbun *et al*. (2004)

Table 2.1: Thermophysical parameters for Io's surface from the literature.

All of these thermal observations require a minimum two-component surface thermal model to match the data. In all cases, one "bright" component has a fairly high albedo and a high thermal inertia. This "bright" component is likely associated with condensed patches of SO_2 surface frost; this component will referred to as the "frost surface" for the rest of this work. The second "dark" component has a lower albedo and thermal inertia. This "dark" component may be associated with either pyroclastic dusts or fine-grained sulfur allotropes; this component will be referred to as the "non-frost" surface for the rest of this work. Although these observations are consistent with a two-component surface thermal model, the range of parameters which fit the data is surprisingly wide ($\alpha_F = 0.475$ to 0.70, $\alpha_{NF} = 0.103$ to 0.34,

Γ_F = 56.65 J m^{-2} K^{-1} s$^{-1/2}$ to ∼∞, Γ_{NF} = ∼0 to 40 J m^{-2} K^{-1} s$^{-1/2}$). One of the key goals of this work is to further constrain these parameters based on recent observations.

2.4 JOVIAN PLASMA TORUS OBSERVATIONS

Jupiter's magnetosphere is the largest and strongest in the solar system and traps ionized atoms and molecules that are supplied by Io's atmosphere. These ionized particles (primarily O+, S+, and electrons) form the Jovian plasma torus and sweep past Io at 57 km/s causing atmospheric heating, sputtering from the surface, and changes to circumplanetary winds. Jupiter's magnetic field is tilted 10° relative to the rotation axis which leads asymmetries in the interaction between Io and the plasma torus depending on Io's System III longitude. For a detailed review of the Jovian plasma torus, see Saur *et al*. (2004).

In late 1973, Pioneer 10 detected Io's ionosphere with a peak dayside electron density of ∼6×10^{10} m^{-3} and gave the first hint of the interaction between Io's atmosphere and the Jovian plasma torus (Kliore *et al*., 1975). These observations also helped explain earlier ones that had detected Jovian decametric radio emission (Bigg, 1964). The next direct observation of Jovian plasma torus' interaction with Io's atmosphere came in 1979 from Voyager 1 which flew through the Jovian plasma torus and measured the number densities of ions and electrons and their spectra (Bridge *et al*. 1979a; 1979b; Broadfoot, 1979; Scarf *et al*., 1979, Warwick *et al*, 1979; Bagenal and Sullivan, 1980). The Voyager 1 spacecraft observed that the number density increased by six orders of magnitude between the innermost magnetopause (∼47 R_J) and closest approach (∼5 R_J) and indicated an electron temperature of ∼10^5 K in the plasma torus. There were also observations of strong atomic and molecular auroral emission near Jupiter's poles, high frequency electrostatic waves, strong whistler mode turbulence, and discrete whistlers (Broadfoot, 1979; Scarf *et al*., 1979).

Since Voyager 1, the Galileo and Cassini spacecrafts have taken new measurements of the Jovian environment and further refined our knowledge of the Jovian plasma torus. Models of the Galileo flybys have proven that Io has no intrinsic magnetic field (Kivelson *et al*., 2001; Saur *et al*., 2002). Galileo observations also revealed that the electron number density in the plasma torus is $\sim 3.6\times10^{3}$ cm^{-3} with a temperature of $\sim 1.2\times10^{6}$ K (Frank *et al*., 1996). These are nominal values for the undisturbed plasma torus and vary with Io's System III longitude (e.g. the electron number density peaked at $\sim 1.8\times10^{4}$ cm^{-3} at closest approach).

2.5 COMPUTATIONAL STUDIES

Spatially resolved observations have still not uncovered the dominant atmosphere production mechanism on Io. Our atmospheric model will attempt to answer this unresolved question. There have been several attempts to model Io's rarefied atmosphere, starting with Ingersoll *et al.* (1985). Ingersoll *et al.* vertically integrated the conservation equations and argued for the existence of sublimation-driven flow. They assumed turbulent atmospheric flow, a negligible effect from planetary rotation, and uniform frost coverage controlled by a surface in instantaneous radiative equilibrium with solar radiation. They found that pressure-driven supersonic flow develops as gas sublimates from areas near the warm subsolar region and condenses in the colder regions near the terminator. Similar results were found by Moreno *et al.* (1991) who allowed the atmosphere to vary with altitude and also included a crude radiative transfer model to account for atmospheric cooling to space and atmospheric heating from the surface. Both found that the net sublimation region extends from the subsolar point to a solar incidence angle $\theta \leq 37^{\circ}$ with their particular assumptions. The net condensation region, where the atmospheric pressure becomes higher than the vapor pressure of SO_2, was found to occur beyond about 37º. Strobel *et al*. (1994) were the first to report on the importance of plasma heating on

the vertical structure of Io's atmosphere. They developed a radiation-conduction model including the effects of solar, Joule, and plasma heating and found that the upper atmosphere is heated predominantly by Joule and plasma heating.

Wong and Johnson (1995) computed the effect of plasma heating on Io's sublimation atmosphere and found it inflated the upper atmosphere significantly. In 1996, Wong and Johnson (1996) improved upon their previous model by including photochemistry and tracking the daughter species of SO_2. More recently, Wong and Smyth (2000) refined the plasma model to allow incoming plasma ions to reaccelerate after a collision with a neutral in the atmosphere. Their result, which was qualitatively consistent with results of other models, showed that SO_2 was the dominant atmospheric species (compared to SO, S, O, O_2, and ions) and that the SO_2 column density dropped significantly on the nightside. Their ratio for the SO_2 density at the subsolar point to that of the nightside was $\sim 10^3$ and they suggested that other condensable species (S and O) follow this trend. In 2004, Smyth and Wong (2004) incorporated electron chemistry into their atmospheric model and found that the number densities of O, SO, S, and O_2 were greatly enhanced nearly everywhere and became comparable to SO_2 at high altitudes and on the nightside. These simulations all modeled the atmosphere as a continuum; this is a poor approximation at high altitudes and away from the subsolar region (see Fig. 3 in Austin and Goldstein (2000)).

There have been many attempts to model the Jovian plasma torus as well as its interaction with Io's atmosphere. There are two broad classes of methods used to simulate the Jovian magnetosphere: one either solves the magnetohydrodynamic (MHD) equations (Linker *et al*., 1991; Linker *et al*., 1998; Combi *et al*., 1998; Kabin *et al*., 2001) or uses an electrodynamic model (Saur *et al*., 1999; 2000; 2002).

Linker *et al*. (1991) solved the complete set of time-dependent MHD equations and found that field-aligned currents form Alfvén wings downstream of Io

and that the plasma flow diverts around Io. Linker *et al*. (1998) was able to reproduce many aspects of the Galileo flyby with MHD computations including a high plasma density (caused by ion pickup), low plasma temperature, and a depression in the magnetic field magnitude in Io's wake. Combi *et al*. (1998) applied a three-dimensional multi-scale MHD model to simulate plasma flow past Io's atmosphere. They were able to quantitatively explain variations in plasma density and temperature along the Galileo spacecraft's trajectory. Kabin *et al*. (2001) included a day-night asymmetry in Io's atmosphere and were able to reproduce several of the smaller features observed in the Galileo December 1995 flyby. Lipatov and Combi (2006) used a hybrid kinetic (for ions) and MHD (for electrons) model to simulate the interaction between the plasma flow and Io's atmosphere. With the hybrid method, they were able to resolve the ion motion more accurately and account for the anisotropic velocity distribution of the ions. They were also able to reproduce the Galileo I0 flyby double peak magnetic field structure.

Saur *et al*. (1999) developed a three-dimensional, two-fluid model (electrons and one ion species) to simulate the interaction between the Jovian plasma torus and Io's atmosphere. Their model self-consistently calculates the electric field around Io as well as the density, temperature, and velocity of both fluid species but assumes a constant unperturbed Jovian magnetic field. They find that anisotropic conductivity is essential to properly understand the current systems around Io and that the electric field is twisted past Io due to the Hall Effect. Saur *et al*. (2000) extended the model with an improved treatment of electron heat flux along magnetic flux tubes and used it to simulate the auroral emission of OI 1356 Å from Io's atmosphere. They compared their simulations to auroral observations (Roesler *et al*., 1999) and were able to explain the brighter anti-Jovian spot as being due to the Hall Effect. Saur *et al*. (2002) applied their electrodynamic model to the I0, I24, and I27 Galileo flybys of Io and showed that all of the Galileo spacecraft's observations can be explained without

an intrinsic magnetic field (Saur *et al*., 2002; Kivelson *et al*., 2001). They were also able to reproduce the double peak magnetic field structure measured during the Galileo I0 flyby which is caused by diamagnetic and inertia currents.

Some pure modeling of Io's surface thermal distribution has been done. Kerton *et al*. (1996) modeled Io's temperature distribution while including the effects of latent heat of SO_2 frost sublimation/condensation, thermal inertia, internal heat flow, and the solid state greenhouse effect. The solid state greenhouse effect allows for a porous surface where sunlight is able to penetrate deep into the surface layers. For SO_2 frost they chose $\alpha_F = 0.75$ and to define the thermal inertia they used parameters similar to those on other planetary bodies resulting in: $\Gamma_{MIN} \sim 25$ J m^{-2} K^{-1} s$^{-1/2}$, $\Gamma_{MAX} \sim 100$ J m^{-2} K^{-1} s$^{-1/2}$. They find that the surface temperatures are decreased by each effect except for the internal heat flow (which they assumed to be zero for most of their computations). Thermal inertia was found to have the largest effect (~14 K) when the thermal conductivity was close to the value of other planetary regolith materials. The latent heat caused a peak temperature drop of ~5 K and the solid state greenhouse effect dropped the peak temperature another ~2 K.

Several simulations have been performed using particle methods which can accurately model Io's rarefied atmosphere. Pospieszalska and Johnson (1996) used Monte Carlo calculations to characterize the effect of ion bombardment on the vertical structure and loss rate of Io's atmosphere. They found that the energy removed from the atmosphere by sputtering becomes a significant fraction of the plasma energy deposited for large ion cross-sections and that this affects the exobase temperature, but leaves the exobase altitude and density virtually unchanged. Austin and Goldstein (2000) used the DSMC method to simulate the circumplanetary flow on Io. They presented a two-dimensional axi-symmetric simulation of sublimation/condensation driven flow and suggested that the atmospheric flow never

reaches much past the terminator due to rapid condensation beyond the terminator shock or due to obstruction by non-condensable gases. Recently, Moore *et al.* (2009) used DSMC to simulate Io's sublimation atmospheric vertical dynamics throughout eclipse in the presence of non-condensable species (such as O_2 or SO). They found that even moderate non-condensable mole fractions significantly slowed the condensation of the SO_2 atmosphere onto the surface as it cooled, because of the formation of a thick diffusion layer of non-condensable gas near the surface.

CHAPTER 3: COMPUTATIONAL METHODS & MODELS

3.1 OVERVIEW

Here we present a fully three-dimensional model of Io's sublimation atmosphere computed using the DSMC method (Bird, 1994). The atmospheric density is controlled by the local vapor pressure and local areal coverage of SO_2 surface frost. The gas densities span the range from highly collisional (near the peak surface frost temperature at low altitudes) to free molecular flow (at high altitudes and on the nightside). Previous models of Io's atmosphere have been either one-dimensional, in which only the vertical structure and temporal evolution are investigated, or two-dimensional, which are axi-symmetric about the subsolar point. Also, some previous computational models approximated Io's rarefied atmosphere as a continuum, whereas our model uses the DSMC method which is valid throughout the entire atmosphere. Our three-dimensional simulation is able to model asymmetries in atmospheric parameters such as density, temperature, and flow velocity due to planetary rotation and an inhomogeneous frost distribution.

Our current DSMC code includes many adaptations and modifications of Bird's original DSMC procedure (Zhang *et al.*, 2003; Stewart *et al.*, 2009, Moore *et al*., 2009; 2011; 2012; Walker *et al*., 2010; 2011; 2012). The particles experience a gravitational body force and therefore travel along ballistic trajectories after sublimating from the surface. The rotational and vibrational energy states of SO_2 molecules are tracked and internal energy exchange occurs during collisions. Rotational energy levels are considered to be continuous while vibrational energy states are discrete due to the relatively cold temperatures in Io's atmosphere; all three

modes of vibration are treated for SO_2. The vibrational and rotational states are initially populated at the inner boundary (the surface of Io) by assuming that sublimated molecules are in thermal equilibrium with the surface. During the gas dynamics calculation, the atmosphere is assumed to be optically thin, so that any radiation emitted from an SO_2 molecule is lost to space or Io's surface. For a detailed account of the internal energy exchange and radiation modeling, see Zhang *et al.* (2003). Plasma heating is modeled by two separate methods. In Section 3.2.8, an energy flux method is summarized while Section 3.4.3 summarizes a particle description of the plasma. The surface frost coverage is modeled using derived frost fractions from hyperspectral images acquired by Galileo's NIMS (Douté *et al.,* 2001). The implementation of the surface frost model is discussed in detail in Section 3.2.3. Similar to plasma heating, the surface temperature is modeled by two separate methods. In Section 3.2.3, the surface temperature distribution is modeled with an integrated thermal inertia based on the approach of Saur *et al*. (2004). In Section 3.3.2, the surface temperature distribution is modeled by solving the one-dimensional heat conduction with depth into the surface and accounting for the effects of thermal inertia, latent heats of sublimation and condensation, endogenic heating, eclipse by Jupiter, and radiation from Jupiter. The planetary rotation of Io is included through the spatially and temporally varying temperature distribution model but the Coriolis force is neglected. In light of the most recent simulations that include the pressure of plasma from the Jovian plasma torus, the Coriolis may not be negligible. The ratio of inertial to Coriolis forces is measured by the Rossby Number

$$Ro = \frac{U}{2\omega \sin(\phi) L} \tag{3.1}$$

where U is the velocity in the system, ω is the rotation rate, and L is the length scale of the motion. For Io, $U \approx 300$ m/s, $\omega = 4.1 \times 10^{-5}$ s^{-1}, and $L \approx 8500$ km (winds flow approximately three quarters of the way around the planet in the prograde direction

from Io's peak pressure region to the dawn terminator due to the plasma pressure). The Rossby number at the equator ($\phi = 90°$) is Ro~0.86, meaning that Coriolis forces in this scenario are comparable to the inertial forces. Simulations without the plasma pressure have larger Rossby numbers of ~2.8. Lastly, 26 persistent hot spots are also modeled based on Keck AO observations (Marchis *et al*., 2005). See Section 3.3.5 for the details of hot spot modeling.

The following sections are arranged to clearly delineate the model progression for these atmospheric simulations. First, in Section 3.2, the physical and numerical models included in the original simulations (discussed in Chapter 4) are reviewed in detail. Second, in Section 3.3, the major updates – an updated thermal model and hot spots – to the original model for the second round of DSMC atmospheric simulations (discussed in Chapter 6) are explained. Finally, in Section 3.4, the final updates – a particle description of the plasma, photo-chemistry, and surface sputtering – to the model for the third and final round DSMC atmospheric simulations (discussed in Chapter 7) are explained. This structure is selected to make it clear to the reader the physics included in each simulation and how the complexity of the simulations has progressed.

Table 3.1 – 3.3 summarize the differences between the three models. Only refinements are included for Chapter 6 and 7. It should be assumed that unless a physical model is mentioned, it uses the original model from the Chapter 4 simulations. Lastly, to clarify which work is my own and which was done by others, each item lists the primary author(s) of the work:

Results Chapter	Physical Model	Author
CHAPTER 4	Single species – SO_2. Tracks rotational and vibrational energy states as well as radiation from those excited states	Ju Zhang
	Three-dimensional and global (all latitudes and longitudes)	Bénédicte Stewart
	Parallel (decomposed across 360 processors in the azimuthal direction)	Bénédicte Stewart, Chris Moore, **Andrew Walker**
	Variable gravity	Victor Austin
	Exponentially stretched vertical grid and uniform lateral grid	Victor Austin
	Two-component surface (frost and non-frost)	**Andrew Walker**
	Inhomogeneous SO_2 surface frosts based on Galileo NIMS observations (Douté *et al*., 2001)	**Andrew Walker**
	Surface temperature distribution based on an integrated thermal inertia derived by fitting to radiance observations (Sinton and Kaminski, 1988)	**Andrew Walker**, Chris Moore
	Temperature-dependent residence time of SO_2 molecules on the non-frost surface	**Andew Walker**
	Plasma heating by a radial energy flux	Victor Austin
	Load balanced by forcing the same number of molecules per column of cells	**Andrew Walker**

Table 3.1: A summary of the work done by each graduate student on the planetary DSMC code for the simulation results of Chapter 4.

Results Chapter	Physical Model	Author
CHAPTER 6	Parallel (decomposed across 360 processors in both the azimuthal *and polar* directions).	**Andrew Walker**
	Temporally adaptive vertical grid that fits to the mean free path	Chris Moore
	Vacuum buffer cell that extends the vertical extent of the domain to reduce aphysical escape	Chris Moore
	Surface temperature distribution modeled by solving the one-dimensional heat conduction equation including the effects of thermal inertia, latent heats of sublimation and condensation, endogenic heating, radiation from Jupiter, and eclipse by Jupiter	**Andrew Walker**
	Hot spots on Io's solid surface	**Andrew Walker**

Table 3.2: A summary of the work done by each graduate student on the planetary DSMC code for the simulation results of Chapter 6.

Results Chapter	Physical Model	Author
CHAPTER 7	Particle description of the plasma	Chris Moore
	Ions from the Jovian plasma torus move along pre-computed magnetic field lines	Chris Moore
	Photo-chemistry (dissociation and ionization)	Bénédicte Stewart, Chris Moore
	Chemical reactions between the ions and neutral atmosphere which allows for physical sources for the daughter species of SO_2	Chris Moore, **Andrew Walker**
	Surface sputtering of frost surface	Chris Moore
	Surface sputtering of non-frost surface	**Andrew Walker**

Table 3.3: A summary of the work done by each graduate student on the planetary DSMC code for the simulation results of Chapter 7.

3.2 ORIGINAL MODEL FOR CHAPTER 4 SIMULATIONS

The first DSMC atmospheric simulations are global, three-dimensional, and parallel. Only the dominant dayside species, SO_2, is modeled. The surface model includes a two-component surface (frost and non-frost) and accounts for the inhomogeneous surface frosts observed by Galileo NIMS (Douté *et al*., 2001). Each surface component is modeled to have an independent surface temperature controlled by an integrated thermal inertia which is determined by fitting to radiance observations (Sinton and Kaminski, 1988). In addition, SO_2 molecules which adsorb to the non-frost surface stick for a residence time that is dependent on the non-frost surface temperature. Plasma heating due to ions from the Jovian plasma torus is modeled by a radial energy flux. Load balancing is achieved by computing a weighting function which forces each column of cells to have roughly the same number of molecules.

3.2.1 DSMC METHOD

The range of flow densities on Io fluctuates greatly from ~10^{11} cm^{-3} at low altitudes near the peak surface frost temperature to fewer than 10^3 cm^{-3} at high altitudes on the nightside. The atmosphere on and near the nightside is of such low density that the mean free path exceeds the length scales associated with gradients in the gas properties. In such conditions, continuum models break down and a rarefied gas dynamic technique must be applied. In such rarefied flow conditions, the DSMC method (Bird, 1994) is the most suitable choice. DSMC is advantageous because it is physically accurate in all flow regimes, although it becomes computationally expensive at high densities. In the DSMC method, the flow is modeled by computational particles (representing a far greater number of real particles) that move and collide. Note that in this context "particles" refers to both molecules and atoms. Atmospheric properties in a cell, such as temperature and density, are extracted by

sampling and averaging over all of the computational particles within the cell. The collision model used is the variable hard sphere (VHS) model (Bird, 1994), with the appropriate parameters for SO_2 and all daughter species (SO, S, O_2, and O).

3.2.2 3D GEOMETRY AND PARALLELIZATION

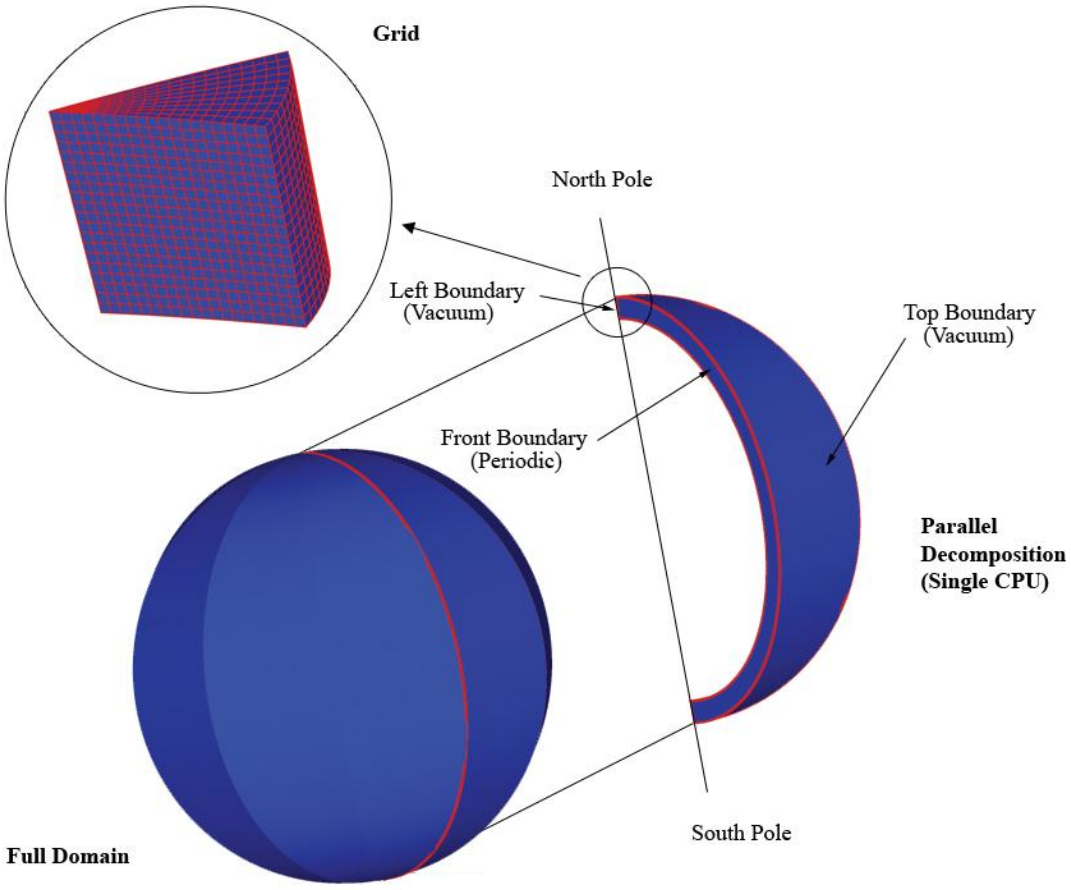

Figure 3.1: Decomposed spherical domain with relevant boundaries labeled. The full domain is in the lower left corner and single processor's domain is extracted (right) to show the geometry of the domain decomposition. To the upper left is an enlarged view of the north pole of a single processor showing the cell structure. The azimuthal domain shown for a single processor is exaggerated for clarity. (*From of Bénédicte Stewart (2010)*).

The computational model uses a three-dimensional spherical geometry with a coordinate system in which west is the direction of increasing longitude. The lower edge of the domain is the surface, which is defined to have a unit sticking coefficient

based on our sublimation model (Wagman, 1979; Zhang *et al*., 2003). Particles which strike the surface have a probability of striking either frost or non-frost (sulfur allotropes or pyroclastic dusts) depending on the frost fraction for that surface cell. The grid size exceeds the mean free path in longitude and latitude, but grid convergence studies were performed showing that the length scale of gradients in these directions remains satisfactorily greater than the cell size. The large numbers of computational cells and simulated particles require the use of parallel computers (Stewart *et al.*, 2009). The boundaries between processors are message passing interfaces so that when a particle crosses from processor A to B, all of its properties are passed from A to B.

The domain spans all latitudes and longitudes and from Io's surface to 200 km altitude. The upper edge of the domain has a vacuum boundary condition such that all particles crossing that boundary are deleted. This boundary condition for the upper edge is acceptable because the number densities at that altitude are very low ($\sim 10^{-3}$ of the gas number density near the surface) and there is little gas escaping that does not have escape velocity. Any error that this causes will be confined to minor changes in the radial velocity.

The grid is stretched exponentially (not shown in figure) in the radial direction to keep the cell height equal to or less than the local mean free path $\lambda = 1/\left(\sqrt{2}\pi n d^2\right)$, where $d = 7.16\times10^{-10}$ m is the effective diameter of SO_2 molecules. For a surface temperature of 120 K, the mean free path directly above the surface is ~1.5 m, but the mean free path grows exponentially with altitude and increases rapidly with solar zenith angle. At a lower surface temperature of 115 K, the local mean free path is ~7.5 m. The grid stretching rate depends only on the local surface temperature which results in a different grid stretching across processors. The cell size at high altitudes is limited to 5 km so as to remain smaller than the scale height of the atmosphere. The scale height, H, is approximately 8.3 km at the surface, where $H = RT/g$, R is the gas

constant, T is the gas temperature, and g is the gravitational acceleration at that altitude.

The cell sizes in latitude and longitude have a resolution of 1º, giving 180 cells in the polar direction and 360 cells in the azimuthal direction. The domain is decomposed in the azimuthal direction between 360 processors, with each processor receiving 1º of longitude (see Figure 3.1). Each processor simulates 21,600 cells and approximately 10 particles per cell are needed to give adequate statistics implying a minimum of $\sim 2\times10^5$ particles per processor. In fact, to yield adequate statistics at high altitudes, many more than $\sim 2\times10^5$ particles per processor are needed because the particles are distributed non-uniformly with altitude (and the grid spacing is uniform above ~30 km) with the majority of particles in the cells near the surface. The number of particles per processor is kept roughly constant by altering the weighting function to force the number of particles in each column of cells to be uniform (see Section 3.2.5). In the simulations presented, about 10 million particles are used per processor. The data are also time-averaged over the last 250 seconds of the simulation to decrease noise. Time-averaging is justified because the solution varies slowly in time and the time-average duration is much less than Io's rotational period of 42 hours. For each of the final data sets, $\sim 10^{12}$ particles are sampled throughout the entire domain.

3.2.3 INHOMOGENEOUS SURFACE MODEL

Douté *et al.* (2001) determined the SO_2 surface frost distribution based on the IR emission from Io's surface. Their fraction of frost covering the surface is given with one degree resolution in both latitude and longitude. There were no data available between longitudes of 0º W to approximately 60º W because these longitudes were not observed. Results at polar latitudes have a low degree of reliability because of the highly oblique viewing angle. We obtained an electronic

version of the data for the frost fraction from Sylvain Douté and, where no data were available, we computed the frost fraction using a linear interpolation scheme between 0º W to 60º W and pixel by pixel for polar latitudes. The resulting surface frost fraction utilized in the present work is shown in Figure 3.2. Notice that the frost fraction is quite low in the linearly interpolated region because the frost fractions on the edges of the observed domain at 0º W and 60º W are low. There are two large regions of high frost concentration on the anti-Jovian side at 50º N and 260º W and also at 60º S and 240º W. Both are regions where no large "persistent" volcanoes exist; however, these high frost concentration regions show a longitudinal correlation with the distribution of plumes at lower latitudes (Douté *et al.*, 2001; Geissler *et al.*, 2004; Marchis *et al.*, 2005). A region at 310º W and 10º N with a very low frost concentration corresponds to the location of Loki.

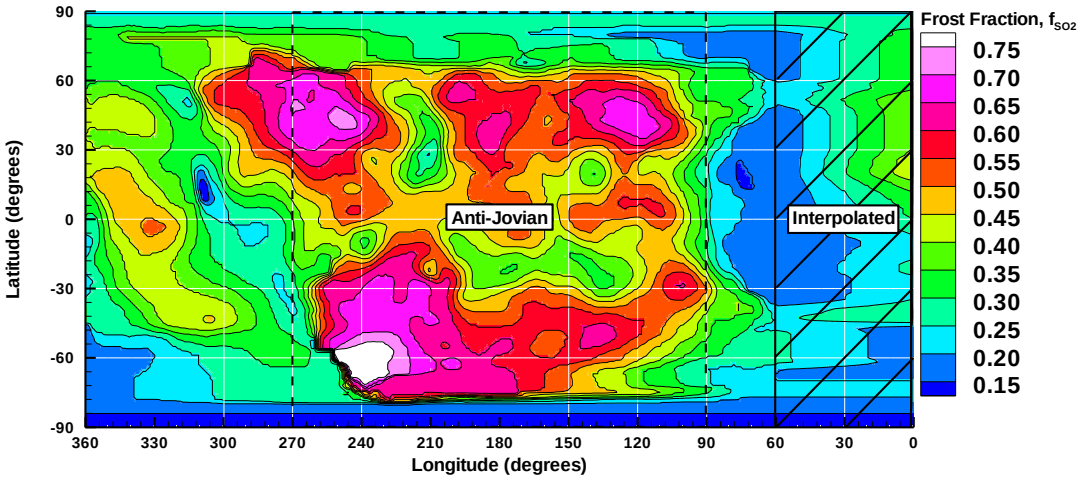

Figure 3.2: Contours of the fractional coverage of surface frost, f_{SO_2}, as obtained from Douté *et al*. (2001). The cross-hatched area indicates longitudes that are linearly interpolated. The dashed rectangle from 90º to 270º encloses the anti-Jovian hemisphere.

The frost and non-frost covered areas within each surface pixel are assumed to be separate and discrete (with a length scale on the order of kilometers). Lateral heat conduction between SO_2 frost and non-frost covered areas is thus assumed to be

negligible as the vertical heat fluxes into the top layer of the surface (with a length scale on the order of centimeters (Kerton *et al*., 1996)) will dominate any lateral heat fluxes. Each area element has its own independent temperature based on the emissivity, ε (assumed to be unity for both the frost and non-frost, similar to the value of 0.9 used by Veeder *et al*. (1994) and Kerton *et al*. (1996)), and thermal parameter, *Mc*, of that surface type. *Mc* (Saur and Strobel, 2004) is a thermal parameter derived by fitting to 20 and 30 μm radiance observations (Sinton and Kaminski, 1988). The latent heats of sublimation and condensation are neglected as minor effects compared to the thermal inertia (Ingersoll *et al.*, 1985; Kerton *et al*., 1996). The frost coverage fraction, f_{SO_2}, was used to modify the number of SO_2 gas molecules sublimated from surface frost. The sublimation rate of SO_2 molecules, N_{sub} [m^{-2} s^{-1}], is given by

$$N_{sub} = \frac{P_{VAP}}{\sqrt{2\pi k_B T_F m_{SO_2}}} f_{SO_2}, \tag{3.2}$$

where m_{SO_2} [kg] is the molecular mass of SO_2, k_B is the Boltzmann constant, the equilibrium vapor pressure, P_{VAP} [Pa], is defined by the Clausius-Clapeyron equation

$$P_{VAP} = Ae^{-B/T_F}. \tag{3.3}$$

Here $A = 1.52\times10^{13}$ Pa, $B = 4510$ K (Wagman, 1979), and T_F is the SO_2 surface frost temperature. The surface temperature (of either frost or non-frost), T_S [K], is determined by solving the radiative balance equation

$$\frac{dT_s}{dt} = \begin{cases} \frac{\varepsilon\sigma}{Mc}\left(T_{s,eq}^4 - T_s^4\right) \rightarrow dayside \\ \frac{\varepsilon\sigma}{Mc}\left(T_{\min}^4 - T_s^4\right) \rightarrow nightside \end{cases}. \tag{3.4}$$

Here σ is the Stefan-Boltzmann constant, T_{min} is the minimum (frost and non-frost) temperature, and $T_{s,eq}$ is an idealized radiative equilibrium solution for the surface temperature distribution (and the initial condition for Equation 3.4) defined by

$$T_{s,eq} = (T_{ss} - T_{\min}) \times \cos^{1/4}(\psi) + T_{\min}, \quad 3.5$$

where ψ is the solar zenith angle. The minimum temperature T_{min} is assumed to be 90 K based on the observations by the Galileo PPR (Spencer *et al.*, 2000, Rathbun *et al.*, 2004). The surface temperature distribution tends toward the equilibrium solution $T_{s,eq}$ but differs from it because of the thermal inertia of the surface.

The value of $T_{s,eq}$ at the subsolar point is defined to be T_{ss} (the subsolar temperature) and is the maximum possible temperature if there is no thermal inertia; however, this is not the value of the surface temperature at the subsolar point due to the thermal inertia of the surface. T_{ss} is parameterized to be either 120 K or 115 K for the separate cases shown in Chapter 4. The actual peak T_F is calculated to be 114.3 K when $T_{ss} = 115$ K and 119.1 K when $T_{ss} = 120$ K. As will be seen later, a peak temperature of 115 K yields column densities that agree with the lower bound of Lyman-α observations (Feaga *et al.*, 2009). A 120 K subsolar temperature yielded column densities that are approximately five times larger and are above the upper range of observations (Jessup *et al.*, 2004; Spencer *et al.*, 2005). The 120 K case serves as an upper limit on possible circumplanetary flow strengths. The thermal parameter, *Mc*, is chosen independently for the frost and non-frost surfaces, with *Mc* chosen to be 3500 J K^{-1} m^{-2} for frost and 388 J K^{-1} m^{-2} for non-frost. The values of *Mc* for frost and non-frost are chosen to provide an approximate match to the nightside cooling rate of the brightness temperature seen in Galileo PPR observations (Rathbun *et al.*, 2004). This thermal model cannot simultaneously match both the observed nightside cooling rate and the longitudinal lag between the subsolar point and the location of the peak frost temperature (Rathbun *et al.*, 2004). The updated thermal model which solves this problem is discussed in Section 3.3.2.

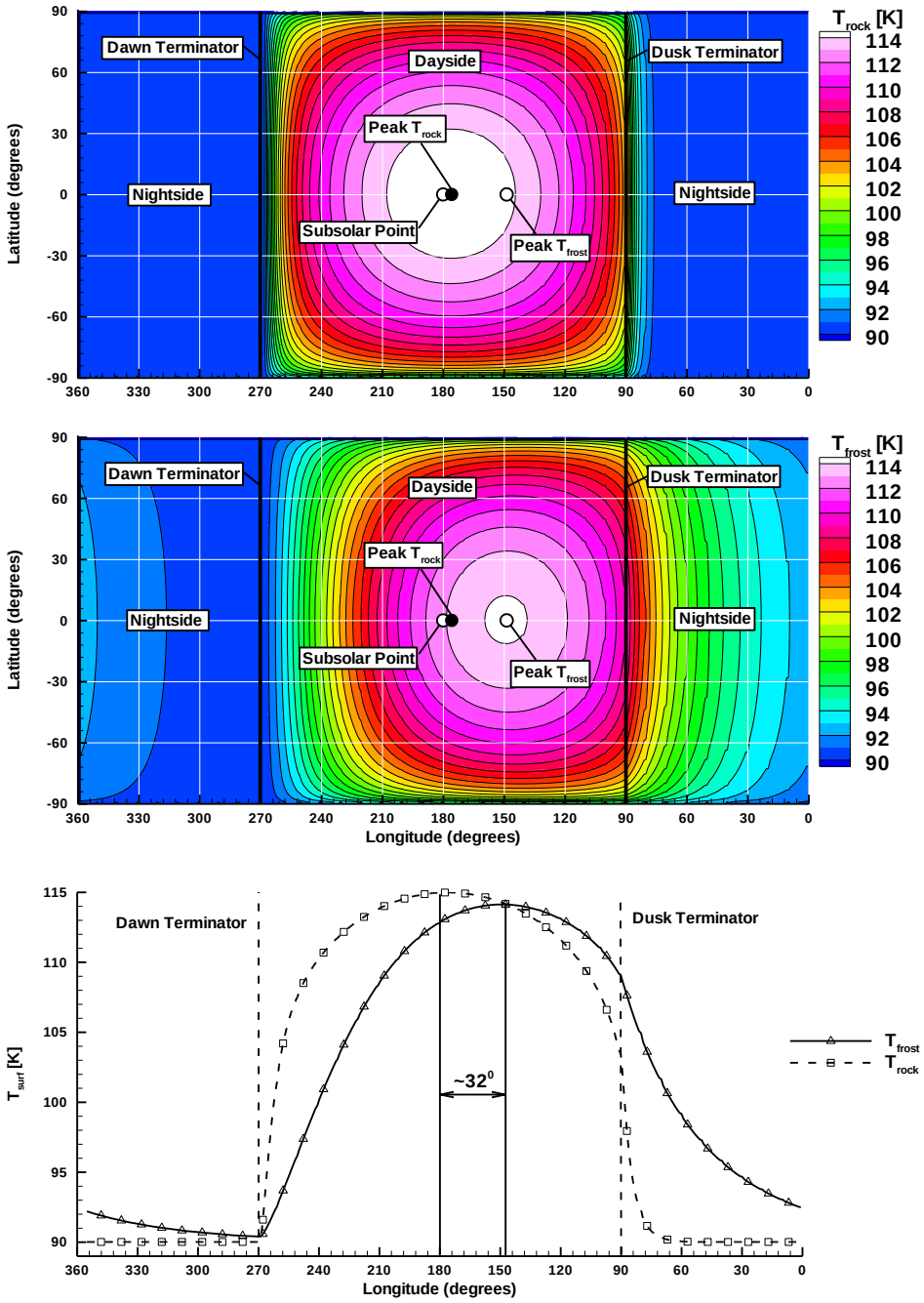

Figure 3.3: Color contours of (a) non-frost surface temperature (T_{NF}) and (b) surface frost temperature (T_F) as a function of latitude and longitude. (c) T_F and T_{NF} at the equator as a function of longitude. The subsolar longitude is 180º for all cases.

Due to its higher thermal inertia, the frost surface warms and cools more slowly than the non-frost surface. The frost does not reach its peak temperature until

~32º of rotation (or 3.5 hours) after the subsolar point as seen in Figure 3.3b. Because of this lag, the frost surface has only cooled to approximately 110 K at the dusk terminator. The exponential decrease of the frost surface temperature continues throughout the nightside and it is only just before dawn that T_F cools to within 1 K of the non-frost surface that is at 90 K. The non-frost surface temperature has a much lower thermal inertia and therefore follows radiative equilibrium closely (Figure 3.3a). The lower thermal inertia causes the non-frost surface temperature to reach its peak temperature only 4º of rotation (or 30 minutes) after the subsolar point, and it cools correspondingly quickly after dusk.

In addition to scaling the number of computational particles sublimated from the surface, the frost fraction is used to determine the probability of a particle landing on frost or non-frost if it hits the surface. If a particle lands on a frost covered surface, it is deleted from the computation, while a particle landing on a non-frost surface will remain stuck to the surface for a period of time (a residence time) dependent on the surface temperature. Particles landing on the frost covered areas are deleted because the sticking coefficient is defined to be unity for the vapor pressure model we use (Wagman, 1979) and the sublimated flux should model any (indistinguishable) particles that would be re-emitted from the frost surface. Due to memory limit issues, the exact location of particles stuck to the non-frost surface is not retained. Instead, resident particles are re-emitted randomly throughout the 1º×1º cell in which they hit the surface. The residence time on the non-frost surface (in seconds) is

$$t_{RES} = \frac{e^{\Delta H_S / k_B T_{NF}}}{\nu_0} \qquad 3.6$$

where $\nu_o = 2.4\times10^{12}$ s^{-1} is the lattice vibrational frequency of SO_2 within its surface matrix site and ΔH_s ($\Delta H_s/k_B = 3460 \pm 40$ K) is the surface binding energy of SO_2 on a surface of its own frost, and T_{NF} is the non-frost surface temperature (Sandford and

Allamandola, 1993). The two constants ΔH_s and ν_o assume a monolayer or more of SO_2 covering the non-frost surface. A longer residence time is also examined that is a thousand times longer than the short residence time given by Eq. 3.6 for SO_2 on SO_2 frost. The higher value represents residence times that could possibly occur with a highly porous surface (Matson and Nash, 1983) where particles undergo multiple reflections before being emitted into the atmosphere.

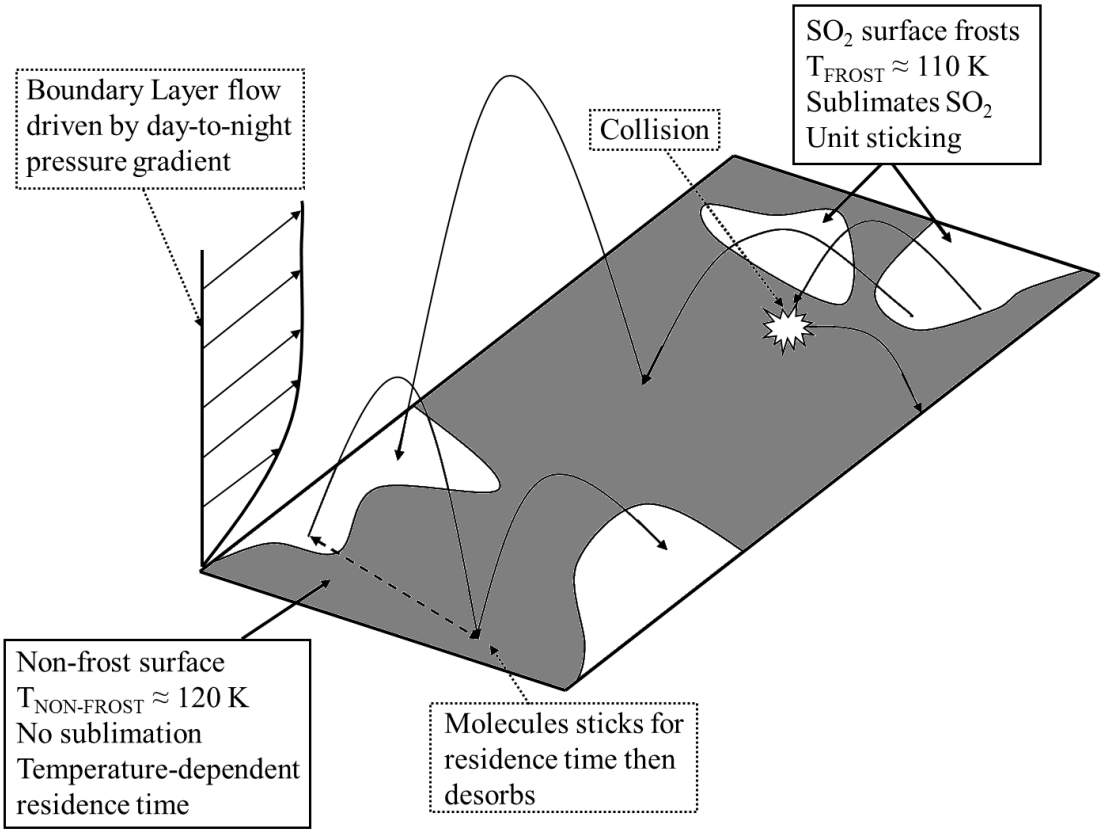

Figure 3.4: A schematic depicting Io's surface with segregated areas of frost (white) and non-frost (gray) with circumplanetary winds driven by the day-to-night pressure gradient flowing over the surface. Molecules which land on the surface have a unit sticking coefficient on the SO_2 surface frosts but have a temperature dependent resident time on the non-frost surface.

The residence time of an SO_2 molecule on non-frost surface (based on Eq. 3.6) on the cold nightside (90 K) is ~2×10^4 s which is over a quarter of Io's night (~7.5×10^4 s) and therefore most particles that fall on the nightside non-frost surface

will desorb at least once before dawn. The number of particles stuck to the non-frost surface will also be partially replenished by the condensation of thin nightside atmosphere. For the long residence time (LRT) model, the residence time at 90 K is $\sim 2\times10^7$ s and therefore nearly all the sublimated gas which falls on the nightside non-frost surface will remain stuck until dawn. At dawn the non-frost surface warms quickly and the residence time shortens dramatically to a few seconds for the short residence time of SO_2 on the non-frost surface and to approximately one and a half hours for the long residence time. As a result, the atmospheric density is *enhanced* near the dawn terminator by particles desorbed from the warming non-frost surface. For the short residence time (SRT) model the rapid rate of warming causes the enhancement to occur in a small band (~10º in longitude) stretching from pole to pole. This enhancement occurs over a much larger area (nearly the entire morning side) for the long residence time model. We refer to this outflux as the dawn atmospheric enhancement or DAE.

3.2.4 INITIAL CONDITIONS

Io's atmosphere varies slowly in time when the effects of planetary rotation and non-uniform frost coverage are included and eclipse is neglected. However, different physical time scales are relevant as the simulation approaches the final quasi-steady result. The time scales relate to (i) the thermal distribution of Io's surface, (ii) the distribution of SO_2 temporarily stuck to the non-frost surface areas, and (iii) the gas dynamics of the entire collisional molecular atmosphere. The quasi-steady state atmosphere is thus computed via a three step process. In step (i), the surface temperature distributions for the SO_2 frost and non-frost surfaces are determined with no atmosphere present. The temperature distributions of the SO_2 frost and non-frost surfaces are obtained from Eq. 3.4 with appropriate values of *Mc*

for SO_2 frost and non-frost surfaces, respectively, and allowed to relax to a steady state over three rotations of Io.

The quasi-steady state non-frost surface temperature distribution (shown in Figure 3.3a) computed in step (i) allows for the computation of the appropriate SO_2 surface frost density [cm^{-2}] on the non-frost surface based on the frost coverage and time of day. The thin layer of SO_2 on the non-frost is never thicker than ~10 μm and therefore should not affect the thermal properties of the non-frost below. In step (ii), the number of particles stuck on the non-frost is determined by simulating a very low number of particles (~100,000 per processor) without collisions. A quasi-steady state is achieved rapidly by using this relatively small number of particles and time averaging to yield adequate statistics for the SO_2 surface frost density on the non-frost surface. The non-frost surface boundary condition (i.e. the SO_2 number density stuck to the non-frost surface) is allowed to relax to steady state over one Io rotation.

With the surface boundary conditions now fully determined, the final quasi-steady atmosphere can be obtained by "cloning up" the particles used to obtain the non-frost surface boundary condition. The ~10^5 particles per processor are "cloned up" to ~10^6 particles per processor by altering the weighting function (the number of real particles each simulated particle represents). Collisions are turned on in step (iii) and relaxation is allowed to occur for about 30 minutes of rotation which is long enough for cloned particles to travel through several ballistic trajectories and thereby allow the cloned particles' spatial positions and velocities to diverge through collisions and randomization at the surface. The simulation then progresses for ~4 hours until the atmospheric winds have fully developed and the atmosphere is near a final quasi-steady state. This three step process reaches quasi-steady state at least an order of magnitude faster than beginning the calculation with a full complement of colliding particles and computing multiple rotations of Io. The atmosphere is in a final quasi-steady state when the gas properties such as temperature and density have

only small time variations attributable to the slowly changing surface temperature as Io rotates.

The approach to a quasi-steady is summarized in the following bulleted list:

- **Quasi-steady-state temperature distribution**
  - 3 rotations
  - Decoupled from atmosphere
- **Quasi-steady-state non-frost boundary condition**
  - 3 rotations
  - ~100,000 molecules per processor
  - No collisions
- **Quasi-steady-state atmosphere**
  - ~4 hours
  - Clone up to ~3 million molecules per processor
  - Turn on collisions

3.2.5 LOAD BALANCING

Io's atmosphere has large density variations which in simple DSMC could result in large variations in the number of particles per cell. Because of the large scale nature of the calculation, the maximum number of particles per cell is limited to ~100. Since the density varies over five orders of magnitude or more in the domain, 100 representative particles in the highest density cell would mean that many cells would on average have zero particles present. This statistical issue necessitates the use of a spatially variable particle weighting function. The weighting function adjusts the ratio of computational particles to real particles in every column of cells based upon the surface area and surface temperature of the cell at the base of the column. When a particle passes from one cell to a neighboring cell with a different weight, it is cloned or destroyed depending on the ratio of the two cell weights. For more details on weighting functions see Bird (1994). We have been careful when using weighting functions because they do not conserve mass, momentum, and energy exactly;

however, in the limit of large particle numbers, they are conservative on-average. The weighting function is implemented such that each column of cells will have the same number of computational particles at each time step. This is necessary because of the geometry of the spherical coordinate system which reduces the volume of cells near the poles as well as the large variations in density due to the exponential variation of SO_2 vapor pressure.

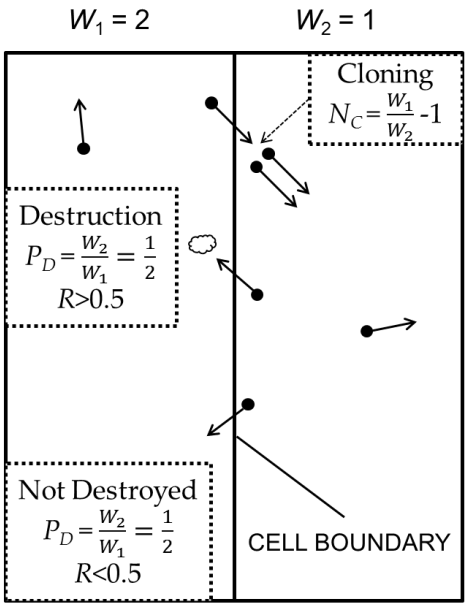

Figure 3.5: Schematic diagram depicting the stochastic process of cloning and destruction when particles pass to a cell with a different weight. Particles that pass from a $W = 2$ cell to a $W = 1$ cell will have a clone particle created. The clone particle will exist at the same location and have all the same particle properties (velocity, internal energy, etc.). Clone particles are randomized through collisions and/or interactions with the surface. If a particle passes in the opposite direction, $W = 1$ to $W = 2$, then the particle will have a 50% chance to be destroyed (e.g. deleted from the computation).

3.2.6 Calculation of Vibrational Temperatures

Disk-averaged mid-infrared observations of the ν_2 vibrational mode of SO_2 (Spencer *et al*., 2005) are an important constraint on our model. Properly calculating the vibrational temperature which was used by Gratiy *et al*. (2010) to compare to the mid-infrared observations is difficult because of the high characteristic temperature of

the ν_2 vibrational mode and the relatively cold temperatures present in Io's atmosphere. The following section summarizes the statistical difficulties in calculating vibrational temperature of the ν_2 mode.

The calculation of the gas vibrational temperature in the ν_2 vibrational mode of SO_2 is computationally difficult because the atmosphere in certain areas (especially areas where the plasma does not reach) is quite cold (<90 K). The vibrational temperature is calculated from (Bird, 1994):

$$T_{vib} = \frac{T_{ch}}{\ln\left(n_0/n_1\right)} \tag{3.7}$$

where T_{vib} is the vibrational temperature, T_{ch} is the characteristic temperature of the vibrational mode, n_0 is the number of molecules in the ground state, and n_1 is the number of molecules in the first excited state. Although vibrational levels above the first excited state are modeled in our code, such states are exceedingly rare in our simulations because plasma energy is only indirectly transferred into vibration by collisions and the gas is nearly free molecular where it is translationally hot (>300 K). Therefore, we will assume that higher excited states can be neglected for purposes of computing the minimum resolvable gas temperature. The total number of molecules in a cell is then equal to the sum of molecules in the ground state and the first excited state based on this assumption. Then the vibrational temperature can be re-written as:

$$T_{vib} = \frac{T_{ch}}{\ln\left(\left(N - n_1\right)/n_1\right)} \tag{3.8}$$

The minimum vibrational temperature which can be resolved for a total number of molecules per cell, N, can be calculated if we suppose $n_1 = 1$ (i.e. the lowest possible non-zero vibrational temperature which our simulation can compute occurs when only one molecule out of N is excited and the rest are in the ground state). Substituting for $n_1 = 1$ into Eq. 3.8:

$$T_{vib} = \frac{T_{ch}}{\ln(N-1)} \qquad 3.9$$

A reasonable estimate for the maximum feasible number of molecules per cell that can be sampled (assuming a time-average over 500 time steps and ~500 instantaneous molecules per cell) is $N \approx 2.5\times10^5$. Since we use a time step (Δt = 0.5 s) larger than the mean collision time (and time to cross a cell) in the lower atmosphere, the molecule properties are sufficiently randomized each time step such that each sample is likely unique. The characteristic temperature of the ν_2 vibrational band of SO_2 is T_{ch} = 745 K. For these values, the minimum vibrational temperature that can be resolved is ~60 K. As the vibrational temperature we wish to resolve decreases, the number of molecules needed to resolve that vibrational temperature increases exponentially. Luckily, the coldest temperatures in the dense atmosphere do not drop much (<5 K) below 60 K (confirmed by temporally and spatially resolved one-dimensional DSMC simulations) and therefore we can compute vibrational temperatures by time-averaging runs such that the total number of particles per cell is sufficient. Presently, we are not able to resolve cold vibrational temperatures above 100 km in altitude because the number of particles per cell drops below the required threshold and longer time-averages result in non-unique samples.

3.2.7 Superposition of Volcanic Plumes on the Sublimation Atmosphere

Since the relative contribution of volcanic plumes to Io's atmospheric column is non-negligible, especially locally, it is reasonable to assume that they should affect the observed disk-averaged ν_2 vibrational band of SO_2 at 19.3 μm. Therefore, pre-computed volcanic plumes were superimposed on the simulated sublimation atmosphere (see Figure 3.6) and their effect on the disk-averaged band depth is investigated with a backwards Monte Carlo radiative transfer code in Section 4.5 (Gratiy *et al.*, 2010). The model uses ten volcanoes, listed in Table 3.4.

Unfortunately, there is no comprehensive list of plume activity during Spencer *et al.'s* (2005) observations and so we chose the plumes based on their activity during the Galileo mission. We exclude highly episodic plumes (such as Tvashtar) and superimpose onto the sublimation atmosphere only those plumes that were generally active throughout the Galileo observations. We use Geissler *et al.*'s (2004) timeline of plume activity based on observed surface changes to determine the plumes that were "consistently" active throughout Galileo (Table 3.4).

Plume	Longitude, Latitude	Type
Kanehikili	40W, 18S	Prometheus
Masubi	55W, 44S	Prometheus
Amirani	115W, 26N	Prometheus
Thor	135W, 40N	Prometheus
Prometheus	155W, 2S	Prometheus
Culann	159W, 20S	Prometheus
Zamama	174W, 18N	Prometheus
Marduk	210W, 27S	Prometheus
Pele	258W, 19S	Pele
Loki[1]	309W, 13N	Prometheus

Table 3.4: Active plume list (Geissler *et al.*, 2004). [1]Active, Rathbun *et al.* (2002).

The volcanic plumes were computed separately using the same DSMC code in a smaller domain centered on the volcanic vent on a very finely resolved grid (Zhang *et al.*, 2003). The volcanoes were then superimposed onto the simulated sublimation atmosphere by adding the volcanic plume number density to the sublimation atmosphere number density. The local velocity, translational, rotational, and vibrational temperatures are then all mass-averaged based on the respective contribution from the plume and sublimation atmosphere. Note that there is no self-consistent interaction between the global atmosphere and the superimposed plumes during the independent simulations of the plumes and the sublimation atmosphere.

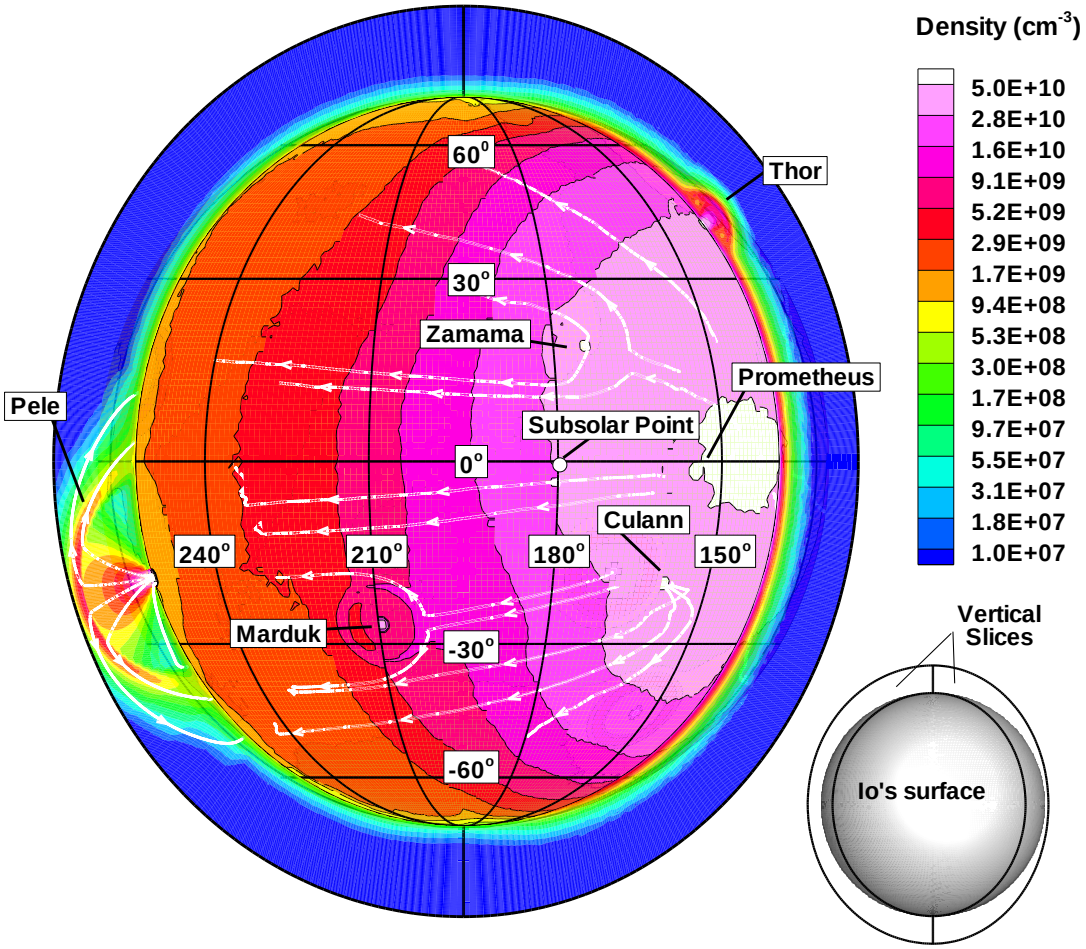

Figure 3.6: The density of the superimposed baseline sublimation and volcanic atmospheres at ~100 m above the surface plus two near-limb slices showing the vertical density field. Note that the viewing angle has been altered so that Pele is visible (i.e. the subsolar point is not at the center of the disk) and that the slices showing the vertical density profile on either side of Io's disk were selected to cut through two plumes and are not on the limb, hence the surface seen is not the full disk (see inset). Streamlines (white) are shown to illustrate the gas flow in the plumes and the diversion of the circumplanetary winds around the plumes. The streamlines are seen to end near where net condensation begins as the gas flows into the surface.

The simulation uses two general volcanic types, each of which can be either dayside or nightside (when the sublimation atmosphere is minor). Dayside plumes (computed with a surface temperature of 112 K) are used when the sublimation atmospheric density near the surface is large enough that the gas falling to the surface from the canopy is turned via a re-entry shock above the sublimating atmosphere.

When the sublimation atmosphere is negligible (i.e. nightside at a T_F of 90 K), the gas falls unimpeded from the canopy to the surface (Zhang *et al.*, 2004). Each of the plumes is appropriately superimposed as a dayside or nightside plume depending on the plume's location and the local near-surface sublimation atmospheric density. We classify large volcanoes with a ring radius exceeding ~400 km and shock heights of several hundred kilometers as Pele-type plumes. The Pele-type plumes have a virtual vent temperature of 650 K, a velocity of 900 m/s, and a mass flow rate of 1.1×10^4 kg/s (Zhang *et al.*, 2003). Smaller volcanoes are simulated as Prometheus-type plumes with a ring radius of ~180 km and a shock height of 120 km. Our Prometheus-type plumes have a virtual vent temperature of 300 K, a velocity of 500 m/s, and a mass flow rate of 5.9×10^3 kg/s.

3.2.8 PLASMA HEATING

In the simple energy flux method, the plasma energy, originating in the Jovian magnetospheric torus (Frank *et al.*, 1996), is assumed to enter radially from the top of the domain uniformly over the entire satellite. Excitations of translational and rotational modes by the plasma are accounted for by depositing an equal amount of energy into each degree of freedom while vibrational excitation by the plasma is neglected for lack of a suitable model. The plasma energy flowing down through a column is depleted, dependent on the gas density, as it is absorbed by the gas in a given cell. The remaining energy travels down the column of cells until it is completely depleted or reaches the surface. For a detailed account of the plasma heating model, see Austin and Goldstein (2000).

The plasma energy flux at the top of the domain is taken to be 5.0 erg s^{-1} cm^{-2}. Previous models have used a plasma energy flux of 1.3 erg s^{-1} cm^{-2} (Linker *et al.*, 1989; Pospieszalska and Johnson, 1996; Austin and Goldstein, 2000) based on the fraction of plasma energy that reaches the exobase as opposed to that

which is deflected around Io. We use a higher value as an upper limit on the plasma flux. A lower value of 1.0 erg s^{-1} cm^{-2} was found to have a negligible effect on the vertical density structure of the atmosphere (compared to 5.0 erg s^{-1} cm^{-2}) but did alter the vertical thermal structure (Moore *et al.*, 2009); however, using a lower value of 1.0 erg s^{-1} cm^{-2} leads to problematic noise in the calculation of the 3D vibrational temperatures which is prohibitively expensive to circumvent computationally (see Section 3.2.6).

This plasma model lacks the momentum transfer from the plasma to the atmosphere, direct vibrational excitation of SO_2 molecules via collisions with ions and electrons, a more accurate plasma energy distribution over Io's leading and trailing hemispheres, re-acceleration of ions and electrons after collisions with the neutral atmosphere, and realistic electric and magnetic fields. The more sophisticated particle description of the plasma, discussed in Section 3.4.3 includes all of these effects. The discussion of simulation results in Sections 4.2, 4.3, and 4.4 should be read with the understanding that the actual plasma impingement on Io's atmosphere is non-uniform and this non-uniform impingement can lead to nearly an order of magnitude difference in the amount of plasma energy which interacts with the atmosphere. This could significantly change the locations at which the plasma energy reaches the surface as well as the vertical thermal structure of the atmosphere.

3.3 THE UPDATED MODEL FOR CHAPTER 6 SIMULATIONS

After analyzing the results presented in Chapter 4, it became clear that the atmosphere is most sensitive to the surface temperature distribution and that a more sophisticated model was desired. Instead of using an integrated thermal inertia fit to radiance observations (Sinton and Kaminski, 1988), a more sophisticated thermal model solves the one-dimensional heat conduction equation and accounts for the effects of thermal inertia, latent heats of sublimation and condensation, endogenic

heating, radiation from Jupiter, and eclipse by Jupiter. Hot spots are also included and are modeled as warm disks with zero net mass flux (e.g. they are not plumes or sources of sublimation) based on Keck AO observations (Marchis *et al*., 2005). Also, as part of further development of the computational model, the domain decomposition was extended to allow parallelization in two directions: azimuthal and polar. The vertical domain was also extended to high altitudes by a vacuum buffer cell where particles are tracked without the influence of collisions. This vacuum buffer cell reduces unphysical escape and evaporative cooling via particle escape from the top of the atmosphere.

3.3.1 3D GEOMETRY AND PARALLELIZATION

The domain spans all latitudes and longitudes and from Io's surface up to 1400 km. A vacuum buffer cell was added which extends the vertical domain from 400 km to 1400 km. In the vacuum buffer cell we only model the movement of particles (collisions are neglected). The vacuum buffer cell reduces vertical escape to a negligible level; only particles which have a velocity greater than 65% of escape velocity will escape the top of the vacuum buffer cell. Estimating the peak surface temperature to be ~120 K and assuming a Maxwellian speed distribution, this corresponds to the tail of the speed distribution with less than 0.001% of particles possessing speeds greater than 65% escape velocity. Only 1 in 10^7 molecules will aphysically escape the domain.

The vertical grid below 400 km is resolved by 400 cells using 5 adaptable "linear segments" with 20% of the total gas column density in each segment. The cell sizes in each segment are computed based on the local gas properties at the segment endpoints and the cell sizes vary linearly between those endpoints. Initially, the grid starts with uniform 1 km cells and then the local gas properties are sampled for 750 time steps. Based on the sampled local gas properties, the "linear segments" and their

cell sizes are adapted each consecutive 750 time steps. The linearly segmented adaptive grid stretching is used in place of an exponentially stretched grid for computational efficiency because linear segments enable the cell indices of a particle to be calculated analytically whereas the exponentially stretched grid required a more costly searching technique. The "linear segments" grid stretching method allows each column of cells to have a different vertical grid stretching which can make visualization quite difficult. Therefore, a separate uniform output grid is used to analyze the data. The output grid uses the same resolution in latitude and longitude as the collision grid but uses uniform 1 km vertical resolution. See Moore *et al*. (2011, 2012) for details on the "linear segments" grid stretching method.

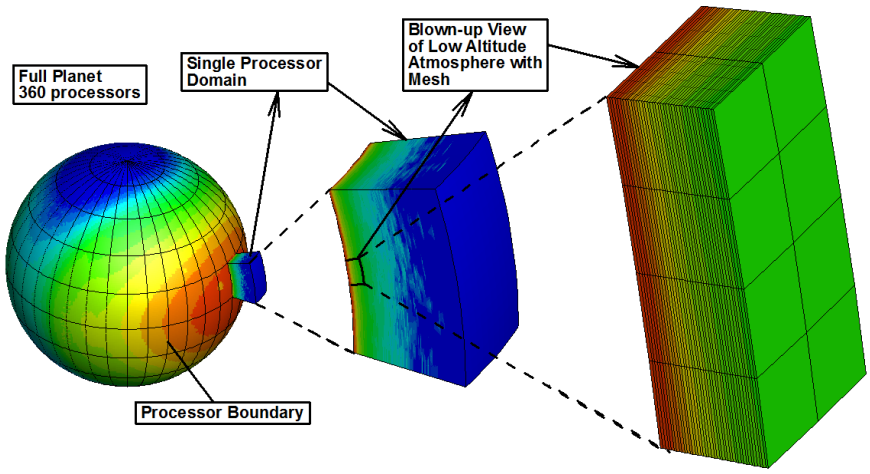

Figure 3.7: On the far left, the full planet domain is shown at an altitude just above the solid surface with a single processor highlighted and then expanded to show the fall off in density with altitude. The single processor's near surface domain is further expanded to show the aspect ratio of the mesh at low altitudes (large lateral cell sizes and near mean free path sized vertical cell sizes).

The cell sizes in latitude and longitude have a resolution of 1 degree, giving 180 cells in the polar direction and 360 cells in the azimuthal direction. For these simulations, the parallelization was extended to the polar direction such that the domain is decomposed in both azimuthal *and* polar directions with each processor

simulating 10° of longitude and 18° of latitude. Each processor simulates 36,000 cells with about 2 million particles. The data are also time-averaged over the last 250 seconds of the simulation to decrease noise.

3.3.2 Updated Thermal Model of Io's Solid Surface

In Section 3.2.3, the surface thermal model solved a simple differential equation with an integrated thermal inertia. In the updated thermal model, the SO_2 surface frost and non-frost temperatures are determined by solving the one-dimensional heat conduction equation with the respective thermal parameters for the SO_2 frost and non-frost surfaces

$$\rho c \frac{\partial T(\theta,\phi,z,t)}{\partial t} = \frac{\partial}{\partial z}\left[k \frac{\partial T(\theta,\phi,z,t)}{\partial z} \right], \tag{3.10}$$

where ρ is the density, c is the specific heat, k is the thermal conductivity, t is time, z is the depth into the surface, θ is the latitude, ϕ is the longitude, and T is the solid temperature (of frost or non-frost). The parameters ρ, c, and k (if independent of z) can be grouped together to a single thermal parameter known as the thermal inertia, Γ. The boundary conditions at the upper surface ($z = 0$) and at a depth where there are no diurnal changes ($z = d$) are given, respectively, by:

$$\begin{aligned} k \frac{\partial T(\theta,\phi,z,t)}{\partial z}\bigg|_{z=0} &= \varepsilon\sigma T^4(\theta,\phi,z=0,t) \\ -(1-\alpha)\left(F_S(\theta,\phi,t) + F_J(\theta,\phi)\right) &- q_{SUB}(\theta,\phi,t) + q_{COND}(\theta,\phi,t) \end{aligned} \tag{3.11}$$

$$k \frac{\partial T(\theta,\phi,z,t)}{\partial t}\bigg|_{z=d} = Q_T \tag{3.12}$$

$$F_S = F_{S-MAX}\cos(\theta)\sin(\phi + \omega t) \tag{3.13}$$

$$F_J = F_{J-MAX}\cos(\theta)\sin(\phi) \tag{3.14}$$

where ε is the emissivity, σ is the Stefan-Boltzmann constant, α is the albedo, F_S is the solar flux, F_J is the flux of radiation from Jupiter, q_{SUB} and q_{COND} are the heating terms due to the latent heat of sublimation and condensation, respectively, $F_{S\text{-}MAX}$ is the maximum solar flux, ω is the planetary angular rotation rate, $F_{J\text{-}MAX}$ is the maximum Jupiter flux, and Q_T is the endogenic heating of the passive background and does not include the additional heating from hot spots. The total endogenic heating rate will be the sum of the passive background and hot spot endogenic heating rates. $Q_T = 1.0$ W m^{-2} will be used in this work as modeling of Galileo PPR observations showed that it fits the data best (Rathbun *et al*., 2004). The total endogenic heating rate is well constrained to be ~2.5 W m^{-2} and our simulations are consistent with this total endogenic heating rate by emitting ~1.0 W m^{-2} from the passive background and ~1.5 W m^{-2} from the hot spots. The heating rate from hot spots is calculated by integrating the emitted flux from all hot spots and then dividing by Io's surface area (Marchis *et al*., 2005). $F_{S\text{-}MAX}$ is chosen to best match the thermal fits by Rathbun *et al*. (2004) using the same thermal parameters as their inhomogeneous model. This thermal profile was fit to Galileo orbits I24 (October 10, 1999), I25 (November 25, 1999), I27 (February 22, 2000), I31 (August 5, 2001), I32 (October 15, 2002), and I33 (January 17, 2003). The heliocentric distance and resulting solar flux for each Galileo orbit that were used are listed in Table 3.5. The solar flux varies by approximately 15% between the cases where Io is closest to and furthest from the sun but the effect of this solar flux variation is not clearly seen in Figure 7 of Rathbun *et al*. (2004). The best fit $F_{S\text{-}MAX}$ is found to be 54.6 W m^{-2} and corresponds approximately to a date in late 2000. This is the maximum solar flux value used in the simulations presented in Chapters 6 and 7.

The emissivity, ε, is assumed to be unity (Rathbun *et al*., 2004). We neglect heating of the surface by plasma impact since our plasma energy flux is negligible (1.3 mW m^{-2}) compared to the other heating terms. The thermal inertia, Γ, and bond

albedo, α, values for the frost and non-frost surfaces are found through a parametric study discussed in Section 5.1. The other important parameters related to the thermal model are summarized in Table 3.6.

Orbit Name	Date	Io Distance from Sun (AU)	$F_{S\text{-}MAX}$ (W m^{-2})	% Variation from 54.6 W m^{-2}
I24	10-Oct-99	4.96	55.92	+2.42
I25	25-Nov-99	4.96	55.82	+2.24
I27	22-Feb-00	4.98	55.50	+1.65
I31	5-Aug-01	5.11	52.53	-3.79
I32	15-Oct-02	5.27	49.51	-9.32
I33	17-Jan-03	5.31	48.73	-10.75

Table 3.5: The date, heliocentric distance, solar flux, and variation from the chosen solar flux value for each of the Galileo orbits used for the determination of the best fit parameters.

Io is tidally locked and therefore only the sub-Jovian hemisphere sees the radiated flux from Jupiter. In addition, Io's sub-Jovian hemisphere experiences a solar eclipse for ~2 hours during each rotation. The eclipse model resolves the timescale of ingress and egress; Jupiter's shadow is realistically swept across Io's disk over the ~3 minutes of ingress and egress corresponding to Io's disk being in Jupiter's penumbra. Both of these effects are incorporated in the surface thermal model. The blackbody radiation from Jupiter uses $T_{JUP} = 130$ K and therefore the "Jupiter heating" is a relatively small but steady heating term (~0.67 W m^{-2} at the sub-Jovian point); however, eclipse by Jupiter has a large effect on the global surface thermal distribution. The sub-Jovian hemisphere will see 2 hours less sunlight per day than the anti-Jovian hemisphere; therefore, the sub-Jovian hemisphere will be relatively cooler than the anti-Jovian hemisphere. This will be shown in the following sections to have important implications for the sub-Jovian/anti-Jovian hemisphere asymmetry observed in both the mid-infrared (Spencer *et al*., 2005) and Lyman-α (Feaga *et al*., 2009) where the sub-Jovian hemisphere consistently has lower column densities than

the anti-Jovian hemisphere. Latent heat effects due to sublimation and condensation of SO_2 gas molecules are also treated, but it will be shown *a posteriori* that they have negligible impact on the surface temperature. Radiative exchange between the surface and the atmosphere is neglected; this is because the atmosphere is optically thin in most locations and gas absorption occurs only in narrow bands.

Parameter	Value
Emissivity, ε	1
Best Fit Solar Flux, F_S	54.6 W m^{-2}
Jupiter Blackbody Temperature, T_{JUP}	130 K
Passive Background Endogenic Heat Flux	1.0 W m^{-2}
Eclipse Duration	2 hours
Ingress/Egress Duration for Io Disk	3 minutes

Table 3.6: The fixed parameters in the thermal model.

The thermal model is discretized following the method outlined in Spencer *et al*. (1989). Following their parameterization, the depth into the surface, z, is replaced with $\zeta = z/l_S$ where $l_S = \sqrt{(k/\rho c \omega)}$ is the skin depth (between about 10 cm and 1 m depending on the thermal conductivity). This reduces Eqs. 3.10, 3.11, and 3.12 to

$$\frac{\partial T(\theta,\phi,\zeta,t)}{\partial t} = \omega \frac{\partial^2 T(\theta,\phi,\zeta,t)}{\partial \zeta^2} \tag{3.15}$$

$$\sqrt{\omega}\Gamma \frac{\partial T(\theta,\phi,\zeta,t)}{\partial \zeta}\Big|_{\zeta=0} = \varepsilon\sigma T^4(\theta,\phi,\zeta=0,t) - (1-\alpha)\left(F_S(\theta,\phi,t) + F_J(\theta,\phi)\right) - q_{SUB}(\theta,\phi,t) + q_{COND}(\theta,\phi,t) \tag{3.16}$$

$$\frac{\partial T(\theta,\phi,\zeta,t)}{\partial \zeta}\Big|_{\zeta=1} = \frac{Q_T}{\Gamma\sqrt{\omega}} \tag{3.17}$$

We forego the additional scaling of the temperature by the subsolar equilibrium temperature as described by Spencer *et al*. (1989). After solving for the quantities of interest, the discrete equivalents of Eqs. 3.15, 3.16, and 3.17 are

$$T_i^{n+1} = T_i^n + \frac{\omega\Delta t}{\Delta\zeta^2}\left(T_{i+1}^n - 2T_i^n + T_{i-1}^n\right) \quad 3.18$$

$$T_0^{n+1} = T_0^n + 2\frac{\omega\Delta t}{\Delta\zeta^2}\left(T_1^n - T_0^n\right) - \frac{2\sqrt{\omega}\Delta t}{\Gamma\Delta\zeta}\left(\varepsilon\sigma {T_0^n}^4 - (1-\alpha)\left(F_S + F_J\right) - q_{SUB} + q_{COND}\right) \quad 3.19$$

$$T_{S-1}^{n+1} = T_{S-1}^n + 2\frac{\omega\Delta t}{\Delta\zeta^2}\left(T_{S-2}^n - T_{S-1}^n\right) + \frac{Q_T\Delta\zeta}{\Gamma\sqrt{\omega}}. \quad 3.20$$

Here S is the number of slabs in depth and $\Delta\zeta$ is the thickness of each slab. The values for $S = 32$ and $\Delta\zeta = 0.25$ were taken from Spencer *et al*. (1989) but were also independently tested for convergence. The fraction of frost and non-frost (discussed in detail in Section 3.2.3) present at the surface are assumed to be uniform in depth (e.g. SO_2 frost patches are frost throughout the depth of the solid). Io's rotation was discretized with a time step $\Delta t = 100$ s and this (time step) was also tested for (time step) convergence. The time step is reduced to 0.5 seconds when modeling the full atmosphere to resolve the mean time between collisions. These equations apply to both the frost and non-frost surfaces where T, α, and Γ are the respective parameters of a given surface. Section 5.2 shows a comparison between the results of the original and updated thermal models.

3.3.3 INITIAL CONDITIONS

To achieve a quasi-steady state, the thermal model must converge on a "deep temperature", T_{DEEP}, which is the temperature at the lower boundary of the one-dimensional domain (e.g. tens of centimeters below the solid surface of Io). The frost and non-frost surfaces are allowed to have independent values of T_{DEEP}. When endogenic heating is included, the lower boundary condition must instead converge to a heat flux and the temperature at the lower boundary will be depth dependent. An arbitrary temperature (120 K) is initially defined for the temperature of the entire domain and then T_{DEEP} at a particular latitude and longitude is computed by averaging the temperature of that point throughout an entire day (e.g. the diurnal average). The

updated T_{DEEP} is then assigned and the process is iterated through several Io rotations (including the effect of eclipse) until T_{DEEP} (or the heat flux with endogenic heating) converges to within 10^{-3} K. This relaxation process is computed uncoupled from the atmosphere and therefore the latent heats of sublimation and condensation are not included. Including the latent heats of sublimation and condensation and coupling the atmosphere to the surface thermal model during this equilibration process would be computationally prohibitive (as it increases the computational time by several orders of magnitude). However, as will be shown later, the effect of latent heat is relatively minor. The rest of the steps for achieving a quasi-steady state are the same as those described in Section 3.2.4.

3.3.4 LOAD BALANCING

With the updated thermal parameters from the parametric study described in Section 5.1, it became necessary to improve the load balancing so that it forced the number of molecules per column to remain roughly constant. In the previous model, described in Section 3.2.5, the weight was based only on the sublimated flux of molecules from the surface which is dependent on T_F. However, when a large numbers of molecules are desorbing from the non-frost surface, this can lead to large load imbalances which can slow simulations considerably. Both the sublimated flux and the flux of molecules that desorb from the non-frost surface are considered if the weight is based on the total number of particles in a column of cells. Furthermore, the weight between different columns of cells was limited to vary by only up to three orders of magnitude because the cold polar temperatures (~55 K) can lead to large gradients in the weight that produce cloning errors.

3.3.5 HOT SPOTS

Name	Longitude	Co-Latitude	Area (km^2)	Temperature (K)
Surt	337	49	68	458
Fuchi	328	65	2222	285
Sengen	314	122	15	492
Loki	308	80	10875	332
Dazhbog	302	37	5166	338
Hephaestus	289	90	531	331
Ulgen	288	132	502	368
Unnamed	281	41	11	568
Daedalus	274	70	572	360
Pele	257	110	37	566
Pillan	244	104	674	363
Isum	209	62	141	387
Marduk	209	117	132	428
Zamama	174	73	42	414
Culann	165	111	348	338
Prometheus	156	94	644	335
Tupan	142	112	95	378
Malik-Thor	135	54	236	433
Amirani	115	70	334	366
Unnamed	93	129	931	358
Gish Bar	91	76	1116	350
Zal	79	64	158	376
Tawhaki	77	90	797	375
Masubi	56	135	204	426
Janus	39	97	27	559
Uta	22	127	71	432

Table 3.7: The name, co-latitude, longitude, area, and surface temperature of 26 persistent hot spots observed by Marchis *et al.* (2005).

Keck AO infrared observations (Marchis *et al*., 2005) provide the basis to model 26 persistent hot spots on Io's surface (see Figure 3.8). Each hot spot is assumed to be a circular disk on the surface with a temperature, area, and position

(latitude and longitude to the nearest degree) taken from Tables 3, 5a, 5b, and 5c of Marchis *et al*. (2005). SO_2 molecules which land on the hot spot surface thermally equilibrate with the surface and then desorb instantaneously since the residence time at >300 K is less than 10 μs (much smaller than the simulation time step of 0.5 s). The area covered by hot spots is assumed not to sublimate (as any SO_2 surface frost would vaporize rapidly at the hot spot temperature) and there is zero net mass flux from the hot spots (i.e. they are not plumes). Table 3.7 shows the temperature, areas, and positions of the 26 hot spots.

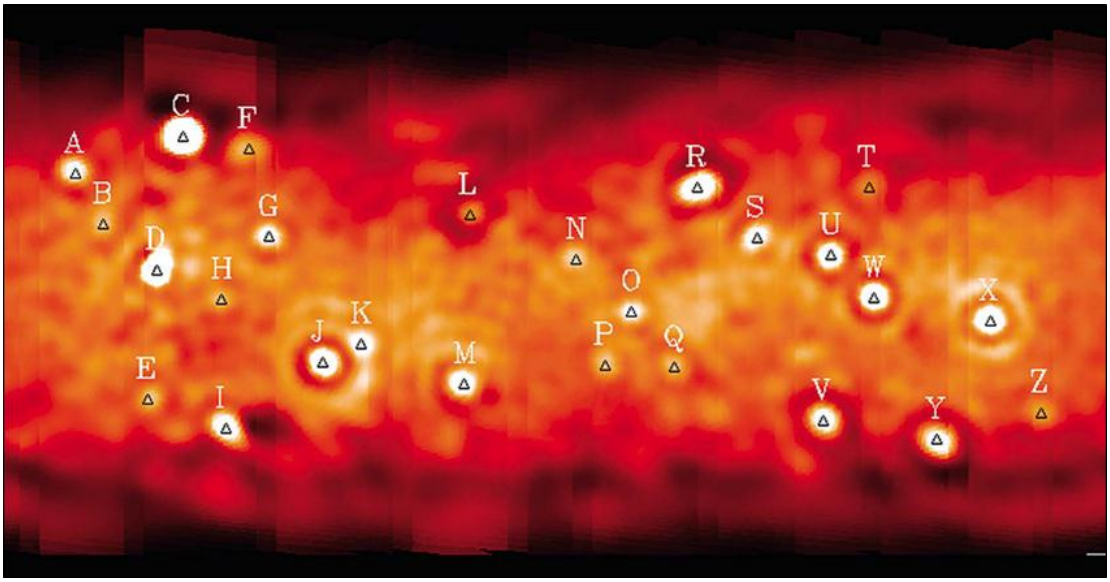

Figure 3.8: The global IR intensity observed by Keck AO. Each letter marks the location of a persistent hot spot. Note the rings around some hot spots (e.g. U, W, X) are artifacts of adaptive optics. (*From Marchis et al. (2005), courtesy of Elsevier*).

Many of the hot spots have areas smaller than the 1°×1° used in the gas dynamic simulations. Despite the grid resolution being larger than some hot spots, the area covered by these hot spots is properly resolved by computing the corresponding radius of a hot spot from the observationally inferred area and then checking whether a molecule hit within the radius of a specific hot spot.

3.4 THE UPDATED MODEL FOR CHAPTER 7 SIMULATIONS

The largest limitation of the simulations presented in Chapters 4 and 6, is that only the dominant dayside species, SO_2, is modeled. In the final set of DSMC atmospheric simulations, the original plasma heating model is altered to describe the plasma instead as a flux of energetic particles instead of an energy source term, and allow for the modeling of plasma chemistry and surface sputtering. The inclusion of plasma and photo-chemistry creates a physical source for the daughter species of SO_2 (S, SO, O, O_2) which was lacking in previous simulations. S^+ and O^+ ions are also modeled in addition to SO_2 and its daughter species. These ions from the Jovian plasma torus track Jupiter's magnetic field lines and cause sputtering if they impact Io's condensed SO_2 surface frosts. Because the ions and fast neutrals travel at such high velocities, the mean time between collisions for these particles is roughly 100 times smaller than for particles in the neutral atmosphere and therefore a sub-stepping technique is implemented for computational efficiency.

3.4.1 INITIAL CONDITIONS

To achieve a quasi-steady state, the surface temperature distribution, the density of SO_2 molecules stuck to the non-frost surface, photo and plasma chemistry, and surface sputtering must all reach a periodic solution. First, the surface temperature distribution is converged over 250 complete orbits of Io as discussed in Section 3.3.3 because latent heat exchange is a minor effect and therefore the surface temperature is decoupled from the atmosphere. Next, the atmosphere is computed with very few particles (~20,000 per processor) and under the influence of only a small number of collisions by using a collision limiter set to 0.1. The collision limiter forces the number of collision selections to be limited to 0.1 times the number of particles in a cell. This small number of collisions is sufficient to randomize most cloned high energy particles that could lead to a runaway memory overflow. These

computations proceed for three orbits until the number of particles stuck to the non-frost surface has reached a periodic solution.

Next, photo-dissociation is turned on and the neutral atmosphere is dissociated until each of the daughter species of SO_2 reaches a quasi-steady state. S and O are deleted from the computation when they strike the surface while O_2 is assumed to be non-condensable and therefore diffusely reflects from the surface whether it impacts either SO_2 frost or non-frost. SO is partially non-condensable (50%) and diffusely reflects from the surface half the time and is deleted from the computation the rest of the time. O_2 builds up because it is fully non-condensable and the only loss process, escape, is very slow compared to the timescale for the photo-dissociation of SO_2. After three rotations of Io, the daughter species of SO_2 besides O_2 have reached a periodic solution.

In the final step, the plasma is turned on which allows the following physics to occur: plasma chemistry, plasma pressure on the neutral atmosphere, plasma heating, and surface sputtering. With plasma chemistry turned on, the O_2 has a loss process (via dissociation) and therefore is able to reach a quasi-steady over three more full rotations of Io's atmosphere. Surface sputtering will sputter some of the SO_2 gas that has adsorbed to the non-frost surface and alter the global coverage. After a set of three final rotations, the atmosphere has reached a quasi-steady state and can be cloned up to ~50,000 molecules per processor. The relatively low number of computational particles is due to the time limit on the TACC supercomputers (24 hours). The computations can only run for ~15 minutes of Io time in 24 hours on the supercomputers and higher numbers of molecules would tend to slowdown the computation and reduce the time-average interval. The collision limiter is also set back to 4.0 (since the gas in equilibrium after ~3 collisions).

3.4.2 LOAD BALANCING

Previously, cell weights were adapted every time step but this can lead instabilities in conjunction with the particle description of plasma which tends to be very noisy. Therefore, load balancing is further refined to only adapt cell weights after a pre-defined number of time steps so as to increase the number samples and decrease the noise in the updated cell weight. In addition, the weighting function is limited to change by no more than a factor of two each time it adapts, to avoid massive cloning or destruction of particles. Lastly, the high energy neutral particles that are created by photo-dissociation in the neutral atmosphere (which still move on the gas time step) can travel large distances in a single time step. Therefore, near the pole where a grid singularity exists and the cell size becomes small, the weight must be kept constant to avoid massive cloning of high energy particles which can cause memory overflow in the molecule structure. I have chosen to restrict the weight so it never drops below the vapor pressure equilibrium weight equivalent to 100 K.

3.4.3 PARTICLE DESCRIPTION OF THE PLASMA

Moore (2011) created a particle description of the energetic ions and electrons in the Jovian plasma torus to enable accurate calculations of chemical reactions, atmospheric heating, plasma pressure, and ion motion (Moore, 2011; Moore *et al*., 2012). His work is briefly summarized here. Because the ion timescale for the motion and collision rate is so much shorter than the neutral gas time step (0.5 seconds), it was preferable to implement a plasma sub-step rather than simulate the neutral gas on the much smaller plasma time step (0.01 seconds). During the plasma sub-steps, the neutral gas is assumed fixed while ions and electrons move along field lines.

The only body force acting on the neutral gas is gravity but an additional Lorentz force due the electric and magnetic fields must be included for the movement of ions. The acceleration due to the gravity and the Lorentz force is given by

$$a = -\vec{g}\left(\frac{R_{Io}}{r}\right)^2 + \frac{q}{m}\left(\vec{E} + \vec{v} \times \vec{B}\right). \quad 3.21$$

Here $\vec{g}$ is the gravitational acceleration at Io's surface, R_{Io} is the radius of Io, r is the radial position of the ion with respect to the center of Io, q is the unit charge, m is the mass of the ion, $\vec{E}$ is the electric field, $\vec{v}$ is the velocity of the particle, and $\vec{B}$ is the magnetic field. Electrons are assumed to move with the ions to sustain charge neutrality. The gyro-motion of ions along magnetic field lines is also modeled because it is comparable to the neutral gas density length scale. Conversely, the gyro-motion of electrons is neglected because it is always small compared to the neutral gas density length scale.

The magnetic field, $\vec{B}$, and bulk plasma velocity, $\vec{v}$, are taken from multi-scale MHD simulations (Combi *et al*., 1998). The electric field is computed by taking the cross product of the bulk plasma velocity with the magnetic field:

$$\vec{E} = -\vec{v} \times \vec{B} \quad 3.22$$

Note that the ambipolar electric field is neglected in this work because it is computationally prohibitive to simulate enough particles such that the ambipolar field is not dominated by noise. The ambipolar field is expected to cause a slight twist of the electric field due to the Hall Effect (Saur *et al*., 1999).

The particle description of the plasma also allows for both electron-heavy and heavy-heavy chemical reactions to be treated. Currently, all electron-heavy collisions are neglected; for the proposed treatment of electron-heavy interactions see Moore (2011). Heavy-heavy interactions are treated by either the TCE model (with Arrhenius rate coefficients) or with cross sections from MD/QCT simulations (Deng *et al*., 2011; Parsons *et al*., 2012). A list of the included heavy-heavy interactions is given in Table 3.8.

Collision type	Reaction	Reference
Elastic	$SO_2 + O \rightarrow SO_2 + O$	1
Dissociation	$SO_2 + O \rightarrow SO + 2O$	1
Dissociation	$SO_2 + O \rightarrow O_2 + O + S$	1
Dissociation	$SO_2 + O \rightarrow 3O + S$	1
Dissociation	$SO_2 + S \rightarrow SO + O + S$	1†
Dissociation	$SO_2 + S \rightarrow O_2 + 2S$	1†
Dissociation	$SO_2 + S \rightarrow 2O + 2S$	1†
Dissociation	$O_2 + O \rightarrow 3O$	2
Dissociation	$O_2 + S \rightarrow 2O + S$	2†
Charge Exchange	$O^+ + O \rightarrow O + O^+$	3
Charge Exchange	$S^+ + S \rightarrow S + S^+$	3
Radiative Recombination	$SO + O \rightarrow SO_2 + \gamma$	4
Recombination	$O + SO + M \rightarrow SO_2 + M$	5
Recombination	$2O + M \rightarrow O_2 + M$	5
Recombination	$O + S + M \rightarrow SO + M$	5

Table 3.8: Heavy-heavy interactions included in the DSMC code. [1]Deng *et al.*, 2011; [2]Johnson, *et al.*, 2002; [3]Smirnov, 2000; [4]Singleton and Cvetanović, 1988; [5]Moses *et al.*, 2002; †Cross section obtained by scaling corresponding $SO_2 + O$ reaction. *Table from Moore (2011).*

The TCE model (Bird, 1994) allows Arrhenius rate coefficients to be converted to collision cross-sections. The TCE model for collisions is only used in this work when MD/QCT data are not available. In the MD/QCT method, an ensemble of binary collisions is simulated with a randomly determined impact parameter (Deng *et al*., 2011; Parsons *et al*., 2012). These collisions between particles are modeled by computing classical trajectories on potential surfaces describing the interaction. The primary reactions of interest for plasma bombardment on Io's atmosphere are $O + SO_2$ and $S + SO_2$. Currently, only the $O + SO_2$ reaction has been modeled and the $S + SO_2$ cross section is scaled by the mass ratio of O to S. From the ensemble of reactions, the probability of a given reaction occurring is determined. To determine the proper cross-section for a given reaction, the probability is simply multiplied by the total collision cross-section (Deng *et al*., 2011; Parsons *et al*., 2012).

The total collision cross section is determined by a VHS fit to MD/QCT data below relative collision speeds of 2 km/s and directly by the MD/QCT viscosity cross-section data above relative collision speeds of 2 km/s because the VHS cross section (based on low temperature viscosity measurements) overestimates the actual total collision cross section when extrapolated to very high energies (>10 km/s).

3.4.4 PHOTO-CHEMISTRY

Reaction	Rate Coefficient† (s^{-1})	Rate Coefficient‡ (s^{-1})	Excess Energy (eV)
$SO_2 + h\nu \rightarrow SO + O$	1.0×10^{-5}	5.9×10^{-6}	0.44
$SO_2 + h\nu \rightarrow O_2 + S$	6.3×10^{-7}	1.9×10^{-6}	0.75
$SO_2 + h\nu \rightarrow SO_2^+ + e^-$	4.2×10^{-8}	3.9×10^{-8}	12.0
$SO + h\nu \rightarrow S + O$	1.8×10^{-5}	2.3×10^{-5}	0.62
$SO + h\nu \rightarrow SO^+ + e^-$	1.8×10^{-8}	3.2×10^{-8}	8.62
$O_2 + h\nu \rightarrow 2O$	9.4×10^{-8}	1.6×10^{-8}	1.48
$O_2 + h\nu \rightarrow O_2^+ + e^-$	1.8×10^{-8}	1.7×10^{-8}	19.30
$S + h\nu \rightarrow S^+ + e^-$	7.6×10^{-9}	4.0×10^{-8}	6.30
$O + h\nu \rightarrow O^+ + e^-$	7.6×10^{-9}	7.8×10^{-9}	21.60

Table 3.9: Photo-chemistry reactions included in our model. †Rates from Summers and Strobel (1996). ‡Rates from Heubner (1992). Table from Moore *et al*. (2011).

Photo-chemistry plays an important role in Io's neutral atmosphere (Summers and Strobel, 1996) and is included for the results shown in Chapter 7. In the current photo-chemistry model, the atmosphere is assumed to be optically thin and the reflected light from the surface is neglected. Photo-chemistry only occurs in regions outside of Io's shadows while Io is not in eclipse. When a photo-reaction event occurs for a molecule, the internal energy (of the ionized or dissociated particle) is assumed to be transferred into relative translational motion of the product(s). Any products of the photo-reaction are assumed to have no internal energy, are given an additional mean excess energy (~1 eV for photo-dissociation and ~10 eV for photo-ionization;

Heubner, 1992), and have randomly oriented velocity vectors. The photo-chemical reactions included in our model are listed in Table 3.9.

Note that the rate coefficient for $O_2 + h\nu \rightarrow 2O$ is roughly two orders of magnitude smaller than the rate coefficients for dissociation of SO_2 into either SO + O or O_2 + S. In fact, the $O_2 + h\nu \rightarrow 2O$ rate coefficient is sufficiently small that O_2 will not reach a steady state within a single Io orbit. For a detailed treatment of photo-chemistry, see Stewart *et al*. (2011) and Moore (2011). To work appropriately with the updated thermal model, photo-chemistry is turned off during eclipse.

3.4.5 SURFACE SPUTTERING

The impact of energetic ions onto Io's surface can cause sputtering which may be important when the SO_2 surface frost temperature is less than ~105 K (Moore, 2011) because the VPE atmosphere will then be thin enough for energetic ions to reach the surface. The surface sputtering model incorporated into the DSMC code by Moore (2011) has been extended to deal with non-uniform surface frosts and adsorbed SO_2 molecules on a non-frost substrate. When an ion hits the surface, a random number from 0 to 1, $r(0,1)$, will be drawn to determine whether it hit the frost or non-frost surface within a cell.

$$P_F = f \qquad r(0,1) < f \tag{3.23}$$

$$P_{NF} = 1 - f \qquad r(0,1) > f$$

Here P_F is the probability that an ion hits the frost surface and sputters (described in Section 3.4.5.1), P_{NF} is the probability that an ion hits the non-frost and sputters (described in Section 3.4.5.2), and f is the frost fraction in that surface cell. As long as the thickness of the target solid is sufficiently thick, sputtering is caused by a mechanism known as a collision cascade. In the collision cascade, a single energetic ion impacts the surface and collides with multiple molecules or atoms in the target

solid. In turn, each of these particles collides with several other particles inside the solid. The cascade continues until particles in the surface layer are impacted by particles that are part of the collision cascade. These agitated surface molecules may then be ejected (or sputtered) from the surface (see Figure 3.9). Therefore, the "cascade" process will extend over a considerable region of the target solid compared to the size of the incident ion.

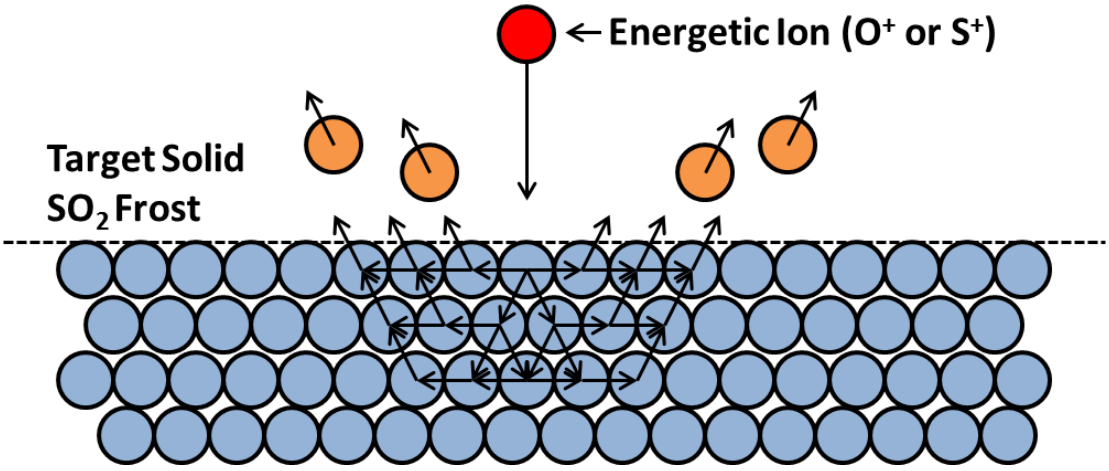

Figure 3.9: A schematic showing the collision cascade process. An energetic ion strikes the surface and then the collision cascade process causes particles to be ejected from the surface.

3.4.5.1 Sputtering of Thick SO_2 Surface Frosts

If an ion hits the thick SO_2 frost surface, then the method outlined by Moore (2011) is followed and is summarized here. Note that fast neutrals do not currently cause surface sputtering because they generally do not have high enough energies to cause sputtering. The number of molecules or atoms sputtered from a surface for each incoming ion is known as the bulk sputtering yield. Sigmund (1969) derived the backward scattering bulk sputtering yield, Y, for ions in the collision cascade regime for a rough surface (as expected on Io) where the angular dependence of the incident ion drops out.

$$Y = \Lambda \alpha n_S S_n \qquad 3.24$$

Here Λ is the sputtering efficiency, α is the fraction of energy deposited into the solid that does not contribute to sputtering, n_S is the density of the target atoms in the solid, and S_n is the elastic stopping power of the ion given by

$$S_n = \frac{1}{1-m} C\gamma^{1-m} E_i^{1-2m}. \quad 3.25$$

For the relatively low energies of the co-rotating ions in the Jovian plasma torus, $m \approx 0$ and S_n reduces to

$$S_n = C\gamma E_i, \quad 3.26$$

where E_i is the incident ion energy and γ is defined by

$$\gamma = \frac{4m_A m_B}{(m_A+m_B)^2}. \quad 3.27$$

Here m_A is the mass of the incoming energetic ion and m_B is the molecular mass of a molecule or atom in the target solid. C is defined by:

$$C = \frac{1}{2}\pi\lambda_0 d^2, \quad 3.28$$

where d is the effective diameter of the target particles. C is a constant in the Thomas-Fermi cross-section for the case $m \approx 0$. Note that C is the hard sphere cross-section, σ, with an additional factor of $\lambda_0/2$. C can be rewritten in terms of the hard sphere cross-section and then substituted back into Eq. 3.24 to yield

$$Y = \Lambda\alpha n_S \frac{\sigma}{2}\lambda_0\gamma E_i \quad 3.29$$

The bulk sputtering yield, Y, is linear in the incident ion energy, and for the case of O^+ or S^+ ions impacting SO_2 frost surface, the ion energy is the only free parameter. The constants Λ and α have been estimated by Johnson (1990). For oxygen and sulfur ions sputtering thick SO_2 frost, α was found to be 0.4 and 0.25, respectively (Johnson, 1990). Sigmund (1969) chooses $\lambda_0 = 24$ to match the differential Born-Mayer cross-sections at lower energies.

The bulk sputtering yield derived in Eq. 3.29 assumes no temperature effects; however, experiments have shown that sputtering yield will increase exponentially with increasing surface temperature. One can modify Eq. 3.29 to account for the variation in sputtering yield due to the SO_2 frost surface temperature, T_F:

$$Y = \Lambda \alpha n_S \frac{\sigma}{2} \lambda_0 \gamma E_i \left(1 + \frac{Y_1}{Y_0} e^{-\Delta E / k_B T_F}\right) \quad 3.30$$

$Y_1 = 16$, $Y_0 = 2.8 \times 10^4$, and $\Delta E = 0.056$ eV are constants determined from experimental data (Lanzerotti *et al*., (1982).

Sputtered particles are assigned energies based on the Thompson energy distribution

$$f_E(E_i) = \frac{A_E E_i}{(E_i + E_b)^2} \quad 3.31$$

Here A_E is a constant estimated from experimental data and E_b is the effective binding energy of the surface.

3.4.5.2 Sputtering of Thin SO_2 Frost Layers Stuck to the Non-Frost

As described in Section 3.2.3, particles which land on the non-frost surface will stick for a period of time dependent on Eq. 3.6. When the non-frost surface temperature is sufficiently cold, gas particles will stick for long periods of time and create a thin frost layer ranging from ~1 to ~1,000 monolayers in thickness. The bulk sputtering yield (Eq. 3.30) assumes a semi-infinite target solid (Sigmund, 1969). When the thickness of the target solid becomes comparable to or thinner than the penetration depth of the incident ion, Eq. 3.30 will break down because the full collision cascade will not occur. To determine when the collision cascade breaks down, the total extent of the collision cascade must be computed. Sigmund (1969) derives the total depth of the cascade for $m \approx 0$ to be $\sim \Delta x$ which is defined to be:

$$\Delta x = \frac{2}{NC} = \frac{4}{(N\sigma\lambda_0)} \quad 3.32$$

For SO_2 frost, $N \approx 2.5\times10^{25}$ m^{-3} and $\sigma = 1.6\times10^{-18}$ m^{-2} which yields $\Delta x \approx 40$ Å or ~6 monolayers. This result is supported by Hou *et al*. (1979) who computed the thickness required for sputtering of Cu by Ar+ to give the full bulk yield predicted by Eq. 3.30. They found that only 3 monolayers were required for the full collisional cascade to develop and that the sputtering yield fell off linearly below that thickness. They also tested sputtering of Cu by He and found that it required ~10 monolayers thickness before the full collisional cascade could develop. They attributed this greater thickness to the larger mass ratio for Cu/He ($m_R \approx 16$) sputtering compared to Cu/Ar ($m_R \approx 1.6$). For the ions of interest in the Jovian plasma torus, the mass ratios are SO_2/S ≈ 2 and SO_2/O ≈ 4. The mass ratios are midway between those of Cu/Ar and Cu/He sputtering and therefore, the number of monolayers required for the full collision cascade should lie roughly between 3 and 10 monolayers. I have chosen to use 6 monolayers as the cutoff thickness for the full sputtering yield of both O and S ions on SO_2 frost. Because the mass ratios of SO_2/S and SO_2/O sputtering are similar to Cu/Ar, we can assume that the sputtering yield will also fall off linearly when the thickness is smaller than ~6 monolayers.

When an ion hits the very thin frost coating on the non-frost surface, the thickness, d_T, (in number of monolayers) will be calculated based on the number of particles stuck to the non-frost surface, n_{NF}[m^{-2}]:

$$d_T = n_{NF} d^{-3} \quad 3.33$$

Here $d = 3.43$ nm is the spacing of SO_2 molecules in the frost. If the d_T is larger than 6 monolayers, Eq. 3.30 will be used to determine the sputtering yield. If d_T is smaller than 6 monolayers, then Eq. 3.30 will be linearly scaled based on the thickness of the SO_2 layer.

$$Y = \Lambda\alpha N \frac{\sigma}{2} \lambda_0 \gamma E_i \left(1 + \frac{Y_1}{Y_0} e^{-\Delta E/kT_F}\right) \qquad d_T > 6\ monolayers \tag{3.34}$$

$$Y = \Lambda\alpha N \frac{\sigma}{2} \lambda_0 \gamma E_i \left(1 + \frac{Y_1}{Y_0} e^{-\Delta E/kT_F}\right)\left(\frac{d_T}{6}\right) \qquad d_T < 6\ monolayers$$

Regardless of whether d_T is greater than or less than Δx, the energy distribution of the sputtered SO_2 is assumed to be the same Thompson energy distribution described in Eq. 3.31. Note that the thin coat of SO_2 frost on the non-frost is assumed to be uniformly distributed when computing the bulk sputtering yield.

CHAPTER 4: NUMERICAL SIMULATIONS OF IO'S ATMOSPHERE WITH THE ORIGINAL SURFACE THERMAL MODEL

4.1 OVERVIEW

Early models of Io's atmosphere suggested the occurrence of supersonic flow driven by a day-to-night pressure gradient; however, the models were continuum models and Io's atmosphere is significantly rarefied except at low altitudes near the subsolar point. We might infer that non-negligible errors were created by modeling the atmosphere as a continuum and a rarefied model such as DSMC must be used to investigate the dynamics of Io's atmosphere. Previous work by Austin and Goldstein (2000) properly accounted for rarefaction but modeled the domain as an infinitely expanding wedge. A global three-dimensional *rarefied* atmospheric model is created to accurately model the dynamics of Io's atmosphere.

Both disk-resolved and disk-averaged observations of Io's atmosphere have shown an asymmetry between the anti-Jovian and sub-Jovian hemispheres (Strobel and Wolven, 2001; Feaga *et al*., 2009; Spencer *et al*., 2005). The higher column densities on the anti-Jovian hemisphere were explained as correlating with the distribution of plumes. Disk-resolved millimeter observations have shown a prograde wind on the leading hemisphere at eastern elongation which is unexplainable with simple atmospheric models (Moullet *et al*., 2008). We investigate whether the sublimation atmosphere is at least partly responsible for the sub-Jovian/anti-Jovian hemisphere asymmetry and whether the suggested prograde wind is due to an interaction between the sublimation atmosphere and volcanic plumes.

The effects on Io's atmosphere of planetary rotation, heating due to plasma bombardment, inhomogeneous surface frost, SO_2 residence time on non-frost surface, subsolar temperature, and volcanic plumes are examined for several subsolar longitudes. The atmosphere is simulated at 6 subsolar longitudes corresponding to 0º, 60º, 120º, 180º, 240º, and 300º W longitude. The column densities of the sublimation atmosphere with and without volcanic plumes for each subsolar longitude are compared in Section 4.5. See Section 3.2.7 for the details of how volcanic plumes were superposed on the sublimation atmosphere. The T_{ss} examined is either 120 K or 115 K. The value of 120 K yields column densities five times larger than the 115 K values; and such high column densities are above the upper range of recently observed columns (Jessup *et al.*, 2004; Spencer *et al*., 2005), while the lower temperature of 115 K was found to agree approximately with the lower range of observed columns (Feaga *et al.*, 2009; McGrath *et al.*, 2000). Each subsolar longitude is also simulated with a longer residence time of SO_2 on non-frost surface to account for the possible high porosity of the surface (see Section 3.2.3). The parameters that were varied for the three different atmospheric simulation cases are shown in Table 4.1.

Case	Residence Time Model	Peak T_{SS} (K)
1	Long	115
2	Short	115
3	Long	120

Table 4.1: Parameters for the three atmospheric cases shown in Sections 4.2 - 4.4.

The baseline simulation (Case 1) is chosen to be an atmosphere with T_{ss} = 115 K, 180º W subsolar longitude, with the LRT model, and no volcanic plumes included. An atmosphere with T_{ss} = 115 K and SRT model will hereafter be referred to as Case 2, and an atmosphere with T_{ss} = 120 K and the LRT model will be referred

to as Case 3. Both Cases 2 and 3 are also at a subsolar longitude of 180º W and have no volcanic plumes included. Locations on Io will be given both in Iocentric longitude as well as local time of day for clarity. Note that a 24 hour day Earth-style reference time is superposed on Io's 42 hour day. The reference points for the local time are: 6:00 am - dawn terminator, 12:00 pm (noon) - subsolar point, 2:08 pm – Peak T_F, and 6:00 pm - dusk terminator.

4.2 OVERALL FLOW FEATURES

Circumplanetary flow develops as the high vapor pressure region near the peak T_F pushes gas toward the low vapor pressure region on and near the nightside. Because the vapor pressure is exponentially dependent upon the surface temperature, the vapor pressure drops rapidly near the terminator. The net sublimation region, where the vapor pressure is greater than the atmospheric pressure, is largely confined to a circular region around the peak T_F (which lies at 148º W or ~2:10 pm) for the baseline atmosphere. However, there is an additional region of mass outflux (desorption) on the morning side between 260º W to 200º W (6:40 am to 10:40 am) and 40º N to 30º S due to the DAE (see Figure 4.1). For the baseline case, the sublimation region extends ~45º east of the peak T_F, ~105º to the west, and ~60º to the north and south. For a case with an anti-solar temperature of 50 K and a subsolar temperature of 130 K Ingersoll *et al.* (1985) found that the net sublimation region extended ~37º away from the subsolar point. No direct comparison can be made between our work and Ingersoll *et al.* (1985), but our sublimation region possibly extends further to the north, south, and west than Ingersoll *et al.* (1985) because their simulations had relatively cold temperatures near the terminator. These would sublimate very little gas based on vapor pressure equilibrium likely creating regions of net condensation. The greater westward extent of the sublimation region is due to the DAE.

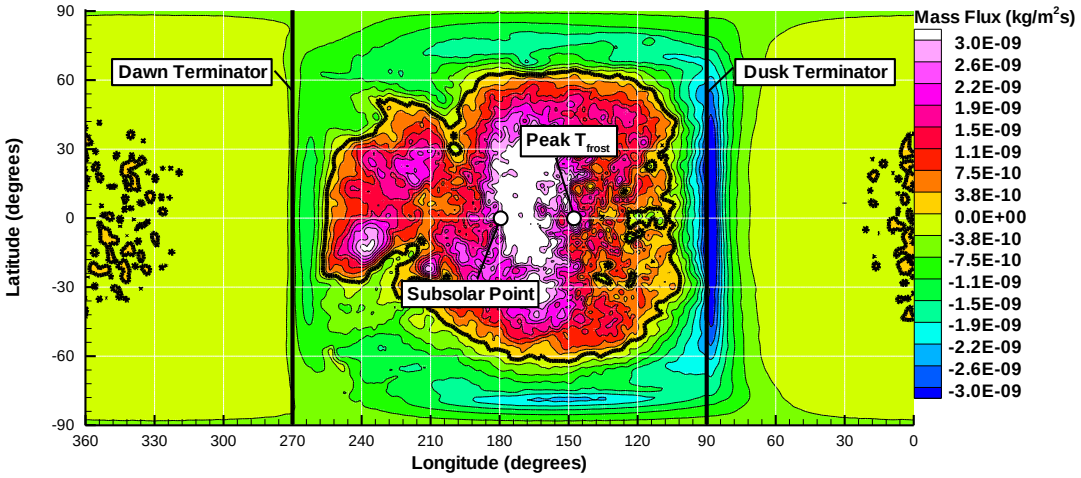

Figure 4.1: The net mass flux of SO_2 gas from surface for the baseline atmosphere (Case 1). The heavy black line contour denotes zero net mass flux. Areas of positive mass flux are regions of mean sublimation while areas of negative mass flux are regions of mean condensation. The mean mass flux within 60º longitude of the peak T_F are higher in the west than in the east because of the underlying frost fraction.

For the baseline atmosphere (Case 1), condensation occurs primarily on the dayside in a ring (~15º to 30º thick) near the terminator. The condensation is weaker near the dawn terminator because of the additional desorption of SO_2 molecules from the non-frost surface, whereas these molecules have nearly all desorbed near the dusk terminator. Condensation occurs nearly everywhere on the nightside due to the circumplanetary flow which originates on the dayside and condenses on the nightside. There are small patches of mean sublimation on the nightside near the anti-solar point where the computed mean vertical velocity is slightly positive due to noise. When T_{ss} is increased from 115 K to 120 K (Case 3, not shown), the circumplanetary flow is enhanced considerably as expected. The higher T_{ss} leads to a much larger day-to-night pressure gradient than exists for the 115 K atmospheres. Also, the eastward extent of the sublimation region does not change significantly while the westward extent increases to higher latitudes on the morning side between 260º W and 240º W (6:40 am to 8:00 am).

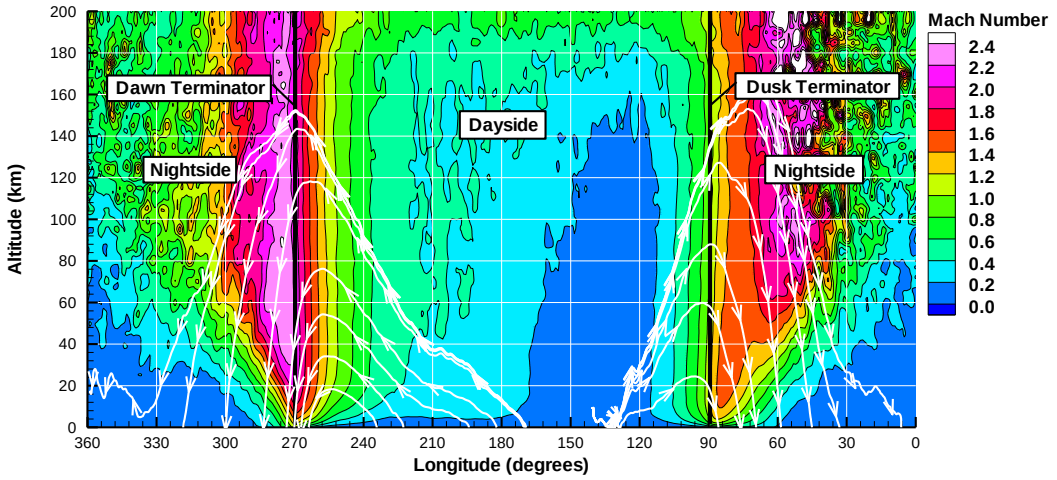

Figure 4.2: Color contours of the Mach number for a cross-sectional slice through the atmosphere at the equator for the baseline atmosphere. Streamtraces showing the dayside to nightside flow are displayed in white

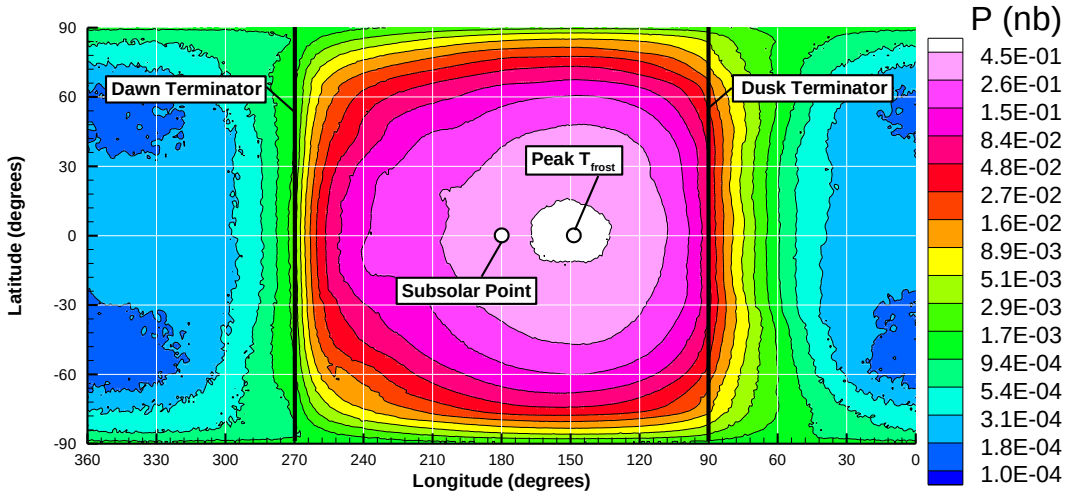

Figure 4.3: Color contours of the pressure (nbar) at an altitude of 4 km as a function of latitude and longitude for the baseline atmosphere. The pressure peaks at ~0.5 nbar and drops to less than a 0.1 pbar on the nightside at this altitude.

For the baseline atmosphere, the circumplanetary flow does not originate at the point of maximum vapor pressure, but instead at a point ~10º east (~2:40 pm) (compare Figure 4.2 and Figure 4.4a with Figure 4.3) because the atmosphere is unsteady. The westward momentum of the column of gas above the region of peak pressure, which developed based on the past day-to-night pressure gradient, must be

slowed by the momentum flux from the surface in order for the flow to re-equilibrate with the current gas pressure and originate from the region of peak pressure. Because the timescale associated with reducing the momentum of the flow to zero is on the order of 1 hour, there is a ~10º lag in the origin of the flow as Io rotates. The region of origin of the winds also varies for different subsolar longitudes the dayside frost fraction changes as Io rotates (and therefore the pressure field varies).

As flow diverges from the point of origin, it is accelerated toward the nightside by the high day-to-night pressure gradient (see Figure 4.3) and also pushed to higher altitudes by the upward momentum of the sublimation atmosphere (see Figure 4.2). The winds are not directly away from the region of origin because the inhomogeneous surface frost alters the pressure field leading to a slight curvature of the streamtraces (see Figure 4.4a). The pressure gradient between the warmest point on Io and the terminator is strong enough to drive the flow supersonic. For the baseline atmosphere at 30 km altitude, the flow is supersonic at all latitudes and longitudes around the terminator (Figure 4.4a). As the gas flow passes onto the nightside, the density (and collision rate) drop to the point where the flow essentially becomes free molecular. The gas flow that has been accelerated to supersonic speeds then continues on ballistic trajectories through the thin nightside atmosphere until it condenses on the cold nightside surface. For Case 2, the flow near the terminator goes supersonic at nearly all latitudes and longitudes except near the dawn terminator (Figure 4.4b). The difference between the two cases is explained by the DAE. As discussed in Section 3.2.3, the magnitude of atmospheric column enhancement for the baseline atmosphere extends over a much larger area than in Case 2 because of the LRT used in the baseline (Case 1). In Case 2, the DAE occurs in a very small longitudinal band starting at the dawn terminator. The smaller spatial extent but more pronounced column density enhancement of Case 2 is more efficient in blocking the westward flow (see streamtraces in Figure 4.4b). For Case 3, the flow is similar to the

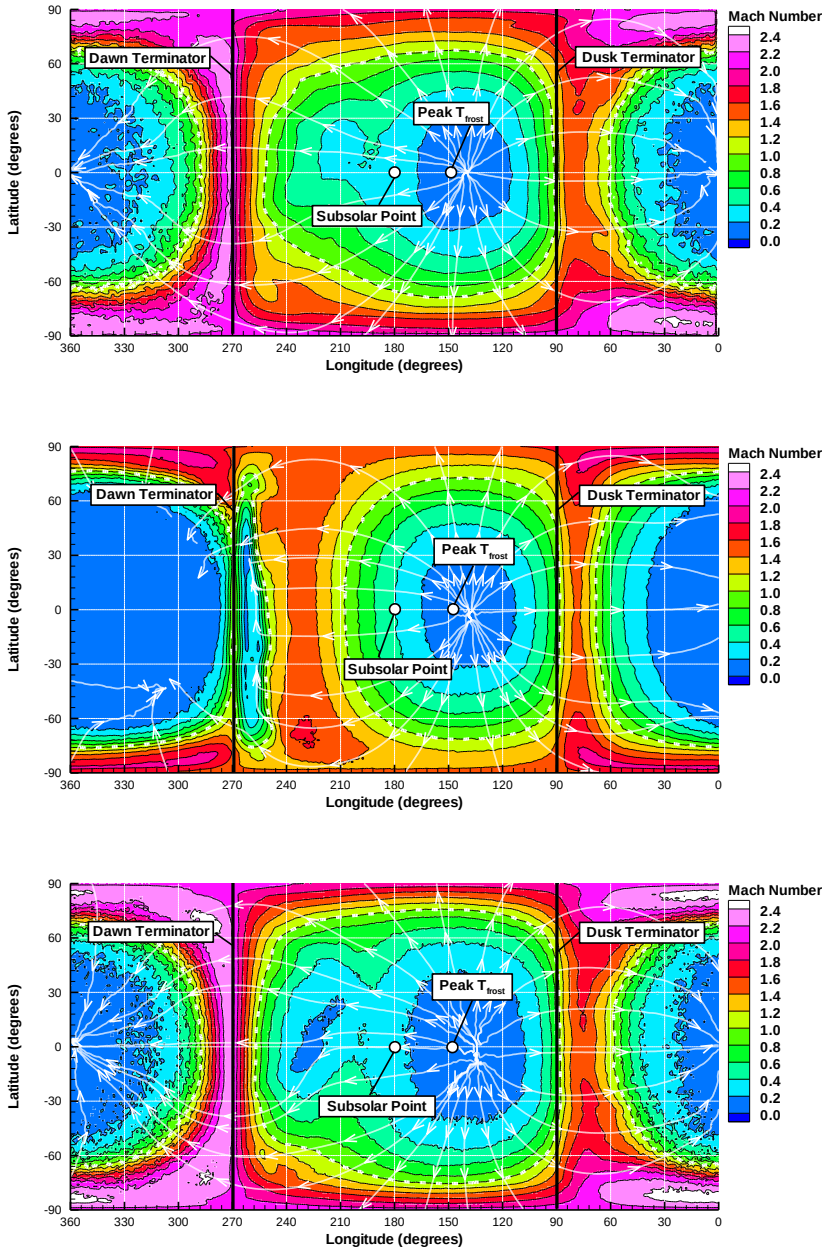

Figure 4.4: Color contours of the Mach number at an altitude of 30 km as a function of latitude and longitude for (a) the baseline atmosphere, (b) Case 2, and (c) Case 3. The dawn and dusk terminators are denoted by the thick black vertical lines. Streamtraces (in white) track the flow away from ~135º W toward the nightside for the baseline atmosphere. Note that much of the curvature of the streamtraces is due to projection effects. The sonic line is shown by the dashed white line.

baseline atmosphere but the flow is a bit stronger due to the higher pressure gradient from the 120 K subsolar temperature (See Figure 4.4c).

Irregular flows up to ~50 m/s do develop where strong frost gradients occur. These irregular flows are more visible on the nightside where the surface temperature is nearly constant. Of course, the flow there is nearly free molecular. The flow below 2 km altitude is subsonic near the dusk terminator (see Figure 4.2). However, due to slip in rarefied flow, winds within 15 m of the surface at the equator near the dawn terminator remains supersonic. The difference in the low altitude Mach numbers between the dusk and dawn terminators is due to the higher pressure gradient that exists near the dawn terminator.

For the baseline atmosphere at 30 km near the equator, the westward flow goes supersonic at 250º W (7:20 am) and remains supersonic until 285º W (5:00 am). The eastward flow goes supersonic at 90º W (6:00 pm) until 60º W (8:00 pm). There are slight variations in these distances at low latitudes attributed to variations in the frost fraction (Figure 4.4a). Near the poles, the north/south flow goes supersonic on the dayside at 70º N/S, respectively, and remains so until the same latitudes on the nightside. For Case 2 at 30 km near the equator, the westward flow first goes supersonic at 205º W (10:40 am) and remains supersonic until 250º W (7:20 am). At 250º W, the flow is blocked by the DAE. The eastward flow goes supersonic at 90º W (6:00 pm) until 70º W (7:20 pm). The difference in the extent of the eastward supersonic flow between the baseline and Case 2 atmospheres is again explained by the different residence time models. As discussed in Section 3.2.3, molecules do not remain stuck for the entire night (in the SRT model of Case 2) and therefore the nightside atmosphere is thickened by these molecules desorbing from the surface. The thickened atmosphere *decreases* the day-to-night pressure gradient and reduces the Mach numbers in all directions. Near the poles, the north/south flow goes supersonic on the dayside at 75º N and 70º S, respectively, and remains supersonic until ~75º on the nightside. The region of north/south supersonic flow has a slightly larger extent in the baseline atmosphere than Case 2. For Case 3, the supersonic regions near the

equator at 30 km occur largely in the same regions as the baseline atmosphere. The flow travels approximately 4300 km to the dawn terminator and only about 1400 km to the dusk terminator from its point of origin (at ~140º W or 2:40 pm).

The Mach number increases with altitude up to the top of the domain. For the baseline atmosphere, at an altitude of 30 km, the peak Mach numbers have equatorial values of $M = 2.20 \pm 0.05$ near the dawn terminator and 1.50 ± 0.05 near the dusk terminator. The error estimates are based on noise fluctuations in adjacent cells. The Mach number varies around the supersonic region near the terminator due to the variations in pressure caused by variations in the surface frost coverage and also the DAE. In the LRT model, regions of low frost coverage tend to enhance the local Mach number (because they decrease the local pressure) while regions of high frost tend to decrease the local Mach number (because they increase the local pressure). The north/south flow is stronger in magnitude than the east/west flow and also varies because of the inhomogeneous surface frost. The north/south flow is stronger than the east/west flow because of the higher north/south pressure gradient. Flow to the east is accelerated by a smaller pressure gradient since the frost remains warm well after dusk (6:00 pm). Flow to the west is relatively stronger because the frost is cold (90 K) just before dawn (6:00 am) and therefore the pressure gradient is nearly equal to that driving the north/south flow. The only difference between the north/south flow and the westward flow is the underlying frost fraction which is lower near the poles and leads to a slightly increased pressure gradient to the north and south. At the longitude of the peak T_F, the maximum Mach number of the northern flow is ~2.30 while the southern flow at the same longitude has a maximum Mach number of ~2.42. The southern flow is faster than the northern flow because the (interpolated) frost fraction (and hence the pressure) is lower near the south pole than the north pole.

For Case 2, the flow Mach number near the dawn terminator is closer to that found near the dusk terminator because the DAE blocks the westward flow

(effectively keeping the flow from being accelerated to the high Mach numbers seen in the baseline case). The westward flow away from the DAE is nearly supersonic (at 270º W; 6:00 am) and reaches a magnitude of $M = 0.95$ because the pressure is very high compared to the nearby nightside (and early morning dayside) vapor pressures. The shorter residence time smoothes the inhomogeneities caused by the surface frost coverage and also leads to slightly higher densities (on the evening side) as many molecules are desorbed quickly from the warm non-frost surface on the dayside. In Case 2, the morning side densities tend to be lower than the baseline case. This is because the DAE covers most of the morning side (in the baseline case), whereas the DAE is confined to a thin region near the dawn terminator in Case 2. The higher densities on the evening side do not result in higher eastward Mach numbers compared to the baseline case, because of the thickened nightside atmosphere. The peak Mach number on the equator at 30 km altitude is 1.48 ± 0.05 near the dawn terminator and 1.41 ± 0.05 near the dusk terminator. The variation in the Mach number around the terminator is also decreased because the pressures are more uniform around the ring.

For Case 3, at the equator, the Mach number is ~2.34 near the dawn terminator and ~1.56 near the dusk terminator. The difference in Mach number between the two terminators is due to the thermal inertia of the frost which decreases the pressure gradient toward the dusk terminator. The north/south flow is similar in morphology to the baseline case but has slightly elevated values due to the increased pressure gradient at 120 K.

For the LRT atmospheres, the Mach numbers change significantly as a function of subsolar longitude as Io rotates because the underlying frost fraction varies. The mean surface frost fraction on the dayside with the subsolar longitude (Figure 4.5) resulting in stronger or weaker day-to-night pressure gradients. The Mach number tends to increase near either terminator when a region of low mean

frost fraction is near that terminator (as this increases the pressure gradient which drives the flow), and to decrease near regions of high mean frost fraction. For the short residence time atmospheres, the Mach numbers tend to be larger at all subsolar longitudes compared to the corresponding LRT atmosphere. The SRT atmospheres also exhibit smaller variations in the Mach number as a function of subsolar longitude due to smaller variations in the pressure field compared to the LRT atmospheres.

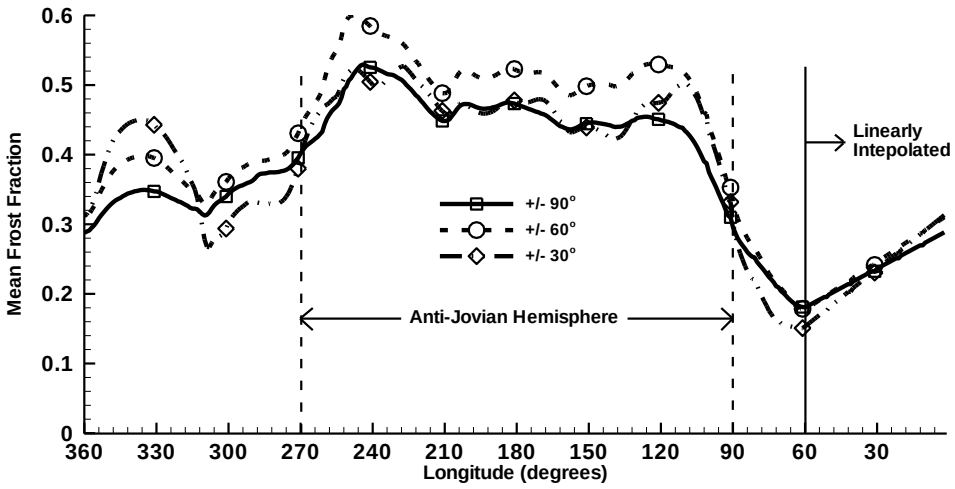

Figure 4.5: The latitudinally averaged frost fraction as a function of longitude. Three different averages were considered: between ± 30º, ± 60º, and ± 90º latitude (i.e. from pole to pole). The anti-Jovian hemisphere has a higher mean frost fraction than the sub-Jovian hemisphere for all cases.

4.3 TRANSLATIONAL, ROTATIONAL, AND VIBRATIONAL TEMPERATURES

Figure 4.6 shows color contours of translational temperature, T_{trans}, in a cross-sectional slice of the atmosphere through the equator for the baseline atmosphere. The increase in translational temperature near the dusk (90º W or 6:00 pm) and dawn (270º W or 6:00 am) terminators corresponds to a non-equilibrium region. The temperature increase is due to the accelerated gas flows which originated on the dayside falling through the thin upwelling nightside atmosphere and experiencing a weak shock (see streamtraces in Figure 4.2). T_{trans} exhibits an interesting structure

due to the plasma heating model for the baseline atmosphere. Near the surface, T_{trans} closely tracks T_F because the SO_2 gas is nearly in thermodynamic equilibrium with the surface (Figure 4.6). Below 2 km altitude at the location of the peak T_F (148º W or ~2:10 pm) the sublimated SO_2 gas is radiating vibrationally and rotationally as it travels upward and spreads laterally (Moore *et al.*, 2009). Above 2 km altitude, T_{trans} increases with altitude due to the plasma heating, despite the gas continuing to expand and radiate. For these two reasons, the lower atmosphere around 150º W has a volume of cold gas bracketed above and below by warmer gas (as seen in Figure 4.7). Above 2 km, T_{trans} becomes dependent upon the plasma energy flux reaching that location. The column is much thicker above the peak T_F region, so the plasma energy flux is absorbed by the upper atmosphere (above 2 km), leaving the lower atmosphere unaffected as seen in Figure 4.6 and Figure 4.8a. The altitude at which the plasma is completely absorbed by the atmospheric column decreases away from the region of peak T_F (because the column decreases).

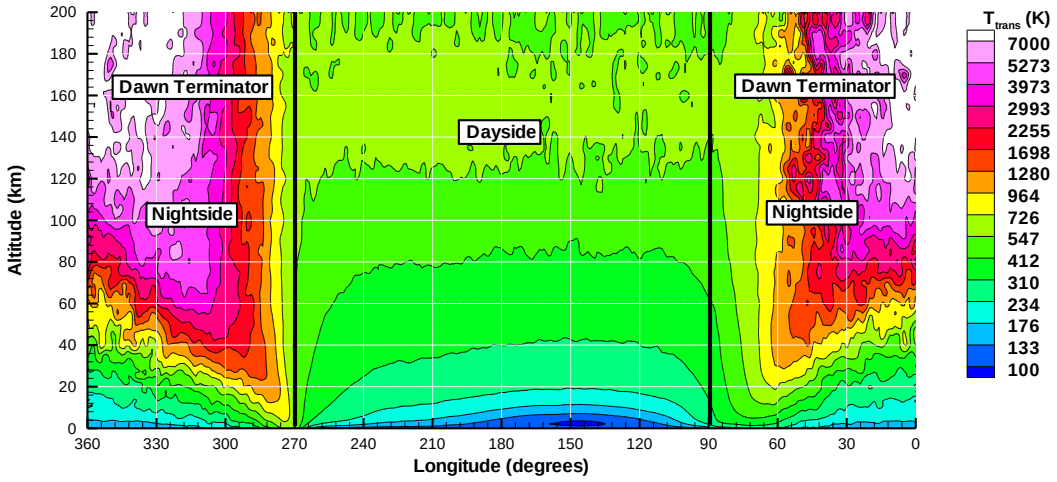

Figure 4.6: Contours of T_{trans} for a cross-sectional slice through the atmosphere at the equator for the baseline atmosphere.

For Case 3, the thermal structure of the atmosphere is similar in morphology, but the altitude at which complete plasma depletion occurs is higher everywhere on

the dayside because of the increase in column. The thicker column leads the plasma depletion altitude directly above the peak T_F to increase from 2 km (for the baseline atmosphere) up to 5 km. The cool gas (bracketed between the surface-warmed gas and the plasma-warmed gas) above the peak T_F for the T_{ss} = 120 K atmosphere cools to much lower temperatures than for the T_{ss} = 115 K cases (to as low as 50 K) because of the strong gas dynamic expansion and emission of radiation.

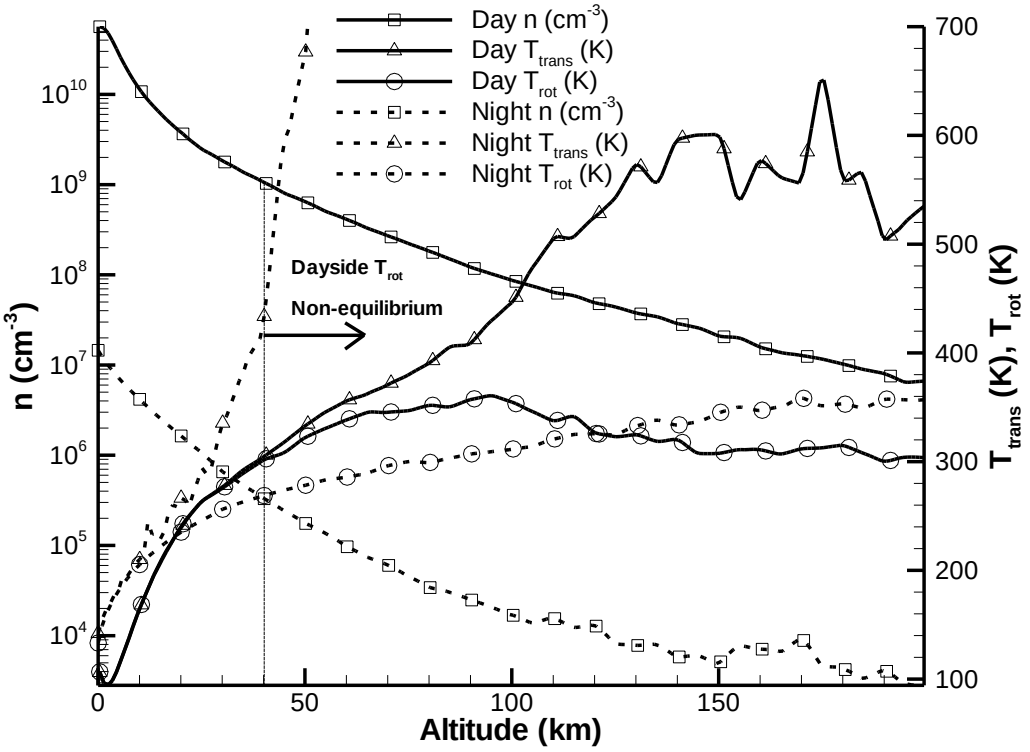

Figure 4.7: T_{trans}, T_{rot}, and number density as a function of altitude at the equator for longitudes at the peak T_F (dayside) and at 330º W (nightside) for the baseline atmosphere (subsolar longitude of 180º W).

Figure 4.8a shows that T_{trans} at 4 km altitude is approximately 100 K near the region of peak T_F; the SO_2 gas is sublimated in thermal equilibrium with the surface, cools while it radiates and expands laterally up to ~2 km, and is then plasma heated partially back to its original temperature in the remaining 2 km. At 4 km altitude,

(over the region of peak T_F) T_{trans} *increases* as T_F (and therefore column) *decreases* because the plasma penetrates deeper into the atmosphere. At 4 km altitude near the equator, T_{trans} is ~300 K at 260º W (6:40 am) but rises to ~700 K at 275º W (5:40 am). The 233% T_{trans} increase between these two locations is due to a non-equilibrium region on the nightside from two gas flows passing through each other without collisions. T_{trans} near the dusk terminator is lower because the flow is weaker and therefore gas flow streaming down through the thin sublimation atmosphere creates a weaker non-equilibrium region. Additionally, T_{trans} is higher near the poles due to the stronger flows that exist there. Case 2 (Figure 4.8b) is similar to the baseline case near the dusk terminator; however, the temperatures there are lower due to the weaker flows compared to the baseline case. There are significant differences between Case 2 and the baseline case near the dawn terminator. Nearly all the molecules stuck to the surface desorb in the DAE and this creates a region of lower column density just after the DAE (265º W or 6:20 am). In this region, the pressure gradient is too weak to drive winds and the gas condenses on the surface. Therefore T_{trans} is dependent only on the plasma heating and is ~210 K in this region. In the region to the east of the DAE near the equator (255º W or 7:00 am), where the westward flow is still supersonic, T_{trans} peaks at ~375 K. T_{trans} near the poles is also correspondingly cooler compared to the baseline atmosphere due to the weaker north/south flows that exist in Case 2.

For Case 3 (as seen in Figure 4.8c), the morphology is similar to the baseline atmosphere. T_{trans} near the terminator tends to be higher (than the baseline atmosphere) because of the stronger flows and hence stronger non-equilibrium regions. Conversely, T_{trans} (at 4 km altitude) near the peak T_F is quite low because of the increased altitude of plasma depletion.

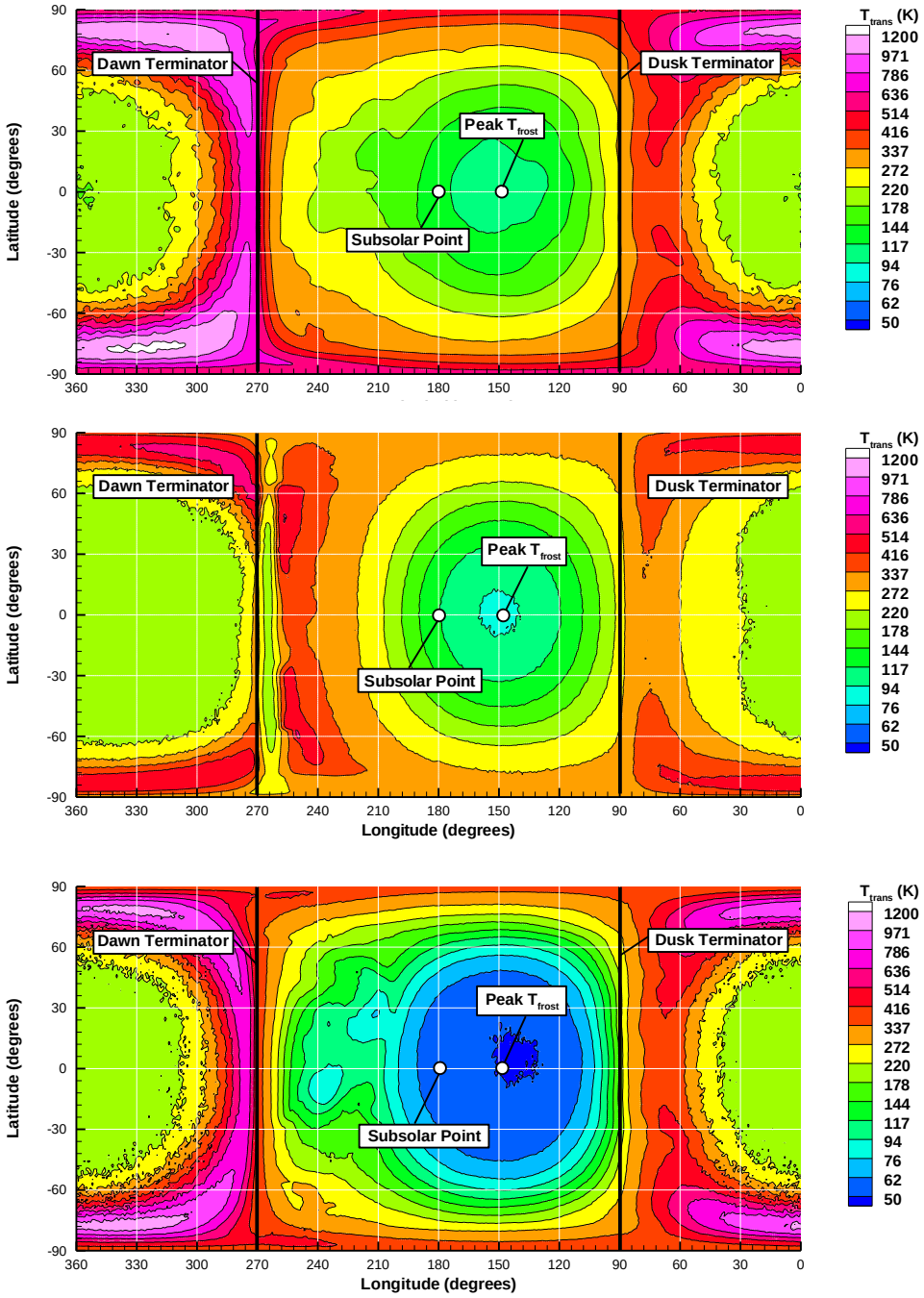

Figure 4.8: Color contours of T_{trans} at an altitude of 4 km as a function of latitude and longitude for (a) the baseline atmosphere, (b) Case 2, and (c) Case 3. The dawn and dusk terminators are denoted by the thick black vertical lines. Note the exponential color bar.

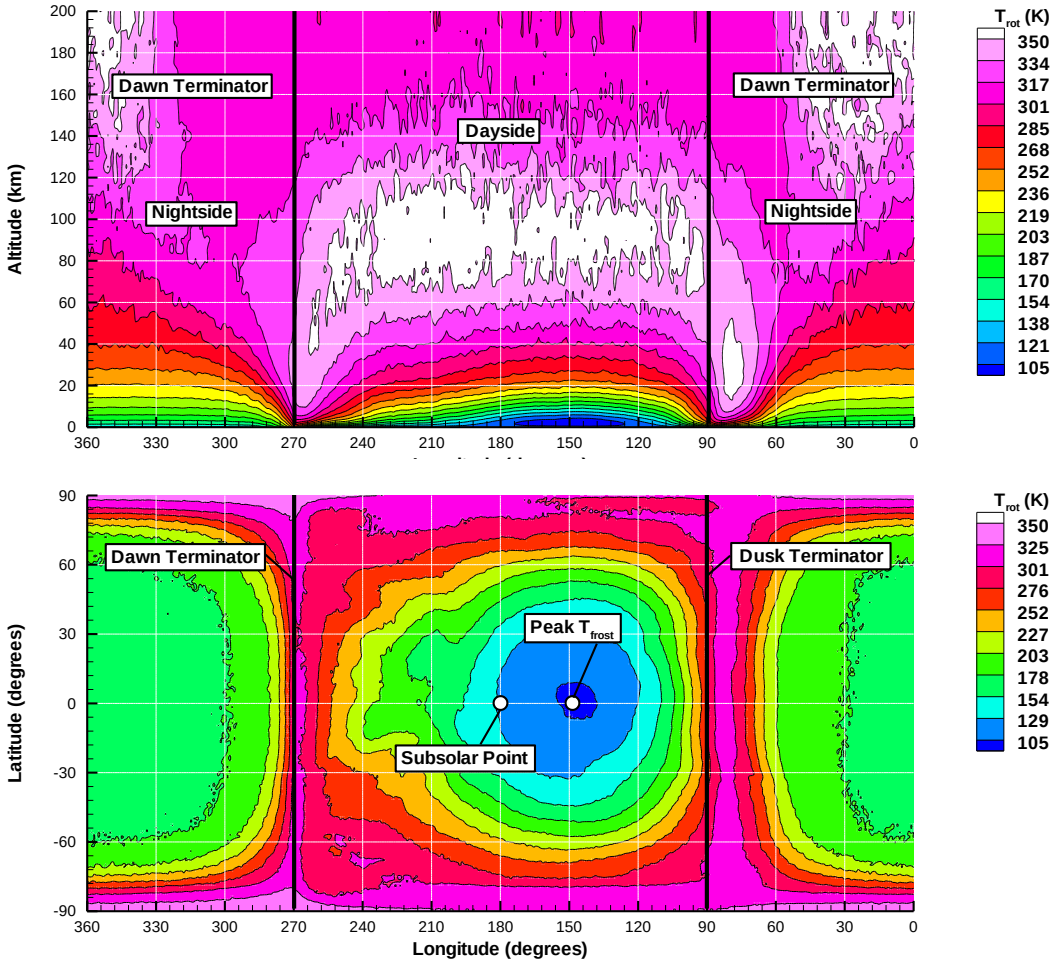

Figure 4.9: (a) Contours of T_{rot} for a cross-sectional slice through the baseline atmosphere at the equator. (b) Contours of T_{rot} for a slice through the atmosphere at an altitude of 4 km. Note the different temperature scales for figures (a) and (b).

The rotational temperature, T_{rot}, is maintained in equilibrium with T_{trans} by collisions; departures from thermal equilibrium occur because the collision rate drops as the density decreases with altitude. In the baseline atmosphere (T_{ss} = 115 K), T_{rot} is in equilibrium with T_{trans} at altitudes below 40 km on the dayside and nowhere on the nightside (Figure 4.7, Figure 4.9a, and Figure 4.9b). As seen in Figure 4.7, T_{rot} is in equilibrium with T_{trans} when the gas density is greater than ~10^9 cm^{-3}. As the density decreases below this value the collision rate for rotational excitation drops below the

threshold needed to sustain equilibrium with T_{trans}. At higher altitudes, T_{trans} continues to increase due to plasma energy input whereas T_{rot} warms more slowly as the energy input from collisions and plasma is not sufficient to balance the energy loss from microwave radiation. For Case 3 (T_{ss} = 120 K), thermal equilibrium is maintained up to ~60 km altitude on the dayside because of the thicker column which raises the altitude of the threshold density (10^9 cm^{-3}) from 40 km to ~60 km; the nightside is unaffected by the change in T_{ss}.

For the baseline atmosphere, the vibrational temperature of the ν_2 vibrational mode of SO_2, T_{vib}, is only in equilibrium with T_{trans} very near the surface; everywhere away from the surface T_{vib} is highly non-equilibrium. I neglect showing ν_1 and ν_3 because their characteristic temperatures are much higher than ν_2 and it is computationally infeasible to get adequate statistics for the excited states of these vibrational modes when the atmosphere is much colder than their characteristic temperatures. The ν_2 band is of special importance because it is used in Section 4.5.1 to compare to disk-averaged mid-infrared observations of this vibrational mode (Spencer *et al*., 2005). In Figure 4.10a, contours of T_{vib} are shown for the same cross-sectional slice shown in Figure 4.9. The nightside is weakly populated at all longitudes and altitudes and there are nearly zero vibrationally excited SO_2 molecules above an altitude of 100 km leading to T_{vib} = 0. The two mechanisms which can yield a vibrationally excited SO_2 molecule in our current model are collisions and sublimation from the surface (since the departing molecule is assumed to be in thermal equilibrium with the surface). Direct plasma-induced excitation is not modeled in this chapter. Vibrational de-excitation of an SO_2 molecule occurs rapidly for the ν_2 band which has an Einstein A coefficient of $A_{1\rightarrow 0} = 0.88$ s^{-1} (Radzig and Smirnov, 1980). A rough estimate of the mean time between collisions can be calculated from:

$$\tau = \frac{\lambda}{\bar{c}} \qquad 4.1$$

where λ is the mean free path and $\bar{c}$ is the mean velocity of molecules in the gas. For T_{ss} = 115K, the mean time between collisions, τ, is about 0.05 s in the atmosphere just above the surface. Although, the mean time between collisions is shorter than the radiative lifetime of the ν_2 band, not all collisions will vibrationally excite an SO_2 molecule. In fact, relatively few collisions actually excite vibration. The vibrational collision number Z_v is the average number of collisions required before a collision which transfers vibrational energy occurs (Bass *et al.*, 1971). Z_v is a function of temperature and the relative collision energy but it is generally around 300 and never drops below 100 for the conditions present in Io's atmosphere (Zhang *et al.*, 2003). Therefore, it takes ~300 collisions before a molecule undergoes a collision which transfers vibrational energy. Therefore the mean time between vibrational exciting collisions, τ_{vib}, at the location of the peak T_F near the surface is roughly 15 s. Therefore, the vibrational excitation rate by collisions is much slower than the de-excitation rate by radiative emission and this is true everywhere in the atmosphere. In conclusion, near the surface from which the gas sublimates, T_{vib} is in near equilibrium with T_{rot} and T_{trans}, but T_{vib} rapidly becomes non-equilibrium with increasing altitude.

Without another mechanism to populate the ν_2 band, T_{vib} would rapidly asymptote to zero away from the surface. Io's plasma torus supplies such a mechanism. In the energy flux model (see Section 3.2.8), the plasma heating causes T_{vib} to increase (through collisions with molecules that absorbed plasma energy into their translational and rotational modes) where the atmosphere is sufficiently collisional (dense) and at altitudes above which the plasma has not yet been depleted. When the atmosphere is relatively thick (e.g. near the subsolar point), the plasma energy is completely absorbed by the atmosphere above a certain altitude. For T_{ss} = 115 and 120 K, the altitudes at which complete plasma depletion occurs are

2 km and 5 km, respectively. The probability of vibrational energy transfer increases with increasing collision energy. Also, the collision rate increases with T_{trans}. If the energy flux model were altered to allow for direct plasma-induced excitation by depositing an equal amount of energy into vibration, then we would likely see much warmer T_{vib} at high altitudes; however, the ν_2 band radiation emitted from high altitudes would still likely remain relatively small due to the low densities. This is largely what occurs when the plasma is described instead as particles and vibrational energy is exchanged through high energy collisions between ions and neutrals (see Chapter 7).

The latitudinal and longitudinal dependence of T_{vib} can be seen in Figure 4.10b which shows a slice of the atmosphere at a constant altitude of 4 km. On the nightside, T_{vib} is too cold to resolve; however, the nightside T_{vib} are unimportant for comparison to observations of the dayside atmosphere (Gratiy *et al.*, 2009).

The T_{vib} contours seen in Figure 4.10b exhibit a bullseye pattern on the dayside. T_{vib} is actually colder near the peak T_F because little of the plasma energy reaches this altitude. The "hot" ring of ~95 K T_{vib} corresponds to the region where plasma has penetrated *and* the gas is still sufficiently dense to be collisional. Both the plasma penetration depth and the gas density depend on the T_F which is ~110 to 112 K in the region below the hot ring. If we look at higher altitudes, then the radius of the bullseye ring will shrink because the gas is not sufficiently dense to have vibrational excitation collisions even with the additional energy from plasma heating. The peak T_{vib} occurs in a "dome" corresponding to areas where the plasma can penetrate and the gas is sufficiently dense (see Figure 4.10a). Below this dome the gas is colder because the plasma does not penetrate into the gas and collisions (without the input of plasma energy) are rarely energetic enough to excite the vibrational modes. Outside of the dome, the gas is not sufficiently collisional to transfer translational and rotational energy absorbed from the plasma to the vibrational states.

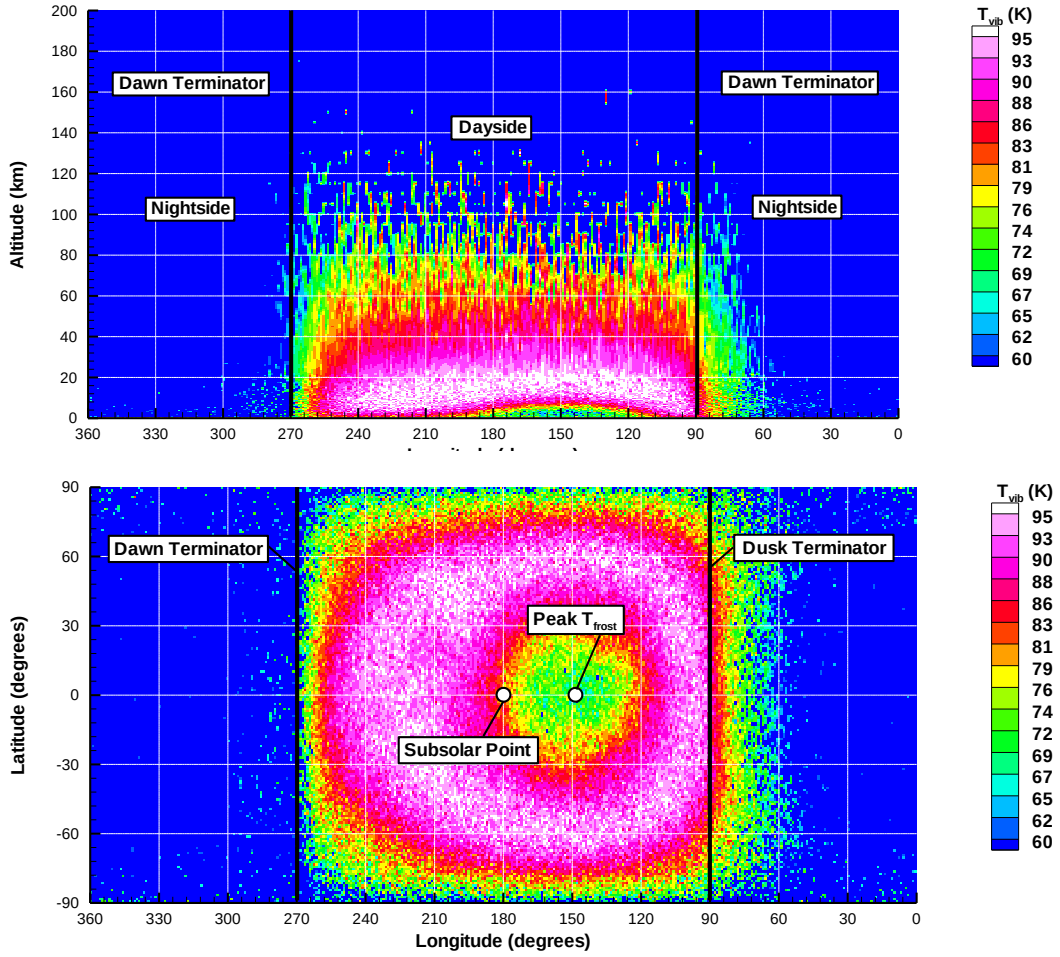

Figure 4.10: (a) Color contours of T_{vib} for a cross-sectional slice through the atmosphere at the equator. (b) Color contours of T_{vib} as a function of latitude and longitude at an altitude of 4 km. Results shown are for the baseline atmosphere.

The plasma energy flux can travel through the entire column of gas and strike the surface at longitudes beyond ~40º east and ~100º west of the peak T_F. The differences between the east and west are due to the additional column from the DAE to the west. Likewise, the plasma flux strikes the surface at latitudes beyond ±50º. When T_{ss} = 120 K, the plasma reaches the surface at approximately 55º east and 110º west of the peak T_F. Also, the plasma does not reach the surface until beyond latitudes ±70º. The thicker column at 120 K absorbs more plasma energy allowing the plasma energy flux to reach the surface only on the fringes of the dayside disk.

4.4 NUMBER AND COLUMN DENSITIES

The vertical column density is found to be predominantly controlled by the surface temperature (exponential dependence), the molecular residence time of SO_2 on the non-frost surface having the second largest effect, the surface frost coverage having a comparatively small effect (proportional), and winds having an even lesser effect. The exponential dependence of the vapor pressure (and hence sublimated flux of SO_2) on T_F explains the overwhelming influence of T_F on the column density (Figure 4.11a, b, and c). The increased departures from hydrostatic equilibrium on the morning side of the disk (compared to the evening side) are all due to the DAE. In Figure 4.11a, b, and c, the effect of inhomogeneous surface frost on the column density above the surface is evident. The inhomogeneities are seen most strongly on the nightside where the temperature is nearly constant. The column density is larger near regions of high frost fraction and smaller in areas of little frost. Circumplanetary flow is found to have a negligible effect on the column density for all cases.

For the baseline atmosphere, the *peak* equatorial vertical column density is 4.7×10^{16} cm^{-2} (at 148º W or 2:10 pm) and the subsolar vertical column density is 3.20×10^{16} cm^{-2} (at 180º W or 12:00 pm) with error estimates of $\pm5\times10^{14}$ cm^{-2}. The error is based on the noise in cells adjacent to the subsolar and peak equatorial values. The difference between the subsolar and peak vertical column densities is due to the thermal lag discussed in Section 4.2. The morning-side vertical column densities are increased beyond the hydrostatic equilibrium values due to the extended DAE. The nightside vertical column densities at 345º W (1:00 am) vary from 4.5×10^{12} cm^{-2} at 65º S and to 1.3×10^{13} cm^{-2} at the equator due to the latitudinal variation in temperature. The longitudinal variation in nightside vertical column densities is more complicated because of the high surface frost temperatures immediately adjacent to the dusk terminator on the nightside. At 85º W (local time ~6:20 pm), the surface

frost temperature is ~106 K with a corresponding vertical column density of 1.1×10^{15} cm^{-2}. The various nightside column densities vary nearly two orders of magnitude due to the high thermal inertia of surface frosts. The vertical column densities inferred from Lyman-α (Feaga *et al.*, 2009) are slightly higher than our sublimation atmosphere. As mentioned in the introduction, Feaga *et al.* (2009) determined the dayside peak vertical column density to be 5.0×10^{16} cm^{-2} on the anti-Jovian hemisphere, 4.2×10^{16} cm^{-2} at the anti-Jovian point, and 1.5×10^{16} cm^{-2} at the sub-Jovian point. The agreement with our simulations is relatively good and could be improved by increasing our assumed subsolar temperature of the surface to 116 K. However, it is important to note that the simulated vertical column densities do not include the column from active volcanoes so a 1 K increase in surface temperature may not be needed when the column densities due to volcanoes are accounted for.

For Case 2, the column density is negligibly affected by the surface frost fraction (on the dayside) and is completely controlled by T_F as seen by comparing Figure 4.11b with Figure 3.3b. In the short residence time model, the mean residence time on the non-frost surface at 115 K is approximately 5 s (Sandford and Allamandola, 1993). This residence time is short compared to both the ballistic time and the timescale on which the surface temperature varies. Also, the mean frost fraction at any given longitude never increases beyond 0.60 (see Figure 4.5). Molecules which hit the surface will therefore have a 40% or greater chance of hitting a non-frost surface and being promptly desorbed. In areas where the frost fraction is even lower, the likelihood of molecules desorbing from the surface increases and therefore these areas will be relatively more populated by molecules that have collided with the surface. Therefore, molecules which hit the non-frost surface are able to flow/diffuse over long distances to regions of lower pressure and laterally equilibrate the pressure such that it is only based on the T_F. This type of far reaching pressure control for hot and dry (non-frost) surfaces was discussed by Ingersoll *et al.*

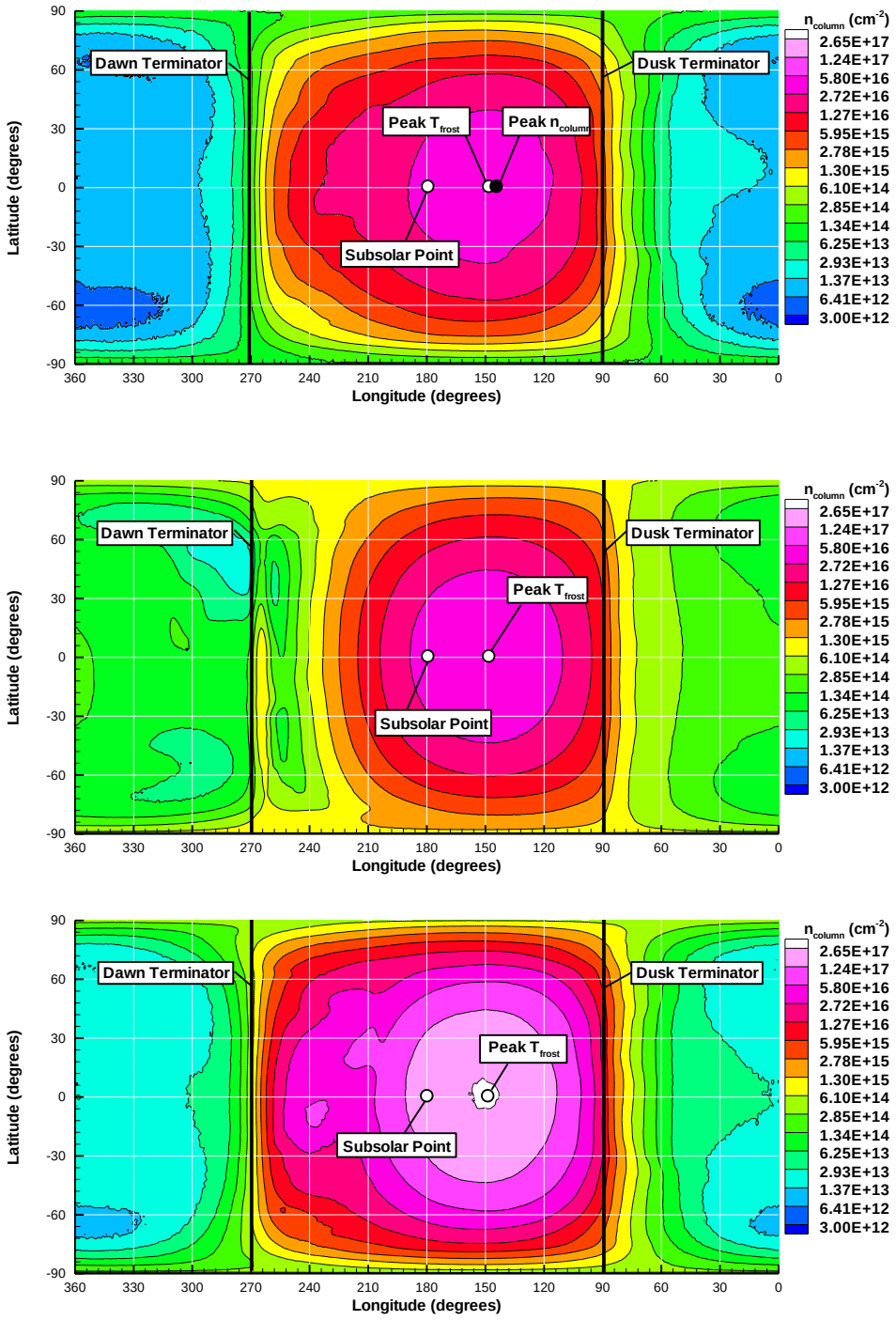

Figure 4.11: Color and line contours of the column density as a function of latitude and longitude for (a) the baseline atmosphere, (b) Case 2, and (c) Case 3.

(1989). The column density increases everywhere on the dayside because of the rapid rate at which molecules escape from the warm non-frost surface into the

atmosphere when the residence time is short. For Case 2, the peak equatorial column density is 5.45×10^{16} cm^{-2} (at 148º W or 2:10 pm) and the subsolar vertical column density is 3.7×10^{16} cm^{-2} (at 180º W or 12:00 pm). The Case 2 column densities are ~10% higher than the baseline atmosphere. The vertical column density also departs from hydrostatic equilibrium for Case 2 at the location of the DAE (Figure 4.11b). At this location, the atmosphere is not sustained by sublimation from the frost, but instead by the rapid desorption of all the SO_2 gas which condensed onto non-frost surface during the night.

For Case 3, the peak equatorial vertical column density is 2.73×10^{17} cm^{-2} and the subsolar vertical column density is 1.85×10^{17} cm^{-2}. These T_{ss} = 120 K column densities are five times as large as the T_{ss} = 115 K values and are above the upper range of observed column densities (1.25×10^{17} cm^{-2} – Jessup *et al*., 2004; 1.5×10^{17} cm^{-2} – Spencer *et al*., 2005). The T_{ss} = 120 K values are thus an upper limit on the vertical column densities and associated flow strengths.

When the baseline atmosphere has volcanoes superimposed, the column density near "persistent" volcanoes increases dramatically while the subsolar vertical column density remains the same as there are no "persistent" volcanoes close to the subsolar point for the baseline atmosphere's subsolar longitude of 180º W. The peak equatorial value however increases to 1.0×10^{17} cm^{-2} because of the additional column from Prometheus. The peak dayside vertical column density increases to ~7×10^{17} cm^{-2} near the center of Prometheus (at 140º W).

Plasma heating is found to alter the vertical density profile of the atmosphere but not change the vertical column density. The vertical column remains unchanged despite the plasma heating because it is sustained by the vapor pressure at the surface which is dependent only on T_F. Plasma heating inflates the atmosphere everywhere on the planet for all cases (see Figure 4.12).

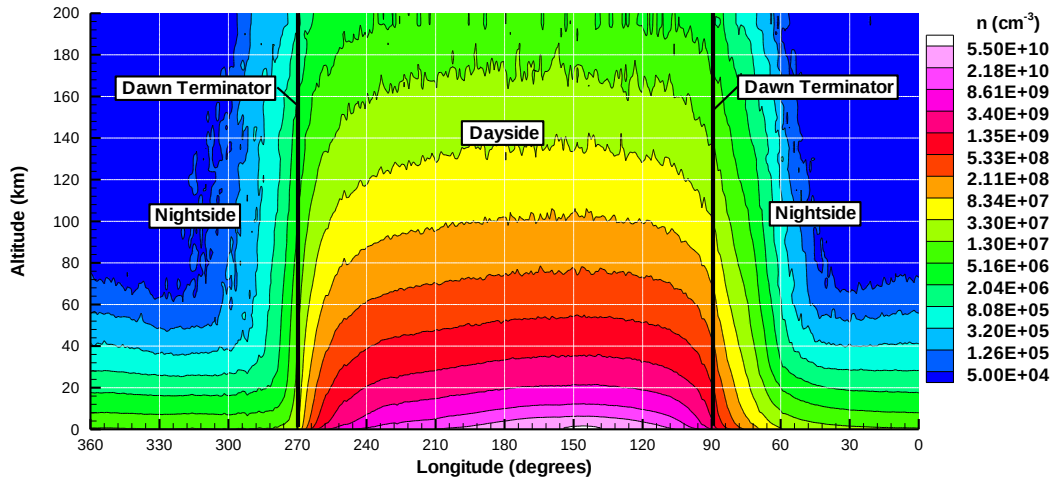

Figure 4.12: Color and line contours of the number density for a cross-sectional slice through the atmosphere at the equator for the baseline case.

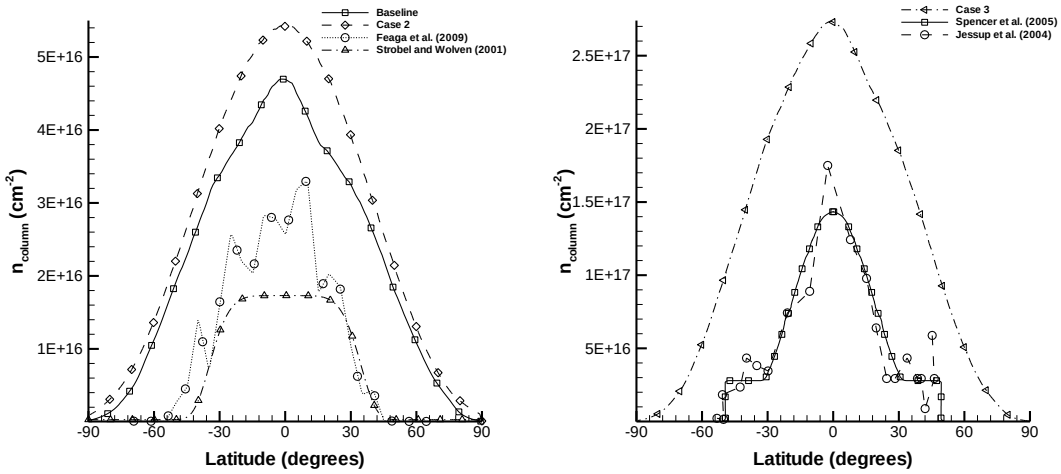

Figure 4.13: (a) The latitudinal variation in column density for our simulated baseline atmosphere, Case 2 (both at 148º W), Strobel and Wolven's empirical model (2000), and data extracted at 150º W from Feaga *et al*.'s (2009) global dayside atmosphere. (b) The latitudinal variation in column density for Case 3 (at 148º W), Jessup et al., (2004) at 153º W, and Spencer *et al*., (2005) at 180º W. Case 3 is compared to a different set of observations since the T_{SS} = 120 K is chosen to fit the high end of observations.

Besides comparing the magnitude of the vertical column densities at specific locations, the overall morphology can be compared (see Figure 4.13a). A striking feature of the Lyman-α inferred vertical column densities is the sharp falloff in

column near ±45º latitude (Strobel and Wolven, 2001; Feaga *et al.*, 2009). The latitudinal variation in our modeled column densities exhibits a much smaller decrease at mid-latitudes than those inferred from the Lyman-α observations. The column density variation in our model is directly related to T_F which at the peak T_F essentially follows a $\cos^{1/4}(\psi)$ latitudinal variation. There are several possible explanations for the differences between the Lyman-α results and our model column densities. These include: i) unobserved (and un-modeled) latitudinal variations in the T_F distribution, ii) volcanic plumes located primarily at low latitudes, or iii) ion-etched surface frosts near the poles.

To examine the first possibility, the average global dayside atmospheric column compiled by Feaga *et al.* (2009) is used to infer the required latitudinal variation in T_F to support the column. Feaga *et al.'s* global dayside map averages several instantaneous maps at different subsolar longitudes and as a result the longitudinal variation in the column is dependent only on the frost fraction and volcanic plumes (e.g. time of day effects are removed). The global dayside map still retains information on the latitudinal variation of the atmospheric column. Based on the results stated earlier in this section, the column densities are not significantly affected by the circumplanetary winds. Therefore, we assume that an analytic atmosphere in hydrostatic equilibrium based only on T_F and the frost fraction is a fairly accurate approximation (especially away from the morning side where the DAE affects the atmosphere). With this analytic representation for the column density, the global dayside atmosphere based on Lyman-α (obtained from Feaga *et al.* (2009)) can be inverted to find the required latitudinal variation in T_F (as seen in Figure 4.14). The observed Lyman-α column variation requires T_F to drop much faster than predicted by a $\cos^{1/4}(\psi)$ law. At ±45º latitude, the temperature inferred from Lyman-α observations (Feaga *et al.*, 2009) is ~104 K which is ~8 K colder than our current

model. Such a sharp drop in the surface temperature is also not seen in thermal data from the Galileo PPR observations (Rathbun *et al.*, 2004).

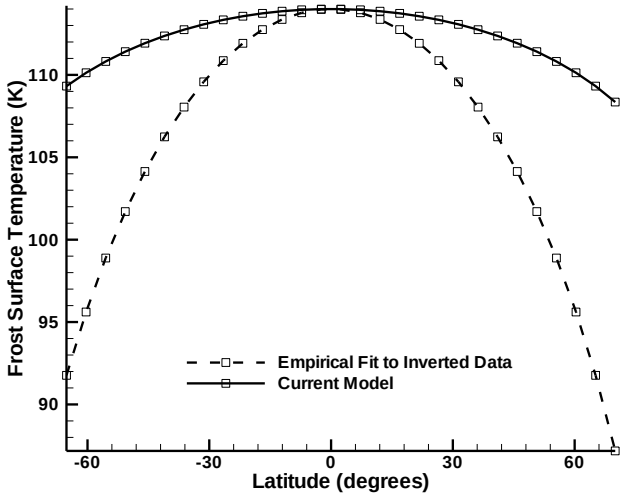

Figure 4.14: A comparison of the latitudinal temperature variation derived from Lyman-α inferred columns with our current model's latitudinal temperature variation. Our current model has a $\cos^{1/4}(\psi)$ latitudinal variation at the longitude of the peak T_F.

The second possibility is that the column is primarily supported by volcanic activity. Many of the large "persistent" volcanoes on Io are clustered in a band within $\pm 30^{o}$ of the equator (Geissler *et al.*, 2004) which does correlate with the equatorial "belt" atmosphere seen in the Lyman-α observations. The arguments both for and against volcanoes being the primary constituent of the atmosphere are presented by Spencer *et al.* (2005). Among the arguments against, the instantaneous column density maps (Feaga *et al.*, 2009) are surprisingly smooth whereas a volcanically supported atmosphere should be regional and patchy (as seen in Figure 3.6). Also, the instantaneous maps showed little temporal variation while several of the large volcanoes are known to have had temporal variations during the observational period (Feaga *et al.*, 2009).

The third possibility is that the plasma is impacting the surface at latitudes beyond ±45º. The plasma ions and neutrals could alter the composition of the surface frost and reduce the sublimation atmosphere near the poles. This possibility is explored in the simulations of Chapter 7 when surface sputtering is incorporated into the atmospheric model.

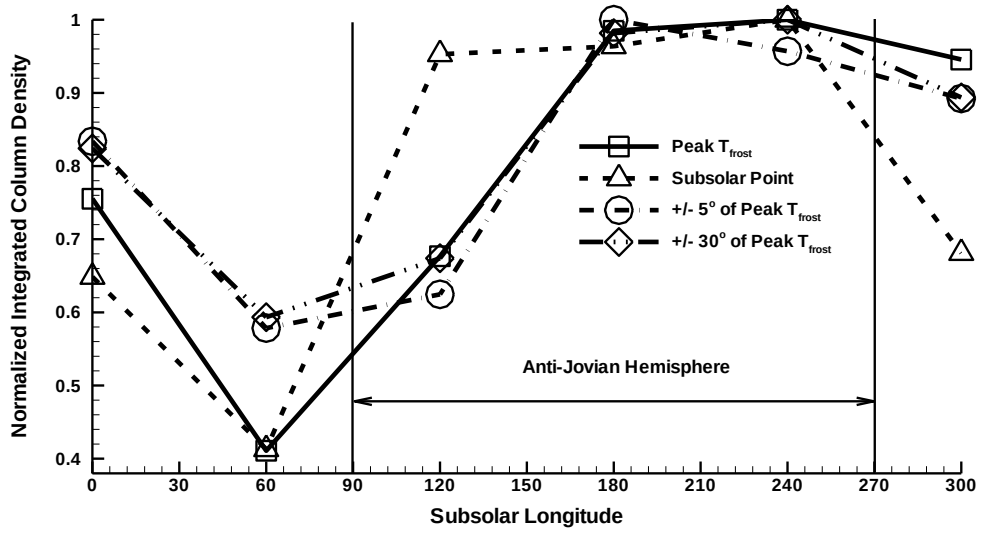

Figure 4.15: The integrated column density (normalized by the maximum value) for subsolar longitudes of 0°, 60°, 120°, 180°, 240°, and 300°. Each subsolar longitude has the column density integrated along the following paths or areas: the longitude of peak T_F from the north to south pole, the subsolar longitude from the north to south pole, in a 5° by 5° region around the point of peak T_F, and in a 30° by 30° region around the point of peak T_F. All integration areas show roughly the same trend. Eclipse of the sub-Jovian hemisphere is not considered.

Another major feature of the Lyman-α inferred column densities is the anti-Jovian/sub-Jovian hemisphere asymmetry, where the anti-Jovian hemisphere exhibits higher column densities than the sub-Jovian hemisphere. To compare with the Lyman-α observations, the column densities at six subsolar longitudes (each the product of a full numerical simulation) are averaged along different geometries and compared (see Figure 4.15). The column densities peak at the anti-Jovian point (180º W) and 240º W and show the expected overall trend with the anti-Jovian

hemisphere having higher averaged column than the sub-Jovian hemisphere. The anti-Jovian/sub-Jovian column density asymmetry in Figure 4.15 is caused solely by the surface frost fraction (Douté *et al.*, 2001). Note that eclipse of the sub-Jovian hemisphere is not modeled here but is included the simulations presented in Chapter 6.

The Lyman-α inferred dayside column densities (at a given subsolar longitude) are also nearly constant with local time of day which does not match our current sublimation atmosphere model. A possible reason for the discrepancy is that the surface frosts have an even higher thermal inertia than modeled here and therefore the surface frosts have nearly uniform surface temperature throughout the day. Another explanation is that the atmosphere is not only supported by sublimation but also by equatorial-biased volcanic plumes.

In Figure 4.13b, the latitudinal variation of the vertical column density of Case 3 is compared to the upper range of recent observations (Jessup *et al*., 2004; Spencer *et al*., 2005). Case 3 is much higher than either observational data set at all latitudes. The upper range data sets can also be compared with the baseline and Case 2 atmospheres (although they are not plotted together). Both Jessup *et al.* (2004) and Spencer *et al*. (2005) predict much higher column densities (2 to 3 times larger) than the baseline or Case 2 atmospheres. Their column densities correspond to a subsolar temperature of ~118 K.

A detailed comparison of our atmospheric model to the observations in the mid-IR, Lyman-α, and millimeter ranges is presented next. We apply a new three-dimensional spherical-shell radiative transfer code utilizing a photon backward Monte Carlo method to simulate spectra and images from the atmosphere, which can then be directly compared to observations. This analysis provides important feedback for improvement of the physical parameters which govern the atmospheric model's dynamics.

4.5 COMPARISONS TO OBSERVATIONS

Much of the work presented in this section was performed by Sergey Gratiy (Gratiy *et al*., 2009; 2010) using a backward Monte Carlo ray-tracing code he developed called Rassvet. Rassvet was applied to the computed atmospheric data sets shown in the preceding sections of Chapter 4 in order to compare to several observational data sets (see Gratiy *et al*. (2009) for a detailed explanation of Rassvet). These data sets include: mid-infrared disk-averaged observations of the ν_2 vibrational mode of SO_2 in Io's atmosphere (Spencer *et al*., 2005), Lyman-α observations of inferred SO_2 column density (Feaga *et al*., 2009), and millimeter band observations of Io's circumplanetary winds (Moullet *et al*., 2008). These comparisons provide an important validation of the atmospheric modeling and the results presented in Gratiy *et al*. (2010) are summarized in the following sub-sections. For a detailed discussion of the atmospheric validation see Gratiy *et al*., 2010.

4.5.1 MID-INFRARED SPECTRA

Rassvet is applied to the atmospheric model (both sublimation and composite) to simulate the disk-integrated spectra at 19.3 μm (Spencer *et al*., 2005). Subsolar longitudes at 0°, 60°, 120°, 180°, 240°, and 300° W are investigated to compare the longitudinal variation in band depth to the 19.3 μm observations (Spencer *et al*., 2005). We find that there is negligible variation in the band depth as a function of subsolar longitude for the SRT sublimation atmosphere model (see Figure 4.16). This is because the SRT atmosphere tends to smooth the column density and makes it dependent only on the local surface temperature despite inhomogeneities in the underlying frost fraction. When a volcanic component is added to the atmosphere, the SRT atmosphere still has poor agreement with the disk-averaged band depth because the majority of the atmosphere is sustained by sublimation.

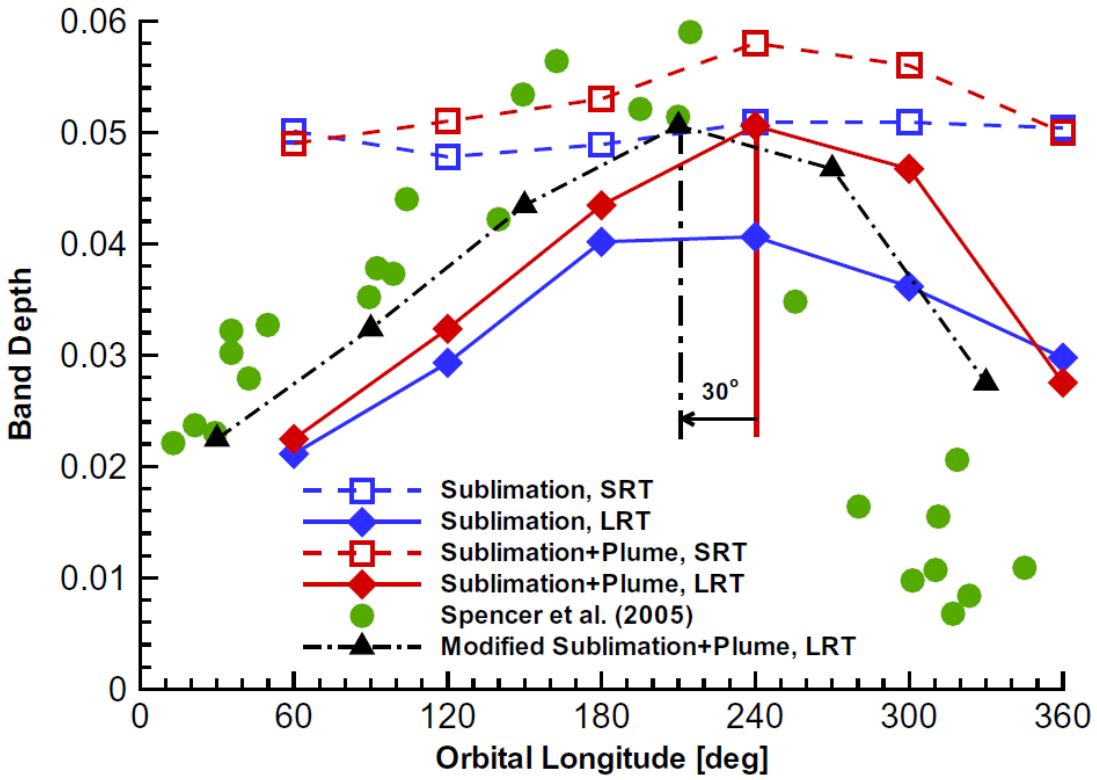

Figure 4.16: The longitudinal variation of the 19.3 μm band depth derived by Rassvet for four different atmospheric models compared to that derived from observations (Spencer *et al*., 2005). The best fit occurs when the composite LRT atmosphere is shifted by 30° to reduce the lag between the subsolar point and the peak column density region. (*Figure from Gratiy et al. (2010); Courtesy of Elsevier*).

The LRT sublimation atmosphere is a much better fit to the observations (Spencer *et al*., 2005) than either of the SRT atmospheres because it allows molecules to remain trapped on the surface long enough that the column density is dependent on the local frost fraction. In Figure 4.16, the LRT sublimation atmosphere peaks at 180° and 240° W because the frost fraction (Douté *et al*., 2001) is higher on the anti-Jovian hemisphere. When a volcanic component is included, the LRT composite atmosphere yields the best fit to the 19.3 μm band depth longitudinal variation. This is because the volcanic centers are biased towards the anti-Jovian hemisphere and tend to increase the band depth on that hemisphere. A fundamental feature of the four atmospheric models is the ~30° shift in the peak band depth which coincides with the

thermal lag between the subsolar point and the peak column density region. If the LRT composite atmosphere's band depth profile is shifted 30° to lower subsolar longitudes then there is much better agreement between the simulations and observations (Spencer *et al*., 2005). It is shown in Chapter 5 that the more sophisticated thermal model still leads to a ~30° lag between the subsolar point and peak T_F.

4.5.2 LYMAN-α IMAGING

Next, Rassvet is applied to disk-resolved Lyman-α observations taken during 1997–2001 (Feldman *et al*., 2000; Strobel and Wolven, 2001; Feaga *et al*., 2009) of Io's atmosphere in order to constrain the atmospheric column density distribution further. Lyman-α images consistently show bright areas near the poles of ~2 kR and lower intensity regions near the equator (~0.7 kR). Feaga *et al*., (2009) analyzed these Lyman-α observations and inferred SO_2 column densities that show little longitudinal variation but have a steep drop-off in SO_2 column densities at mid-latitudes (~45° N/S).

The Rassvet simulated images of Io's atmosphere utilizing the LRT composite modeled atmosphere (see Figure 4.17) yield intensities that are quite different from the observed Lyman-α images. The simulated images tend to have very low intensity along the eastern limb due to the thicker atmosphere (from the thermal lag). Intensities grow toward the western limb since the atmosphere is thin near dawn and the Lyman-α is not significantly attenuated there by the neutral atmosphere. This is at odds with the observed Lyman-α images that show bright polar regions and dark equatorial regions implying an equatorial atmosphere. Active volcanoes tend to completely absorb the Lyman-α intensity leaving voids in the simulated images. The discrepancies between the observed and simulated images are partially addressed by the more sophisticated thermal model discussed in Sections 3.3.2 and Chapter 5.

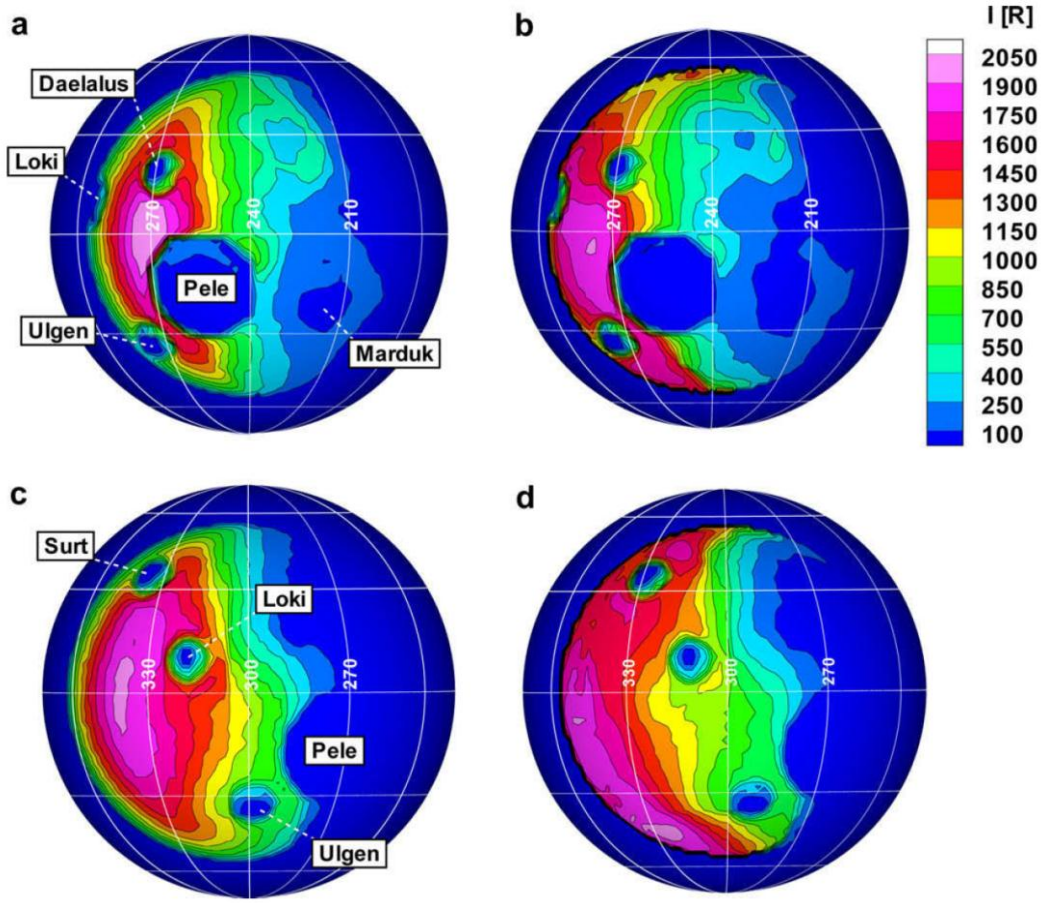

Figure 4.17: Modeled Lyman-α images of Io (in Rayleighs) at subsolar longitudes of 240° W (a and b) and 300° W (c and d). The left and right columns use different surface reflectance models. (a and c) use a Lambert surface with $A_L = 0.047$ while (c and d) single scattering approximation of Hapke under the assumption of a linear mixture. (*Figure from Gratiy et al. (2010); Courtesy of Elsevier*).

4.5.3 MILLIMETER-WAVE OBSERVATIONS

Lastly, Rassvet is applied to disk-integrated millimeter wavelength observations of Io's dayside atmosphere (Moullet *et al*., 2008). Observations were taken on the leading (subsolar longitude of 90° W) and trailing (subsolar longitude of 270° W) hemispheres. The primary conclusion of Moullet *et al*. (2008) was that the observations of the leading hemisphere were best fit by a super-rotating atmosphere in the prograde direction with an equatorial velocity of 170–300 m/s. We simulate the disk-integrated millimeter observations of Moullet *et al*. (2008) at the following

frequencies: 216.643, 221.965, 251.199 and 251.210 GHz. When the Doppler shifts are computed accounting only for the thermal Doppler broadening, the profiles are too narrow compared to the observations (see Figure 4.18a). If additional Doppler broadening due to the dynamic winds of the atmosphere is included, then the simulated line profiles agree much better with the observations (see Figure 4.18b). The super-rotating atmosphere that is inferred from the millimeter observations is not produced by our atmospheric simulations. Instead, as described in Section 4.2, the circumplanetary winds largely diverge in all directions away from the peak pressure region in the atmosphere. As will be shown in Chapters 6 and 7, the wind patterns can change substantially due to the influence of different underlying surface temperature distributions or the plasma pressure in more refined simulations.

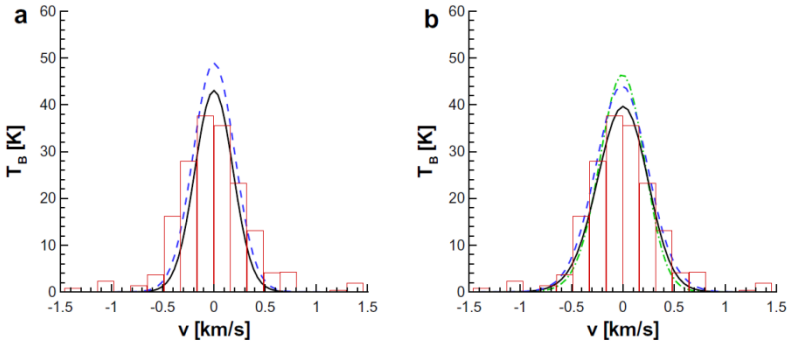

Figure 4.18: Simulated emission profiles of the 216.643 GHz line on Io's leading side. (a) Line profiles from the sublimation (solid line) and composite (dashed line) atmospheres formed by thermal Doppler broadening alone. (b) Line profiles from the sublimation (solid line) atmosphere with an additional broadening due to circumplanetary flow and composite (dashed line) atmosphere with additional broadening due to both circumplanetary flows and velocity dispersion within the plumes. The case for a composite atmosphere broadened only by the velocity dispersion in the plumes is also presented (dash-dot line). Histograms represent the Moullet *et al*. (2008) IRAM 30-m telescope data. (*Figure from Gratiy et al. (2010); Courtesy of Elsevier*).

CHAPTER 5: A PARAMETRIC STUDY OF THERMOPHYSICAL PARAMETERS FOR IO'S SURFACE

The results of Chapter 4 show that the SO_2 surface frost thermophysical parameters determine the morphology of the atmosphere due to the exponential dependence of the vapor pressure on the surface frost temperature. Specifically, in Section 4.5, much of the disagreement with observations seemed to be dependent on the thermal model. The disagreement between the DSMC atmospheric simulations and mid-infrared observations appeared to be due to the phase lag between the peak T_F and the subsolar point. Also, the differences in the latitudinal variations of simulated and Lyman-α observed column densities appear to be due to the assumption that the nightside will be at a uniform temperature of 90 K and that the temperature will drop as $\cos^{1/4}(\theta)$. Therefore, a more sophisticated thermal model was developed next (discussed in Section 3.3.2) but the controlling variables of the thermal model, i.e. the thermophysical parameters of the SO_2 surface frost and non-frost, were poorly constrained (see discussion in Section 2.3). Hence, a parametric study is used to constrain Io's surface thermophysical parameters by using a least-squares error method and fitting to mid- to near-UV (Jessup *et al*., 2004) and Galileo PPR brightness temperature observations (Rathbun *et al*., 2004).

5.1 PARAMETRIC STUDY OF THERMOPHYSICAL PARAMETERS

The first step in the parametric study is to set physical limits on the thermal inertia and albedo of both the SO_2 frost and non-frost. In the fitting process, the frost Bond albedo is allowed to vary from 0.55 to 1.0 based on correlations between regions of moderately high Bond albedos observed by Simonelli *et al*. (2001) and

regions of high frost fraction (Douté *et al*., 2001) that set a physical limit on the minimum SO_2 frost Bond albedo at 0.55. For the rest of this work, albedo will implicitly refer to Bond albedo for brevity. The non-frost albedo is thus fixed once the frost albedo has been determined because Io's global mean albedo is well constrained to be ~0.52 (Simonelli *et al*., 2001) and therefore the SO_2 frost and non-frost albedos weighted by their average areal coverage must give the mean global albedo. The frost and non-frost thermal inertias are allowed to vary between 0 and ∞ (although in practice the upper limit was placed at 10,000 J m^{-2} K^{-1} $s^{-1/2}$, a value large enough to easily contain the best fit parameters).

In step (i) of the fitting process, mid- to near-UV observations of the anti-Jovian hemisphere column density (Jessup *et al*., 2004) are used to infer SO_2 surface frost temperatures assuming vapor pressure equilibrium starting from

$$N_{OBS} = \frac{P_{VAP}}{m_{SO_2} g}, \tag{5.1}$$

where N_{OBS} is the observed SO_2 column density (Jessup *et al.*, 2004), m_{SO_2} is the molecular mass of SO_2, g is the gravitational acceleration at Io's surface, and P_{VAP} is defined by the Clausius-Clapeyron equation (see Eq. 3.3). Substituting Eq. 3.3 into Eq. 5.1 and then solving for T_F yields

$$N_{OBS} = \frac{Ae^{-B/T_F}}{m_{SO_2} g} \rightarrow T_F = \frac{B}{\ln(A/(N_{OBS} m_{SO_2} g))}. \tag{5.2}$$

Note that the assumption of VPE only holds when the atmosphere is dominated by sublimation rather than desorption from the non-frost surface (which occurs over a portion of the morning dayside atmosphere) and there is no net transport of mass. When the atmosphere departs substantially from VPE (>20%), a VPE correction factor, β, must be applied to the T_F inferred from mid- to near UV observations (Jessup *et al.*, 2004). The details of how β is calculated and applied are described in step (iv).

In step (ii), a brute force search through frost albedos and thermal inertias is performed with the thermal model described in Section 3.3.2 simulating T_F for each combination of α_F and Γ_F. The simulated and inferred T_F are compared at the locations listed in Table 2 of Jessup *et al*. (2004) and the quality of the fit for that particular combination of thermophysical parameters is computed based on a least-squares error method in which each data point is given equal weight.

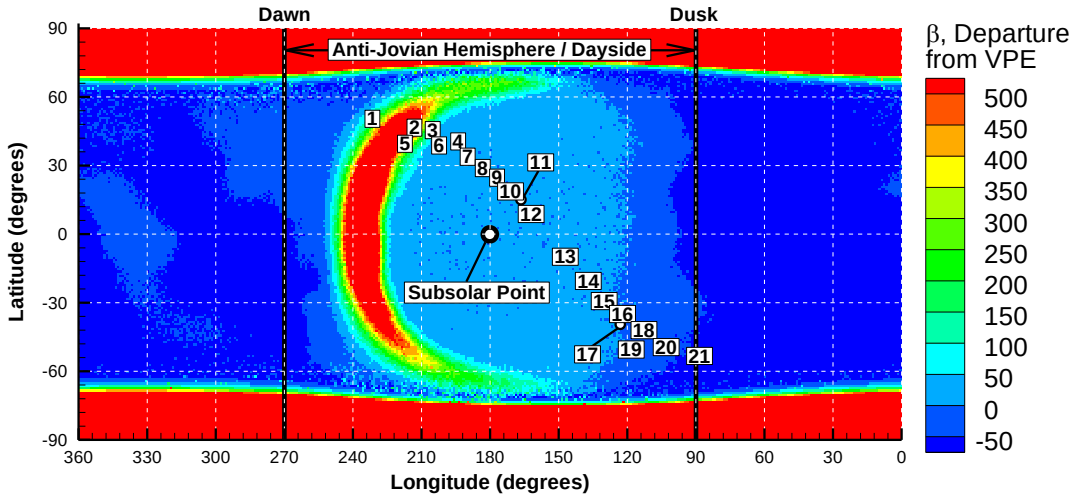

Figure 5.1: The percent difference as a function of latitude and longitude between the analytic atmospheric SO_2 column density based on equilibrium with the surface frost temperature and the column computed in the DSMC simulation with best fit parameters. The central (subsolar) longitude is located at the anti-Jovian point (180° W). Squares represent the mean location of the mid- to near-UV observations. See Figure 2 in Jessup *et al*. (2004) for the areal coverage of each bin number. Note that bin 13 from Jessup *et al*. (2004) has been removed because of the large volcanic contribution of Prometheus; therefore, bin notations in the present work above 12 are offset by 1 compared to their data.

In Step (iii), a brute force search through Γ_{NF} is performed with the frost thermophysical parameters fixed as the best fit parameters from step (ii). For each Γ_{NF}, the simulated brightness temperature distribution, T_B, is calculated by summing the radiated flux from the frost and non-frost surface areas in a given surface cell and finding the equivalent blackbody temperature. The observed T_B distributions, to

which the simulated T_B distributions are compared, were taken at several different subsolar longitudes but then combined as a function of time of day (Rathbun *et al*., 2004). The underlying frost fraction for each observation was undoubtedly different and therefore, the frost fraction is assumed uniform (50% frost / 50% non-frost) for the calculation of the simulated T_B distribution since the mean frost fraction is near 50% (see Figure 4.5). The simulated and observed T_B distributions (Rathbun *et al*., 2004) are then compared and a best non-frost Γ_{NF} is found via a least-squares error method where each point is given equal weight. Thus, both the frost and non-frost thermophysical parameters are constrained before iterating to correct for the initial assumption of VPE.

In step (iv), the errors generated from the initial assumption of VPE are corrected by computing and applying the VPE correction factor, β, to the inferred T_F. Figure 5.1 shows the percent difference between the atmospheric SO_2 column density in VPE with modeled T_F and the actual SO_2 column density computed in subsequent DSMC simulations of the atmosphere using the best fit thermophysical parameters after completing steps (i), (ii), and (iii). Note that the DSMC simulated atmosphere used for this comparison does not include the effect of intermolecular collisions because it would be prohibitively expensive in terms of computation time. To calculate β (at a central longitude of 180° W), the percent difference is computed at each of the locations observed by Jessup *et al*. (2004) where the percent difference is

$$\beta = 100\,\frac{N_{DSMC} - N_{VPE}}{N_{VPE}} \qquad 5.3$$

In Figure 5.1, the departure from VPE is small (<10%) near noon and on the dusk portion of the disk but large (>100%) on the morning portion of the disk because the quick thermal response of the non-frost surface at dawn leads to rapid desorption of SO_2 molecules from the non-frost surface. This atmospheric enhancement near dawn was discussed in Chapter 3 and 4 and termed the "dawn atmospheric

enhancement" or DAE. Departures from VPE due to transport of mass by circumplanetary winds are minor and dwarfed by the desorption of SO_2 from the non-frost surface. Due to the DAE, the original assumption of VPE breaks down near the dawn terminator and β must be applied to the surface frost temperatures (Jessup *et al*., 2004) that are being fit.

The areas near the poles exhibit large variations from VPE because the statistics in the DSMC simulation break down there; however the mid- to near-UV data (Jessup *et al*., 2004) used for the least squares fitting does not extend to these regions. There are no molecules near the poles due to the constant weight (used in the DSMC simulations) near the poles and the continuously dropping P_{VAP} with latitude. Unfortunately, the simulations require a constant weight near the poles because the equilibrium P_{VAP} drops so precipitously near the poles (~10^{12} times lower at 70 K compared to the subsolar P_{VAP} at ~120 K). Computational errors arise from massive cloning and destruction of molecules (even when the gas is collisionless) when the weight is allowed to adapt freely and balance the number of computational SO_2 molecules in each column of cells.

β, calculated in Eq. 5.3, is applied to the mid- to near-UV inferred column densities (Jessup *et al*., 2004):

$$N_{CORR} = \frac{N_{OBS}}{(1+\beta/100)} \rightarrow T_F = \frac{4510K}{\ln(^{1.52\times10^{13}}/_{N_{CORR}m_{SO_2}g})}. \quad 5.4$$

This yields "corrected" VPE column densities, N_{CORR}, which can be inverted to find the "corrected" T_F that will be used for the next iteration of the fitting process (steps (ii) and (iii)). Steps (ii), (iii), and (iv) are then repeated while matching instead to the "corrected" T_F computed via Eq. 5.4. The correction process is iterated until the thermophysical parameters converge to within 5% of the values on the previous iteration. Figure 5.2 shows a flow chart for the logic used in the parametric study.

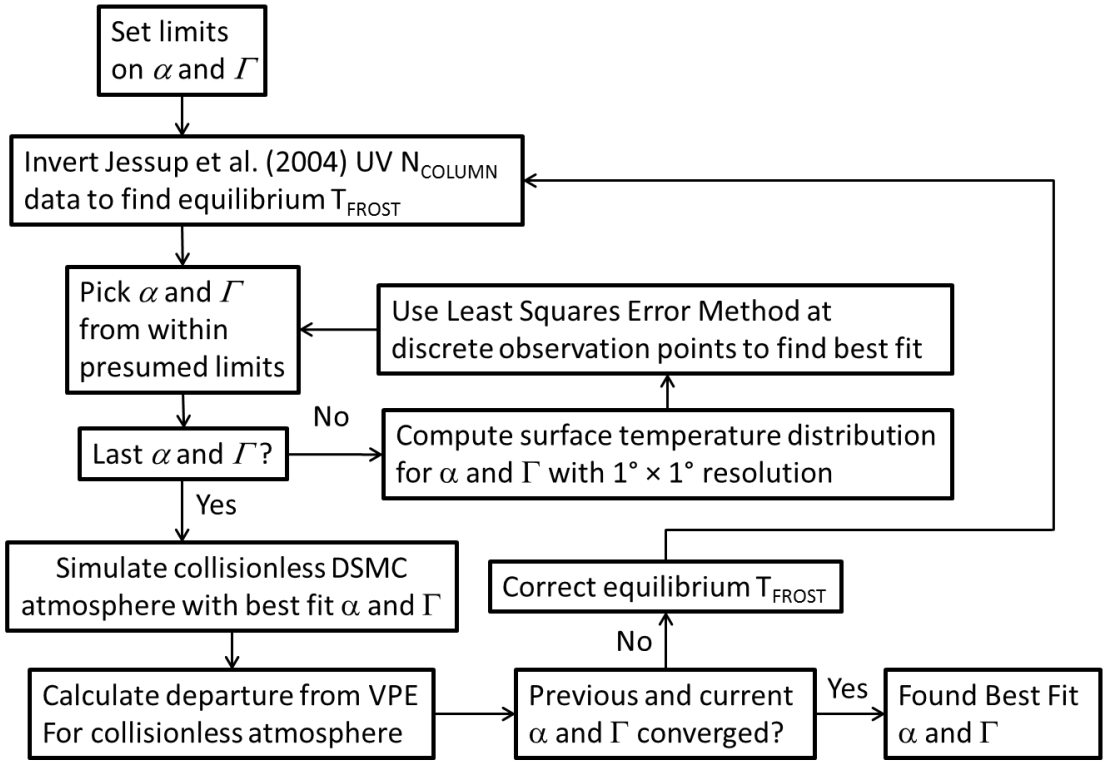

Figure 5.2: A flowchart detailing the logic chain in the parametric study.

5.2 Resultant Thermophysical Properties from Parametric Study

Using the method outlined in Section 5.1, the best fit thermophysical parameters for the frost and then the non-frost surfaces are computed. The best fit parameters are found to be $\alpha_F \approx 0.55 \pm 0.02$ and $\Gamma_F \approx 200 \pm 50$ J m^{-2} K^{-1} s$^{-1/2}$ for the SO_2 frost surface and $\alpha_{NF} \approx 0.49 \pm 0.02$ and $\Gamma_{NF} \approx 20 \pm 10$ J m^{-2} K^{-1} s$^{-1/2}$ for the non-frost surface. The iterative process described in Section 5.1 required three steps to converge to within 5% of the previous values for the thermophysical parameters of interest. Error estimates for each thermophysical parameter represent the range of parameters that lie within ±10% of the best fit χ^2.

5.2.1 FROST BEST FIT PARAMETERS

As discussed in Section 5.1, the constraint $\alpha_F > 0.55$ is applied based on correlations between regions of high mean albedo (Simonelli *et al*., 2001) and high frost fraction (Douté *et al*., 2001). Lower albedos with higher thermal inertias are found to give better fits to the HST observations (Jessup *et al*., 2004); however, these violate the $\alpha_F > 0.55$ assumption. Figure 5.3 shows the best (but unphysical) fit occurring in the lower right hand corner at $\alpha_F \sim 0.50$ and $\Gamma_F \sim 300$ J m^{-2} K^{-1} s$^{-1/2}$. If the domain is extended to even lower albedos and higher thermal inertias, the best fit lies at $\alpha_F \sim 0.46$ and $\Gamma_F \sim 1000$ J m^{-2} K^{-1} s$^{-1/2}$; however, these parameters were deemed unphysical due to the unreasonably low frost albedos (<0.55).

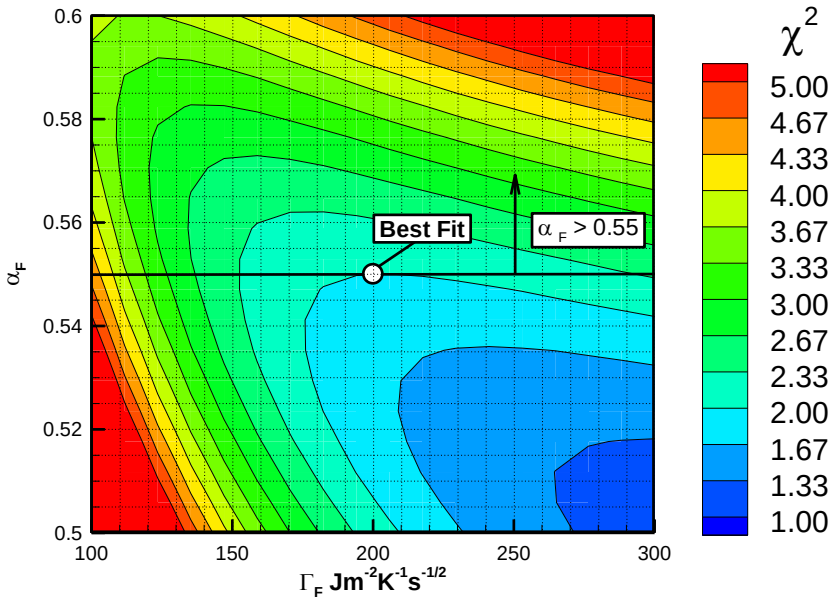

Figure 5.3: χ^2 (least squared error) as a function of frost albedo, α_F, and thermal inertia, Γ_F. The range of α_F extends to 0.50 to emphasize that better fits exist at lower albedos. When the best fit is restricted to an $\alpha_F > 0.55$ it is found at $\Gamma_F \sim 200$ J m^{-2} K^{-1} s$^{-1/2}$ and $\alpha_F \sim 0.55$ for the final iteration.

The simulated T_F using the best fit parameters is plotted in Figure 5.4 along with the observational data (Jessup *et al*., 2004) as a function of the original data's

bin number. The best fit slightly overestimates the peak but generally agrees at large bin numbers (the afternoon region of the surface) except at the edges (bin numbers near 0 and 20). The agreement is worse at small bin numbers (the morning portion of the surface) where the observations become noisy and have little drop-off with solar zenith angle. Simulations of Io's atmosphere above a simplified surface model have recently been performed that include plasma chemistry and sputtering due to energetic ions (Moore *et al*., 2011, 2012). These simulations find that sputtering becomes significant when the surface temperature drops below ~108 K. It may be that the lack of drop-off in observationally inferred T_F near the dawn terminator is due to sputtering which is not included in our numerical model presented here. Sputtering would likely keep the column density fairly constant below ~108 K (Moore, 2011) and reduce the discrepancy between the simulated best fit and observed T_F in bins 1−5. See Section 7.1 for the atmospheric simulation results that include surface sputtering.

The relatively high thermal inertia we find for the frost indicates the presence of at least partially annealed or coarse-grained ice. A process for annealing SO_2 frost on Io was suggested by Sandford and Allamandola (1994) as a result of the large diurnal temperature change for an initially porous low thermal inertia frost. Initially porous SO_2 frost on the surface originating from either circumplanetary flow or volcanic plumes will anneal as the relatively high temperatures during the day allow molecules to break their bonds with the surface, migrate down through the pores of the frost, and eventually fill the pores. The best fit thermal inertia we obtain, $\Gamma_F \sim 200$ J m^{-2} K^{-1} s$^{-1/2}$, also agrees with recent observations and subsequent fits of Io's atmospheric column density variation with heliocentric distance (Tsang *et al*., 2012). The resulting SO_2 surface frost temperature distribution as a function of latitude and longitude with the best fit frost thermophysical parameters and for a subsolar longitude of 180° W is shown in Figure 5.5.

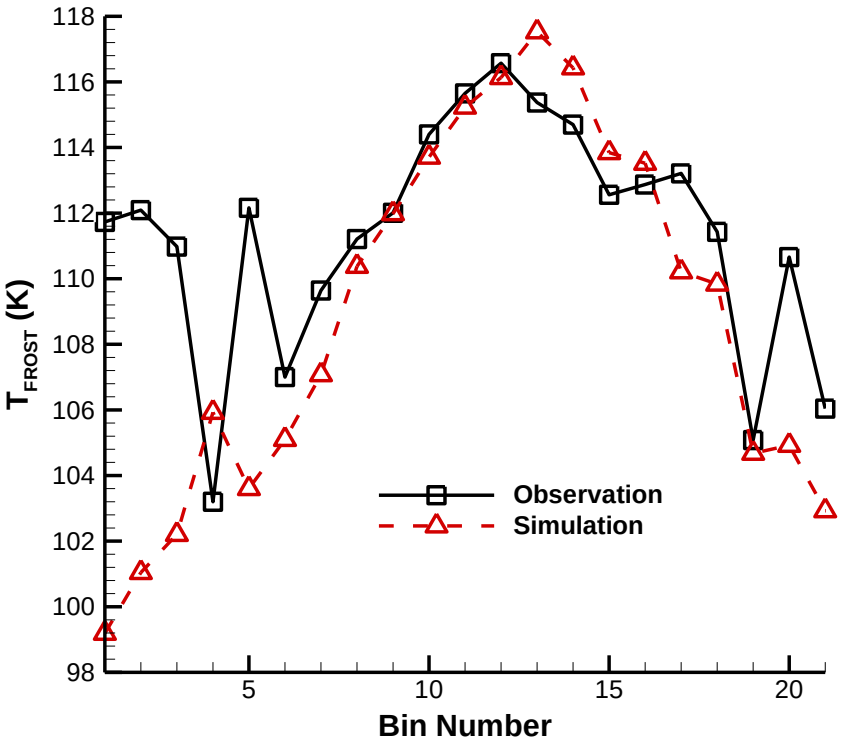

Figure 5.4: A comparison of the observed and simulated surface frost temperatures (with the best fit thermophysical parameters) at the locations (bin number seen in Figure 5.1) of the observations (Jessup *et al.*, 2004).

With the best fit thermophysical parameters, the peak T_F is ~119.4 K on the anti-Jovian hemisphere which is slightly higher than the values of 116.7 K (for a latitudinal fit) and 118 K (for a solar zenith angle fit) derived by Jessup *et al.* (2004) based on VPE. This discrepancy is because the best fit overestimates the peak T_F in order to fit the data points at mid- to high solar zenith angles. The effects of vapor pressure non-equilibrium are quite small (in the region around the peak T_F) as shown in Figure 5.1. The departure of the column density from VPE is less than 10% at the location of the peak T_F and everywhere between 180° W and 90° W at low to mid-latitudes. The subsolar temperature is ~117.3 K (2.1 K colder than the peak T_F). The relatively high Γ_F causes a phase lag between the subsolar point (180° W) and the

peak T_F equal to ~33° which is close to the value of 32° found in the original thermal model of Chapter 4 (see Figure 5.6). The higher thermal inertia used in the updated thermal model yields higher surface temperatures on the nightside (by ~10 K).

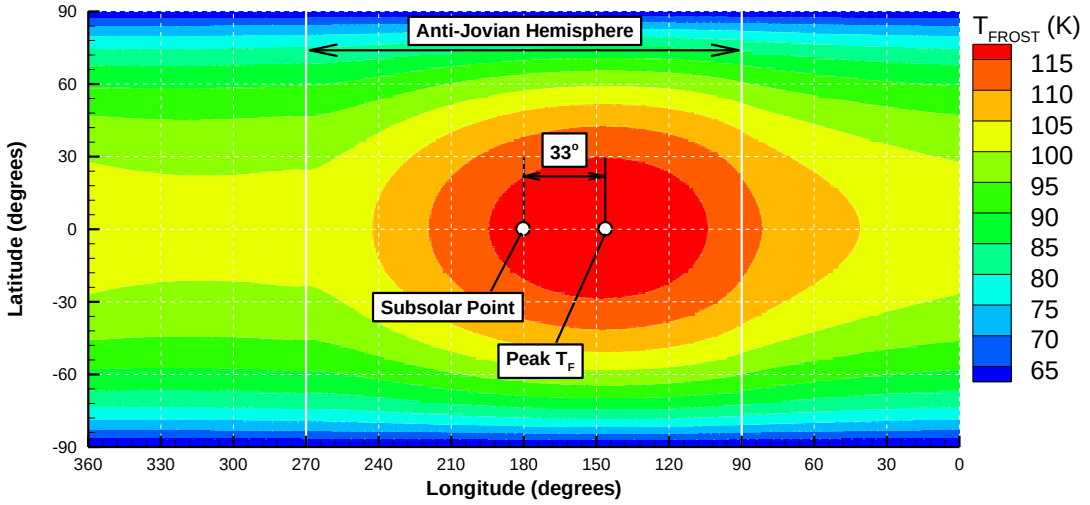

Figure 5.5: The SO_2 surface frost temperature as a function of latitude and longitude. The subsolar point and peak T_F are labeled by white circles. The relatively high thermal inertia of the frost leads to a large thermal lag of 33° between the subsolar point and the peak temperature.

One reason for the more sophisticated thermal model was the poor temperature fits to observationally inferred T_F at high latitudes (Feaga *et al.*, 2009) using the original thermal model (see Figure 4.14). Note that the inversion from column density to T_F assumes vapor pressure equilibrium which is justified by the results of the atmospheric simulations of Chapter 4. The updated thermal model fits SO_2 frost surface temperatures to T_F inverted from a different set of inferred column densities (Jessup *et al.*, 2004). Therefore, we do not expect the fit at low latitudes to be as good as the original thermal model (which had a peak T_F of ~115 K to fit Feaga *et al.*, 2009). The latitudinal variation of the two thermal models as well as T_F inverted from Lyman-α observations (Feaga *et al.*, 2009) are shown in Figure 5.7. As expected, the low latitude fit is better between the observational data and the original

thermal model; however, at high latitudes where the original thermal model departs substantially from the observational data, the updated thermal model has a much improved fit.

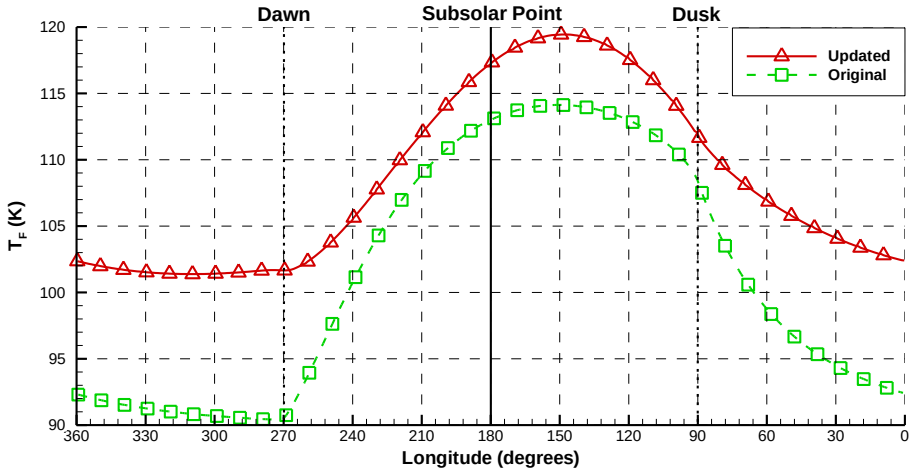

Figure 5.6: A comparison between the original thermal model discussed in Section 3.2.3 and the updated thermal model discussed in Section 3.3.2. The updated thermal model has a higher thermal inertia and therefore smaller diurnal variation.

Figure 5.8 shows three longitudinal T_F profiles at 30° intervals of latitude starting at the equator (0° N, 30° N, 60° N). The equatorial T_F reaches a minimum of 101.1 K approximately 30° (~3 hours) before dawn. Just before dawn, $T_F = 101.6$ K. This does not mean that the given location on the surface is actually warming as it approaches dawn but that the points nearer the anti-Jovian hemisphere are warmer than those further away. This is an effect of eclipse which will be discussed in Section 5.3. The peak T_F of the profile at 30° N is 4.9 K cooler (114.5 K) than the equatorial profile. At all longitudes on the nightside, the 30° N profile is ~3.0 K cooler than the equatorial profile. Lastly, the 60° N profile shows much lower temperatures and smaller diurnal variation as expected due to the smaller amount of absorbed sunlight. The peak T_F drops to 98 K and has a minimum of 88 K during the night.

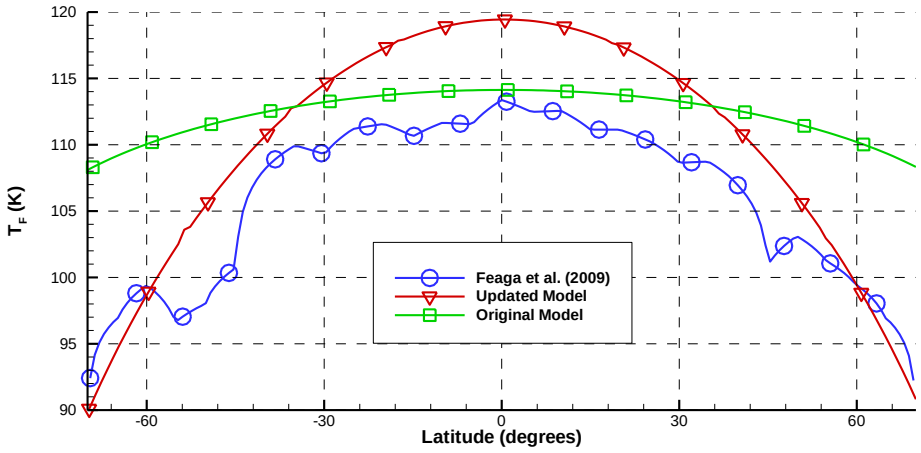

Figure 5.7: A comparison between the latitudinal temperature profiles of the original and updated thermal models as well as a temperature profile inverted from inferred column densities (Feaga *et al*., 2009). This is a re-creation of Figure 4.14 but uses the raw inverted temperature profile from Feaga *et al*. (2009) rather than a best fit. The latitudinal extent is limited to ±70° because that is the limit of the observational data (Feaga *et al*., 2009).

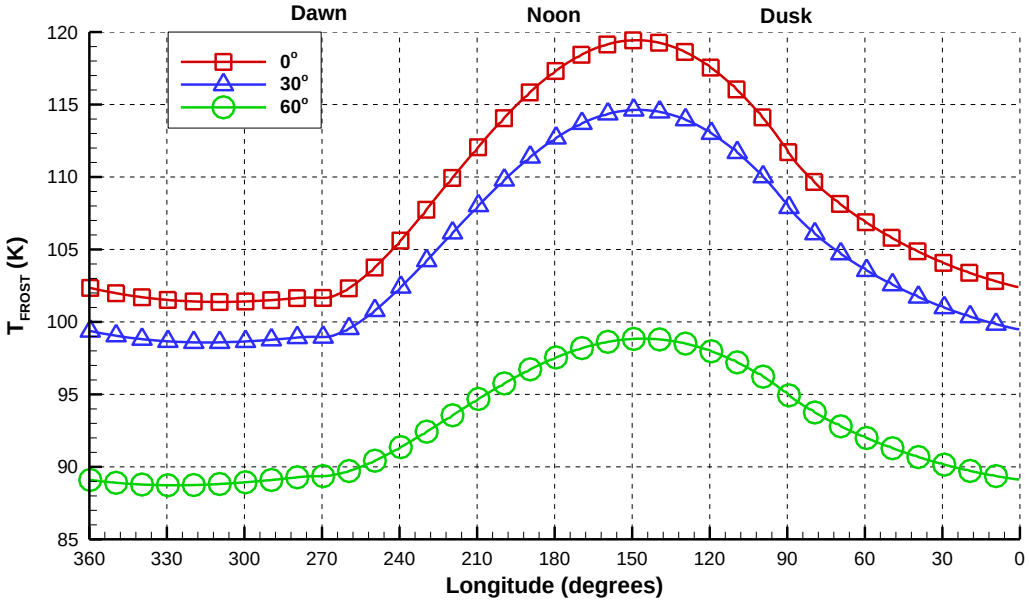

Figure 5.8: SO_2 frost surface temperature profiles as a function of longitude for selected latitudes of 0°, 30°, and 60°.

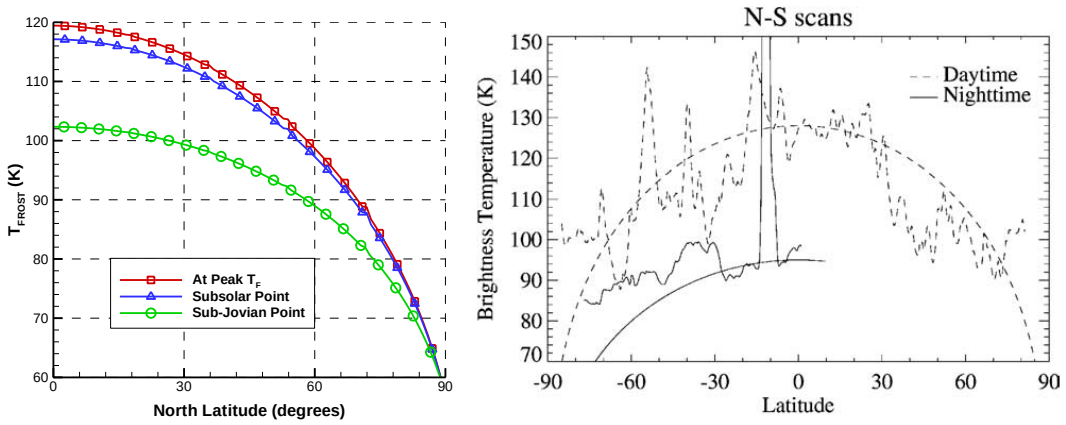

Figure 5.9: (a) Temperature profiles as a function of latitude extracted at the longitudes of several points on Io's surface: the peak T_F, the subsolar longitude (also the anti-Jovian point), and the sub-Jovian point (midnight). (b) Observed brightness temperature profiles as a function of latitude for both daytime and nighttime (*From Rathbun et al. (2004), courtesy of Elsevier*).

Next, we examine the latitudinal dependence of the frost temperature distribution at 180° W subsolar longitude. Figure 5.9 shows three latitudinal T_F profiles for selected longitudes (peak T_F, subsolar longitude, and sub-Jovian point). The equatorial temperatures have already been discussed so we focus on mid- to high latitudes. Near the poles, T_F drops to ~60 K due to the very low diurnally-averaged solar flux for all longitudes. 60 K is ~20 K colder than the coldest temperatures observed by the Galileo spacecraft's PPR (Rathbun *et al*., 2004) and it may be that the poles are areas of excess (un-modeled) endogenic heating as discussed by Rathbun *et al*. (2004) or there may be excess (un-modeled) plasma heating near the poles. The sub-Jovian point's equatorial T_F is ~102 K (17 K colder than the peak T_F on the dayside). Mid-latitudes quickly warm to brightness temperatures observed by the Galileo PPR (Rathbun *et al*., 2004). At ±70° N/S, the observed dayside T_B is ~100 K at the subsolar longitude while the nightside T_B is ~85 K (see Figure 5.9b). In comparison, simulated dayside T_B (not shown) is ~95 K at the subsolar longitude and nightside T_B of ~75–85 K (depending on the local time of day).

5.2.2 NON-FROST BEST FIT PARAMETERS

The best fit for the non-frost thermophysical parameters is shown in Figure 5.10. The best fit occurs at $\alpha_{NF} \approx 0.49$ and $\Gamma_{NF} \approx 20$ J m^{-2} K^{-1} s$^{-1/2}$. As discussed earlier, the best fit α_{NF} is fixed once the best fit α_F is chosen and therefore only Γ_{NF} remains as a free parameter. A larger range of Γ_{NF} was studied than shown in Figure 5.10 and the error was seen to increase monotonically away from the best fit Γ_{NF} (e.g. no other minima were found). A comparison to the brightness temperature, T_B, computed from observations made by the Galileo PPR (Rathbun *et al*., 2004) is shown in Figure 5.11.

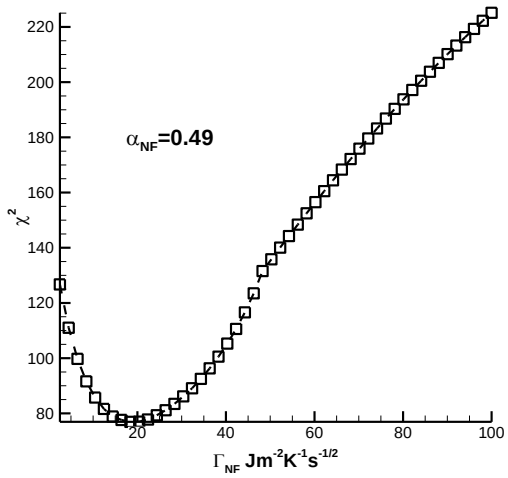

Figure 5.10: χ^2 as a function of non-frost thermal inertia, Γ_{NF}. The non-frost albedo, α_{NF} is constrained to be 0.49 by the frost albedo and mean frost fraction. The best fit occurs at Γ_{NF} ~20 J m^{-2} K^{-1} s$^{-1/2}$.

The peak T_B for the observation is ~130 K and the simulation overestimates the data by ~2 K. The main regions of discrepancy occur during the night (at "times of day" between 15° and 195° W). The simulated brightness temperature is slightly too high just after dusk and before midnight but too low after midnight and before dawn. Better fits to the nightside cooling rate were achieved using a lower (but unphysical) frost albedo with a higher thermal inertia. The minimum T_B (~96 K) for

the observation occurs just before dawn but is ~3–4 K lower in the simulation. The spike in the observation at ~210° (time of day) is a hot spot (Prometheus).

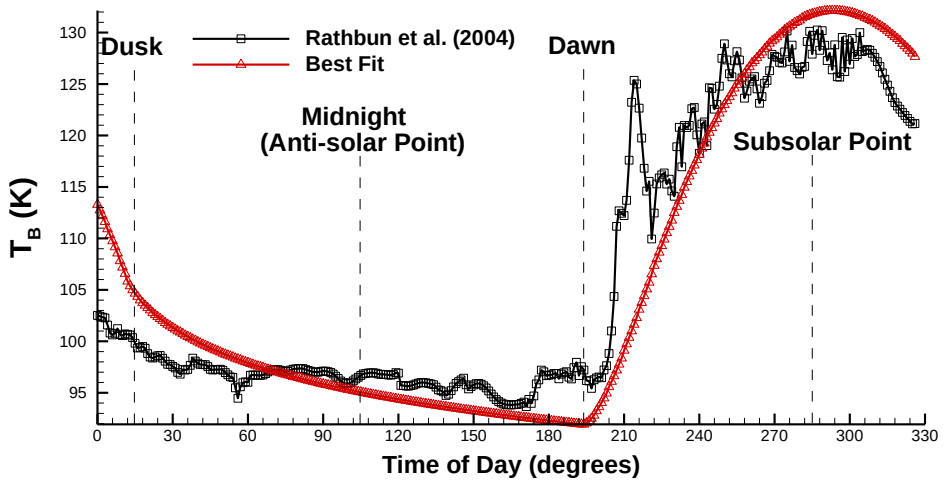

Figure 5.11: A comparison between observed (Rathbun *et al*., 2004) and simulated brightness temperatures. The best fit appears to slightly overestimate temperatures just after dusk (~30°–60° W) and underestimate temperatures just before dawn (~120°–180° W). The single line shown for the observed T_B (Rathbun *et al*., 2004) is an average of several observations taken at different subsolar longitudes but all within 20° latitude of the equator.

The very low thermal inertia of the non-frost surface indicates that it is likely composed of fine-grained particulates. These are likely to be pyroclastic dusts (Rathbun *et al*., 2004) ejected from the many volcanic plumes on Io or sulfur allotropes (also originating from volcanic plumes) which are a major constituent of the reflectance spectra. This apparent high porosity is consistent with the need for a LRT model discussed in Chapter 4 to explain the observed sub-Jovian/anti-Jovian asymmetry in the mid-infrared (Spencer *et al*., 2005). The very low Γ_{NF} will result in the non-frost surface remaining close to radiative equilibrium (the limiting case for $\Gamma_{NF} = 0$).

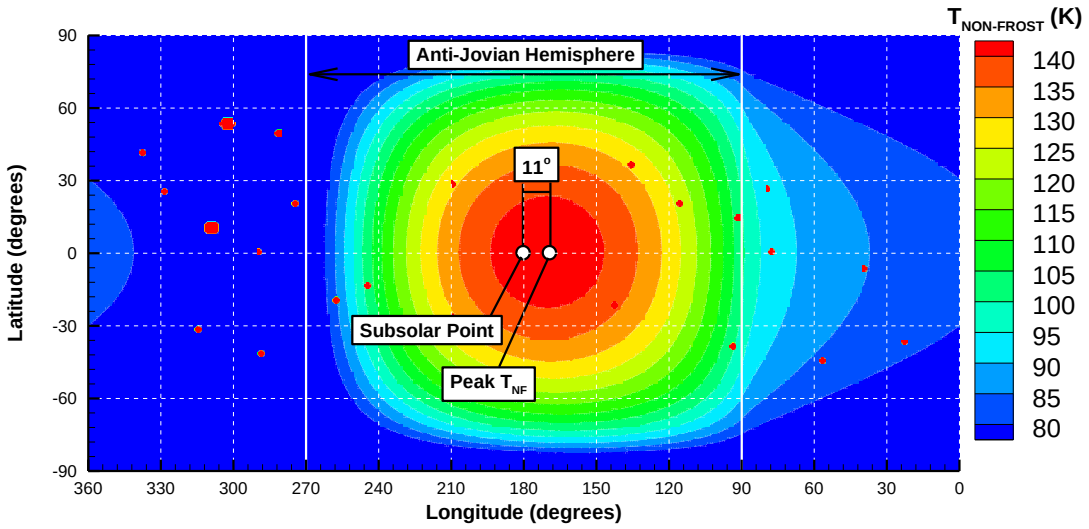

Figure 5.12: The non-frost surface temperature as a function of latitude and longitude. The subsolar point and peak T_{NF} are labeled by white circles. There is only a small thermal lag of 11° between the subsolar point and the peak T_{NF}.

Next, we examine T_{NF} in Figure 5.12 rather than T_B (because T_B includes the effect of both the frost and non-frost surfaces). Currently, T_{NF} can only be inferred from knowledge of T_F and T_B. With much higher spatial resolution in future observations, it may be possible to isolate frost deficient regions in which the brightness temperature would essentially be the non-frost temperature, T_{NF}. In the simulated temperature distribution, the peak T_{NF} is 143.2 K and lags the subsolar point (which is located at the anti-Jovian point for this case) by ~11°. This phase lag due to the Γ_{NF} is small but not insignificant and corresponds to the peak T_{NF} occurring ~1 hour and 15 minutes after high noon. In comparison, the peak T_F occurs 33° or ~3 hours and 50 minutes after high noon. In the original thermal model (see Section 3.2.3), the lag between the subsolar point and the peak T_{NF} is only ~4° or ~30 minutes. Due to the relatively small Γ_{NF} the temperature difference between the subsolar point (T_{NF} = 142.6 K) and the peak T_{NF} is only 0.6 K.

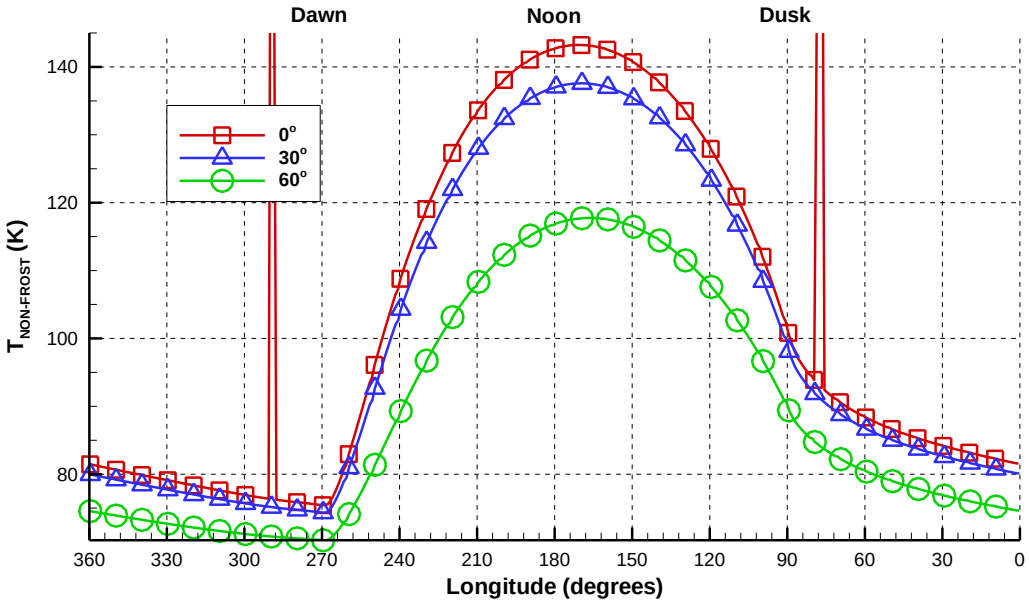

Figure 5.13: Non-frost surface temperature profiles as a function of longitude for selected latitudes of 0°, 30°, and 60°. The spikes at 290° W and 80° W are the hot spots Hephaestus and Tawhaki which lie on the equator.

T_{NF} is shown as a function of longitude for three selected latitudes (0° N, 30° N, and 60° N) in Figure 5.13. Comparing the peak T_{NF} for the mid- and high latitude slices with the equatorial slice, T_{NF} peaks at 137.6 K at 30° N and at 117.7 K at 60° N. The much higher peak T_{NF} compared to T_F at higher latitudes is due in small part to the lower albedo but is largely due to the very low Γ_{NF} that creates a larger diurnal temperature variation. The nightside temperatures only differ by 1.1–1.7 K between the equator and 30° N depending the local time of day. At 60° N, the temperatures are significantly lower and have a smaller variation as a function of time of day; during the night, T_{NF} is 5.2–8.5 K colder than the equatorial temperatures. Unlike T_F which reaches a minimum a significant time (~3 hours) before dawn, T_{NF} decreases monotonically during the night and reaches its minimum temperature (regardless of latitude) just before dawn. This is because the lower Γ_{NF} leads to a much larger temperature variation during the night and therefore the variation in total

insolation absorbed is less extreme. The T_{NF} minima just before dawn are 75.4 K, 74.3 K, and 70.2 K for 0° N, 30° N, and 60° N, respectively.

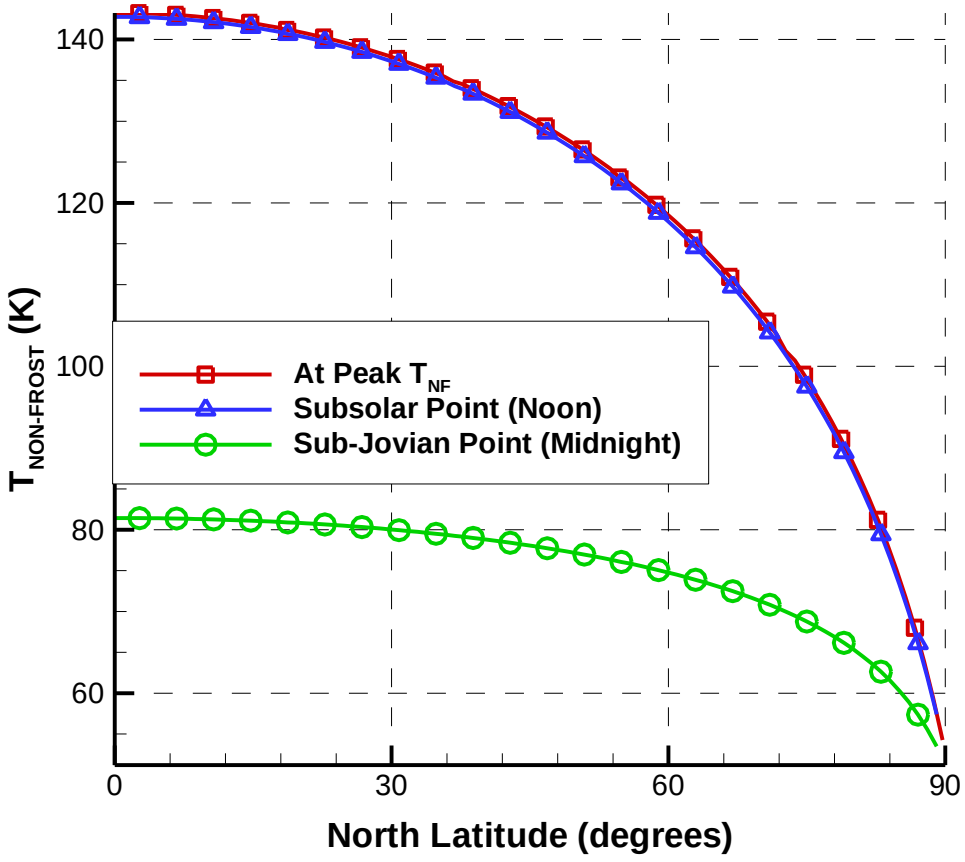

Figure 5.14: Non-frost surface temperature profiles as a function of latitude extracted from Figure 5.12 at the longitudes of several points on Io's surface: the peak T_{NF}, the subsolar longitude (also the anti-Jovian point), and the sub-Jovian point (midnight).

Lastly, the latitudinal temperature variation of T_{NF} is described. Latitudinal profiles at selected longitudes (peak T_{NF}, subsolar longitude/anti-Jovian point, and sub-Jovian point) are shown in Figure 5.14. The small thermal lag arising from Γ_{NF} results in the latitudinal profiles at the peak T_{NF} and at the subsolar point that are nearly identical at all latitudes. The sub-Jovian point latitudinal profile has large differences from the other two dayside profiles. To reiterate, the sub-Jovian point is

midnight for the current simulated temperature distribution and therefore T_{NF} on the equator is very low (81.4 K). At higher latitudes, T_{NF} falls off more slowly than the dayside profiles because the endogenic heating term is constant with latitude, the radiation flux from Jupiter (~0.67 W m^{-2}) is less than the endogenic heating, and the insolation heating term is zero at this instant. The temperature variation is due to the residual thermal energy collected during the day that has not been emitted. If the sub-Jovian point were hypothetically to stay in constant darkness, the latitudinal profile would eventually become nearly uniform. The minimum (polar) temperature would depend only on the endogenic heating rate (1.0 W m^{-2}) and the radiation flux from Jupiter (~0.67 W m^{-2}) would give a very slight temperature increase near the equator. The polar T_{NF} is ~55 K for each of the longitudinal slices investigated in Figure 5.14.

It should be noted that Io has 100–150 mountains which average 6 km in altitude and reach up to 17 km in altitude (Schenk *et al*., 2001); however, in the current model Io is assumed spherical. When these topographical features lie near the terminator, they can shadow a substantial area of the dayside up to ~5° (150 km) away from the terminator. For the non-frost surface, which responds quickly to changes in insolation, these shadows could create local variations in T_{NF}.

5.3 Effects of Eclipse

Lastly, we investigate the temperature variation during and due to eclipse. An important asymmetry in the anti-Jovian and sub-Jovian temperature distributions is created due to eclipse. Since Io is tidally locked, only the sub-Jovian side experiences eclipse and therefore has a decreased net solar flux averaged over its day compared to the anti-Jovian hemisphere. This difference in diurnally integrated solar flux leads to lower temperatures on the sub-Jovian hemisphere even outside of eclipse; therefore, all other things being equal, the sub-Jovian hemisphere will have a thinner atmosphere with a smaller latitudinal extent than the anti-Jovian hemisphere. This

asymmetry has been observed in both the mid-infrared (Spencer *et al*., 2005) and Lyman-α (Feaga *et al*., 2009). Previously, the sub-Jovian/anti-Jovian asymmetry has been explained by the biased distribution of volcanic plumes (with more active volcanic plumes existing on the anti-Jovian hemisphere than on the sub-Jovian hemisphere) or by the inhomogeneous SO_2 frost distribution, as in Chapter 4 (Douté *et al*., 2001). The volcanic plumes likely play a role in the asymmetry, but we suggest that an additional explanation for the sub-Jovian/anti-Jovian column density asymmetry is the fact that the sub-Jovian hemisphere experiences eclipse.

In Figure 5.15a, equatorial T_F profiles before and at several times during eclipse are shown. Prior to entering eclipse, the peak sub-Jovian T_F is 118.5 K. This temperature is 0.9 K cooler than the corresponding peak T_F on the anti-Jovian hemisphere. The temperature difference between the peak T_F on the anti-Jovian and sub-Jovian hemispheres is due to eclipse even though the peak on the sub-Jovian hemisphere is pre-eclipse. As previously stated, the sub-Jovian hemisphere will experience less net sunlight through its day due to eclipse. The effect of eclipse will also be strongest at the sub-Jovian point and diminish with solar zenith angle away from it. At the sub-Jovian point, the amount of sunlight lost during the 2 hour eclipse is ~15% of the total insolation. The diurnal temperature variation is dependent on the total insolation absorbed by the surface and this will be lower on the sub-Jovian hemisphere than on the anti-Jovian hemisphere which sees the sunlight throughout its daylight hours. The blackbody radiation emitted from Jupiter's atmosphere heats the sub-Jovian hemisphere's surface and partially compensates for the cooling due to eclipse; however, eclipse is the dominant effect. The diurnally averaged radiation emitted by Jupiter's atmosphere and then absorbed by Io's surface (~0.67 W m^{-2} over the entire rotation or ~28.1 W h m^{-2}) is only ~25% as large as the amount of sunlight lost due to eclipse (50–55 W m^{-2} for 2 hours or 100–110 W h m^{-2}) at the sub-Jovian point.

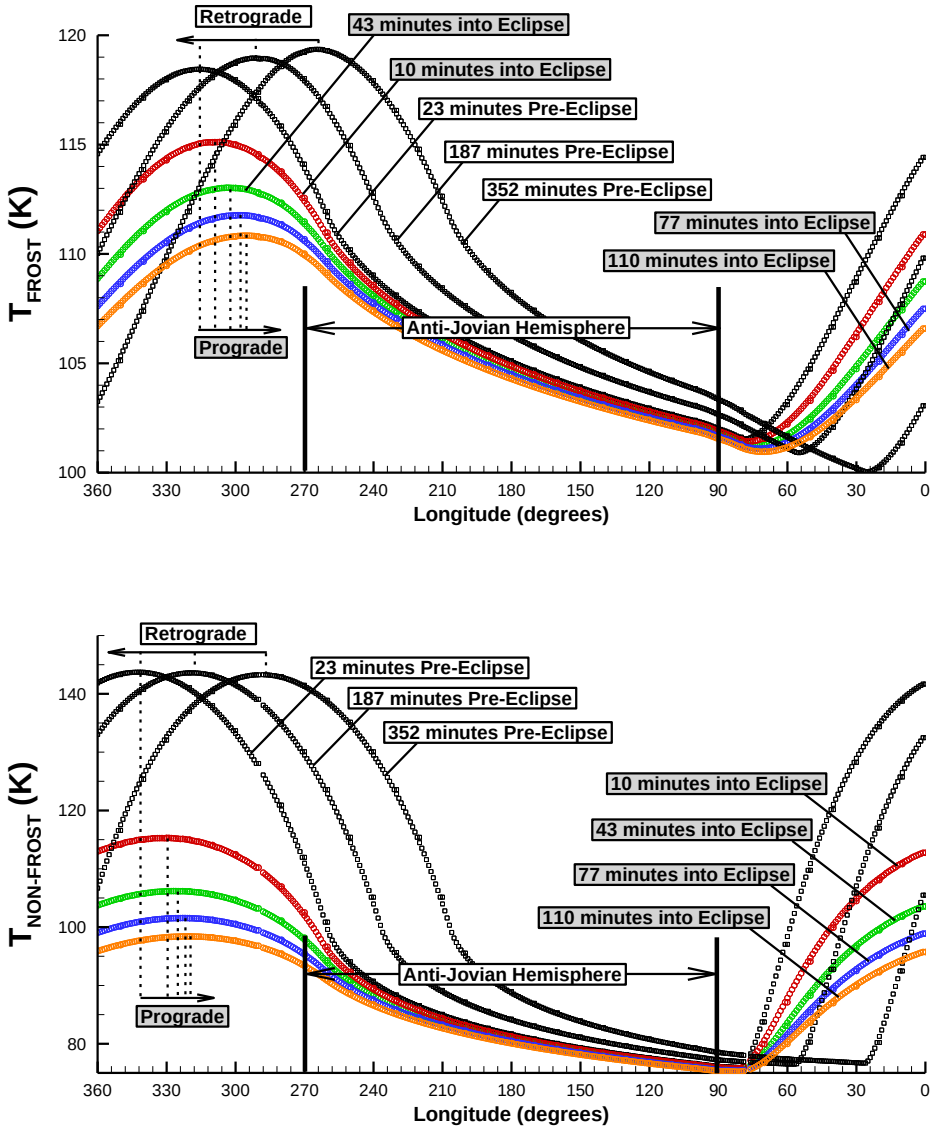

Figure 5.15: Equatorial temperature profiles for (a) T_F and (b) T_{NF} at several times before and during eclipse. The selected times shown are 23, 187 and 352 minutes prior to eclipse. Selected post-eclipse times shown are 10 minutes, 43 minutes, 77 minutes, and 110 minutes into eclipse.

During eclipse, the peak T_F cools to 115.1 K, 113.0 K, 111.8 K, 110.8 K after 10, 43, 77, and 110 minutes in eclipse, respectively. Based on VPE, these temperatures correspond to column densities of 2.4×10^{17} cm^{-2}, 7.6×10^{16} cm^{-2}, 3.7×10^{16} cm^{-2}, 2.4×10^{16} cm^{-2}, 1.7×10^{16} cm^{-2}, respectively; however, during eclipse VPE will not hold because it assumes that the information (temperature change of the

surface) can propagate instantaneously to the gas. Due to the finite speed of sound in the gas (130–350 m/s, depending on the local gas temperature), there will be a lag between the cooling T_F and its effect upon the overlying SO_2 gas column density of the atmosphere. This effect was investigated in the presence of a non-condensable species by Moore *et al*. (2009). The VPE column densities computed above will be compared in Section 6.1 to the actual column densities calculated from the DSMC atmospheric simulations.

Another interesting phenomenon that occurs during eclipse is that the location of the peak T_F moves in the prograde direction whereas it moves in the retrograde direction outside of eclipse (see Figure 5.15). The two causes of this phenomenon both depend on the state of the thermal wave. The thermal wave, seen in Figure 5.16, is the temperature of the solid material (frost or non-frost) as a function of depth into the solid. The first cause of the prograde rotation during eclipse is that the thermal wave has not yet reached a steady state (e.g. has not penetrated as deeply into the solid) in regions closer to dawn (see Figure 5.16). In these regions, the time in sunlight is less than the heat conduction timescale. This effect can also clearly be seen in Figure 5.17 which shows a phase lag between solid frost temperatures at depth and the surface frost temperature for a subsolar longitude of 0° W. The second cause is that eclipse most strongly affects areas near the sub-Jovian point. The deficit of net absorbed sunlight leads to a slightly lower temperature at depth for regions nearer the sub-Jovian point compared to those on the anti-Jovian hemisphere. When eclipse occurs and heating from insolation disappears, each surface area element will radiate at a rate dependent on the state of the thermal wave within the surface. In the absence of the insolation, the regions with the largest energy content (integrated with depth) will tend to have the highest surface temperatures after a time longer than the heat conduction timescale. Figure 5.16 shows the temperature profile with depth into the surface at both 120° and 140° W at two different times (10 minutes prior to eclipse

and 93 minutes into eclipse). The figure shows that the point at 120° W has a lower surface temperature before eclipse but near the end of eclipse (at 93 minutes) it has a warmer surface temperature than that of the surface at 140° W. The same effect can be seen in Figure 5.17 from ~235° W to 290° W.

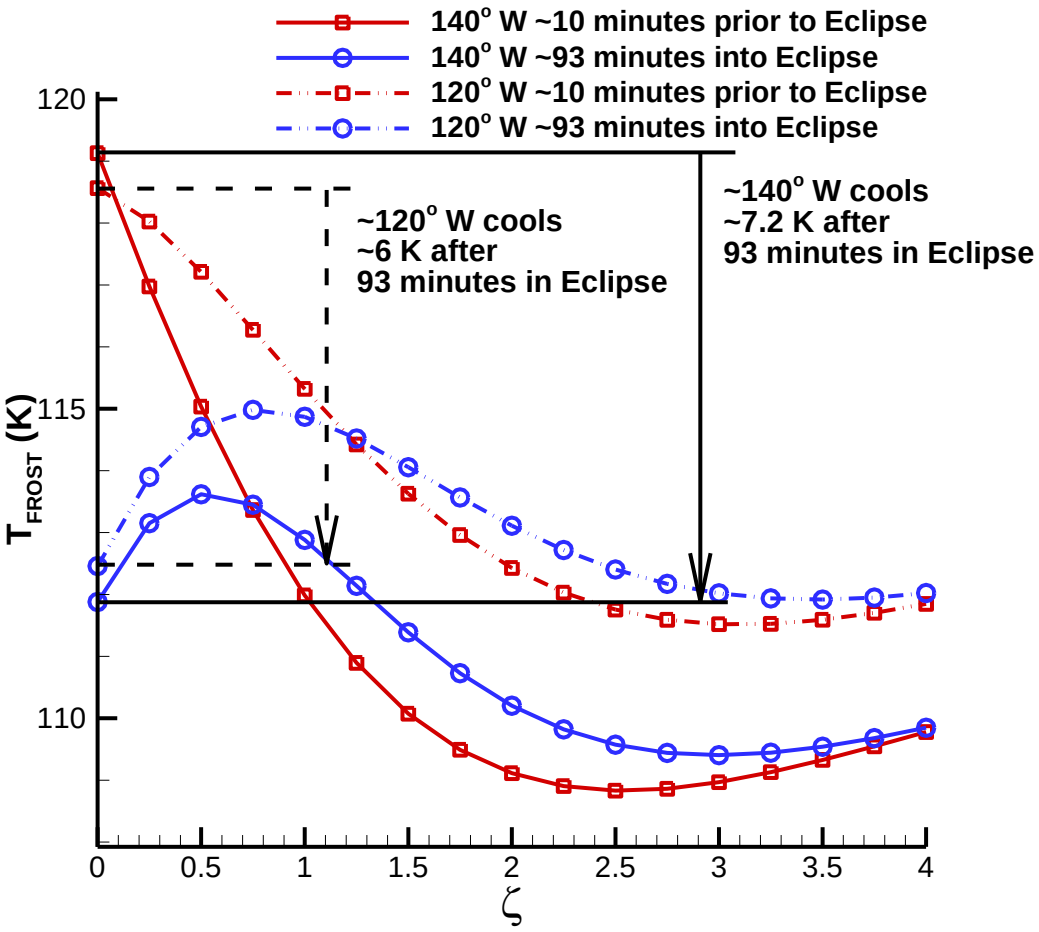

Figure 5.16: A comparison between the temperature as a function of depth at two different longitudes along the equator before and in eclipse. 140° W (solid lines) has a higher surface temperature initially but lower temperature at depth whereas the point 120° W (dashed lines) has a lower surface temperature but higher temperatures at depth. Throughout eclipse the point with the higher "deep temperature" at 120° W of the subsolar point cools more slowly and ends up with a higher surface temperature near the end of eclipse. The ζ range has been truncated to highlight the near surface features.

Changes in equatorial T_{NF} are shown in Figure 5.15b at the same selected times as the T_F data of Figure 5.15a. The non-frost surface experiences larger temperature variations because of the lower Γ_{NF}. After 10 minutes in eclipse, the peak T_{NF} decreases to 115.2 K. The successive peak T_{NF} throughout eclipse are 106.2 K, 101.8 K, 98.5 K at 43, 77, and 110 minutes into eclipse, respectively. The peak T_{NF} also has the same prograde rotation as T_F during eclipse.

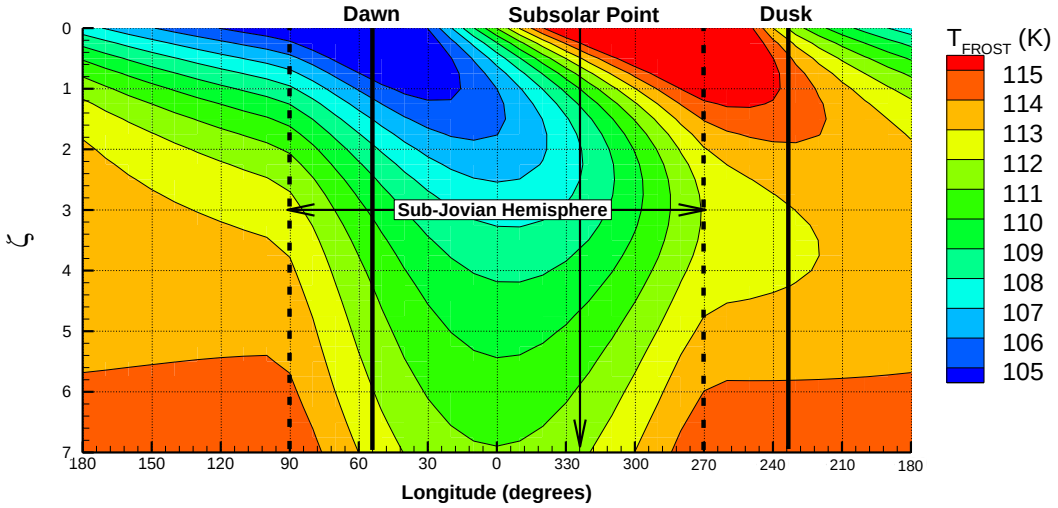

Figure 5.17: The temperature of the SO_2 frost solid as a function of depth and longitude at the equator for a subsolar longitude of ~325° W.

When the sub-Jovian hemisphere exits eclipse it takes several hours for the frost surface to recover to its quasi-steady equilibrium state that existed before eclipse. This can be quantified by the "thermal parameter" defined by Spencer *et al.* (1989):

$$\theta = \frac{\Gamma\sqrt{\omega}}{\varepsilon\sigma T^3} \qquad 5.5$$

The thermal parameter takes the ratio of the characteristic time scale for the surface to radiate a particular amount of heat, $t_R = \Gamma/\sqrt{\omega}\varepsilon\sigma T^3$, to the diurnal timescale, $t_D = 1/\omega$. When $\theta = 0$, the surface is in instantaneous radiative equilibrium

with the insolation, whereas $\theta = \infty$ corresponds to a surface where temperature is only a function of latitude and independent of time of day. Assuming $T_F \sim 115$ K and $T_{NF} \sim 140$ K, then $\theta_F \sim 14.9$ and $\theta_{NF} \sim 0.82$, respectively.

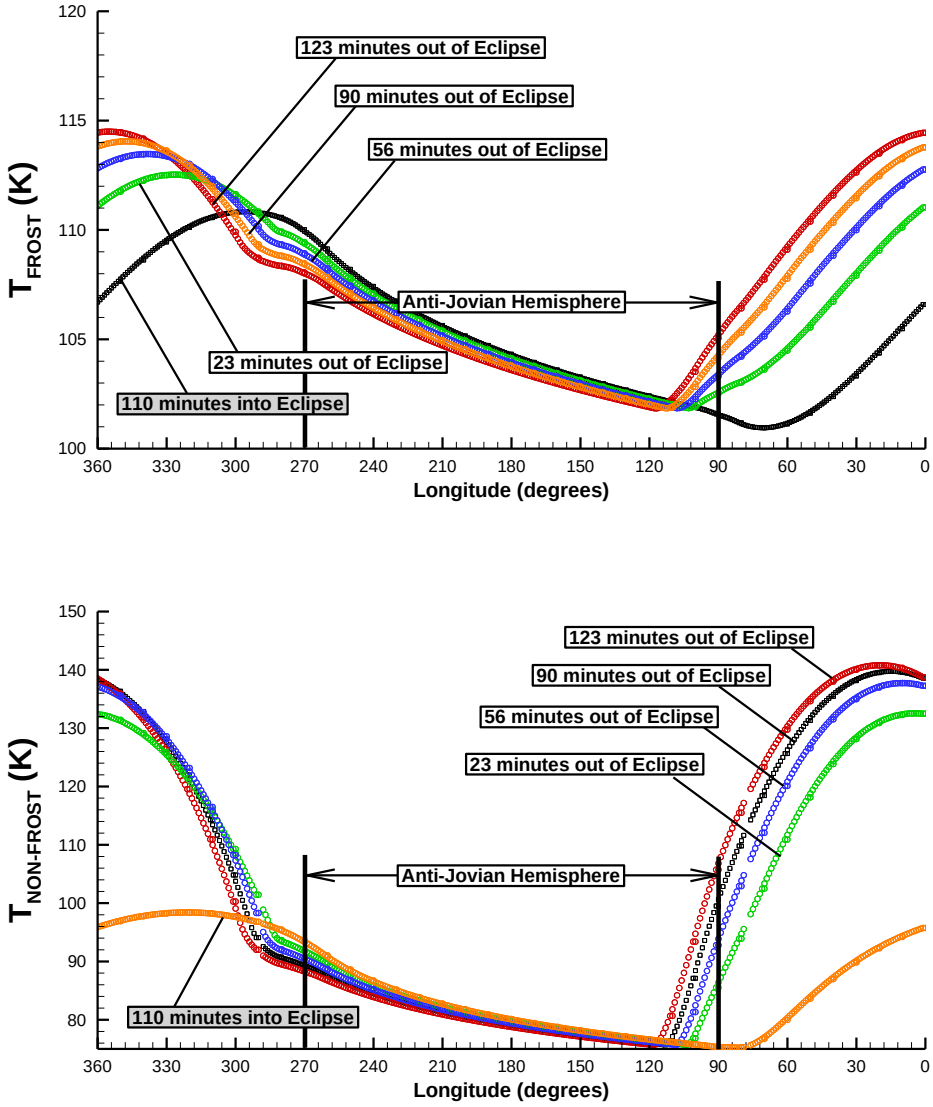

Figure 5.18: Equatorial temperature profiles for (a) T_F and (b) T_{NF} at several times during and after eclipse. The selected times shown are 110 minutes into eclipse (~10 minutes before egress), 23 minutes, 56 minutes, 90 minutes, and 123 minutes after egress from eclipse.

Before ingress into eclipse, T_F is ~118.5 K (Figure 5.15a) but 2 hours after Io exits eclipse the peak T_F has only warmed to ~114.5 K (Figure 5.18a). T_{NF} responds

much more quickly due to its low Γ_{NF} and recovers within ~1.5 K of the pre-eclipse peak value 2 hours after egress from eclipse (see Figure 5.18b). The peak T_{NF} increases rapidly when the non-frost is exposed to sunlight and only 23 minutes after egress from eclipse, the peak T_{NF} has risen ~34 K. Further inhomogeneous thermal structure due to eclipse can be seen in Figure 5.18a between 270° W and 300° W. Unlike the pre-eclipse equatorial thermal profile that decreases monotonically with decreasing longitude on the nightside, the post-eclipse thermal profiles show an unusual structure due to the variation in the temperature at depth between 270° W and 300° W. As described earlier, points further from the sub-Jovian hemisphere will absorb more sunlight throughout the day and therefore will have a higher "deep temperature". The variation in temperature at depth also causes some unusual structure in the thermal profiles between 60° W to 90° W.

The asymmetry between the anti-Jovian and sub-Jovian points can be seen most clearly by comparing their temperature profiles as a function of time of day. In Figure 5.19a, the difference in the peak T_F between the sub-Jovian and anti-Jovian point is ~4.2 K. The anti-Jovian point peaks at ~119.5 K at ~30 hours while the sub-Jovian point peaks at ~115.1 K at ~10 hours. If these T_F are converted to column densities assuming VPE, this corresponds to column densities of 7.63×10^{16} cm^{-2} at the sub-Jovian point and 3.23×10^{17} cm^{-2} at the anti-Jovian point. Based on these estimated VPE column densities, the anti-Jovian point will have a peak column density ~4.2 times larger than sub-Jovian point. Note that on this time axis, eclipse occurs between approximately 4 and 6 hours.

The effect of eclipse can also be seen on the nightside where T_F is ~2 K lower for the sub-Jovian point compared to the anti-Jovian point. This 2 K difference is ubiquitous and can also be seen in Figure 5.19b where the phase difference between the anti-Jovian and sub-Jovian points has been removed such their "noon" occurs at the same time of day on the x-axis. Eclipse does not occur centered on Figure 5.19b

because of the thermal phase lag from the high Γ_F which means that the frost temperatures are shifted more than 180° to remove the phase difference between the sub-Jovian and anti-Jovian points assumed peaks.

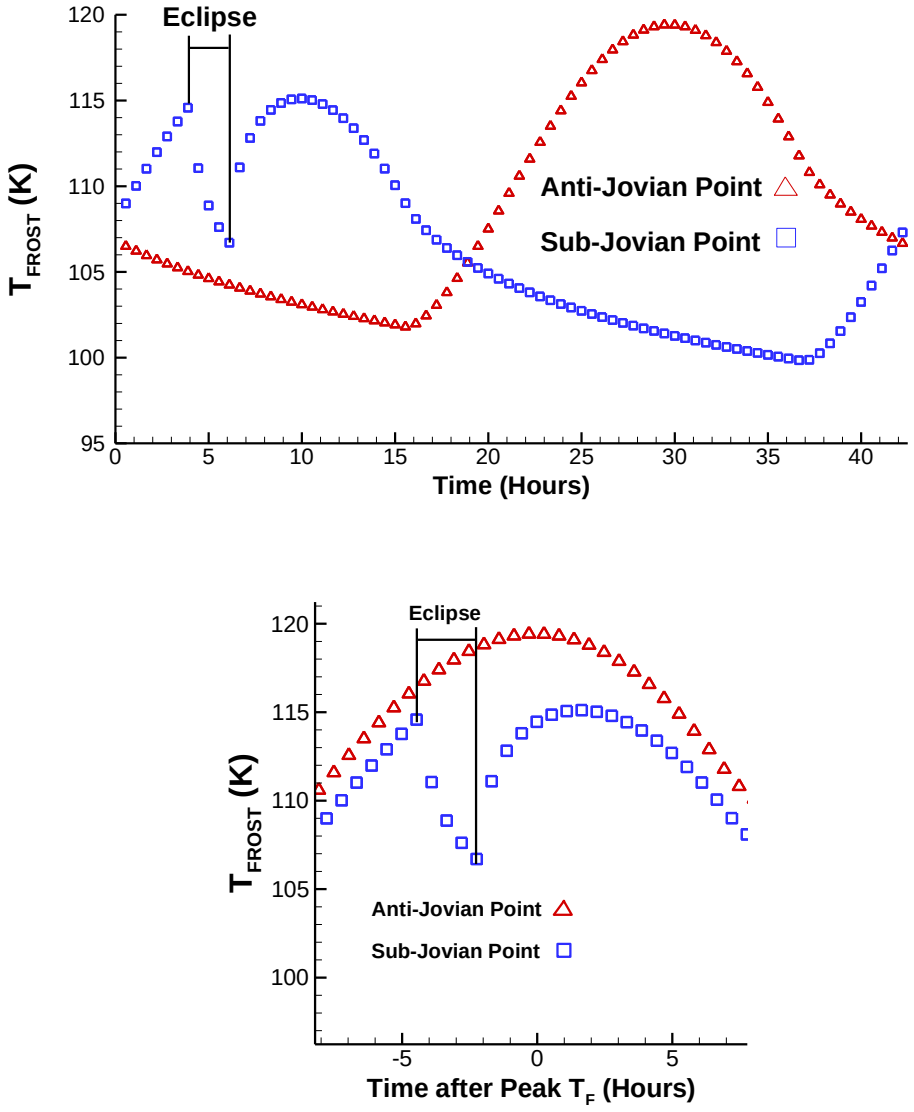

Figure 5.19: (a) A comparison between T_F at the anti-Jovian and sub-Jovian points as a function of time of day and (b) the same data but now with the phase shifted such that the peaks (if eclipse did not occur) coincide and the x-axis reduced to highlight eclipse.

CHAPTER 6: NUMERICAL SIMULATIONS OF IO'S ATMOSPHERE WITH THE IMPROVED SURFACE THERMAL MODEL

Global DSMC atmospheric simulations were carried out using the solid surface boundary conditions for the frost and non-frost described in Section 3.3.2 with the best fit thermophysical parameters obtained in Chapter 5. The simulation results presented describe the atmospheric structure for over 6 hours around eclipse (~2.5 hours before, ~2 hours in eclipse, and ~2 hours after eclipse) and are compared to the anti-Jovian hemisphere. The resulting column densities, number densities, temperatures (translational, rotational, and vibrational), and global winds (velocities, Mach numbers, and streamlines) will be described. Results are compared to Lyman-α observations (Feaga *et al*., 2009) in an attempt to explain the asymmetry between the anti-Jovian and sub-Jovian hemispheres with the updated thermal model. To begin the discussion, the simplest quantity, vertical SO_2 gas column density, will be described since it is inherently two-dimensional (on the surface of a sphere).

6.1 ATMOSPHERIC SO_2 GAS COLUMN DENSITY

Before eclipse, dayside column densities are largely in VPE with the SO_2 surface frosts as illustrated by the elliptical shape of the column density contours that follow the same shape as T_F contours (compare Figure 5.5 with Figure 6.1). The only region of substantial departure from VPE is near the dawn terminator where a significant portion of the atmosphere is sustained by desorption from the non-frost surface. As detailed in Section 3.2.3, the interaction between SO_2 gas and the non-frost surface leads to SO_2 molecules condensing on the non-frost surface during the

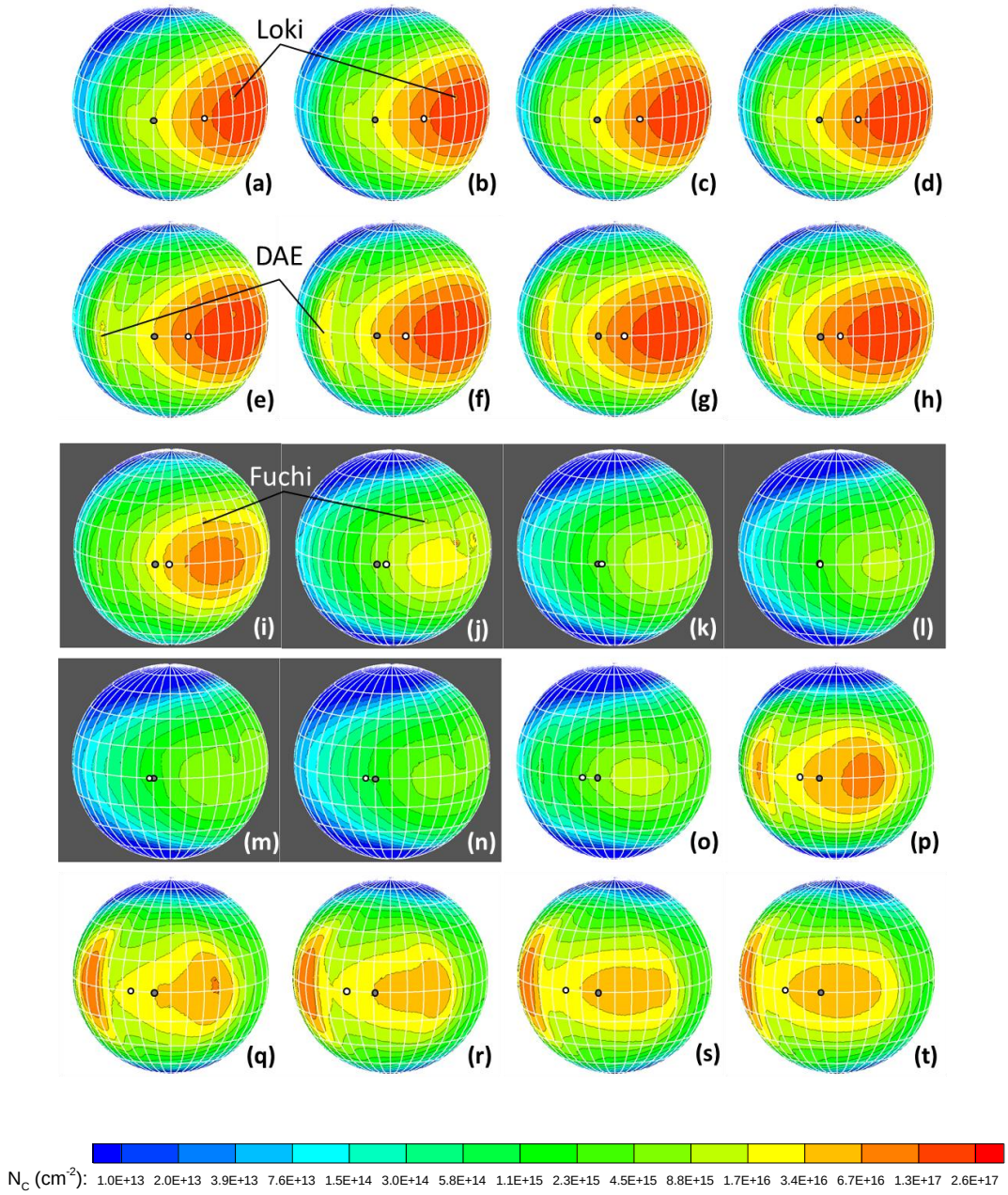

Figure 6.1: Column density contours with the view centered at (10° N, 350° W) as a function of time. The 20 snapshots occur at intervals of 1250 seconds (~21 minutes) starting approximately 2 hours and 40 minutes prior to eclipse and ending ~2 hours after egress from eclipse. Hot spots, Loki and Fuchi, are highlighted in (a) and (b) and (i) and (j), respectively. The white dot denotes the location of the subsolar point while the black dot denotes the location of the sub-Jovian point.

night when it is cool. The condensed gas then rapidly desorbs near dawn when the non-frost surface warms quickly, creating an enhanced atmosphere near dawn (the DAE).

The majority of the atmosphere is in a quasi-steady state during the two and a half hours simulated prior to eclipse. The morphology of the dayside atmosphere remains essentially constant as the subsolar point rotates toward eclipse. The only region where significant unsteadiness exists prior to eclipse is near the DAE. These variations are caused by inhomogeneous surface frosts and the complicated dynamics of the non-frost thermal distribution in eclipse and leaving eclipse. As noted in Section 5.3, the peak equatorial T_{NF} has a prograde rotation during eclipse and when Io exits from eclipse the peak rapidly sweeps back in a retrograde rotation to its quasi-steady location. In the process, the non-frost surface over most of the sub-Jovian hemisphere is thoroughly denuded of SO_2 molecules since the timescale for desorption is very short compared to the timescale on which the peak T_{NF} returns to its quasi-steady state location. At the same time, the peak T_F for the SO_2 frost surface also sweeps quickly back to its quasi-steady state location but this timescale is short compared to the time required to recover the non-frost surface with a thin film of SO_2 molecules. Therefore, the non-frost region of the sub-Jovian hemisphere between 300° and 340° W has a lower density of SO_2 molecules absorbed on the surface.

The DAE is quite small 2.5 hours prior to eclipse because this area of the non-frost surface is thoroughly denuded of SO_2 molecules. As the atmosphere approaches ingress, the DAE grows in size because the density of SO_2 molecules adsorbed on the non-frost also grows. This is because the DAE is near the sub-Jovian point where the atmosphere was thickest prior to eclipse and therefore also has the highest density of adsorbed molecules on the surface during eclipse. In this region, the quick sweeping of the T_{NF} back to its quasi-steady state does not completely denude the surface. This situation of a quasi-steady bulk atmosphere and slightly unsteady DAE (which grows

as eclipse approaches) continues up until ingress into eclipse. The peak column density (directly above the peak T_F), N_C, is ~2.6×10^{17} cm^{-2} 2.5 hours prior to eclipse, and decreases slightly as the atmosphere approaches ingress. Just prior to ingress, the peak N_C has dropped to ~2.2×10^{17} cm^{-2} due to the lower SO_2 frost fraction and slightly cooler T_F due to the diurnally averaged effect of eclipse lowering the amount of sunlight absorbed on the sub-Jovian hemisphere.

When Io enters eclipse, the atmosphere begins to collapse but is partially constrained by the atmospheric speed of sound. The SO_2 gas that condenses on the non-frost will stick for a residence time dependent on the cooling T_{NF}. Just prior to eclipse, the non-frost surface region around the peak T_{NF} (~143 K) remains denuded of SO_2 because the residence time at that temperature is ~1.3 seconds. 10 minutes into eclipse, the peak T_{NF} has cooled to ~115 K which corresponds to a residence time of ~7.7 hours. As the surface continues to cool, the residence time grows exponentially (Eq. 11). The lengthened residence time (longer than an Io day near end of eclipse) means that nearly all of the SO_2 gas which lands on the non-frost surface will condense and stick for the remainder of eclipse.

During eclipse, the column density decreases due to the cooling T_F and T_{NF}. Comparing the DSMC calculated column density (which includes speed of sound effects) with VPE column density based on T_F, we expect that the DSMC column density will be higher due to the finite response time. Figure 6.2 plots the column density as a function of time during eclipse at the location of the peak N_C just prior to eclipse Contrary to naïve expectation it shows that the DSMC calculated column density actually falls quicker than predicted by VPE with the SO_2 frost. The reason for this is a significant portion of the atmosphere is sustained by molecules "hopping" off the warm (~140 K) non-frost surface and VPE assumes that the entire column is sustained by instantaneous response to the frost surface alone. During eclipse, the non-frost surface cools much quicker due to its very low Γ_{NF} and therefore its

contribution to the local atmosphere will disappear quickly. In this case, the timescale for the changes in T_{NF} are much shorter than T_F and therefore the column density decreases more rapidly than expected for VPE based on T_F.

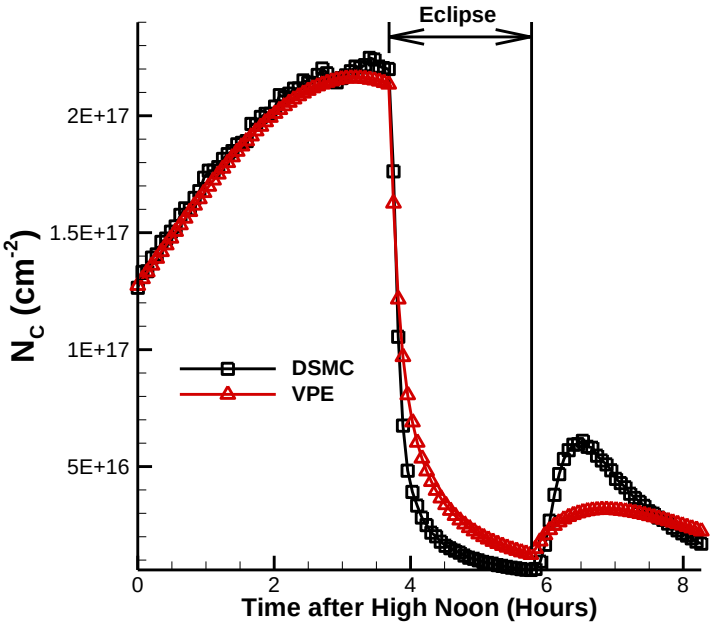

Figure 6.2: A comparison of the VPE and DSMC computed column densities at (0° N, 45° W). Contrary to expectations based on one-dimensional eclipse observations with uniform frost coverage (Moore *et al*., 2009), the VPE column density collapses slower than the DSMC computed column density because VPE neglects absorption onto and desorption from the non-frost surface. As the non-frost surface cools rapidly, that portion of the atmosphere will collapse leaving a diminishing portion of the atmosphere sustained by sublimation from the frost surface.

Near the beginning of eclipse, the VPE and DSMC computed column densities overlap because both are limited by the speed of sound. After ~15 minutes, the DSMC column density diverges from VPE. This occurs because VPE is constrained by the high Γ_F rather than the speed of sound, whereas the low Γ_{NF} causes T_{NF} to decrease rapidly and therefore the collapse of the atmosphere sustained by the non-frost is limited only by the speed of sound and the ballistic time of molecules. The collapse of the other portion of the atmosphere, sustained by SO_2 surface frosts,

is still dependent on the high Γ_F. After eclipse, the DSMC computed column density overshoots VPE because the excess SO_2 gas that condensed on the non-frost surface quickly desorbs as the surface warms. Moore *et al*. (2009) simulated the one-dimensional collapse of Io's atmosphere including the effects of non-condensable species but the surface was considered to be 100% SO_2 frost. They found that a small concentration of non-condensable can considerably slow the collapse of the atmosphere by creating a diffusion layer near the surface.

The influence of Loki (10° N, 310° W) can be seen in nearly all the snapshots of Figure 6.1. Prior to eclipse, the column density above Loki is lower than over the surrounding areas because it is so warm (>300 K) that any SO_2 frosts are rapidly sublimated away. Therefore, no sublimation occurs from Loki's disk because it has no SO_2 frost and it is assumed to be in a quiescent period (Rathbun *et al*., 2002). During eclipse, both the frost and non-frost surfaces cool whereas Loki remains at a constant temperature since its temperature is sustained by volcanism rather than insolation. Since Loki remains at a constant temperature and covers such a large area, molecules that are temporarily "trapped" hopping around on the hot surface will not condense and therefore an inflection occurs where the column density above Loki decreases much more slowly than over the surrounding areas. Loki's column density will only decrease as molecules diffuse away from its hot disk onto the surrounding cold surfaces. This diffusion occurs at an approximately linear rate and therefore, at the beginning of eclipse Loki will have a higher column density. However, Loki's column density will continue to decrease as the frost and non-frost surface cool slowly, and it eventually drops below that of the surrounding areas. As discussed in Appendix A, the pressure over Loki does not equilibrate quickly with the local sublimation atmosphere because the ballistic length scale, $d_B = 8H/\pi$, is smaller than the mean radius of the hot spot. This is in agreement with the earlier work of Ingersoll *et al*. (1989) who defined a horizontal averaging length scale,

$L = \sqrt{2\pi}H \approx d_B$, over which local frost patches control the pressure. Other hot spots are more difficult to see in Figure 6.1 because many are small compared to the lateral cell size (30 km at the equator). Just after ingress into eclipse, for example, Fuchi is visible at (25° N, 328° W) in Figure 6.1i and Figure 6.1j when the surrounding column densities are collapsing more rapidly than the atmosphere over the hot spot due to its constant temperature.

After egress from eclipse, it requires approximately 2 hours for the atmosphere to return to its pre-eclipse morphology. During those 2 hours, the atmosphere has a very complex structure that is due to the underlying changes in surface temperature (both frost and non-frost). Because of the lower Γ_{NF}, T_{NF} increases more rapidly than T_F. During eclipse, a significant amount of the column (~90-95%) condenses onto the surface and approximately half of that will land on the non-frost surface. After egress from eclipse, this material will rapidly desorb from the non-frost surface over much of the dayside but the desorption will be centered over the peak T_{NF} which occurs ~10° east of the subsolar point. Because the amount of material condensed on the non-frost surface is finite (~10^{16} cm^{-2}), nearly all of the SO_2 will desorb from the non-frost surface within ~30 minutes after egress. The frost surface responds more slowly due to its high Γ_F and therefore its contribution to the atmosphere is masked by desorption from non-frost surface until ~30 minutes after eclipse. Due to these different response rates, the atmosphere has a very complex morphology between ~40 minutes after egress and ~2 hours after egress (Figure 6.1p-r). At 40 minutes post-eclipse, the atmosphere is still largely sustained by material desorbing from the non-frost surface. Yet one hour after eclipse, the frost surface has warmed to the point where it contributes a substantial amount to the dayside column densities. For the next hour, the SO_2 gas desorbing from the non-frost surface is condensing on the nearby SO_2 frosts and is being replaced by gas sublimed from the frost surface. Two hours after eclipse, the peak T_F has recovered within 1.5 K as

discussed in Section 5.3. Even at the end of the simulation (~2 hours post-eclipse), however, the effect of eclipse on the atmosphere persists (compare Figure 6.1t with Figure 6.1h).

6.2 Global Winds

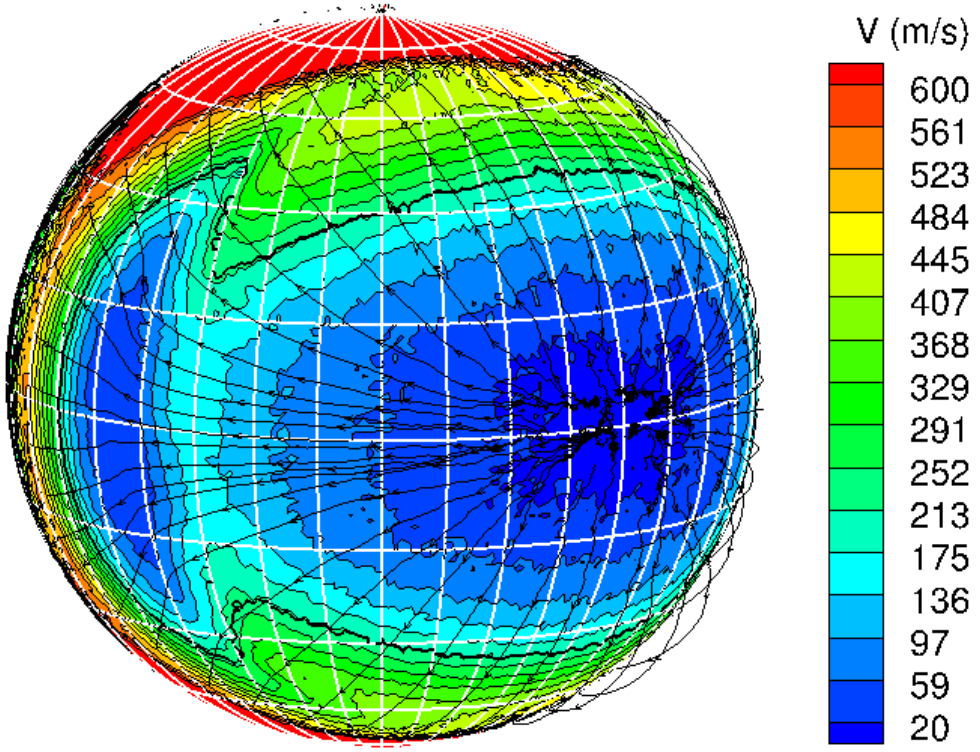

Figure 6.3: Contours of the magnitude of the bulk velocity vector overlaid by streamtraces at 40 km altitude. The snapshot is taken at an instant ~10 minutes prior to eclipse.

The day-to-night pressure gradient driven by the variation in insolation absorbed by the surface drives SO_2 winds that have net sublimation from the region near the peak T_F and net condensation on and near the nightside. Outside of eclipse, the day-to-night pressure gradient is strong enough to drive the winds substantially supersonic in certain regions of the atmosphere (generally near the terminator and outside of the surface boundary layer). The flow structure nominally consists of flow originating at the peak pressure region (centered at the location of the peak T_F) and

diverging in all directions toward the nightside. An oblique shock forms near the dawn terminator as supersonic SO_2 gas condenses on and near the nightside. At 10 km altitude, the peak wind speed is ~500 m/s and increases to ~575 m/s at 40 km (see Figure 6.3). Note that wind speeds are relative to the underlying surface not an Earth-based observer.

An east/west asymmetry does exist due to the gas-surface interaction that creates the DAE. The DAE is a high pressure region which acts as an obstruction to the global winds that flow west from the region of peak pressure (see Figure 6.3 and Figure 6.4). Unsteadiness in the DAE leads to differing flow patterns throughout the simulation time. Prior to eclipse, the DAE is largely growing as the atmosphere approaches ingress and therefore the streamlines which are initially supersonic to the west start to be deflected by the high pressure DAE (see Figure 6.4 and Figure 6.5). Winds that are a significant distance from the equator (latitudes of ±10° or more) will deflect to the north or south whereas those nearer the equator will be forced up and over the high pressure region since that is the path of least resistance. In comparison, the eastward flow continues on much further than the westward flow due to the high Γ_F. The SO_2 frost surface cools very slowly leading to a "finger" of higher pressure extending far onto the nightside (see Figure 6.9). At 40 km altitude, the pressure slowly decreases and the atmosphere is still partially collisional (mean free path ~ 20 km < lateral cell size of 30 km) after passing through ~140° (or 16 hours) of night. Because T_F and therefore P decrease slowly east of dusk, the winds in these regions (not shown) deflect north or south due to the relatively cold mid-latitudes (<90 K) and poles (~55 K).

When the flow becomes only marginally collisional, bordering on free molecular, streamlines can be deceptive. For example, two inter-penetrating non-collisional streams of gas may be interpreted by a streamline tracing program as producing a stagnation flow due to the superposition of their bulk velocities when no

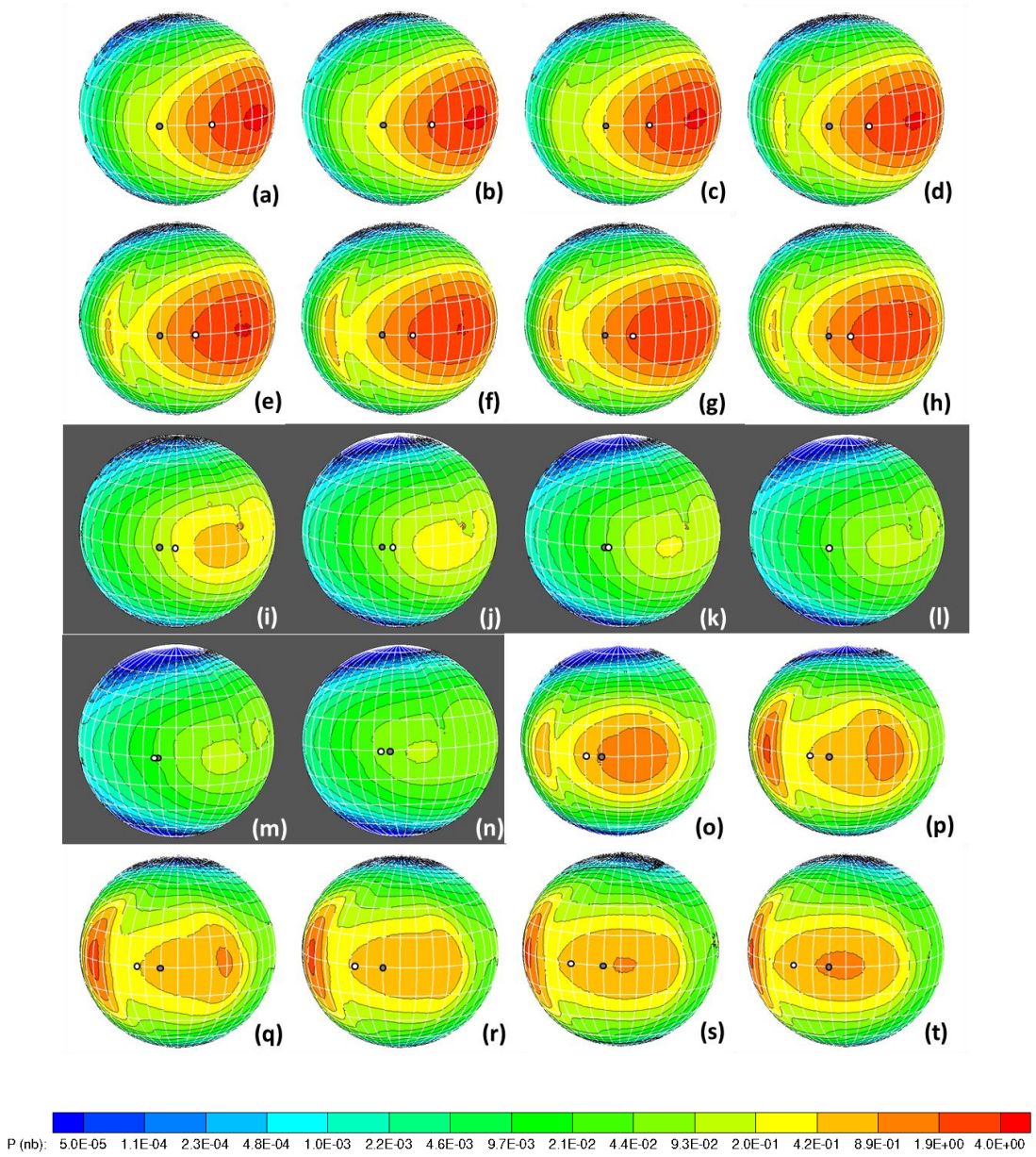

Figure 6.4: Contours of near surface atmospheric pressure (nb) with the view centered at (0° N, 10° W) as a function of time. The 20 snapshots occur at intervals of 1250 seconds (~21 minutes) starting approximately 2 hours and 40 minutes prior to eclipse and ending ~2 hours after egress from eclipse. The white dot denotes the location of the subsolar point while the black dot denotes the location of the sub-Jovian point.

such stagnation flow structure exists. We have been careful here only to draw conclusions on the global dynamics where the streamlines are in regions of collisional flow and therefore, where streamlines are physically meaningful.

As the atmosphere enters eclipse, the column collapses reducing the day-to-night pressure gradient that drives the global winds. Early in eclipse, the pressure gradient is still strong enough to drive the flow supersonic near the terminator but as the atmosphere continues to collapse, the pressure gradient is reduced to the point where the flow is subsonic everywhere and the oblique shock near the dawn terminator disappears. Prior to eclipse, the peak near surface (~1 km altitude) pressure is ~3 nbar whereas the peak pressure has dropped to ~80 pbar just before egress from eclipse (see Figure 6.4). As discussed earlier in Section 5.3, the peak T_F point has a prograde rotation during eclipse leading to the region of peak pressure also moving in the prograde direction. Since the peak pressure acts as the origin of the flow in these simulations, this leads to a prograde rotation of the point of origin for the global winds as the atmosphere approaches egress. Furthermore, eclipse tends to "flatten" the temperature distribution leading to a much more uniform T_F around Io; therefore, the contribution of the inhomogeneous frost fraction becomes more significant in the absence temperature gradients (see Figure 6.1 and Figure 6.4). Late in eclipse, the inhomogeneous frost fraction leads to the separation of the peak pressure into two equally strong but independent high pressure regions. These two regions both act as sources for global winds leading to a small region of stagnated gas between them (see Figure 6.5).

Upon egress from eclipse (see Figure 6.5o), the surface warms and the dayside pressure once again rises while the nightside pressures remain constant. As discussed in Section 6.1, the excess SO_2 gas that condenses on the non-frost surface during eclipse rapidly desorbs upon egress from eclipse. Initially, this causes the atmosphere to be primarily supported by the non-frost surface and therefore the atmosphere has only a ~11° eastern lag between its peak column density and the subsolar point. This in turn causes the circumplanetary flow to originate ~11° east of the subsolar point as opposed to the usual ~33° eastern lag. The day-to-night pressure gradient remains

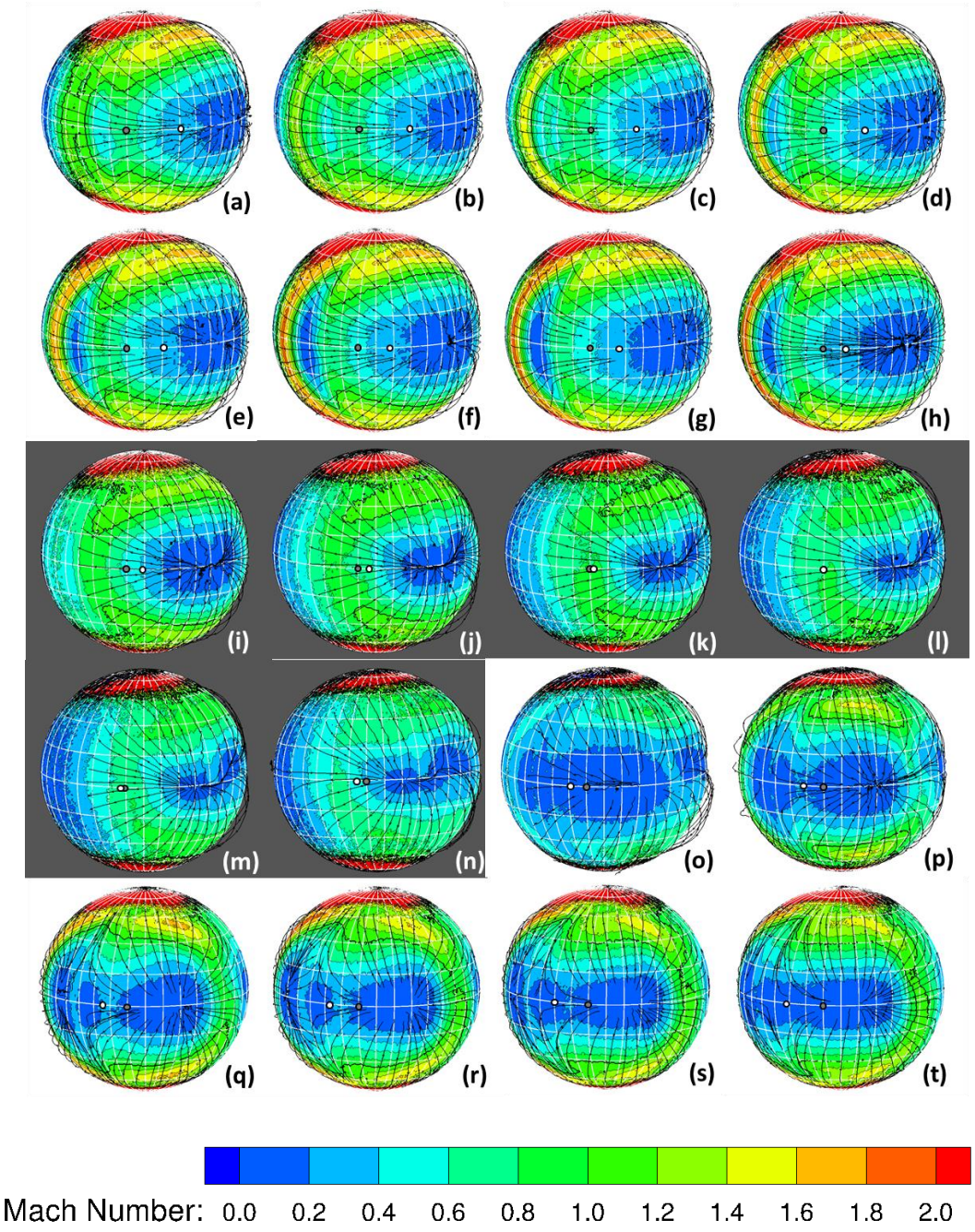

Figure 6.5: Mach number contours overlaid with streamlines with the view centered at (0° N, 10° W) as a function of time. The 20 snapshots occur at intervals of 1250 seconds (~21 minutes) starting approximately 2 hours and 40 minutes prior to eclipse and ending ~2 hours after egress from eclipse. The white dot denotes the location of the subsolar point while the black dot denotes the location of the sub-Jovian point.

fairly weak (subsonic) because of the relatively low pressure atmosphere supported by the non-frost surface. Approximately one hour after egress from eclipse, the

atmosphere establishes a two peak structure (for a second time but due to a different mechanism; see Figure 6.5q) as discussed in Section 6.1. The time scale for the development of this two peak structure is dependent on the thermal inertia of SO_2 surface frost and the residence time of SO_2 molecules desorbing from the warming non-frost surface. Each of these high pressure regions forces flow away toward low pressure regions and the pressure gradient is strong enough to drive some flow supersonic near the terminator. Because the two high pressure regions (seen in Figure 6.5p-t) are roughly equal strength, the two opposing winds form a stagnation flow pattern. The stagnation flow forms roughly 2/3 the distance from the peak pressure to the DAE because the winds from the peak pressure are stronger. Winds that are primarily east/west near the equator are forced north and south. This flow pattern continues to the end of the simulation. Note that the apparently very high/low Mach numbers near the poles (> 75° N/S) are due to poor simulation statistics where the equilibrium vapor pressure has fallen to ~10^{-10} or less of the peak vapor pressure; they are not physically meaningful.

6.3 VERTICAL ATMOSPHERIC STRUCTURE

To this point, only lateral gradients in the atmosphere have been discussed but there are significant vertical gradients in Io's atmosphere due to plasma heating and gravity. Just prior to eclipse, the atmospheric pressure falls off exponentially with altitude and the gas density, n, is ~2.8×10^{17} m^{-3} just above the surface near the peak pressure (see Figure 6.6). The scale height, $H = {k_B T}/{mg}$, is ~8.6 km near the surface but generally increases with altitude due to plasma heating (e.g. at 100 km altitude, n ~ 1.3×10^{14} m^{-3} and $H \sim 36$ km due to the plasma heated gas reaching temperatures near 500 K and the reduced gravity). The only exception to this temperature trend is near ~5 km altitude where a thermal inversion layer exists because the plasma energy that is traveling radially downward through the column of gas is completely absorbed

above that point. Below ~5 km altitude, the subliming SO_2 gas expands upwards adiabatically and cools radiatively, while above ~5 km altitude, the gas is heated by the plasma energy flux.

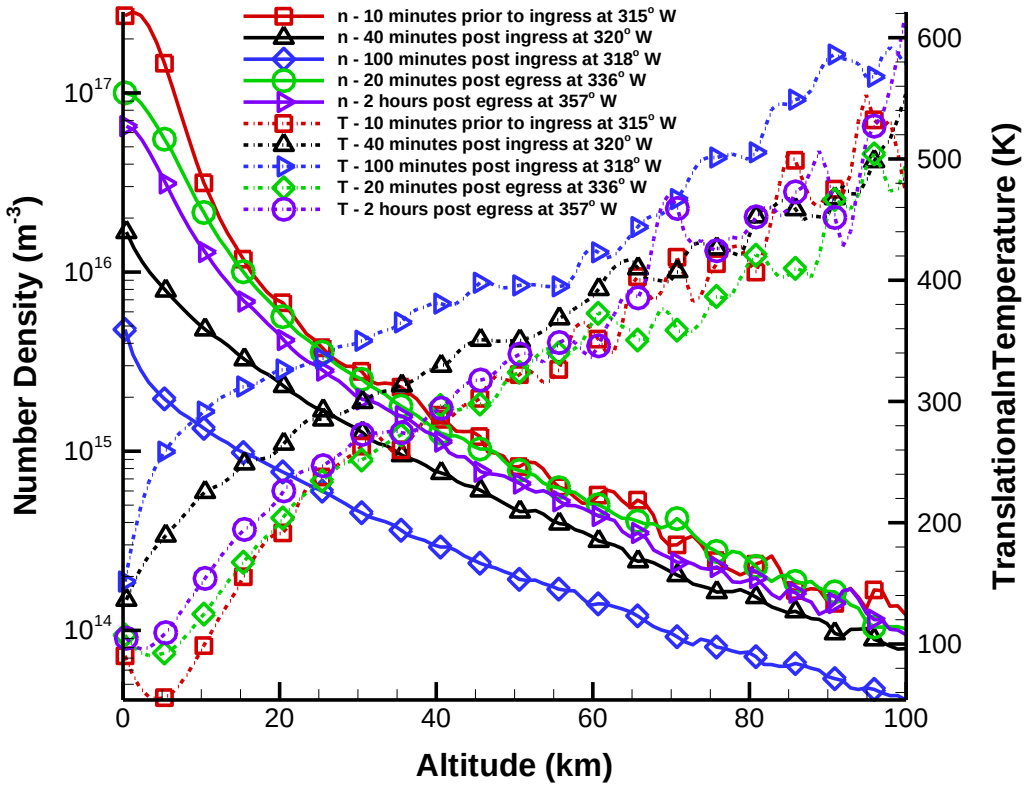

Figure 6.6: Number density (solid lines) and translational temperature (dash-dot lines) as a function of altitude at the instantaneous location of the peak equatorial pressure (hence, at different points on the surface at different times). Data are shown at the following times: ~10 minutes prior to eclipse (0° N, 315° W), ~40 minutes post ingress (0° N, 320° W), ~100 minutes post ingress (0° N, 318° W), ~10 minutes after egress (0° N, 336° W), and ~2 hours after egress from eclipse (0° N, 357° W).

After 10 minutes in eclipse, the peak n near the surface decreases to ~1.6×10^{16} m^{-3} (~5.7% of the pre-eclipse number density; see Figure 6.6). After ~100 minutes in eclipse, the atmosphere has further collapsed to $n_{PEAK} \sim 4.4\times10^{15}$ m^{-3} (~1.6% of the pre-eclipse number density). Twenty minutes after egress from eclipse,

n_{PEAK} rapidly increases to ~1.0×10^{17} m^{-3} (~35.7% of the pre-eclipse number density). Two hours after egress from eclipse, the n_{PEAK} has slightly decreased to ~6.5×10^{16} m^{-3} (~23.5% of the pre-eclipse number density). The overshoot in n_{PEAK} just after egress from eclipse is caused by the excess SO_2 condensed on the non-frost surface during eclipse that rapidly desorbs and inflates the atmosphere. Two hours after egress from eclipse, most of the excess SO_2 has already desorbed from the non-frost surface leaving sublimation from SO_2 surface frosts as the primary support for the atmosphere. At high altitudes, n follows the trend of the near surface value and the only major departure is just before egress from eclipse (~100 minutes into eclipse) where n is roughly 5 times lower than the pre-eclipse values above 20 km altitude.

The vertical thermal profile also undergoes morphological changes during eclipse. Prior to eclipse, there is a thermal inversion layer near the surface in the subsolar region due to the depletion of incoming plasma energy above ~5 km altitude. As the atmosphere collapses in eclipse, the column density becomes thin enough that plasma energy reaches all the way to the surface. After ~10 minutes in eclipse, the inversion layer has disappeared and the gas translational temperature, T_{trans}, at 1 km altitude has increased slightly (~140 K) due to plasma heating. Near the end of eclipse (~100 minutes into eclipse), T_{trans} at 1 km altitude has increased further (~160 K) because the thinner column allows more plasma energy to reach near the surface. Upon egress from eclipse, the atmosphere thickens and the inversion layer is rapidly reestablished. Within ~20 minutes after egress from eclipse, an inversion layer has re-formed but subsequently weakens ~2 hours after egress from eclipse because of the thinner atmosphere at that time. At higher altitudes, the atmosphere is warmed by the plasma heating. T_{trans} increases nearly linearly with altitude above ~20 km before, during, and after eclipse. With the present model, plasma heating leads to temperatures in excess of 500 K at high altitudes. In Figure 6.6, the vertical profile of the atmosphere at the instantaneous location of the peak pressure (as it

moves in time) was investigated. In Figure , the atmosphere is instead sliced along the equator to show the atmospheric structure as a function of both altitude *and* longitude.

Ten minutes *prior to* eclipse, the atmosphere is largely supported by sublimation from SO_2 surface frosts rather than desorption from the non-frost surface. The only exception is near 40° W where the DAE forms (see Figure a). Note that the DAE occurs at a local time of ~8:40 am and the dawn terminator occurs at 6:00 am. The gas density, n, slowly decreases just east of dusk (280° W–285° W) whereas there is an abrupt drop-off in n just west of dawn (75° W–80° W) due to the high thermal inertia of the SO_2 surface frosts. The dayside exobase (the altitude at which the SO_2 gas mean free path is equal to the atmospheric scale height) peaks at ~180 km altitude; from dusk, this exobase altitude decreases linearly with decreasing longitude to ~110 km altitude at the anti-Jovian point (180° W). The exobase reaches a minimum of ~25 km altitude at 80° W.

Forty minutes *into* eclipse, the atmosphere has collapsed significantly but the dayside exobase between 270° W to 360° W remains at ~180 km altitude (see Figure b). The exobase height in that region remains relatively unchanged for two reasons: i) the collapse is partially limited by the speed of sound and, more importantly, ii) Γ_F is large leading to slow changes in T_F. The nightside exobase remains unchanged because the transport of mass from the dayside to nightside by circumplanetary flow is small and changes in flux do not have time to develop. The primary changes to the exobase height occur between 0° W and 90° W. The atmosphere above the DAE (40° W) is most strongly affected because it had been supported by the non-frost surface which has a low Γ_{NF} which means T_{NF} decreases rapidly during eclipse. Therefore, the DAE disappears and the exobase drops to ~60 km altitude. The exobase near dawn (90° W) drops nearly to the surface (only ~10 km altitude).

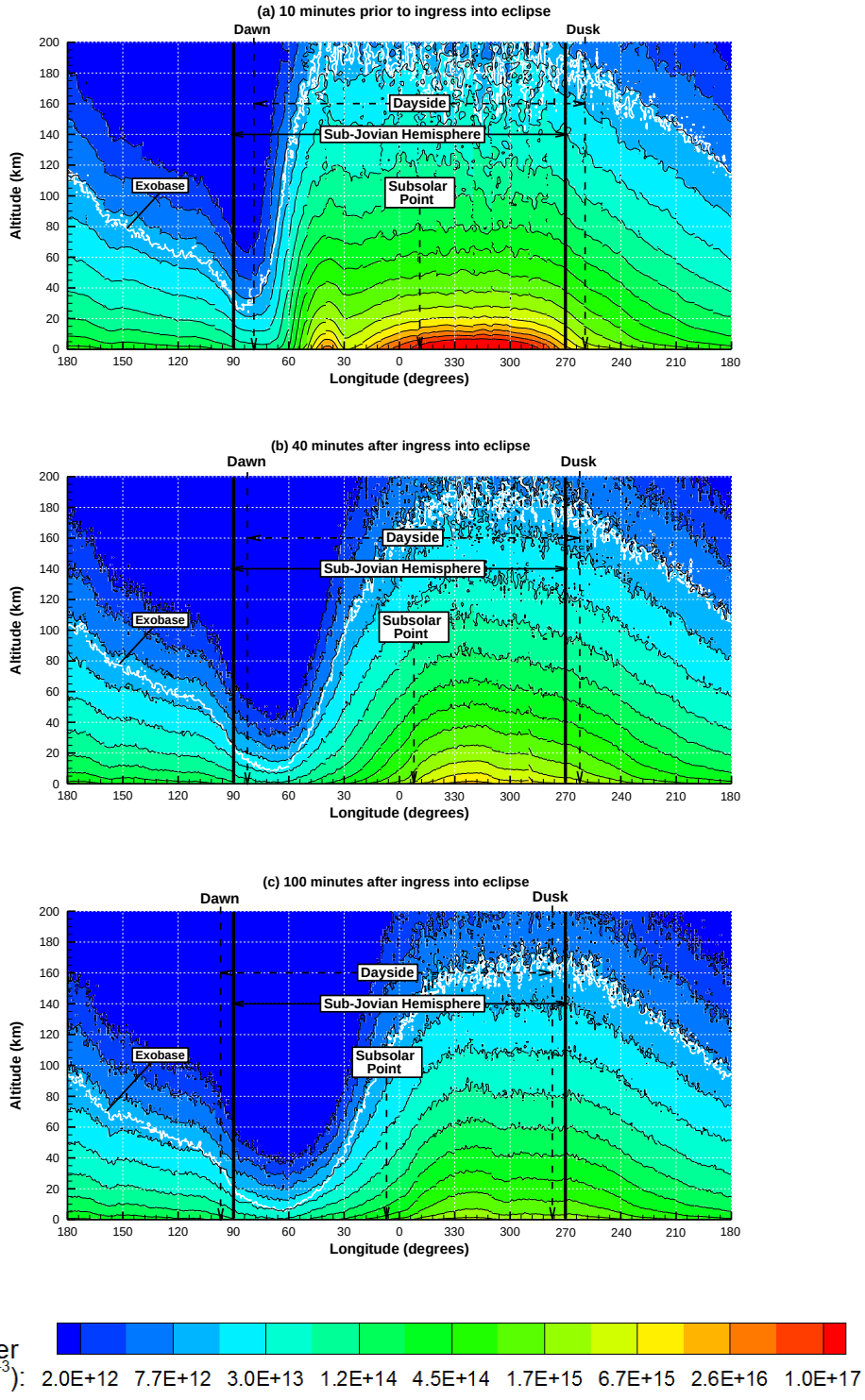

Figure 6.7: Contours of number density as a function of altitude and longitude for five instances near eclipse: ~10 minutes prior to eclipse, ~40 minutes after ingress into eclipse, ~100 minutes after ingress into eclipse, ~20 minutes after egress from eclipse, and ~2 hours after egress from eclipse. The location of the exobase is denoted by a white line.

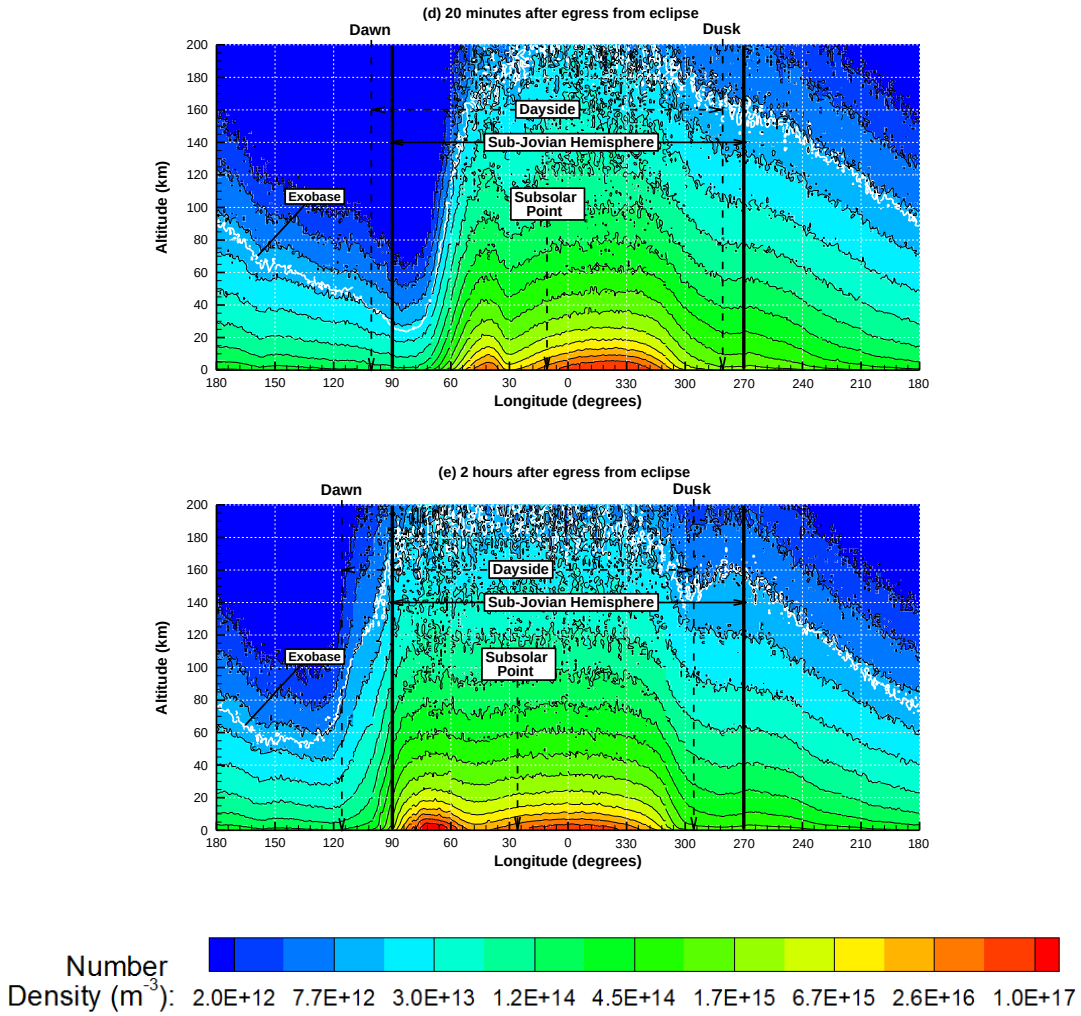

Figure 6.7, cont.: Contours of number density as a function of altitude and longitude for five instances near eclipse: ~10 minutes prior to eclipse, ~40 minutes after ingress into eclipse, ~100 minutes after ingress into eclipse, ~20 minutes after egress from eclipse, and ~2 hours after egress from eclipse. The location of the exobase is denoted by a white line.

One hundred minutes *into* eclipse, the atmosphere has collapsed further and the dayside exobase between 270° W to 360° W descends to ~160 km due to further thinning of the atmosphere (see Figure c). The exobase near dawn (~60° W) ultimately drops to ~7.5 km while the nightside exobase altitudes remain fairly constant. Note that the exobase height at a given longitude on the nightside will decrease in time because the atmosphere has been in night longer.

Twenty minutes *after* egress from eclipse, the peak exobase has recovered to ~160–200 km altitude on the dayside and the minimum exobase altitude has increased from ~7.5 km to ~25 km (see Figure d). Two hours *after* egress from eclipse, the exobase looks fairly similar to the morphology twenty minutes after egress but the minimum has increased to ~50 km (see Figure e). The reason for this increase in the minimum exobase altitude is that the location of the minimum is now on the anti-Jovian hemisphere which has slightly warmer surface temperatures since it never experiences eclipse.

The translational temperature just prior to eclipse seen in Figurea has a morphology similar to that found in Chapter 4. On the dayside, the gas at low altitudes is relatively cold (<120 K) because the overlying atmosphere is thick enough to absorb all of the plasma energy above these altitudes. The plasma energy depletion creates a "dome" of cold gas below which the gas does not experience any plasma heating. The DAE near 40° W is also visible since it becomes thick enough to create a small pocket of cold gas near the surface. Near the dawn terminator, a high temperature ($T_{trans} > 1000$ K) region exists due to shock compression as circumplanetary flow condenses on and near the nightside. At 40 km altitude in the region where the oblique shock is forming, the atmosphere is rarefied (the mean free path is between 10 km to 70 km), and the shock itself is also thick spanning over 700 km. The shock thickness increases with altitude as the atmosphere becomes more rarefied. Near the surface, the mean free path decreases to ~4 km but this is in the boundary layer of the flow. Although the shock looks nearly normal in Figurea and Figuree, this is due to the aspect ratios of the figures which are severely distorted. Each degree of longitude is equal to ~30 km, so the x-axis is compressed by a factor of ~26.7 compared to the y-axis. Therefore, despite the shock appearing normal, it is actually highly oblique.

At high altitudes (>100 km), the dayside translational temperatures become noisy because the number of computational molecules in each column of cells is constrained to be the same (1000 molecules) and the distribution is biased towards lower altitudes. On the nightside, the statistics are better at higher altitudes because the scale height is larger due to plasma energy reaching the surface and heating the atmosphere (compare altitudes between 180–200 km in dayside area between 300° W and 330° W with the nightside, especially between 150° to 210° W, in Figurea).

Forty minutes *after entry* into eclipse, the collapse of the atmosphere allows plasma energy to penetrate to much lower altitudes and the atmosphere is significantly warmer on the dayside (see Figureb). At 1 km altitude, the atmosphere over the peak pressure region warms to ~140 K due to the plasma heating. The atmosphere near the DAE collapses rapidly and the "pocket" of cold gas that existed due to the depletion of plasma energy is replaced by warmer gas through which plasma is able to reach to the surface. At high altitudes between 60° and 90° W (where the oblique shock existed), the shock rapidly dissipates due to the decreased day-to-night pressure gradient. At high altitudes, the data become very noisy due to the extremely low densities ($<10^{10}$ m^{-3}). This is especially true between 70° W to 100° W where the average number of molecules per cell drops below two, resulting in misleading contours. Some residual hot gas (>800 K) still exists but is likely not due to shock compression. The thermal structure of the atmosphere on the nightside remains very similar to the pre-eclipse structure.

Approximately 100 minutes *after* ingress into eclipse, the atmosphere has collapsed further and plasma energy is able to warm the gas near the surface (1 km altitude) to ~160 K (see Figurec). Gas *at* the surface remains in thermal equilibrium at ~111 K. The location where the oblique shock existed prior to eclipse

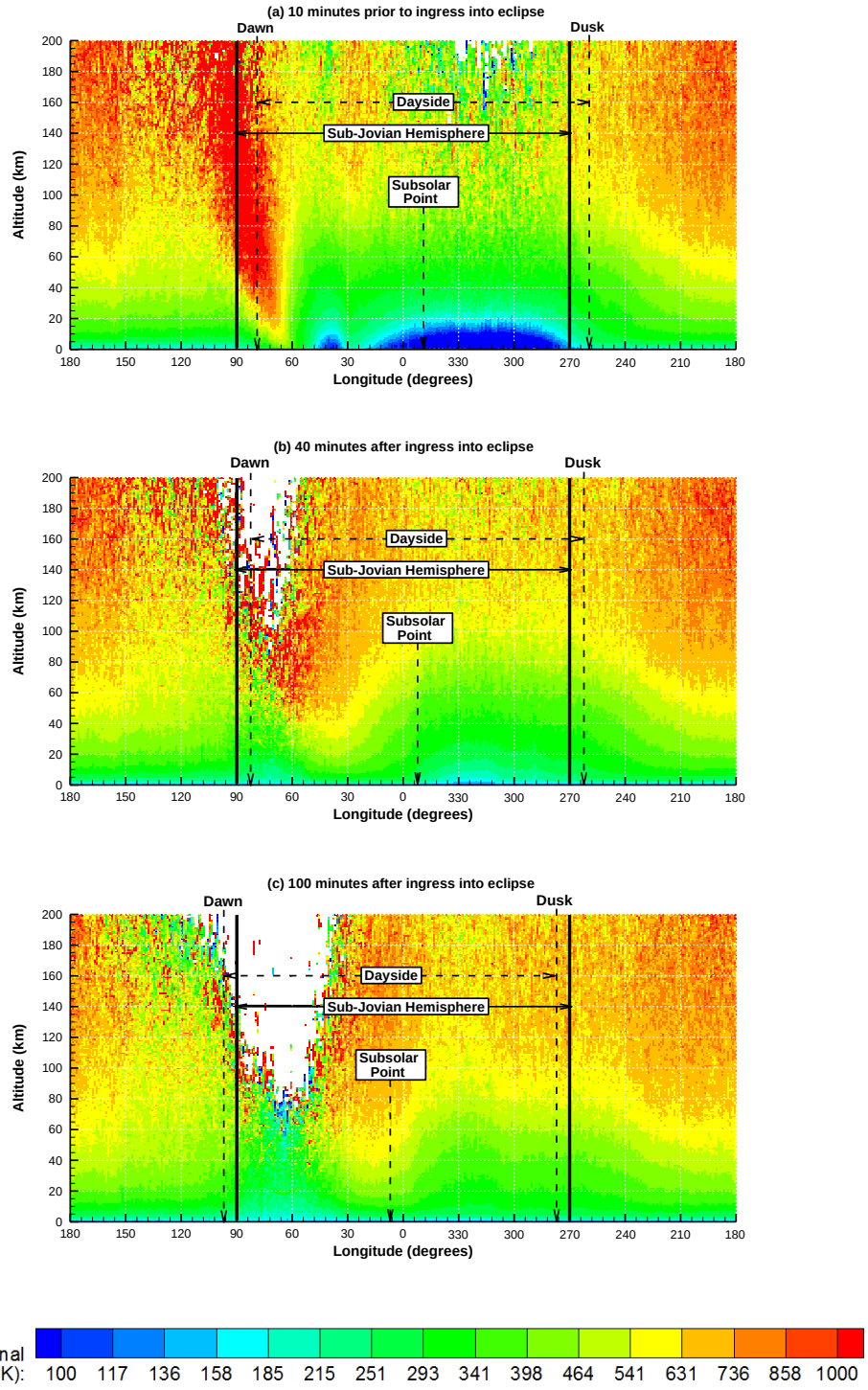

Figure 6.8: Contours of translational temperature as a function of altitude and longitude for 5 times near eclipse: ~10 minutes prior to eclipse, ~40 minutes after ingress into eclipse, ~100 minutes after ingress into eclipse, ~20 minutes after egress from eclipse, and ~2 hours after egress from eclipse. Values are blanked where the T_{trans} < 30 K due to insufficient statistics.

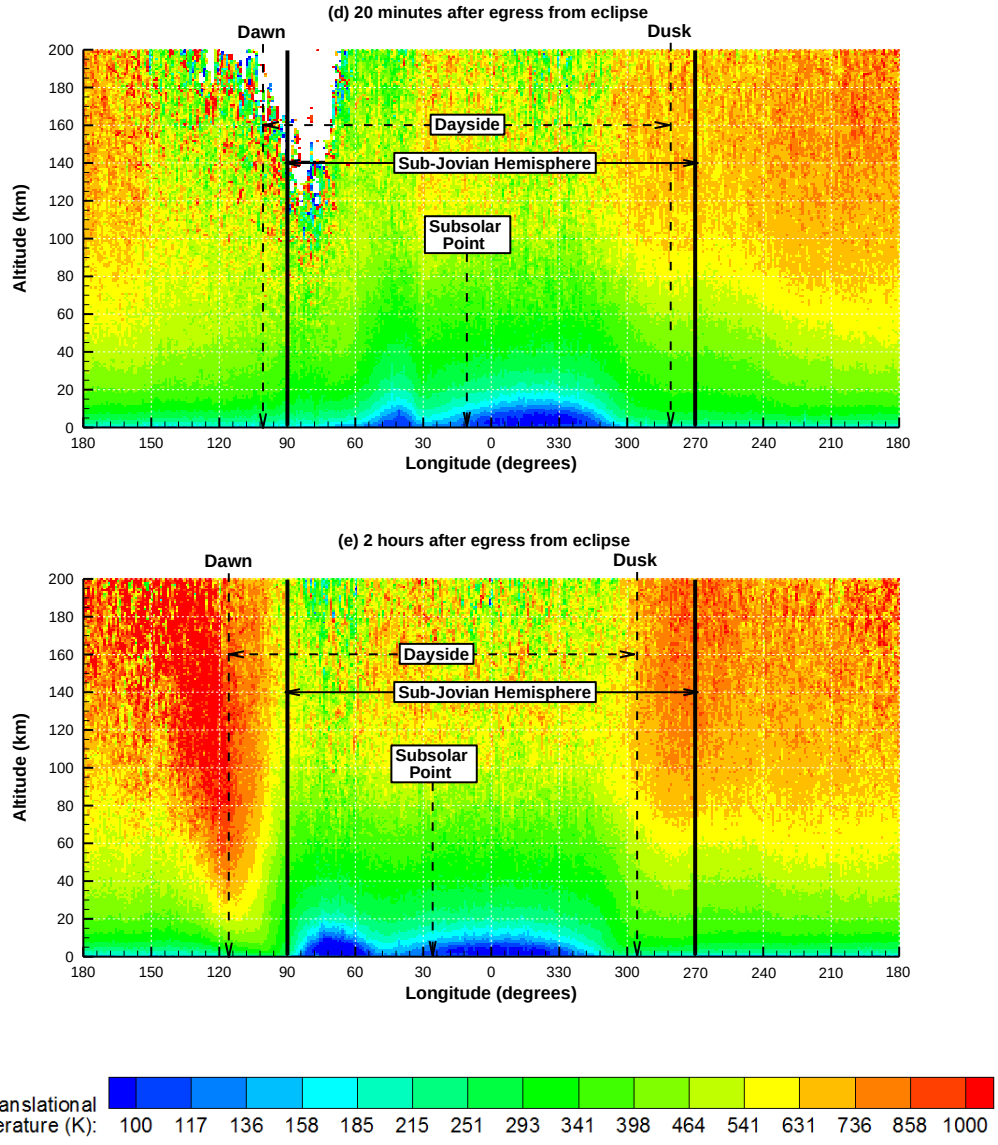

Figure 6.8, cont.: Contours of translational temperature as a function of altitude and longitude for 5 times near eclipse: ~10 minutes prior to eclipse, ~40 minutes after ingress into eclipse, ~100 minutes after ingress into eclipse, ~20 minutes after egress from eclipse, and ~2 hours after egress from eclipse. Values are blanked where the T_{trans} < 30 K due to insufficient statistics.

has dropped to extremely low densities as the day-to-night pressure gradient further decreases. The nightside thermal structure largely remains the same with slight cooling at high altitudes.

Twenty minutes *after* egress from eclipse, the non-frost surface has warmed significantly because of its low Γ_{NF} (see Figured). The material that condensed on the cold (~90 K) non-frost surface during eclipse rapidly desorbs as the non-frost surface warms and the sublimation atmosphere gradually thickens. This causes the "dome" of cold gas on the dayside to reappear. Although the atmospheric column density has begun to increase in the ten minutes after eclipse, the timescale on which the circumplanetary flow equilibrates is much longer. This timescale is controlled by the speed of sound, a_{GAS}, and the distance the gas must travel, d_C. It will vary with altitude but a rough estimate of the timescale at 40 km altitude is $t_C = d_C/a_{GAS} \approx 3$ hours assuming $T_{trans} \approx 400$ K and $d_C \approx 2800$ km (a quarter of Io's circumference). Therefore, the compressional heating from the oblique shock is absent (in Figured) because the SO_2 gas flow is still predominantly subsonic. The DAE is visible from the cold "pocket" of gas that it creates at ~45° W. Noisy conditions exist at high altitudes (>100 km) where the oblique shock existed prior to eclipse.

Two hours *after* egress from eclipse, the atmosphere has nearly recovered from eclipse and the T_{trans} morphology is similar to the atmosphere 10 minutes prior to ingress (see Figuree). The day-to-night pressure gradient is large enough to drive the flow supersonic and the oblique shock near the dawn terminator reappears. The atmosphere over much of the dayside remains thick enough to deplete the plasma energy before it reaches the surface leaving cold gas near the surface. The relative sizes of the cool gas "pockets" formed by the DAE and the peak pressure region change as a function of time. Comparing Figuree to Figurea, the DAE has grown in size while the peak pressure region has not yet fully recovered from eclipse because of the high thermal inertia of the frost surface (see Section 5.3).

6.4 ANTI-JOVIAN VS. SUB-JOVIAN HEMISPHERE

The effects of eclipse on the atmosphere are finally examined by comparing the sub-Jovian atmosphere prior to eclipse with the anti-Jovian hemisphere. Simulated column densities on the anti-Jovian hemisphere's dayside are higher than for the sub-

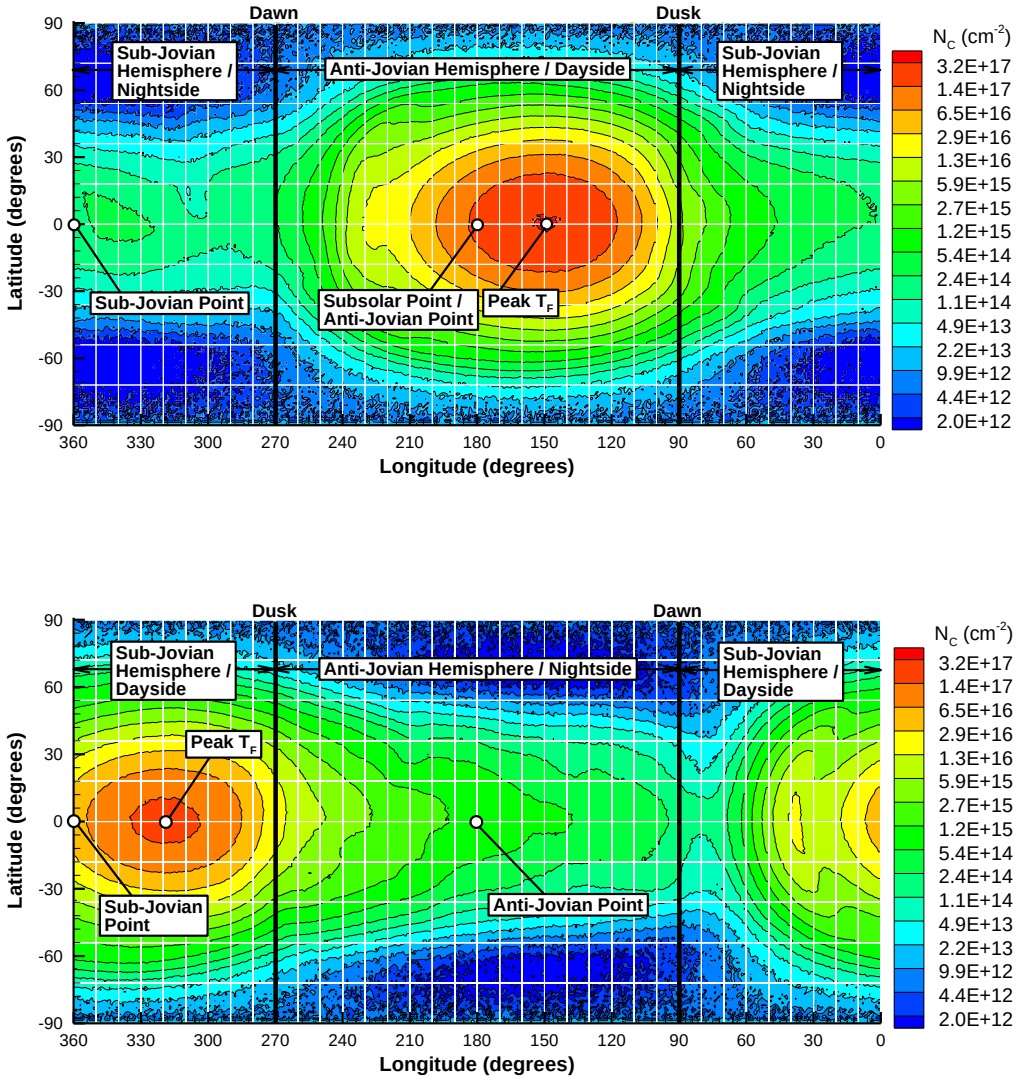

Figure 6.9: A comparison between the anti-Jovian dayside atmosphere and the sub-Jovian dayside atmosphere (at an instant just before ingress into eclipse). The anti-Jovian hemisphere has higher column densities throughout because of the higher underlying T_F.

Jovian hemisphere and the anti-Jovian hemisphere's peak dayside SO_2 gas column density, N_C (~3.2×10^{17} cm^{-2}) is ~45% higher than the sub-Jovian hemisphere's peak of $N_C \approx 2.2\times10^{17}$ cm^{-2} (see Figure 6.9 and Figure 6.10). As seen in Figure 6.9, the morphology of both atmospheres is similar with elliptic contours of column density centered around the peak T_F which in both cases lags the subsolar point by ~33°. This 33° thermal lag means that the peak T_F lags the subsolar point by 3 hours and 50 minutes (see Figure 6.10). Both hemispheres have a long atmospheric "tail" that extends past dusk and onto the nightside. When the nightside is on the sub-Jovian hemisphere, column densities are slightly lower because of the lower underlying T_F due to eclipse's diurnally averaged effect. Both atmospheres have sharp gradients near the dawn terminator where the surface is just coming into sunlight.

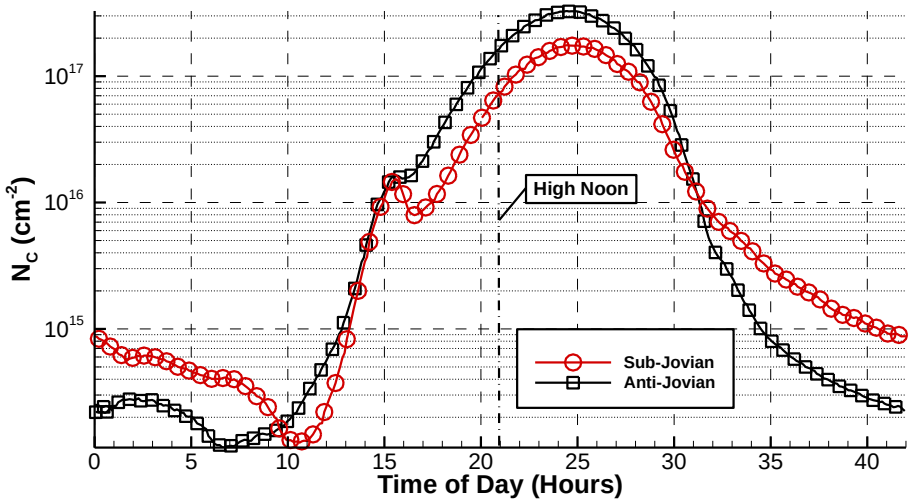

Figure 6.10: Equatorial column densities for the anti-Jovian and sub-Jovian hemispheres plotted as a function of time of day such that "noon" occurs at the same point for each hemisphere. High noon occurs at 21 hours. The DAE occurs at ~15 hours.

To validate these atmospheric simulations, we compare to recent observations of Io's atmosphere. Feaga *et al*. (2009) used Lyman-α observations to illustrate a striking asymmetry between the sub-Jovian and anti-Jovian hemispheres of Io's

atmosphere. In these observations, the anti-Jovian hemisphere was found to have a higher average dayside column density than the sub-Jovian hemisphere. They explained the asymmetry in terms of the distribution of volcanic centers where the anti-Jovian hemisphere has a higher concentration of volcanoes. Our atmospheric simulations show that eclipse is an additional or alternative cause for the anti-Jovian / sub-Jovian asymmetry.

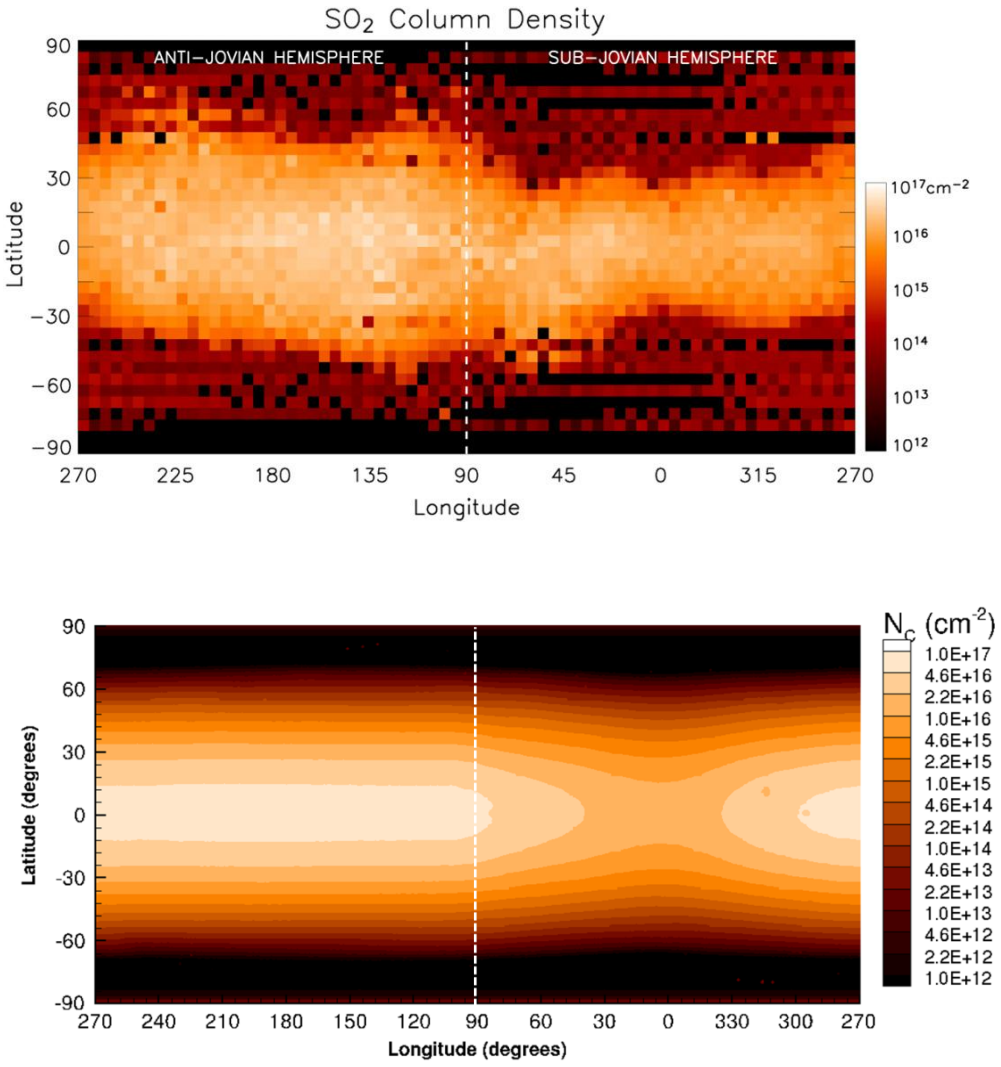

Figure 6.11: (a) Observationally inferred (Feaga *et al*., 2009) and (b) simulated "average dayside" SO_2 column densities. Both (a) and (b) show the Anti-Jovian hemisphere with higher "average dayside" column densities.

Unfortunately, to reconstruct Figure 6 from Feaga *et al*. (2009) requires simulation of an entire Io orbit which is presently computationally prohibitive with a fully collisional atmosphere in DSMC. Instead, we simulate Io's atmosphere in the absence of collisions (free molecular) for an entire orbit. This comparison is justified because the circumplanetary flow driven by molecular collisions does not significantly alter the column density from hydrostatic equilibrium. Forty "snapshots" of Io's atmosphere were thus averaged to create an image of the "average dayside atmosphere".

Figure 6.11 compares the Lyman-α inferred "average dayside" column densities with our simulated (free molecular) column densities that include the effect of eclipse. Both show high "average dayside" column densities on the anti-Jovian hemisphere (on the left of Figure 6.11). The simulation is much smoother than the observation and this could be due to the lack of volcanic plumes in our current model, observational noise, or the effect of the residence time of SO_2 gas on the non-frost surface which tends to smooth atmospheric column densities despite the underlying inhomogeneous SO_2 surface frosts. In our model, longer residence times (by more than a factor of 2) would result in an unphysical build-up of SO_2 frost on the non-frost surface through multiple orbits; therefore, there must be another mechanism for denuding the non-frost surface of the thin layer of SO_2 that builds up during the night. We hypothesize that night time sputtering by high energy ions might keep the surface denuded (Moore *et al*., 2011). This will be investigated in the next chapter. Lastly, comparing both images from Figure 6.11 with Figure 4.5, there is a definite correlation between the atmospheric column density and the SO_2 frost fraction (Douté *et al*., 2001). The possible reasons for this correlation will be explored in Chapters 7 and 8.

CHAPTER 7: NUMERICAL SIMULATIONS OF IO'S ATMOSPHERE WITH CHEMISTRY

In the final set of DSMC atmospheric simulations, the sophisticated thermal model used in Chapter 6 is coupled with a particle description of the plasma that replaces the radial energy flux model used in the results of Chapter 4 and 6. The particle description of the plasma allows for the ions to impart momentum to the atmosphere which is expected to decrease the atmospheric scale height (e.g. compress the atmosphere) on the upstream hemisphere (Saur *et al*., 2002) as well dissociate gas molecules in the neutral atmosphere and create daughter species of SO_2 (SO, S, O, and O_2). Energetic ions will also cause sputtering of SO_2 gas from SO_2 surface frosts and thin layers of SO_2 condensed on the non-frost surface. The final model difference is the addition of photo-chemistry that will further dissociate the neutral SO_2 atmosphere as well as the lesser molecular species, SO and O_2. As in previous chapters, the resulting column densities and global winds will be described; however, since multiple species are created by dissociation of the neutral atmosphere, each atmospheric species will be investigated independently. The results are compared to previous simulations by Moore (2011) and therefore a similar subsolar longitude of 342° W is chosen (~9° prior to eclipse). The sub-plasma point (at 270° W) is therefore separated by 72° from the subsolar longitude.

7.1 ATMOSPHERIC COLUMN DENSITY

The bulk of the dayside atmosphere is composed of SO_2 that is then dissociated into daughter species (O, O_2, SO, S) by S^+ and O^+ ions from the Jovian plasma torus. O_2 is non-condensable (e.g. it reflects diffusely when it impacts Io's

surface). SO is partially non-condensable (0.5 sticking coefficient). These two species (especially O_2) become dominant on the nightside where sublimation from SO_2 surface frosts occurs at a much lower rate due to the exponential dependence of the SO_2 vapor pressure on T_F. On the dayside, the SO_2 daughter species are present in the largest densities (and concentrations) in the densest areas of the SO_2 atmosphere where ions will experience many collisions with the neutral atmosphere. The densities (and concentrations) of daughter species fall off toward the terminator as the sublimation atmosphere thins and ions hit the surface more often and sputter off (only) SO_2 gas. An east/west asymmetry exists due to the high thermal inertia of the SO_2 frost that tends to create a thicker SO_2 atmosphere past dusk than exist just prior to dawn. This thicker SO_2 atmosphere is also a more substantial target for ions and therefore the density (and concentration) of daughter species in this region is also higher. The details of the atmospheric morphology for each species will be discussed in detail in the following sections. Note that in the discussion that follows, the *leading hemisphere* (centered at 270° W) refers to the sub-plasma hemisphere or upstream hemisphere (i.e. the hemisphere which faces the plasma flow), not the leading hemisphere with respect to Io's orbital rotation (which is at 90° W). The results of this section will be compared to previous simulations of the interaction between Io's atmosphere and the Jovian plasma torus (Moore, 2011; Wong and Smyth, 2000) and to previous observations (Jessup *et al*., 2004; Feaga *et al*., 2009; Moullet *et al*., 2010).

7.1.1 Bulk Column Density

Figure 7.1 shows the underlying surface temperature of the SO_2 frost and non-frost. These are shown for reference when analyzing the morphology of the column densities of the SO_2 sublimation atmosphere as well as the SO_2 daughter species. As described in Chapters 5 and 6, the relatively high thermal inertia of the SO_2 frost ($\Gamma_F = 200$ J m^{-2} K^{-1} s$^{-1/2}$) produces a ~33° thermal lag between the subsolar point and

the peak T_F. See Chapter 5 for a detailed description of the T_F and T_{NF} temperature distributions.

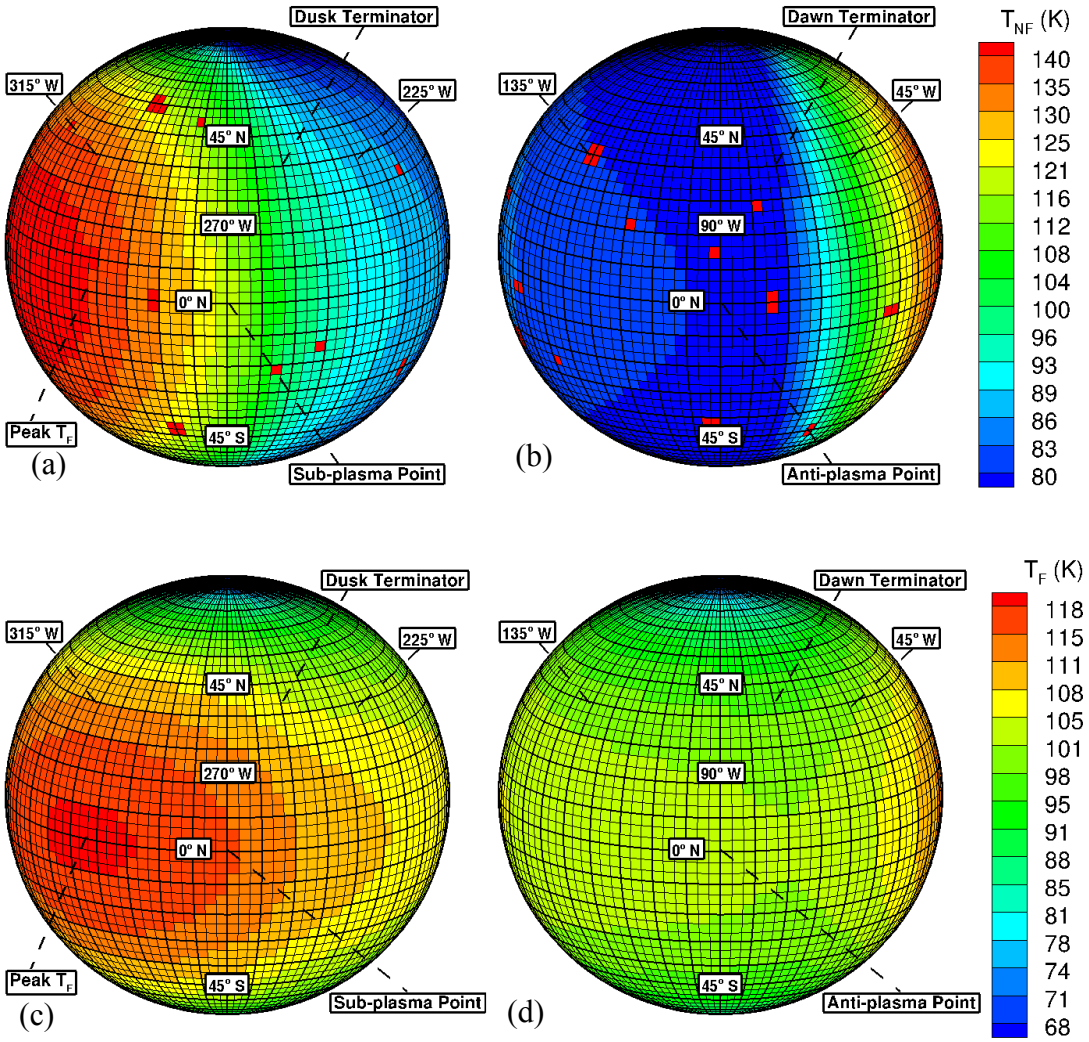

Figure 7.1: Color contours of the non-frost surface temperature as a function of latitude and longitude for (a) the leading hemisphere and (b) the trailing hemisphere. (c) and (d) show the SO_2 surface frost temperature for the leading and trailing hemispheres, respectively. Note that the subsolar point is at 342° W and the sub-plasma point is at 270° W.

The bulk gas column density represents the sum of the gas column densities of SO_2, O_2, O, SO, and S. The bulk column density peaks at ~ N_C ~2.5×10^{17} cm^{-2} over the peak T_F (see Figure 7.2). Over much of the dayside hemisphere, the bulk column density is dominated by SO_2 gas (see Figure 7.3 and Figure 7.4) that tracks VPE to

mid-latitudes where sputtering from SO_2 surface frosts begins to lead to a strong departure from VPE. At mid- to high latitudes, T_F drops below 90 K and the SO_2 sublimation atmosphere column density based on VPE drops below ~10^{12} cm^{-2}; however, the bulk column density is sustained at ~4–8×10^{14} cm^{-2} by non-condensable species such as O_2 and SO (see Section 7.1.3 and Section 7.1.5) as well as sputtering by high energy ions of SO_2 surface frosts (see Figure 7.3).

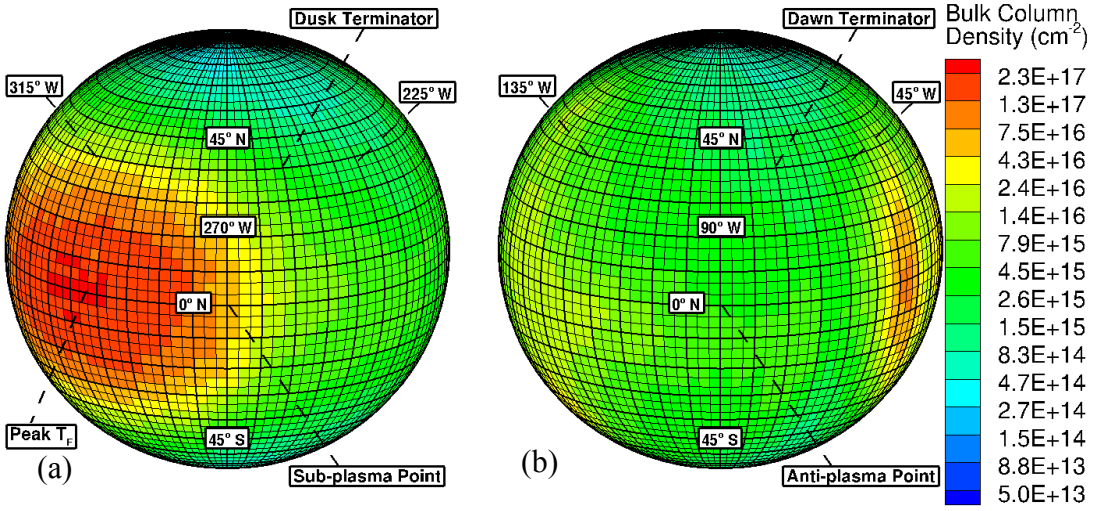

Figure 7.2: The bulk gas column density as a function of latitude and longitude for (a) the leading hemisphere and (b) the trailing hemisphere.

The bulk column density has another local maximum just after dawn due to the dawn atmospheric enhancement (DAE). In this region, the bulk column density increases to ~8×10^{16} cm^{-2} due to the SO_2 molecules that condensed during the cold night but rapidly desorb from the non-frost surface as it warms quickly at dawn (see Figure 7.2b). The bulk atmosphere is thinnest (~4×10^{14} cm^{-2}) where the T_F is coldest (near the poles) because most species are condensable at these surface temperatures (see Figure 7.2). SO_2, S, and O condense out while O_2 remains fully non-condensable and SO is partially non-condensable. O_2 becomes the dominant species in these very cold T_F regions (see Figure 7.6).

7.1.2 SO_2 COLUMN DENSITY

At a subsolar longitude of 342° W, SO_2 column densities at low latitudes are largely in VPE with SO_2 surface frosts. The SO_2 column density reaches a maximum of N_C ~2.35×10^{17} cm^{-2} above the peak T_F of 118.5 K which is in agreement with the results of Chapter 5 and 6. In comparison, Moore (2011) used a peak T_F of 115 K and therefore his simulated SO_2 column densities will be significantly lower ($N_C = 7.4\times10^{16}$ cm^{-2} at 115 K). In the current simulations, the SO_2 column densities at low latitudes follow VPE nearly everywhere except near the DAE (see Figure 7.3). The DAE was not seen in Moore (2011) because he assumed uniform frost coverage (e.g. all gas which impacted the surface was deleted from the computation). The magnitude of the column density enhancement from the DAE is roughly equivalent to that seen in the results of Chapter 6.

It might be expected that sputtering from the nightside surface would denude the non-frost surface of the thin layer of adsorbed SO_2 gas; however, the high thermal inertia of the SO_2 surface frosts causes the temperatures on the nightside to cool very slowly. At midnight, the SO_2 frosts have cooled only to ~104.5 K which supports a VPE column density of ~1.4×10^{15} cm^{-2}. The simulated SO_2 column density is further increased to ~6×10^{15} cm^{-2} by the dynamic transport of SO_2 via strong plasma-driven winds and by surface sputtering (see Figure 7.1 and Figure 7.3). This tenuous atmosphere is nearly thick enough to block further sputtering of SO_2 frosts by high energy ions since Moore (2011) found that column densities above ~10^{15} cm^{-2} will partially block sputtering. In addition, non-condensable species such as O_2 and SO build-up on the nightside and increase the bulk column density above the 10^{15} cm^{-2} threshold and therefore help in shielding the surface from the high energy ions which cause surface sputtering.

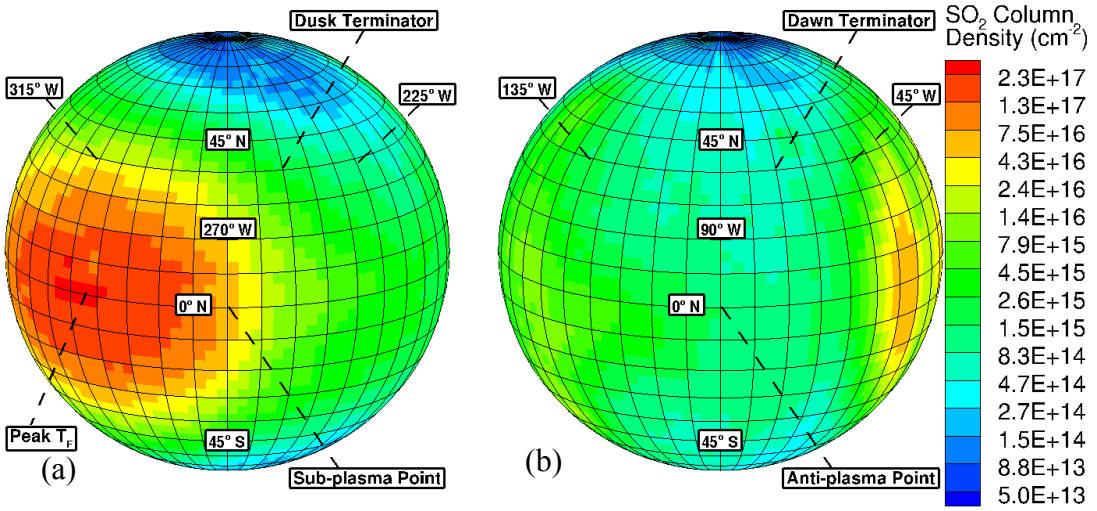

Figure 7.3: The SO_2 column density as a function of latitude and longitude for (a) the leading hemisphere and (b) the trailing hemisphere.

Surface sputtering does become important in supporting the SO_2 atmosphere near the poles where the surface is so cold that only the non-condensable species (O_2 and SO) exist at significant column densities ($>10^{14}$ cm^{-2}). The combined column densities of O_2 and SO are below the threshold to block sputtering and therefore a thin SO_2 sputtered atmosphere that is much thicker than a SO_2 sublimation atmosphere in VPE with the SO_2 surface frosts is created near the poles. A sublimation atmosphere in VPE with 85 K frosts would have a column density of only $\sim 7\times10^{11}$ cm^{-2} which is much lower than the sputtered SO_2 atmosphere's column density of $\sim 10^{14}$ cm^{-2}. The SO_2 column density remains below the threshold to block sputtering ($\sim 10^{14}$ cm^{-2}) not because the surface is shielded by the non-condensable species but because the SO_2 frost fraction is very low near the poles and the amount of SO_2 that builds up on the non-frost is also low. Therefore, ions will often impact that surface but sputter nothing because the surface is barren of condensed SO_2 gas.

The concentration or fraction of SO_2 gas in each column of cells can be calculated by dividing the SO_2 column density by the sum of the column densities of each species:

$$F_{SO2} = \frac{N_{C_{SO2}}}{\sum_{i=0}^{i=N_S} N_{C_i}} \quad 7.1$$

Similar gas fractions are computed for the daughter species of SO_2 by replacing the numerator by the appropriate species column density. SO_2 is the dominant species on the dayside and constitutes over 90% of the gas for zenith angles less than 45° from the peak T_F location (see Figure 7.4). Near the terminator, the SO_2 gas fraction drops to 50–60% with even lower fractions near the poles (~20%). On the nightside, SO_2 is still the dominant atmospheric species before midnight, and ranges from 30–50% depending on the spatial location. The SO_2 gas fraction is especially low (10%) where the surface is coldest (near the poles and just prior to dawn). It is in these locations that O_2 becomes the dominant atmospheric species and SO_2 constitutes only ~20% of the gas fraction.

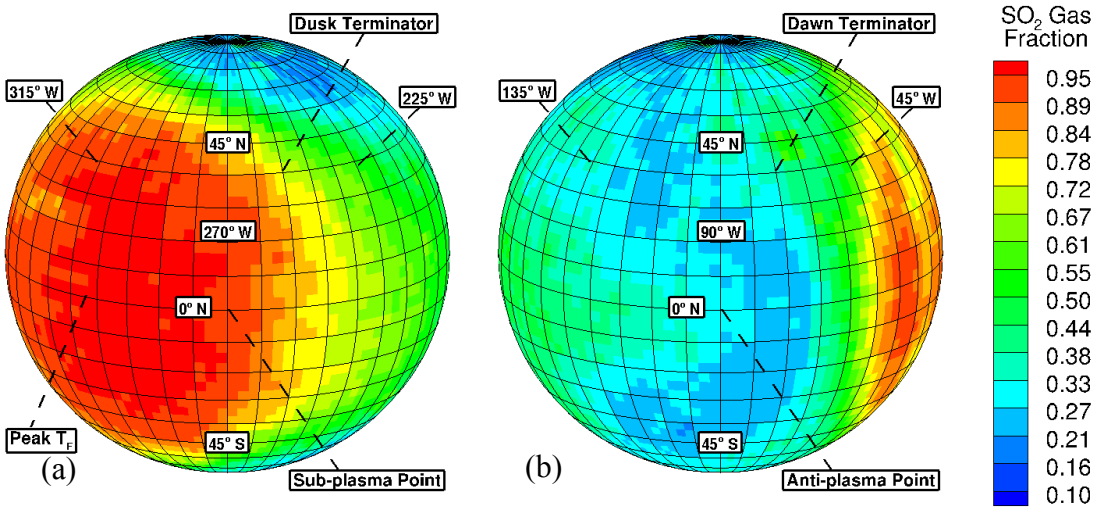

Figure 7.4: The SO_2 gas fraction as a function of latitude and longitude for (a) the leading hemisphere and (b) the trailing hemisphere.

7.1.3 O_2 Column Density

O_2 is created by ion and photo-dissociation of SO_2 gas and is non-condensable at Io's surface temperatures. O_2 has a very different morphology than SO_2 and its daughter species because of its non-condensability (see Figure 7.5).

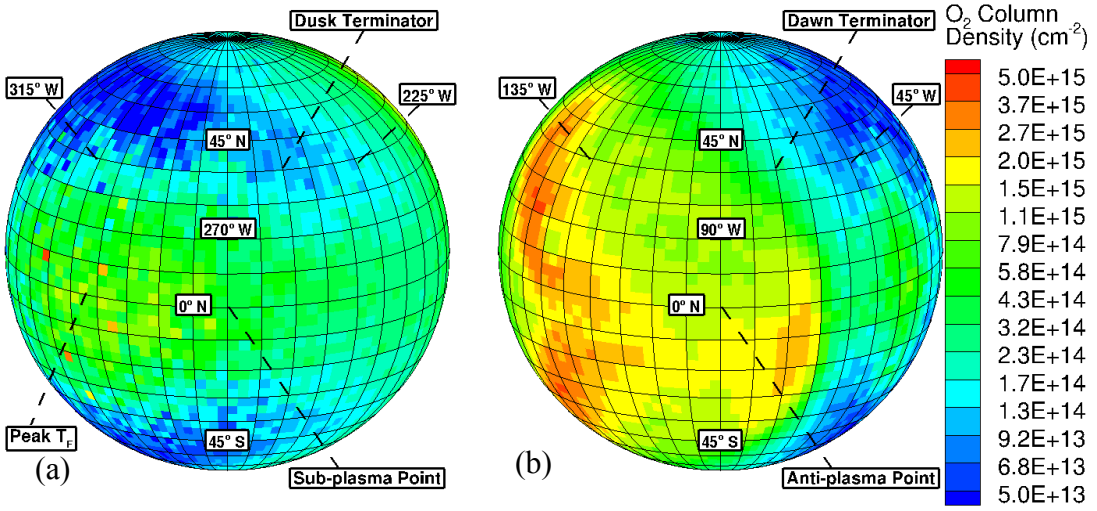

Figure 7.5: The O_2 column density as a function of latitude and longitude for (a) the leading hemisphere and (b) the trailing hemisphere.

Unlike most other species, O_2 column densities do not peak on the dayside because O_2 is non-condensable and is pushed by the circumplanetary winds toward the nightside. The O_2 dayside gas column density is highest (peaking at ~8–9×10^{15} cm^{-2}) where the SO_2 gas column density is highest because photons and ions both have a relatively thick target to dissociate in that region. Although the O_2 dayside column density has a local maximum on the dayside over the peak T_F, this local maximum coincides with the region of extremely low O_2 gas fraction (<1%) because the SO_2 atmosphere is so thick in comparison. The O_2 gas fraction over much of the dayside varies between 1–10% because of the thick SO_2 atmosphere present dominates the bulk atmosphere (see Figure 7.6). Once created by dissociation of SO_2, O_2 will flow toward the nightside (especially near the pole and just prior to dawn) where the surface is coldest. O_2 is the only species in these calculations that is fully non-condensable (SO is only 50% non-condensable) and therefore it will be pushed to regions of the lowest atmospheric pressure where other species will condense out. It becomes the dominant species near the poles ($N_C \approx 2\times10^{14}$ cm^{-2} in Figure 7.5) and makes up ~35–40% of the polar column density present (see Figure 7.6). It is also the

dominant species in certain regions near dawn on the nightside ($N_C \approx 0.5$–2.0×10^{15} cm^{-2} in Figure 7.5) and makes up ~20–40% of the column density (see Figure 7.6). O_2 has a non-uniform column density distribution on the nightside due to strong cyclonic winds that cause O_2 to build up near 140–170° W and ±45° (see Figure 7.20). In this region, the O_2 nightside column densities are ~2–3.5×10^{15} cm^{-2}.

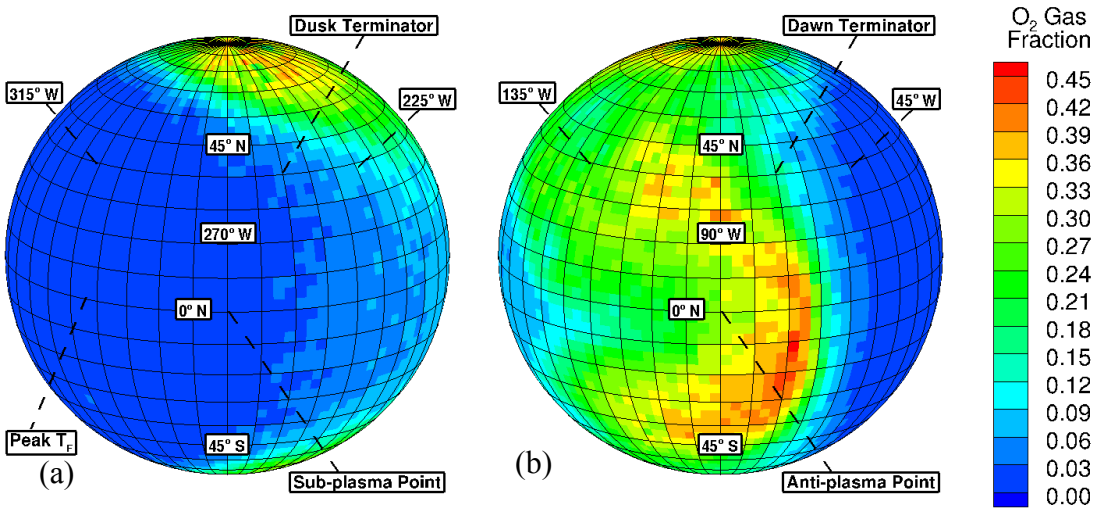

Figure 7.6: The O_2 gas fraction as a function of latitude and longitude for (a) the leading hemisphere and (b) the trailing hemisphere.

The DAE is also a region of high O_2 column density ($N_C \approx 6\times10^{14}$ cm^{-2}) because ions and photons dissociate the relatively dense SO_2 atmosphere; however, the O_2 gas fraction is low (<1%) because of the high SO_2 column density ($N_C \approx 7\times10^{16}$ cm^{-2}). Lastly, the O_2 column density on the dayside has an inflection point due its non-condensability. O_2 is formed in the densest areas of the SO_2 atmosphere but is pushed by the day-to-night pressure gradient (and plasma pressure) toward the nightside. It builds up on the nightside until it reaches a column density that is in equilibrium with the ion dissociation reaction rate of O_2. At dayside mid-latitudes there is less SO_2 gas to dissociate, and although O_2 is pushed by circumplanetary winds toward the poles, the transport of mass is small compared to the amount of O_2 created by dissociation even in the mid-latitude region. Therefore,

the O_2 column density is higher near the peak SO_2 pressure region and high near the poles but lower at mid-latitudes.

7.1.4 Atomic Oxygen Column Density

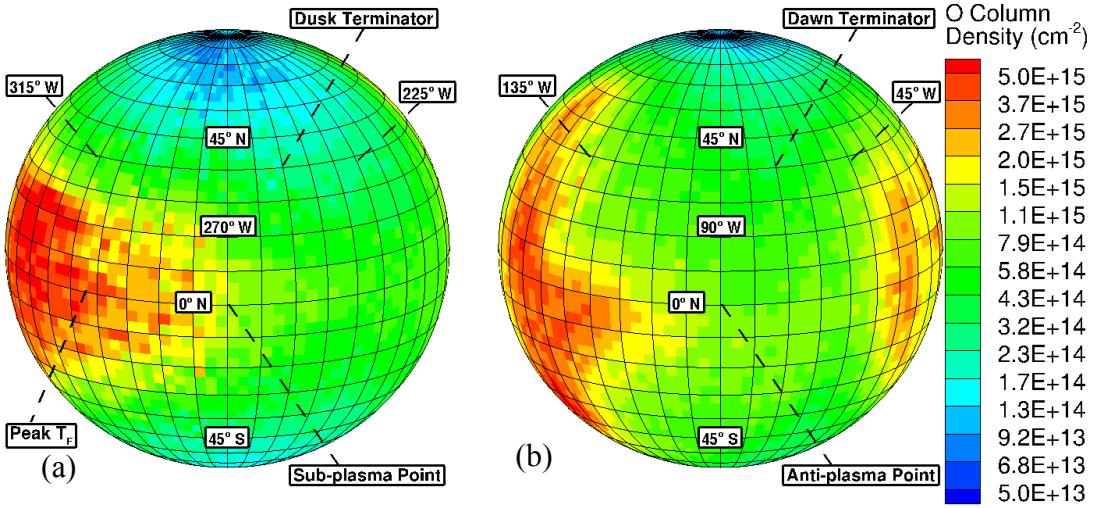

Figure 7.7: The O column density as a function of latitude and longitude for (a) the leading hemisphere and (b) the trailing hemisphere.

O atoms are created by multiple photo-dissociation and ion dissociation reactions. There are three different photo-dissociation reactions (see Table 3.9) and six different ion-dissociation reactions (Table 3.8) that can create O atoms. O column densities are highest over the peak T_F because this region provides the thickest SO_2 gas target for dissociation. O column densities peak at $N_C \approx 5\times10^{15}$ cm^{-2} which is roughly 5 times higher than the O_2 column density in that region. The half an order of magnitude difference in O and O_2 column densities can be explained by the number of pathways by which each can be created. There are only 3 reaction pathways for O_2 creation compared to the 9 reaction pathways for the creation of O. Also, the $SO_2 + h\nu \rightarrow SO + O$ photo-dissociation reaction is dominant over the other SO_2 dissociation reactions. The peak O column density occurs on the dayside but the O

gas fraction is quite low (2–3%) because of the high SO_2 column density present (~2.35×10^{17} cm^{-2}).

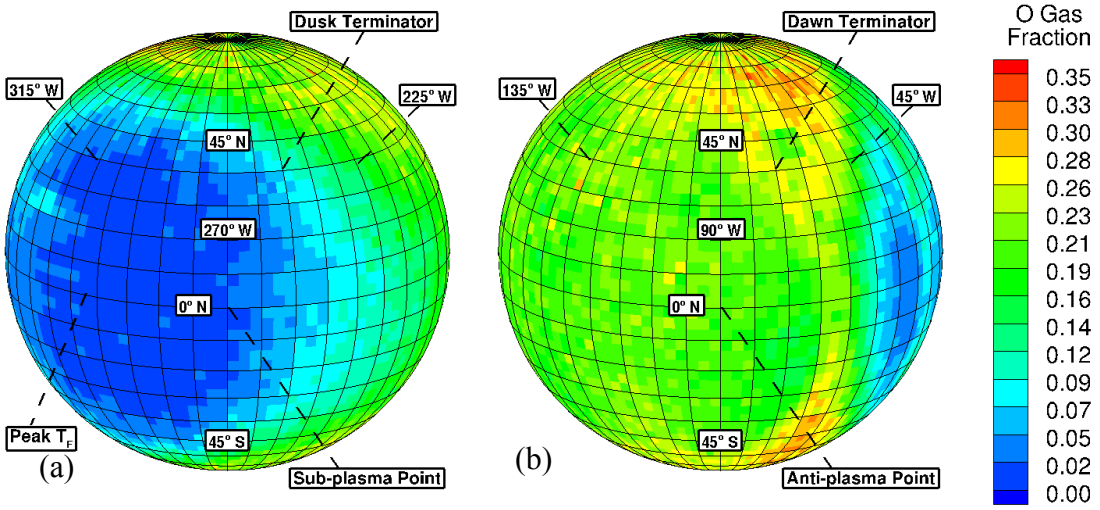

Figure 7.8: The O gas fraction as a function of latitude and longitude for (a) the leading hemisphere and (b) the trailing hemisphere.

Dayside O column densities decrease slowly toward the terminator as the column densities of its parent species also decrease. Near the terminator, O column densities range from ~1×10^{14} cm^{-2} near the pole up to ~8×10^{14} cm^{-2} near the equator. Along the terminator, the equatorial O gas fraction is ~5–8% because of the thick SO_2 atmosphere. Near the poles, the O gas fraction peaks at ~25%. The O gas fraction over much of the nightside is significant because of the high gas fraction of O_2 which is dissociated by ions to form O. On the nightside, the O gas fraction is fairly constant and ranges from ~20–25% but the column densities are highly non-uniform (0.6–4×10^{15} cm^{-2}) due to the build-up of O_2 discussed in the previous section. The O column density increases to ~2.5×10^{15} cm^{-2} at the location of the DAE but the gas fraction decreases to ~5% because the SO_2 atmosphere is much thicker.

7.1.5 SO COLUMN DENSITY

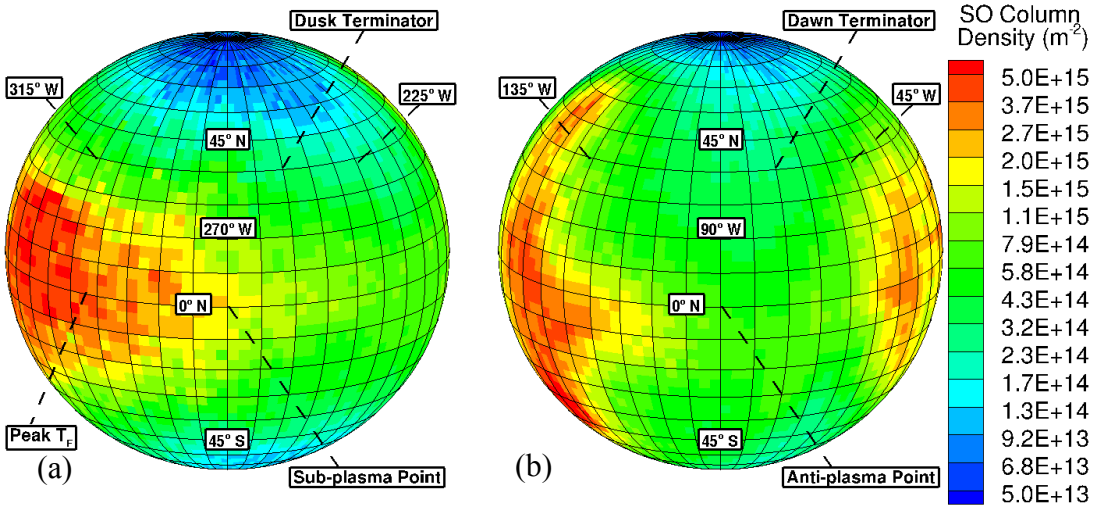

Figure 7.9: The SO column density as a function of latitude and longitude for (a) the leading hemisphere and (b) the trailing hemisphere.

SO gas is created by three different ion and photo-dissociation reactions. The morphology and magnitude of SO and O column densities (compare Figure 7.7 and Figure 7.9) are similar because the photo-dissociation of SO_2 into SO and O is a fast reaction with a rate coefficient approximately two orders of magnitude higher than any other SO_2 photo-dissociation reaction (Heubner *et al.*, 1992; Summers and Strobel, 1996). SO is also created in the dominant pathway for ion dissociation of SO_2 ($SO_2 + O \rightarrow SO + 2O$; Deng *et al.*, 2011). The SO column density peaks at ~5.0×10^{15} cm^{-2} (see Figure 7.9) on the dayside but constitutes only 2–3% of the bulk atmosphere because SO_2 dominates the majority of the dayside atmosphere (compare Figure 7.4 and Figure 7.10). Interestingly, the dominant destruction mechanism for SO ($SO + h\nu \rightarrow S + O$) has a higher reaction rate coefficient than for the creation of SO ($SO_2 + O \rightarrow SO + 2O$; Deng *et al.*, 2011) but the SO column densities on the dayside remain comparable to those of O. This may be due to the partial non-condensability of SO that reduces its loss rate due to sticking on the surface whereas O is condensable and is always lost when it lands on the surface.

SO column densities decrease to ~0.5–1.0×10^{15} cm^{-2} near the dusk terminator and are similar in magnitude to O column densities (compare Figure 7.7 and Figure 7.9). In the equatorial regions near the terminator, the SO gas fraction peaks at ~5–8% (again similar to O). The morphologies of SO and O are very similar over the entire nightside because they are created together through the same SO_2 dissociation reactions.

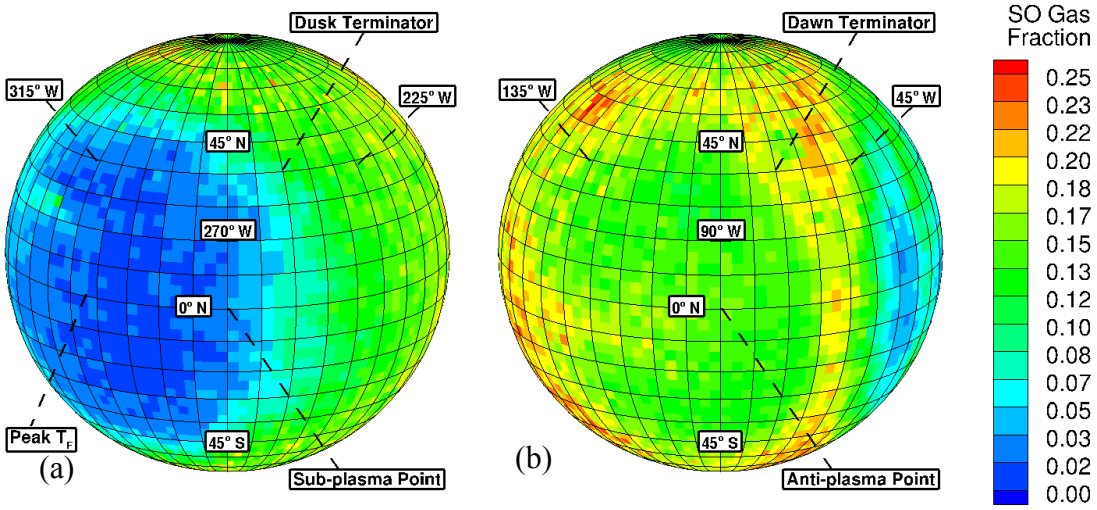

Figure 7.10: The SO gas fraction as a function of latitude and longitude for (a) the leading hemisphere and (b) the trailing hemisphere.

7.1.6 Atomic Sulfur Column Density

S gas is the SO_2 daughter species that has the lowest dayside column densities. This is because it is only created slowly by direct dissociation of SO_2 (i.e. the reaction cross section is small) and the primary mechanism for S creation is the photo-dissociation of SO which is present in much smaller dayside column densities than SO_2 (see Table 3.9). The peak S column density occurs in the densest regions of the SO atmosphere (on both the dayside and nightside) as expected and reaches a maximum of ~1.0×10^{15} cm^{-2}. The S gas fraction is ~0.5% on the dayside hemisphere

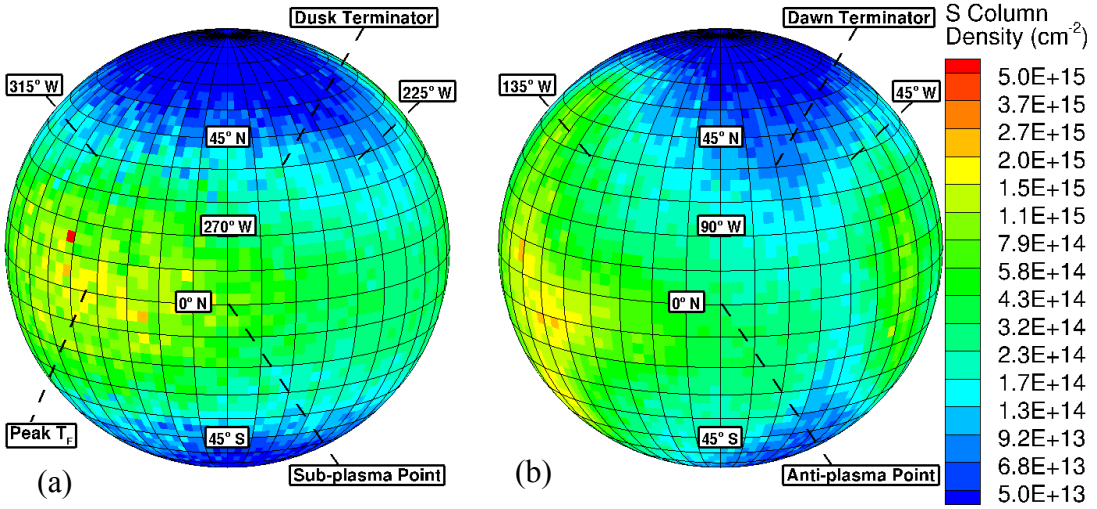

Figure 7.11: The S column density as a function of latitude and longitude for (a) the leading hemisphere and (b) the trailing hemisphere.

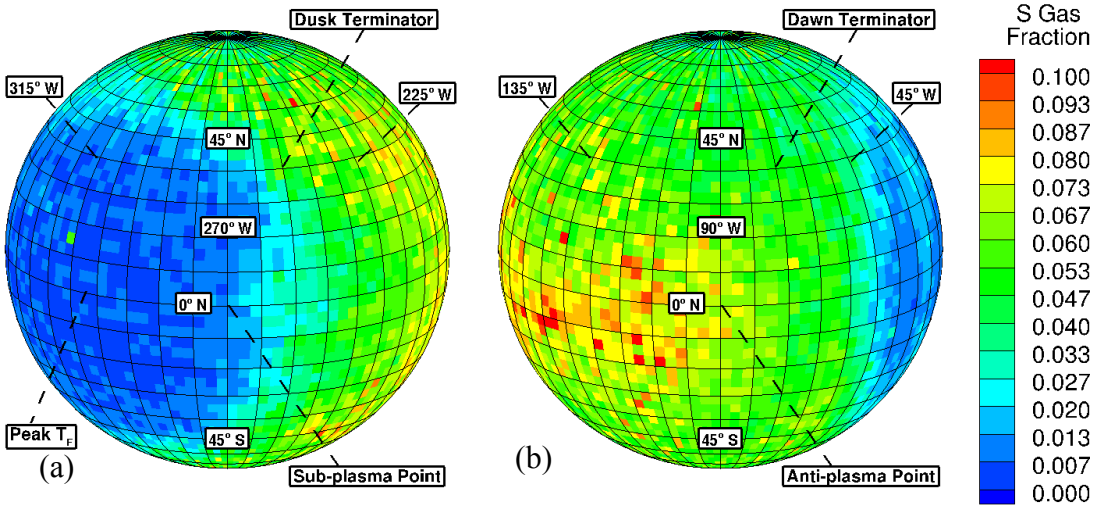

Figure 7.12: The S gas fraction as a function of latitude and longitude for (a) the leading hemisphere and (b) the trailing hemisphere.

because of the slow direct dissociation of SO_2. The S column densities drop to ~1.0–2.0×10^{13} cm^{-2} near the poles and to ~3.0×10^{14} cm^{-2} near the terminator (at the equator). S is nearly always present in concentrations that are half or less of the other daughter species except O_2. In these regions along the terminator, the S gas fraction reaches up to 2–3% near the equator and 3–4 % near the pole.

The S gas fraction after dusk on the nightside on the sub-plasma hemisphere is ~5% with column densities in the range of ~2.0–3.0 $\times 10^{14}$ cm^{-2}. On the anti-plasma hemisphere, the S column densities and gas fraction increase in the region where the other species are building up due to the O_2 cyclonic winds (see Figure 7.20). In these regions the column densities increase to ~2.0$\times 10^{15}$ cm^{-2} and the S gas fraction is ~8–10%.

7.1.7 Comparison to Moore (2011)

Moore (2011) assumed Io's surface is covered by uniform SO_2 frost (100% coverage) with a temperature distribution assuming radiative equilibrium (and therefore no thermal lag). For the current simulations, with Io at a subsolar longitude of 342° W (~9° prior to ingress into eclipse), the thermal lag reduces the angle between the peak T_F (and peak pressure region) and the sub-plasma point by 33° in comparison to the simulations of Moore (2011). He found that the plasma pressure forces strong winds that transport SO_2 toward the nightside and condense near dusk. As discussed in Section 7.2.1, the different surface temperature distribution in the current work leads to winds developing in the prograde direction (opposite to the retrograde winds of Moore (2011)) and therefore no increase in column density is seen past dawn on the nightside. Because the strong winds, driven by both the day-to-night pressure gradient and plasma pressure, flow toward dusk it is difficult to determine whether a corresponding column density increase occurs because it is masked by the relatively thick dusk SO_2 atmosphere from the slowly cooling T_F. Further comparison to Moore (2011) shows that the nightside sputtered atmosphere is considerably thicker in the current work because the warmer T_F on the nightside (Moore (2011) assumed 90 K) leads to not only a thicker sublimation atmosphere but also a thicker sputtered atmosphere because the sputtering rate is exponentially dependent on the SO_2 surface frost temperature. Therefore, the SO_2 atmosphere is

thicker in the present simulations nearly everywhere except on the nightside of the poles where the temperature is colder than 90 K.

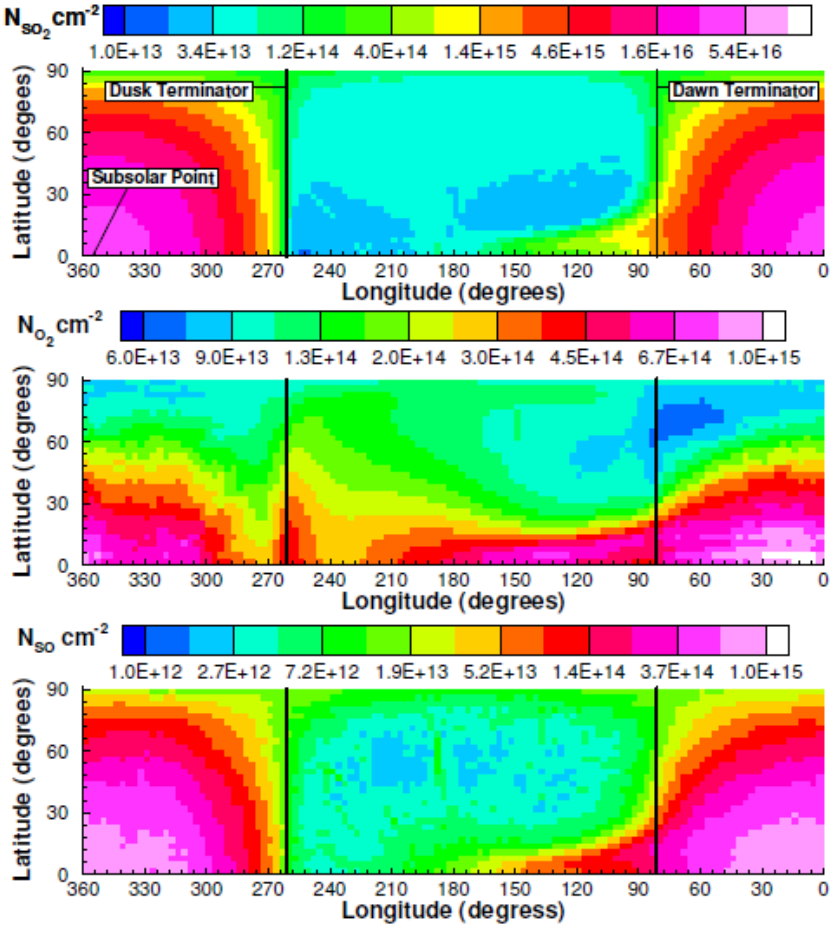

Figure 7.13 : Color contours of column density for SO_2 (top), O_2 (middle), and SO (bottom) as function of latitude and longitude for the northern hemisphere. Note the difference scale for each species. (*From Moore (2011)*).

Accounting for the lower T_F in Moore (2011) and hence lower SO_2 column densities, the O_2 column densities on the dayside are very similar in magnitude in comparison to the present results. Moore (2011) found that O_2 column densities build up along the equator on the nightside past dawn due to strong plasma pressure-driven (retrograde) winds. As described in Section 7.1.2 and Section 7.2.1, the winds in the current simulations are driven the opposite direction (prograde). In the current work,

there is an O_2 build-up along the equator on the nightside but it is likely due to the increased SO_2 along the equator due to the high Γ_F of the SO_2 frosts and not to global winds. In current work, there is a strong north-south pressure gradient due to the very cold poles (~60 K) compared to the uniform 90 K on the nightside used by Moore (2011); however, the O_2 build up at the poles is similar in magnitude to that seen by Moore (2011) who found polar column densities of ~1.0–2.0×10^{14} cm^{-2}. Lastly, the O_2 column densities computed here are have a very different morphology than those in Moore (2011). He found high equatorial column densities on the nightside with a further enhancement near dusk where O_2 built-up. In the current work, cyclonic winds on the nightside cause O_2 to build-up at mid-latitudes near the anti-solar point.

The peak dayside O column density in the simulations of Moore (2011) is similar in magnitude to the current work when accounting for the 115 K peak T_F. O column densities are significantly lower at mid-latitudes on the nightside in the work of Moore (2011) because O_2 is forced along the equator through the nightside toward dusk by retrograde pressure-driven winds. Moore (2011) finds these winds produce a "finger" of higher O column density along the equator protruding through dawn onto the nightside which is not seen here. In the current work, O builds up at mid-latitudes on the nightside near the anti-solar point due to O_2 cyclonic winds (see Section 7.2.2) and subsequent dissociation of O_2.

O and S column densities of Moore (2011) track the current simulations over the majority of the dayside when scaling for the lower peak T_F since the same set of reaction rates and reaction cross-sections are used. As stated previously, the present simulations do not show a column density enhancement past dawn due to the plasma pressure-driven winds on the nightside, and instead the column densities of O and S are higher on the nightside because of the higher T_F and hence thicker SO_2 gas target for ion dissociation. In both simulations, S is present in the smallest gas fraction. The primary differences in morphology occur on the nightside where T_F cools more

slowly due to the relatively high thermal inertia used in the current work. In Moore (2011), the S column densities on the nightside fall to ~10^{12} cm^{-2} which is nearly an order of magnitude below those in the current work.

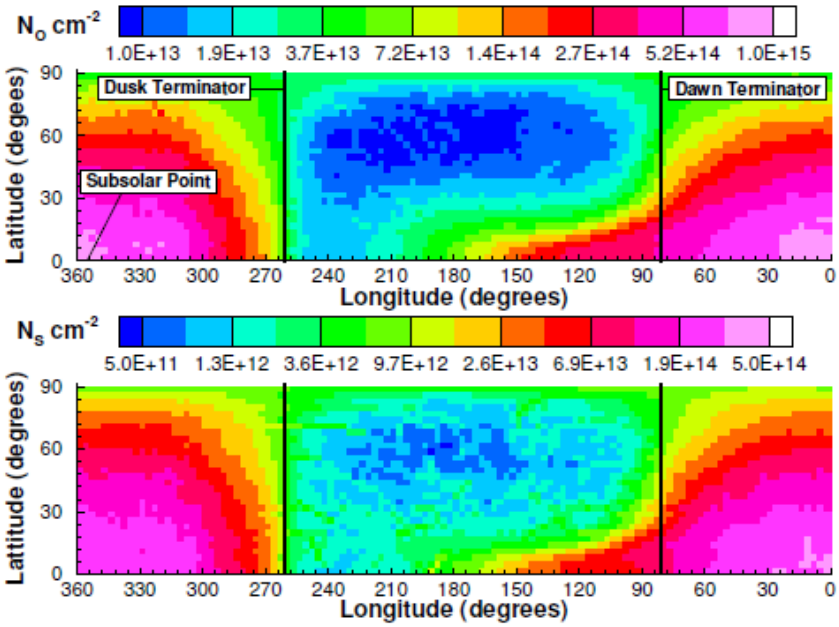

Figure 7.14 : Color contours of column density for O (top) and S (bottom) as function of latitude and longitude for the northern hemisphere. Note the different scale for each species. (*From Moore (2011)*).

7.1.8 Comparison to Wong and Smyth (2000)

Wong and Smyth (2000) used a peak T_F of 120 K and a nightside T_F of 80 K with a $\cos^{3/4}(\theta)$ dependence. They investigated the interaction between the Jovian plasma torus and Io's atmosphere at western and eastern elongation (e.g. Io's dayside atmosphere directly facing the oncoming plasma flow or facing away from the plasma flow, respectively). The case of eastern elongation is compared to because the geometry is closer to the case examined here (just prior to eclipse) than western elongation because of the large thermal lag of the SO_2 surface frosts.

Wong and Smyth (2000) found high peak SO_2 column densities of ~4×10^{17} cm^{-2} (see Figure 7.15) which is slightly higher than the VPE column density

at 120 K of 3.7×10^{17} cm^{-2} but is similar to the SO_2 column density found here (see Figure 7.3 and Figure 7.16a) when scaling for the different peak T_F (118.5 K). They also found that SO_2 was the dominant dayside species over nearly the entire dayside atmosphere and that at high noon SO_2 composed over 95% of the atmosphere which is similar to the current work (see Figure 7.16b). In both their work and the current work, the daughter species of SO_2 constitute less than 10% of the bulk dayside atmosphere.

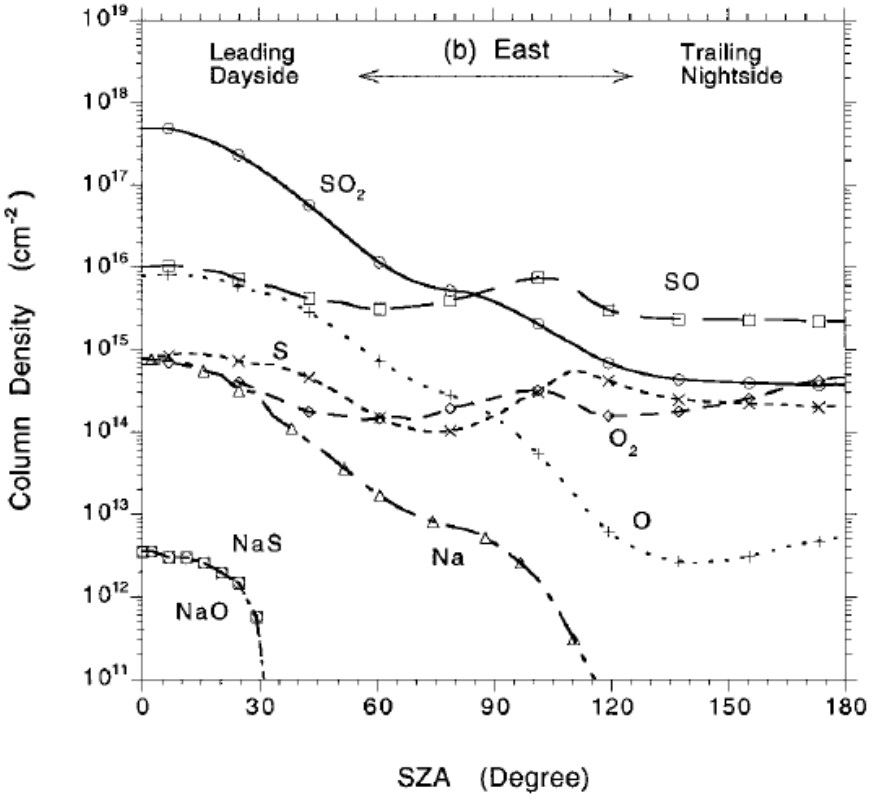

Figure 7.15: Equatorial column densities of atmospheric species as a function of solar zenith angle for the case of eastern elongation. (*From Wong and Smyth (2000), courtesy of Elsevier*).

Near the terminator (along the equator at a solar zenith angle of 90°), they found that the SO_2 column density had dropped to ~5×10^{15} cm^{-2} which is 2 times higher than the present work when choosing to compare to the dusk terminator

(compare Figure 7.15 and Figure 7.16a). In their simulations, SO and SO_2 were the dominant species (with comparable gas fractions of ~45%) while the other species constituted approximately 10% of the atmosphere. This differs from the current work where SO_2 is still the dominant species (~70%) near the dusk terminator but SO is present with a gas fraction of only ~8–10% (see Figure 7.16b). The large variation in the gas fraction of SO is likely due to the different treatments of SO. Wong and Smyth (2000) treated SO as fully non-condensable whereas it is only 50% non-condensable in the current work. Their SO gas fraction would likely reduce to ~20–25% if treated as partially non-condensable and the different surface temperature distribution is likely responsible for the rest of the discrepancy at the terminator. In the current work, the O gas fraction is roughly 5%, and S and O_2 are have the smallest gas fractions at <3% (see Figure 7.16b). The O, S, and O_2 gas fractions agree (~3–5% in the current work, and ~3% in Wong and Smyth (2000)).

Continuing onto the nightside, they find that SO_2 column density at midnight has dropped to ~3×10^{14} cm^{-2} compared to ~6×10^{15} cm^{-2} in the present work (compare Figure 7.15 and Figure 7.16a). They find that SO is the dominant nightside species with a column density of ~2×10^{15} cm^{-2} and O_2 is present at a slightly higher column density (~4×10^{14} cm^{-2}) than SO_2. The higher column densities in the present work at midnight are likely due to the higher T_F from the high Γ_F and also due to sputtering of SO_2 surface frosts (which was not included in the work of Wong and Smyth (2000)). The column density enhancement near the antisolar point is due to transport of mass. Their much higher SO gas fraction (~65% compared ~18–20% in the current work) at midnight is due to their modeling of SO as 100% non-condensable. Also, the gas fraction of SO is suppressed in the current work because of the slowly cooling T_F and hence relatively thicker SO_2 atmosphere present on the nightside. The drastic difference in the O gas fraction at midnight is due to the lack of an ion dissociation reaction ($O_2 + O \rightarrow 3O$; see Table 3.8) in the simulations of Wong and Smyth (2000).

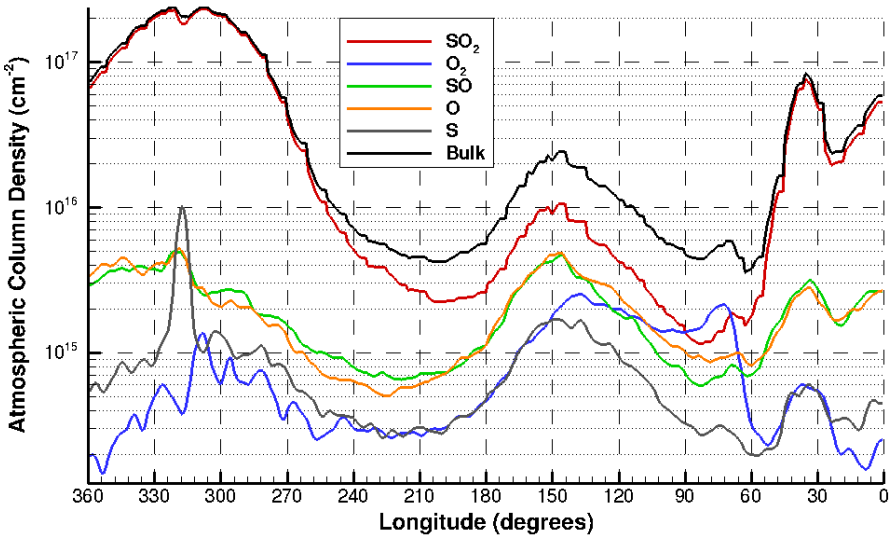

(a)

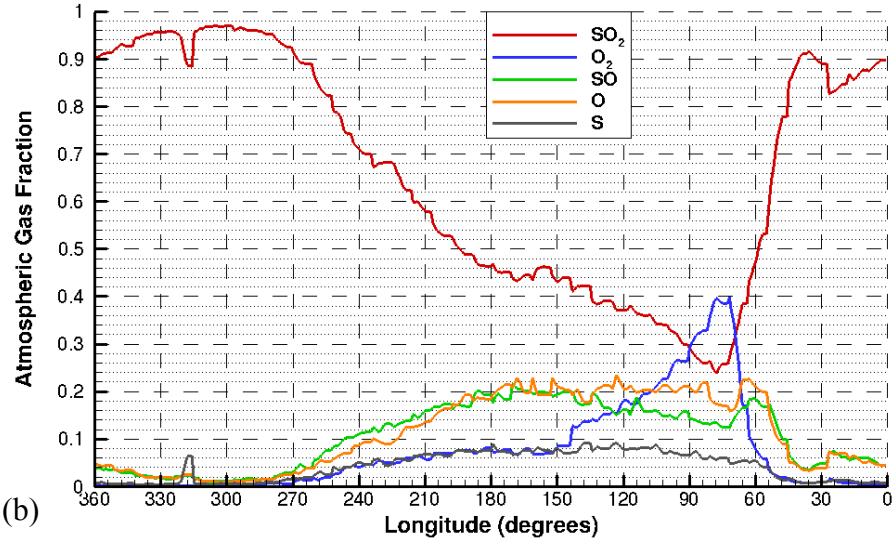

(b)

Figure 7.16: Equatorial (a) column densities and (b) gas fraction for SO_2, O_2, SO, O, and S species at a subsolar longitude of 342° W.

Photo-dissociation of O_2 is very slow. In the current work, O_2 is primarily destroyed by ion dissociation which increases the O gas fraction since O_2 is the dominant species over most of the nightside. S column densities are comparable between the current work and the Wong and Smyth (2000) simulations.

7.1.9 Comparison to Observations

Feaga *et al*. (2006) analyzed HST/STIS observations of Io near western elongation (285°–305° W). They used the S I λ1479 dipole allowed and forbidden transition multiplets to constrain the column density of S in Io's atmosphere. They found a tangential column density near the limb between 3.6×10^{12} cm^{-2} and 1.7×10^{13} cm^{-2}. These observations are much lower than the S column densities in the current work ($0.1–4.0\times10^{15}$ cm^{-2}); however, the current simulations are performed at a different subsolar longitude (342° W).

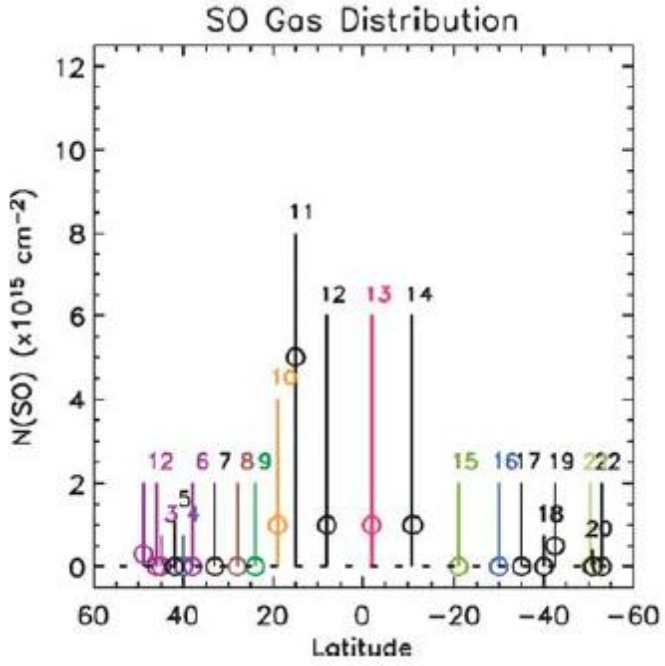

Figure 7.17: SO gas dayside column density as a function of latitude on the anti-Jovian hemisphere. Note that data were not taken at the same longitude but at nearly a 45° angle across the dayside atmosphere (see Figure 2 in Jessup *et al*. (2004)). (*From Jessup et al. (2004), courtesy of Elsevier*).

Jessup *et al*. (2004) used HST/STIS to measure the SO dayside column density on the anti-Jovian hemisphere. The column densities peak at 5.0×10^{15} cm^{-2} but this appears to be an outlier due possibly to a volcanic source and the average SO low latitude column densities are roughly 1.0×10^{15} cm^{-2} (see Figure 7.17). In the

current work, the SO dayside column densities at low latitudes are ~5.0×10^{15} cm^{-2} (see Figure 7.9 and Figure 7.16a) which are 5 times higher than most of those observed by Jessup *et al*. (2004).

Moullet *et al*. (2010) obtained disk-resolved observations with the Submillimeter Array (SMA) at 345 GHz of atmospheric rotational lines for SO_2, SO, and NaCl. They fit data with hydrostatic atmospheres including volcanic sources and found that SO can be primarily explained as being produced by photo-dissociation of SO_2. The mixing ratio (or gas fraction) of SO was ~10% which yields disk-averaged SO gas column densities ranging between 0.5–1.0×10^{15} cm^{-2} which is within a factor of 2–4 of the current simulations that yield disk-averaged column densities of 2.0–3.0×10^{15} cm^{-2}.

7.2 GLOBAL WINDS

In the results of Chapter 4 and 6, global winds were driven purely by the day-to-night pressure gradient caused by the variation in T_F. With the inclusion of a particle description of the plasma, high energy ions from the Jovian plasma torus can transfer momentum to the neutral atmosphere. Depending on the relative orientation of the subsolar point and sub-plasma point, the plasma pressure will sometimes resist the day-to-night pressure gradient while reinforcing it at other times. For the geometry explored here (just prior to entering eclipse), the peak T_F is ~40° away from the sub-plasma point. In the sections that follow, the global wind patterns of the SO_2 atmosphere as well as each of the daughter species will be investigated and compared to each other. Results will also be compared to the previous simulations of Moore (2011) and the IRAM observations of Moullet *et al*. (2008).

7.2.1 SO_2 WINDS

SO_2 winds develop on the dayside due to the combined effect of the day-to-night pressure gradient and the plasma pressure. In the previous results of Chapter 4 and 6, the winds were driven only to the day-to-night pressure gradient and SO_2 was the only species present. The day-to-night pressure gradient (see Chapter 6) forces

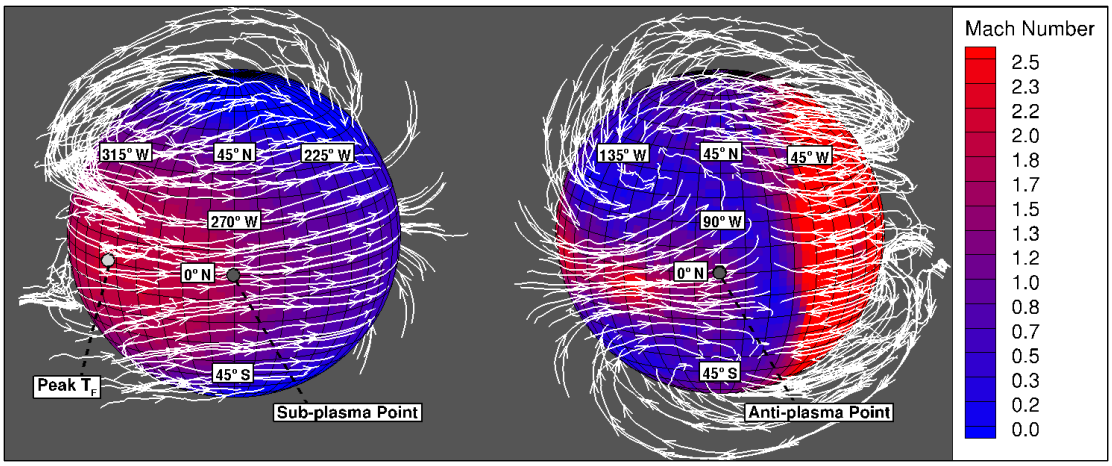

Figure 7.18: SO_2 streamtraces overlaid on contours of Mach number at an altitude of 10 km for the (left) leading hemisphere and (right) trailing hemisphere.

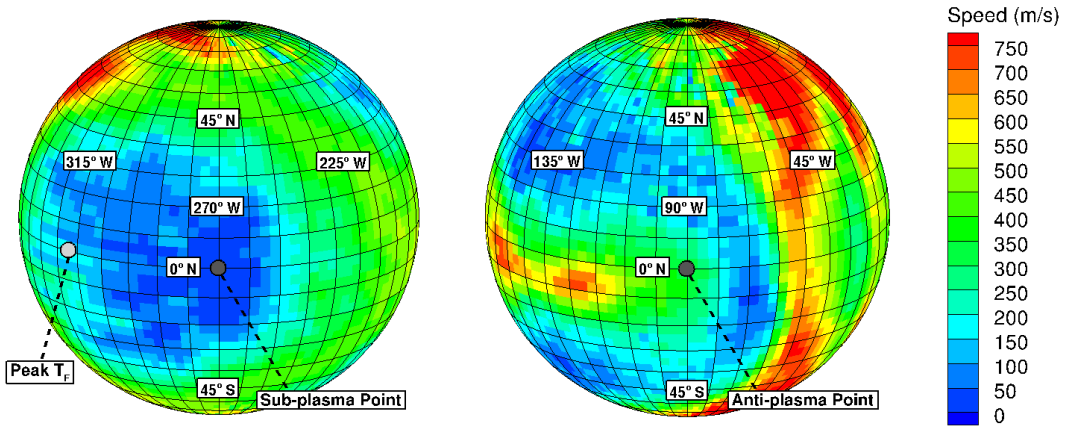

Figure 7.19: Speed of the SO_2 winds at an altitude of 10 km for the (left) leading hemisphere and (right) trailing hemisphere.

winds in all directions toward the nightside. In Figure 7.18, the streamtraces are forced preferentially eastward across the leading hemisphere because the day-to-night

pressure gradient is driving winds eastward at the sub-plasma point. East of the sub-plasma point, the circumplanetary winds are reinforced by the plasma pressure. Although the winds travel a much larger distance toward the dusk terminator from the peak T_F, the winds traveling toward dawn reach much higher Mach numbers because of the larger pressure gradient. Note that the Mach number is that of only the SO_2. At 10 km altitude, the equatorial Mach number is 0.95–1.0 near the dusk terminator and 2.2–2.4 near the dawn terminator (see Figure 7.18). Since the translational temperature is changing, the Mach number does not directly reflect the speed of the flow. At 10 km altitude, the speed of the SO_2 gas is ~250 m/s near the dusk terminator and ~550 m/s near the dawn terminator (see Figure 7.19). Past the dusk terminator, the plasma pressure continues to accelerate the SO_2 winds and the Mach number climbs to 1.55–1.65 with corresponding speeds of ~450 m/s. The asymmetry between dawn and dusk is caused by the same phenomenon that was discussed in Section 6.2. T_F is coldest just before dawn and therefore the column densities tend to be the lowest there because all species except O_2 are at least partially non-condensable. The low column densities just prior to dawn create a larger pressure gradient in the westward direction from the peak pressure region than in the eastward direction where the high thermal inertia of the SO_2 frost causes T_F to cool slowly. The strong westward winds condense just on the nightside of the dawn terminator as gas condenses onto the surface. Near the equator just prior to dawn, the westward winds meet the eastward winds that have traveled ~3/4 around Io (see Figure 7.18). Near midnight, the eastward equatorial winds continue to be accelerated by the pressure gradient from the slowly cooling T_F and the Mach number is ~1.0–1.2 with high velocities 550–700 m/s (see Figure 7.18 and Figure 7.19). The Mach number is lower despite the high velocities due to the high translational temperature (800–1000 K) of the SO_2 gas.

North/south winds also develop from above the peak T_F and are pushed northwest by the plasma pressure but then curve northeast as the day-to-night pressure gradient becomes the larger force near the poles. These winds that pass over the poles will condense out on the cold nightside near the poles and at mid-latitudes or some gas may be entrained by the high speed equatorial eastward winds that developed on the nightside and continue until near the dawn terminator. At 10 km altitude, the north/south SO_2 winds at mid-latitudes on the dayside reach Mach numbers of 1.2–1.4 and speeds of ~300 m/s. Near the poles, the SO_2 wind Mach numbers have decreased to 0.8 – 1.0 but the winds have accelerated to ~650-750 m/s (see Figure 7.18 and Figure 7.19). Again, the lower Mach numbers near the poles are due to the thin plasma heated atmosphere that reaches temperatures of 1600–2000 K. As discussed in Chapter 6, streamtraces can be deceiving in rarefied flows and therefore it is important to compare the mean free path to the radius of curvature of the streamlines. If the nightside atmosphere is significantly rarefied then the apparent entrainment of the north/south flows on the nightside by the strong eastward winds could be the superposition of two free molecular flows. The mean free path of the bulk atmosphere on the nightside is much smaller than for the results of Chapter 4 or 6 because of the build-up of non-condensable species and sputtering from SO_2 surface frosts. At 10 km altitude, the density of the bulk atmosphere near the poles is ~6×10^{13} m^{-3} and the hard sphere mean free path is ~7 km which is much smaller than the radius of curvature (~100 km) of the streamlines shown in Figure 7.18. On the nightside, a shear layer develops between the strong equatorial eastward winds and the sputtered and non-condensable atmosphere at mid-latitudes. This generates vorticity on the nightside which is especially apparent in the large cyclones created by non-condensable O_2 (see Section 7.2.2).

7.2.2 O_2 WINDS

O_2 winds have the same general pattern as SO_2 winds on the leading hemisphere as expected since the atmosphere is collisional and therefore there is little to no velocity slip between the different species. The strong SO_2 winds from the leading hemisphere to the trailing hemisphere drag the O_2 along. Similar to the SO_2 winds, the westward O_2 winds are much stronger than the eastward O_2 winds. At 10 km altitude, the O_2 winds Mach number is 0.95–1.0 with speeds of ~250 m/s near the dusk terminator (see Figure 7.20 and Figure 7.21). These values are similar to those for SO_2 discussed in the previous section. At 10 km altitude near the dusk terminator, the O_2 winds reach higher Mach numbers of 1.8–2.2 and speeds of 600–650 m/s (see Figure 7.20 and Figure 7.21). The key differences between the SO_2 and O_2 winds occur on the nightside where SO_2 condenses on the surface whereas O_2 builds up and is only destroyed by ion dissociation reactions. Eastward and westward O_2 winds meet at the dawn terminator and a stagnation flow develops that forces winds north and south. As these north/south winds travel toward the poles they are pushed back toward the nightside by the combined force from the plasma pressure and the day-to-night pressure gradient. Furthermore, the same shear layer that developed between SO_2 gas at mid-latitudes and the strong equatorial eastward winds creates large O_2 cyclones in the northern and southern hemispheres (see Figure 7.20). The O_2 wind speeds in these cyclones are much lower than the strong eastward equatorial wind that stretches throughout the nightside. O_2 wind speeds near the edge of the cyclone are ~80–100 m/s and reduce to 25–50 m/s near the center (see Figure 7.21). The O_2 Mach number similarly drops to low values (0.1–0.25) inside the cyclones (see Figure 7.20). The same cyclonic winds are not visible in the SO_2

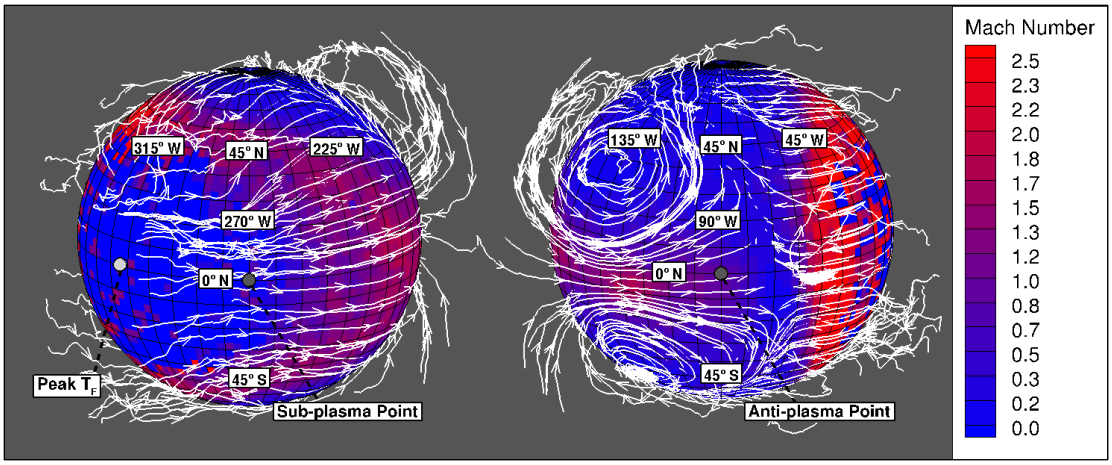

Figure 7.20: O_2 streamtraces overlaid on contours of Mach number at an altitude of 10 km for the (left) leading hemisphere and (right) trailing hemisphere.

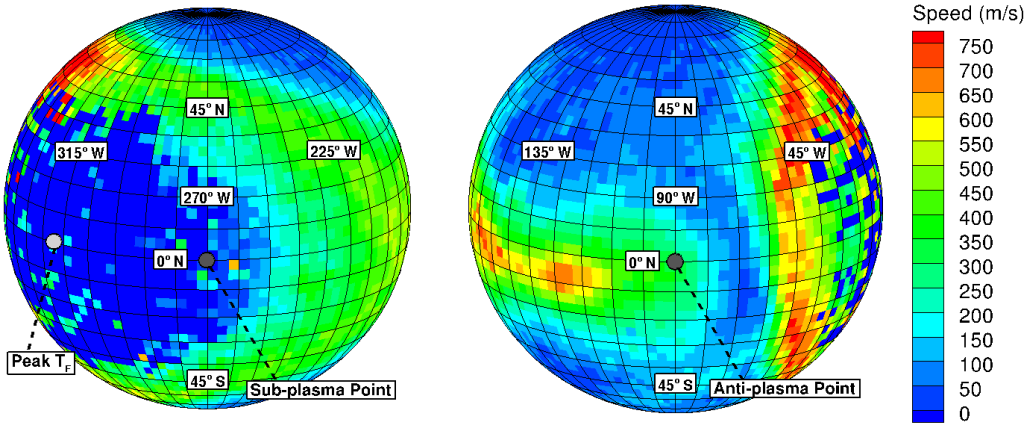

Figure 7.21: Speed of the O_2 winds at an altitude of 10 km for the (left) leading hemisphere and (right) trailing hemisphere.

winds because SO_2 condenses out on the nightside. These cyclones are believed to be real (e.g. not a due to the superposition of free molecular flows) since O_2 builds up along the western edge of the cyclone. This lag in the peak density ($\sim 7.5\times10^{14}$ m^{-3}) compared to the center of the cyclone is likely due differing timescales of the equilibration of the cyclone and Io's rotation rate. Also, the radius curvature of the streamlines is larger than the mean free path inside the cyclone. At 10 km altitude, the O_2 density near the edge of the cyclone is $\sim 1\times10^{14}$ m^{-3} with a mean free path of ~4.3 km which is much smaller than the curvature of the of the streamlines at the

outer edge of the cyclone (>1500 km). These large counter-rotating cyclones in the northern and southern hemispheres would, however, be difficult to observe since they would occur on the nightside away from the limb.

7.2.3O, SO, AND S WINDS

For completeness, the global wind patterns for the three other daughter species of SO_2 (O, SO, and S) are shown. All show similar wind patterns on both the dayside and nightside. This is expected since the winds are collisional on the dayside (with a bulk gas mean free path between 1 m to 5 km at altitudes < 10 km) and therefore there is little to no slip between the species. As is the case for SO_2 and O_2, the species Mach number at 10 km altitude for O winds near the dusk terminator peaks at ~0.9 with speeds of ~300 m/s (see Figure 7.22a and Figure 7.23a). Near the dawn terminator, the equatorial Mach number peaks at ~1.5–1.6 with velocities of ~600–650 m/s. S and SO wind speeds and Mach numbers have similar magnitudes for the dusk and dawn terminator at 10 km altitude (see Figure 7.22a and Figure 7.23a).

O, SO, and S are carried by the strong SO_2 winds that develop on the dayside and flow toward to the nightside. On the nightside, the winds are still partially collisional due to the increased column densities from sputtering and dynamic mass transport. O streamtraces show the most resemblance to O_2 because it is primarily created by dissociation of O_2 on the nightside. The large cyclones seen in the O_2 streamtraces can be partially seen in the O streamtraces. SO is partially non-condensable and also shows vorticity on the nightside. S streamtraces are most similar to SO_2 streamtraces.

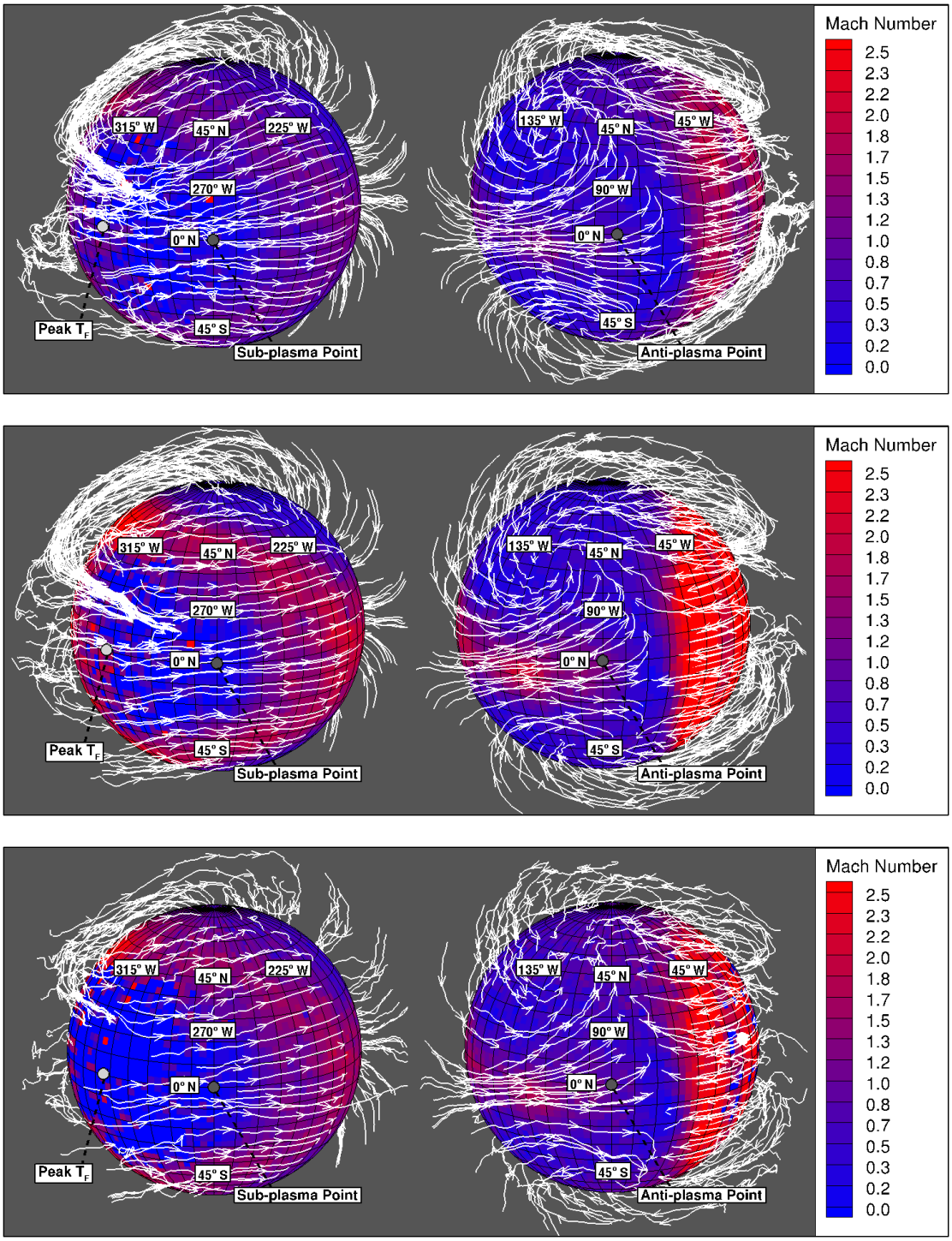

Figure 7.22: O (top), SO (middle), and S (bottom) streamtraces overlaid on contours of Mach number at an altitude of 10 km for the (left) leading hemisphere and (right) trailing hemisphere.

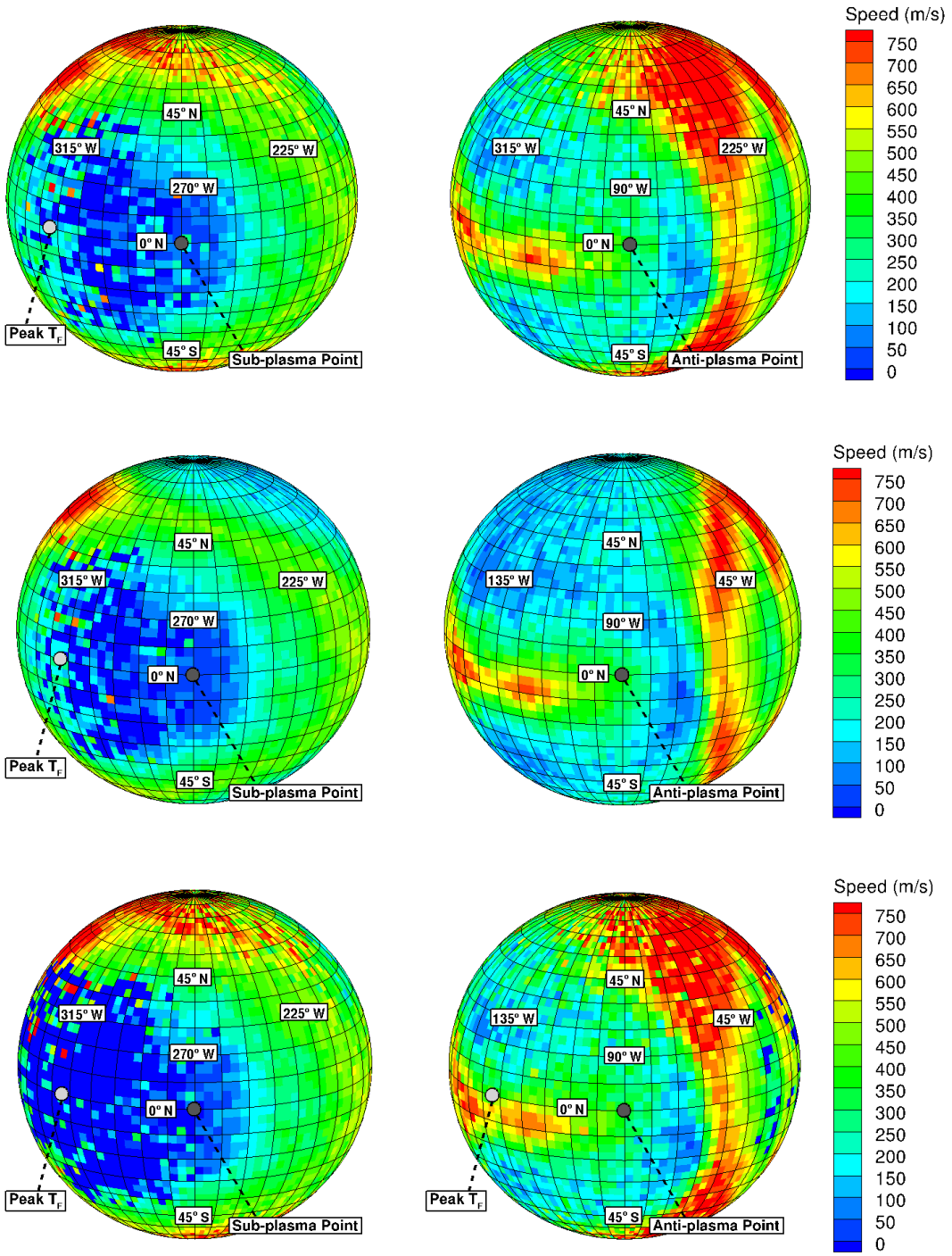

Figure 7.23: O (top), SO (middle), and S (bottom) wind speeds at an altitude of 10 km for the (left) leading hemisphere and (right) trailing hemisphere.

7.2.4 COMPARISON OF WINDS

Moore (2011) found that the plasma pressure significantly resisted the eastward winds created by the day-to-night pressure gradient. In the other direction, westward winds (created by the day-to-night pressure gradient) were reinforced by the plasma pressure and continued throughout the nightside until they reached the dusk terminator where they met weak westward winds and condensed. The wind patterns in the current work differ significantly from those found by Moore (2011) due to the high thermal inertia of the SO_2 frosts (in the current work) that cause the thickest area of the atmosphere to lag the subsolar point by ~33° as compared to the radiative equilibrium thermal model used by Moore (2011). The eastward winds are reinforced by the plasma pressure and continue on through the nightside in the opposite direction to that found in Moore (2011). The winds on the nightside are in the opposite direction because the atmosphere is much thicker past dusk in the current work and therefore the gas does not condense out as quickly.

Moore (2011) found similar O_2 wind patterns on the nightside despite very different underlying SO_2 frost temperatures. In his results, O_2 did create a cyclone near the antisolar point but O_2 column densities did not increase near the center of the cyclone; instead, they were high along the equator throughout the entire nightside. O_2 winds flowed preferentially from dawn toward dusk where the O_2 built up and was stripped off by the plasma. In the current simulations, O_2 does build-up along the equator but is also elevated in the region of the cyclone. Lastly, Moore (2011) found O wind patterns tracked SO_2 wind patterns. We find the same but both the O and SO_2 winds in the current work are in the opposite direction (prograde) on the nightside due to the differing thermal model.

Moullet *et al*. (2008) analyzed millimeter range observations and inferred prograde super-rotating circumplanetary winds (~330 m/s) were needed to fit the

Doppler shifts of the observations at eastern elongation. The subsolar longitude is 90° W at eastern elongation whereas the subsolar longitude is 342° W in the simulations presented in this chapter. In the current simulations, prograde winds do develop over ~3/4 of Io but because the simulations are not performed at eastern elongation, the current results the effect of the plasma at eastern elongation can only be extrapolated. At eastern elongation, the sub-plasma point and subsolar point are antipodal. The peak T_F for this case would occur at ~60° W but the plasma pressure would still resist circumplanetary winds that develop due the day-to-night pressure gradient all along the terminator. It is clear from the simulations that the plasma pressure can have a significant effect on the circumplanetary winds and therefore it is possible that the plasma pressure could overcome the day-to-night pressure gradient on the morning portion of the dayside atmosphere and lead to the observations of the super-rotating prograde winds. Furthermore, volcanic outflow could enhance the situation if the volcano was very near the limb as suggested by Moullet *et al*. (2008).

CHAPTER 8: SUMMARY AND CONCLUSIONS

8.1 INITIAL GLOBAL 3D MODELING OF IO'S ATMOSPHERE

In the first set of global atmospheric simulations, the DSMC method is used to simulate the rarefied gas dynamics on Io. These simulations have improved on the previous work on circumplanetary flow by Austin and Goldstein (2000) by including inhomogeneous frost coverage, three-dimensionality, and a rotating temperature distribution which includes the effects of an integrated thermal inertia. Our model also properly accounts for the rarefied conditions present in much of Io's atmosphere unlike the previous continuum models (Ingersoll *et al.*, 1985; Moreno *et al.*, 1991; Wong and Johnson, 1995; Wong and Johnson, 2000; Smyth and Wong, 2004). Many of our results are in agreement with earlier work, but we have also attempted to reconcile our findings with the following observations: surface temperature (Rathbun *et al.*, 2004), frost fraction (Douté *et al.*, 2001), column density of the atmosphere (Feaga *et al.*, 2009), and mid-IR observations of the ν_2 vibrational band of SO_2 (Spencer *et al*., 2005).

We find that the pressure gradient from the warm dayside to the cold nightside is strong enough to drive the flow supersonic with both T_{ss} = 115 K and 120 K and with a nightside temperature of 90 K. The flow diverges in all directions away from the region of peak T_F and forms a region of supersonic flow near the terminator for all cases. The influence of the residence time was investigated by comparing a SRT model that treats the non-frost surface as being coated by a thin layer of SO_2 (Sandford and Allamandola, 1993) to a LRT model. The SRT model creates a rapid outflux of SO_2 molecules at the dawn terminator that we refer to as the

DAE. The LRT model simulates slower effective desorption rates due to the possibility of multiple bounces within a very porous surface (Matson and Nash, 1983). This model is preferred because it gives a better match to the longitudinal asymmetries in band depth detected in mid-IR observations (Spencer *et al*., 2005; Gratiy *et al*., 2009). The magnitude of the Mach number around the terminator varies due to the asymmetric surface temperature distribution for the SRT model and the DAE. The LRT model exhibits further variations due to the inhomogeneous surface frost. The rotating temperature distribution had significant effects on the structure of the atmosphere. The peak T_F lags the subsolar point by ~32º because of the modeled high thermal inertia of the frost. Therefore, the column density generally lagged the subsolar point by the same amount with minor differences due to the frost map. Such a large lag in T_F is not observed in Lyman-α (Feaga *et al.*, 2009) nor in IR observations (Rathbun *et al.*, 2004), but the high thermal inertia in our model is required to match the nightside cooling rate of the brightness temperature observed by Rathbun *et al.* (2004). The simulations of Chapter 6 resolve these discrepancies by using a more sophisticated thermal model.

By altering the amount of sublimation from the surface based on a non-uniform frost map (Douté *et al.*, 2001) and using a temperature distribution similar to observations (Rathbun *et al.*, 2004), we achieved good agreement with the magnitudes of the column densities observed in the Lyman-α (Feaga *et al.*, 2009). We were, however, unable to reconcile the latitudinal column density morphology inferred from the Lyman-α observations (Feaga *et al.*, 2009). The steep drop in the inferred column near ±45º latitude from Lyman-α observations remained unresolved but could be due to several phenomena discussed in Section 4.4 and 4.5.

8.2 PARAMETRIC STUDY OF THERMOPHYSICAL PROPERTIES

The disagreement between the simulation results of Chapter 4 and observations appeared to be due to the thermal model. Therefore, a parametric study is performed to constrain the thermophysical parameters of Io's surface. A more sophisticated thermal model is used to generate the thermal distributions that were compared to observational data (Jessup *et al*., 2004; Rathbun *et al*., 2004) in order to find the best fit thermophysical parameters via a least-squares error method. The thermal model solves the one-dimensional heat conduction equation with depth into Io's surface and includes the effects of thermal inertia, latent heat of sublimation and condensation, eclipse by Jupiter, and the contribution of radiation from Jupiter. The thermal model solves the heat conduction equation for two separate surface components: SO_2 frosts and non-frost (likely pyroclastic dusts and/or sulfur allotropes). A brute force search through the thermophysical parameters (albedo and thermal inertia) is performed and the resulting simulated SO_2 surface frost temperature distribution is compared to the inferred frost temperatures of Jessup *et al*. (2004) assuming vapor pressure equilibrium. Because the assumption of vapor pressure equilibrium does not hold globally, a VPE correction factor is applied to account for non-equilibrium. The best fit thermophysical parameters for the SO_2 surface frost were found to be $\alpha_F \approx 0.55$ and $\Gamma_F \approx 200$ J m^{-2} K^{-1} s$^{-1/2}$. With the best fit frost thermophysical parameters fixed, the non-frost thermal inertia is varied (α_{NF} was constrained by the mean albedo and mean frost fraction) and the resulting temperature distributions are compared to Galileo PPR observations of the surface brightness temperature (Rathbun *et al*., 2004). Again utilizing the least squares error method, the best fit non-frost thermophysical parameters are found to be $\alpha_{NF} \approx 0.49$ and $\Gamma_{NF} \approx 20$ J m^{-2} K^{-1} s$^{-1/2}$. These thermophysical parameters can help interpret the state of the two surface components. The high Γ_F indicates that the SO_2 surface frosts have

likely annealed due to the temperature variation between day and night (Sandford and Allamandola, 1994). Meanwhile, the low Γ_{NF} indicates that the non-frost surface is likely highly porous and composed of fine grained particulates.

8.3 DSMC Simulations Utilizing Best Fit Thermophysical Parameters

After constraining the thermophysical parameters, they were used to generate the solid surface boundary condition in more refined DSMC atmospheric simulations. The atmospheric simulations focused on the effect of eclipse on the atmospheric winds, temperatures, and densities. Results presented span approximately 6 hours of Io's 42 hour orbit with eclipse occurring near the middle of the simulated time. We found that eclipse causes significant variations in the atmospheric morphology of the sub-Jovian hemisphere.

The SO_2 surface frosts have a high thermal inertia leading to a ~5 K drop in T_F during eclipse; however, this corresponds to a factor of 20 decrease in column density due to the exponential dependence of the SO_2 vapor pressure on T_F. The dayside atmosphere on the sub-Jovian hemisphere becomes thin enough during eclipse that plasma is able to reach to the surface thereby changing the vertical thermal structure. Supersonic circumplanetary flow exists prior to eclipse but becomes subsonic during eclipse because the day-to-night pressure gradient weakens considerably as the surface cools and atmosphere condenses. Before eclipse, an oblique shock exists near the dawn terminator where the supersonic flow condenses on and near the cold nightside. During eclipse, the oblique shock disappears as the day-to-night pressure gradient weakens. The thermal model predicts a prograde rotation of the atmosphere during eclipse (as opposed to the retrograde rotation that exists outside of eclipse) due to the differing amounts of insolation absorbed by the surface due to eclipse. After egress from eclipse, both the SO_2 surface frost and non-frost surface warm (but at

different rates based on their respective thermophysical parameters). The atmosphere begins to recover from eclipse and slowly converges to the pre-eclipse quasi-steady state. The timescale for recovery of the surface temperature distribution to the pre-eclipse quasi-steady state is primarily controlled by the thermal parameter, θ, defined in Section 5.3 (Spencer *et al*., 1989). This "thermal parameter" was calculated to be $\theta_F \approx 14.9$ with the best fit thermophysical parameters. The circumplanetary winds respond over a different timescale (~2 hours) controlled by the speed of sound. Because an excess of SO_2 gas condenses on the cold non-frost surface during eclipse, the post-eclipse DAE becomes comparable in pressure to the peak pressure region (~30° east of the subsolar point). The pressure gradients away from these two high pressure regions drive opposing flows which meet and form a stagnation point flow.

Lastly, the DSMC simulated atmospheres of sub-Jovian and anti-Jovian hemispheres are compared. Eclipse is found to at least partially account for the asymmetry observed in the Lyman-α (Feaga *et al*., 2009). A composite "average dayside atmosphere" is created by simulating an entire Io orbit in the absence of molecular collisions and then averaging the atmosphere at 40 equal intervals throughout the orbit. There is a clear decrease in the sub-Jovian hemispheric column density although the simulation finds much smoother contours than the Lyman-α observations. The differences could be due to interaction of SO_2 gas with the non-frost surface which tends to smooth SO_2 column densities over inhomogeneous frosts or the absence of volcanic plumes in our simulations.

8.4 DSMC Simulations Utilizing a Sophisticated Surface Model and a Particle Description of the Plasma

The interaction between the Jovian plasma torus and Io's neutral atmosphere was simulated using a moderately sophisticated surface thermal model and a particle description of the plasma which allows for momentum transfer from the plasma to the

neutral atmosphere. The energetic ions from the plasma torus create a source for the daughter species of SO_2 through dissociation. Photo-chemistry is also included as a source for SO_2 daughter species. Io's atmosphere was investigated at a subsolar longitude of ~342° W.

On the dayside, SO_2 is found to be the dominant species (>90%) which is in agreement with previous simulations and observations of Io's atmosphere (Jessup *et al*., 2004; Moore (2011); Wong and Smyth (2000)). SO_2 column densities are enhanced over most of the nightside compared to previous simulations by sputtering of SO_2 surface frosts. SO_2 remains the dominant species on the nightside at low to mid-latitudes prior to midnight where T_F is still fairly warm (>104 K). It is no longer the dominant atmospheric species only in regions just prior to dawn and near the poles. In these regions, O_2 becomes the dominant species because it is non-condensable but is a minor species (<5%) over much of the dayside. Column densities of O and SO are very similar in morphology throughout Io's atmosphere because they are created in tandem through ion and photo-dissociation reactions of SO_2. S gas is present in the smallest quantities of all the SO_2 daughter species but its column densities in the simulation are nearly two orders of magnitude higher than the constraints calculated by Feaga *et al*. (2009). SO column densities are in closer agreement to observations (Jessup *et al*., 2004; Moullet *et al*., 2008) and differ from the observations by a factor of ~3–5.

The plasma pressure is found to be comparable to the day-to-night pressure gradient and causes large scale changes in the global wind patterns compared to the results of Chapter 4 and 6. For the subsolar longitude simulated (342° W), the plasma pressure primarily reinforces the day-to-night pressure gradient. Similar to the results of Chapter 6, the westward winds toward dawn reach much higher Mach numbers and wind speeds than the eastward winds. This is because the day-to-night pressure gradient is enhanced by the cold T_F present just prior to dawn. The high Γ_F leads to

slowly cooling T_F and a moderately collisional atmosphere throughout most of the nightside. Eastward winds continue to be accelerated by the plasma pressure on the nightside and strong equatorial winds form that continue on until the dawn terminator where both eastward and westward winds meet. The strong equatorial eastward winds create a shear layer between the equator and the build-up of non-condensables at mid-latitudes. This leads to large cyclones in the northern and southern hemispheres that are especially evident in the O_2 streamtraces since it is non-condensable.

8.5 DISCUSSION

With sophisticated models for both the Jovian plasma torus and Io's surface temperature distribution, many previously unexplained observations of Io's atmosphere and surface can be understood. First, Galileo NIMS (Douté *et al*., 2001) observed that the sub-Jovian hemisphere of Io has a lower mean frost fraction than the anti-Jovian hemisphere. They explained the high mean frost fraction on the anti-Jovian hemisphere as being due to the concentration of volcanic plumes; however, it can also be explained by the interaction of eclipse by Jupiter and surface sputtering by energetic ions from the plasma torus. Even with a relatively high thermal inertia (200 J m^{-2} K^{-1} $s^{-1/2}$), the SO_2 frost surface temperature will drop 5 K or more corresponding to a column density decrease of a factor of 20. Moore (2011) showed that energetic ions can create a sputtered atmosphere with a column density of ~10^{15} cm^{-2}. It seems likely that during eclipse, when the atmosphere partially collapses, energetic ions will reach the surface more often (compared to the anti-Jovian hemisphere's dayside) and therefore will sputter more of the SO_2 frost, possibly denuding certain areas. Io is tidally locked and therefore only the sub-Jovian hemisphere will ever experience eclipse. The sub-Jovian hemisphere will also be preferentially sputtered (to a lesser extent) throughout its entire day, not just during eclipse. This is because eclipse decreases the diurnally averaged solar flux absorbed

by the surface, thereby decreasing the surface temperature (before *and* after eclipse). The lower surface temperature decreases the vapor pressure and the hydrostatic column density above the SO_2 frost allowing a higher number of energetic ions to strike the surface without colliding with the neutral atmosphere. Over geological timescales, this asymmetry in the surface sputtering could lead to the observed difference in the SO_2 surface frost fraction between the sub-Jovian and anti-Jovian hemispheres.

Second, an asymmetry in the column density between the anti-Jovian and sub-Jovian hemispheres has been observed in the disk-resolved Lyman-α (Strobel and Wolven, 2001; Feaga *et al*., 2009) and disk-averaged mid-infrared observations (Spencer *et al*., 2005). Again, these observations were previously explained by the correlation of volcanic plumes on the anti-Jovian hemisphere; however, the asymmetry can also be explained by eclipse by Jupiter. As stated earlier, eclipse decreases temperatures on the sub-Jovian hemisphere throughout the day (not just during eclipse). Therefore, the atmospheric column density will be lower since simulations have shown that the atmosphere is largely in vapor pressure equilibrium with SO_2 surface frosts over the majority of the dayside.

Third, the absence of polar caps (McEwen *et al*., 1988) has long been a mystery because nearly every model of Io's atmospheric dynamics has shown that day-to-night winds will develop and those winds will transport SO_2 that should condense on the cold poles. In the current work, the transport of SO_2 gas to the poles is a very slow process, with a deposition rate of only 10 nm/year. Even on geological timescales, this deposition rate would require a very long time to develop observable polar caps. Also, energetic ions preferentially sputter the poles and the sputtering rate is higher than the deposition rate. Therefore, any SO_2 gas that condenses near the pole will be rapidly sputtered away leaving the poles barren. This is in full agreement with previous statements on polar caps by Ingersoll *et al*. (1985).

8.6 FUTURE WORK

In the present work, the combined effect of the surface temperature distribution and plasma bombardment on Io's atmosphere has been investigated. This covers two of the three major mechanisms by which Io's atmosphere is thought to be supported: sublimation and sputtering from SO_2 surface frosts. The third mechanism, is the intense volcanism produced by tidal forces from the orbital resonance with Europa and Ganymede. Volcanism will produce an atmosphere local to the plume vent that will likely interact with the circumplanetary winds that exist due to the day-to-night pressure gradient. To incorporate mean free path resolved volcanic plumes into the global sublimation and sputtered atmosphere would require large scale two-way coupled parallel simulations. Such simulations would be very useful in further constraining the thermophysical parameters of the surface, comparing to column density observations (Jessup *et al*., 2004; Feaga *et al*., 2009), and for explaining observed prograde rotation of the atmosphere (Moullet *et al*., 2008).

Other important work yet to be done includes modeling the ambipolar electric field as well as enabling electron-heavy interactions. The ambipolar electric field may have important consequences for the global dynamics of Io's atmosphere. Electron-heavy interactions would tend to increase the dissociation of SO_2 and the molecular daughter species.

The final simulations presented in Chapter 7 utilized the MD/QCT cross-sections for heavy-heavy reactions computed by collaborators at Penn State; however, photo-chemistry routines currently use experimental reaction rates rather than MD/QCT cross-sections. MD/QCT computations of photo-dissociation of SO_2 and its daughter species would particularly shed light on the post-dissociation internal energy state of the products.

Current simulations all neglected the Coriolis force; however, when momentum transfer from the plasma to the neutral atmosphere is included, the length scale of the circumplanetary winds becomes very large (~8500 km). The Rossby number which characterizes the ratio of the inertial to Coriolis forces is $O(1)$ (see Section 3.1) and therefore Coriolis forces become important over such long length scales. Future simulations should include the Coriolis acceleration on particles in the atmosphere.

Further extending the surface temperature model to include the effects of porosity may have important effects on the non-frost which is expected to be quite porous. Kerton *et al*. (1996) included a solid state greenhouse effect in the frost and found that surface temperatures were decreased by up to 5 K by allowing sunlight to penetrate some depth into the surface. Porosity will also affect the residence time of molecules stuck on/in the non-frost surface. Although the residence time model already attempts to take into account the porosity with a factor of one thousand increase in the residence time, this factor should be parametrically varied or, if possible, analytically determined based on some assumptions about the size of pores in the surface.

The updated thermal model included in the simulation results of Chapter 6 and 7 did not reduce the thermal lag between the subsolar point and peak T_F as expected; it remained ~30°. Such an east/west asymmetry due to the thermal lag is not observed in the Lyman-α observations. Possibly, the thermal model could be extended to be inhomogeneous with depth. This might allow for there to be little thermal lag between the peak T_F and subsolar point but still retain the small diurnal variation that observations appear to suggest.

Currently, the simulations use frost fraction maps from Galileo NIMS (Douté *et al*., 2001); however, they lack data at high latitudes and for ~1/6th of all longitudes. Ground-based observations with Keck AO (Laver and de Pater, 2008; 2009) have

given more data on the frost coverage on Io's surface but these observations lack resolution and spatial coverage of the Galileo NIMS observations (Douté *et al*., 2001). If the global frost fraction of Io's surface is mapped using ground-based observations or in future fly-bys, the frost map should be updated so that areas do not need to be interpolated/extrapolated.

These large scale parallel simulations have become quite expensive (~10,000 computational hours per 15 minutes of Io time) but it would be ideal to simulate the entire collisional atmosphere for an entire orbit to study the full dynamics of the atmosphere. In Chapter 6, the effect of eclipse on the atmosphere was modeled but the simulations were not carried out long enough or with plasma chemistry enabled and the atmosphere did not to return to the pre-eclipse state. Furthermore, without an entire simulated orbit, the daughter species concentrations may not reach a steady state. The non-condensable species such as O_2 and SO may create a diffusion layer which further slows the collapse of the SO_2 atmosphere during eclipse (Moore *et al*., 2009). Their simulations were 1D and it remains to be seen whether 3D relieving effects would negate the diffusion layer.

There are a variety of recent observations to which the most sophisticated simulations could be compared. Recent observations (Spencer *et al*., 2012) suggest that there is little variation in the disk-averaged SO_2 column density post-eclipse. Running the simulations through eclipse and then computing the disk-averaged SO_2 column density post-eclipse could help determine what could possibly cause this counter-intuitive phenomenon and what, if any, physical effects are missing from the simulations. Furthermore, the simulations that were initially compared to the variation of mid-infrared disk-averaged band depth as a function of subsolar longitude (Spencer *et al*., 2005) did not include the effect of eclipse. It would be useful to recreate this comparison with the most recent simulations to determine the effect of eclipse on the variation of band depth with subsolar longitude.

APPENDIX A: THE INTERACTION BETWEEN LOKI AND IO'S CIRCUMPLANETARY WINDS

A.1 GEOMETRY

In Appendix A, the interaction between circumplanetary winds and the hot spot, Loki, is investigated with simulations on a sub-domain of the entire planet. For these simulations, the domain covers longitudes between 0° W and 90° W, latitudes between 5° S and 5° N, and up to 400 km in altitude (see Figure A.1). The lateral (azimuthal and polar) cell size is 1.6 km (1800×200 cells) while the radial cell size grows exponentially with altitude to resolve the mean free path. The radial cell size is ~5 m near the surface but is limited to 5 km at high altitudes. There are 190 radial cells in total. The domain is decomposed in longitude across 360 processors. The boundary condition on the top surface of the domain is a vacuum boundary condition since a negligible number of particles reach this altitude and are lost. The boundary conditions at 5° S and 5° N are specular reflection. The boundary condition at 0° W located near the peak pressure region is a specular boundary while the boundary condition at 90° W is a vacuum (since the nightside atmosphere there is essentially collisionless; the atmospheric Knudsen number, $Kn_{ATM} = \lambda/H > 1$). The lower surface boundary condition is more sophisticated than the other surfaces and is explained in detail in the next section. The wind pattern in the sub-domain presented in Section A.2 closely matches those presented in Chapter 4; however, the actual global winds likely diverge more than the specular boundaries in this sub-domain simulation allow resulting in some minor non-conformities.

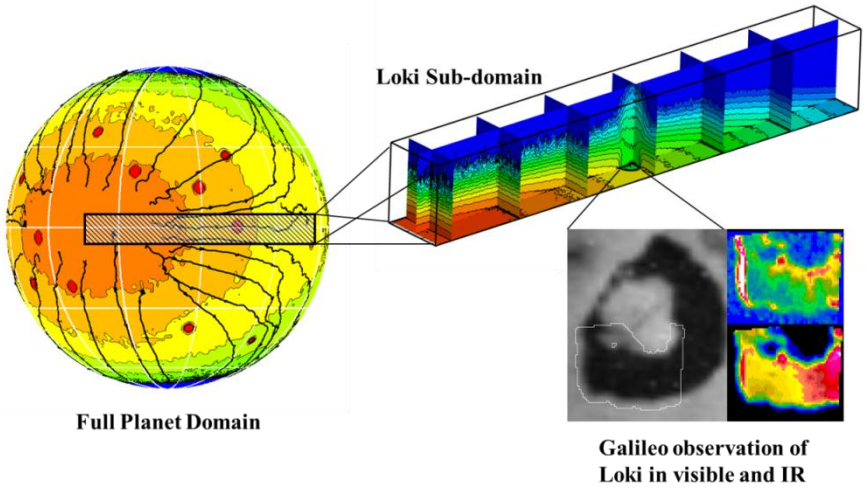

Figure A.1: The global domain of Io's sublimation atmosphere with a cross-hatched area showing the reduced domain for these circumplanetary flow/hot spot interaction simulations. Loki is visible in the center of the sub-domain (which shows contours of the number density in the atmosphere) and an image of the lava lake taken from Galileo is also shown (the dark area is Loki).

A.2 SIMULATION RESULTS

Three cross flow cases are investigated. Case 1 is the simplest case and includes homogeneous surface frosts (uniform 50% SO_2 frost / 50% non-frost surface; Douté *et al*. (2001)), unit sticking on the non-frost surface, and no plasma heating. Case 2 includes inhomogeneous surface frosts and a residence time on the non-frost surface but does not include plasma heating. Case 3 includes inhomogeneous surface frosts, a residence time on the non-frost surface, and plasma heating.

The level of rarefaction over the hot spot can be characterized by defining a "hot spot" Knudsen number ($Kn_{HS} = \lambda/R$) where λ is the mean free path in the local surrounding sublimation atmosphere and R is the effective radius of the "hot spot". An atmospheric Knudsen number can then be defined; $Kn_{ATM} = \lambda/H$. For typical surface frost temperatures, the scale height near the surface varies between 8.3 km at 115 K and 6.5 km at 90 K. For convenience and clarity, the rarefaction will generally be defined by Kn_{HS} rather than Kn_{ATM} (with Kn_{HS} a factor of 6 to 8 smaller than Kn_{ATM} at low altitudes).

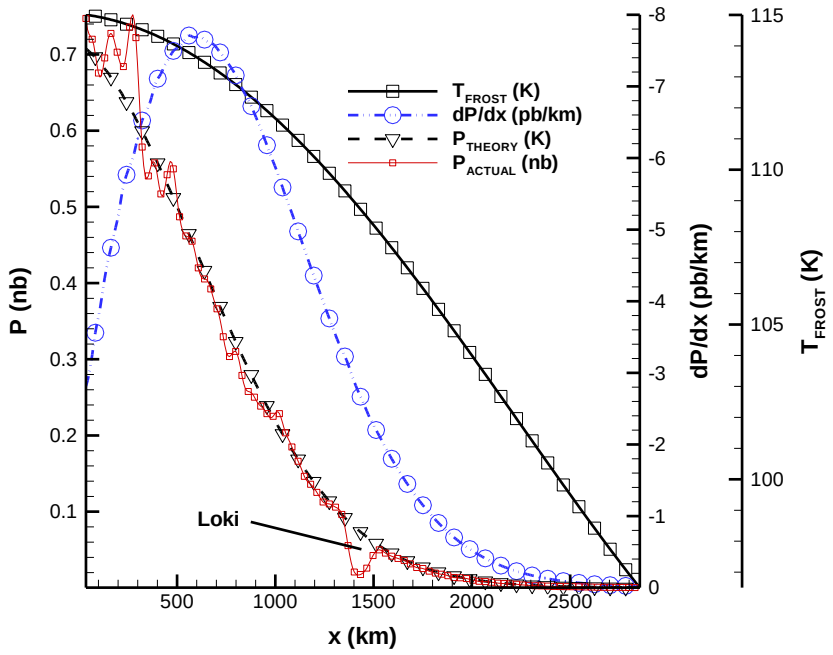

Figure A.2: The surface frost temperature, pressure above the surface based only on vapor pressure equilibrium (P_{THEORY}), the actual pressure above the surface (P_{ACTUAL}), and pressure gradient (based on P_{THEORY}) as a function of x (the distance away from the peak pressure region) along the equator. The actual gas pressure above the surface tracks vapor pressure equilibrium everywhere but in the vicinity of Loki.

For Case 1, the pressure gradient creates rarefied boundary layer flow over the "hot spot". The surface temperature varies from ~115 K to ~90 K and therefore the near surface rarefaction varies from $Kn_{HS} \approx 1\times10^{-4}$ to 0.5 (see Figure A.3). At high altitudes $Kn_{HS} >> 1$. The pressure near the surface varies from ~0.7 nbar at peak pressure to ~1 pbar near the nightside. A favorable pressure gradient, $dP/dx < 0$, exists everywhere but in the region near Loki and the flow accelerates monotonically away from the peak pressure region toward Loki (see Figure A.2). The hot spot surface is a diffuse reflector causing the net x-momentum of the flow to be lost as molecules impact the surface. Furthermore, the mean free path and ballistic length scale are both smaller than the radius of the hot spot ($\lambda < d_{B\text{-}ATM} < R$, where $d_{B\text{-}ATM}$ is the ballistic length scale in the local sublimation atmosphere). The ballistic length scale is defined by $d_{B\text{-}ATM} = 8k_BT / \pi mg$. Thus molecules undergo many collisions along their paths over the hot spot, and the vast

majority of molecules will not pass over Loki in a single ballistic trajectory ($d_{B\text{-}ATM} < 2R$). This combination of parameters leads to a moderately collisional ($Kn_{HS} \approx 1\times10^{-3}$) stagnant gas above Loki. The stagnant gas above Loki creates a substantial upstream adverse pressure. Although, the near surface pressure above Loki is lower than that of the surrounding sublimation atmosphere, the pressure becomes higher than the surrounding atmosphere at ~10 km altitude. As the atmospheric flow encounters the large adverse pressure gradient created locally by Loki, the boundary layer separates and a vortex forms (see Figures A.6a and A.6b). Because of the high x-direction momentum flux of the winds there is significant downstream deflection of the hot gas above the hot spot on the upstream edge. The deflection of the hot spot gas from the vertical is ~35°.

The situation is largely the same for Case 2 (including inhomogeneous surface frosts but neglecting plasma heating). Modeling the residence time on the non-frost surface slightly increases the day-to-night pressure gradient leading to higher momentum flux in the lower atmosphere. This increases the deflection angle to ~45° (see Figure A.6b). For Case 3 (including both inhomogeneous surface frosts and plasma heating), the plasma heating significantly alters the dynamics. The plasma inflates the atmosphere (i.e. higher number densities at higher altitudes); therefore, the atmosphere becomes collisional at higher altitudes. The temperature is also increased by the absorption of plasma energy; however, the effects vary with x because the plasma energy only penetrates down through a fixed column of gas. The resulting pressures at higher altitudes can be seen in Figure A.5. The pressure gradient in Case 3 is much larger than Case 2 and this causes higher flow speeds at higher altitudes (and a higher x-direction momentum flux; see Figure A.4). At high altitudes, the relative size of the adverse pressure gradient created by the hot spot is reduced by the higher pressures due to plasma heating. The pressure gradient remains largely favorable even over Loki and the boundary layer remains attached (see Figure A.4 and Figure A.5).

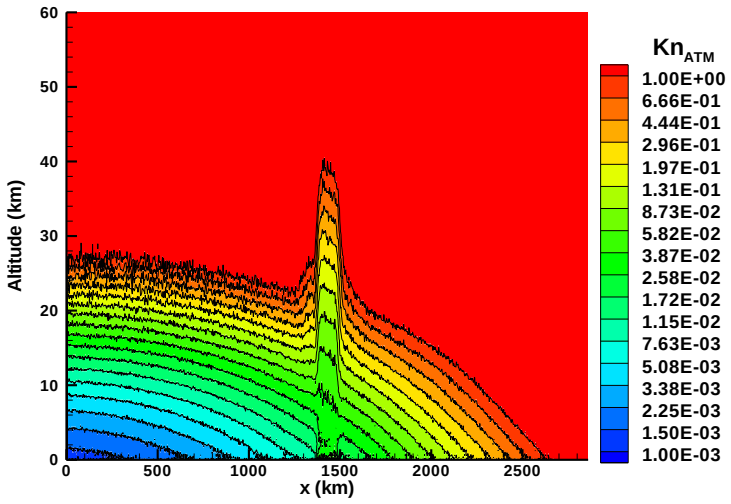

Figure A.3: Kn_{HS} as a function of altitude and x along the equator for Case 1.

For Cases 1 and 2, the hot gas above Loki forms a wake of warm gas because of the comparable radiation and convection time scales of the SO_2 molecules. A fraction of the molecules that impact the hot spot (and subsequently desorb in thermal equilibrium) will convect downstream with the circumplanetary flow; since $Kn_{HS} \approx 1\times10^{-3}$, collisions will transfer translational energy to the rotational and vibrational energy modes. The energy transferred to vibrational modes is radiated rapidly because the largest Einstein A coefficients of the three SO_2 vibrational modes is 0.88 s^{-1}; therefore, each the vibrational mode radiates most of its energy before the SO_2 molecule travels far from the hot spot ($t_{VIB}U/R << 1$, where t_{VIB} is the vibrational radiation time scale). However, the time scale for radiation from the rotational energy states of SO_2, t_{ROT}, is on the order of 250 s at ~300 K ($t_{ROT}U/R \approx 0.5$). The warm gas from Loki cools by e^{-1} after the gas convects ~25 km (or ~0.5R) downstream of the hot spot edge (see Figures A.6a and A.6b). However, this simplifies the situation a bit as the gas must be collisional to transfer energy away from translation and into the rotational and vibrational internal energy states. At higher altitudes, the collision rate drops slowing the rate at which the translational temperature decreases.

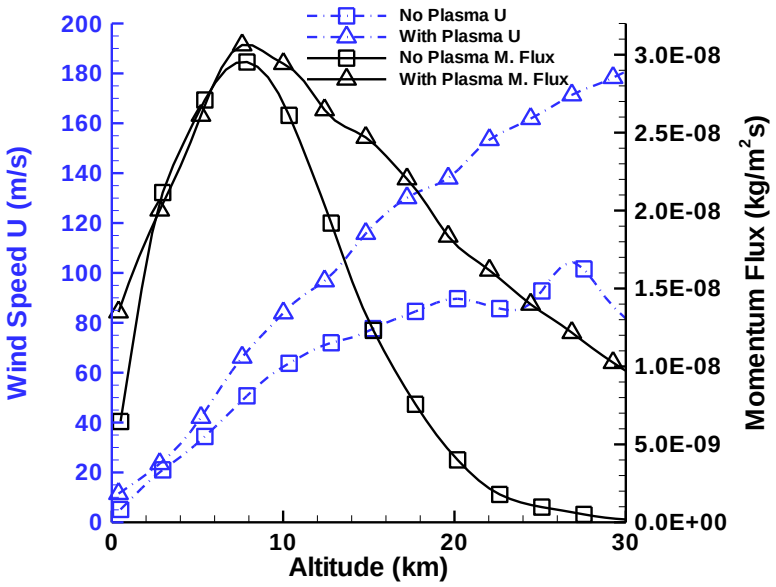

Figure A.4: The number density, *x*-direction wind speed, and *x*-direction momentum flux for Cases 2 and 3 as a function of altitude. These profiles are taken ~70 km upstream of the upstream edge of the hot spot such that they are outside of the vortex created in Case 2. The x-direction momentum flux is very similar for Case 2 and 3 below 10 km but Case 3 has a much higher *x*-direction momentum flux above 10 km (~6 times greater at 20 km).

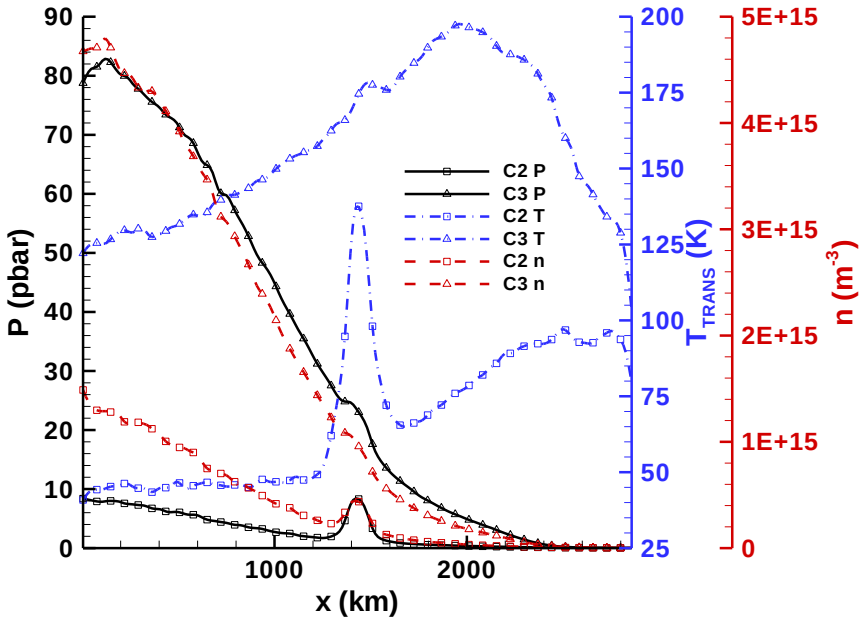

Figure A.5: The pressure, number density, and translational temperature at 20 km as a function of x for Cases 2 and 3. The pressure gradient is much larger in Case 3 than Case 2 resulting in much higher wind speeds and the boundary layer remaining attached.

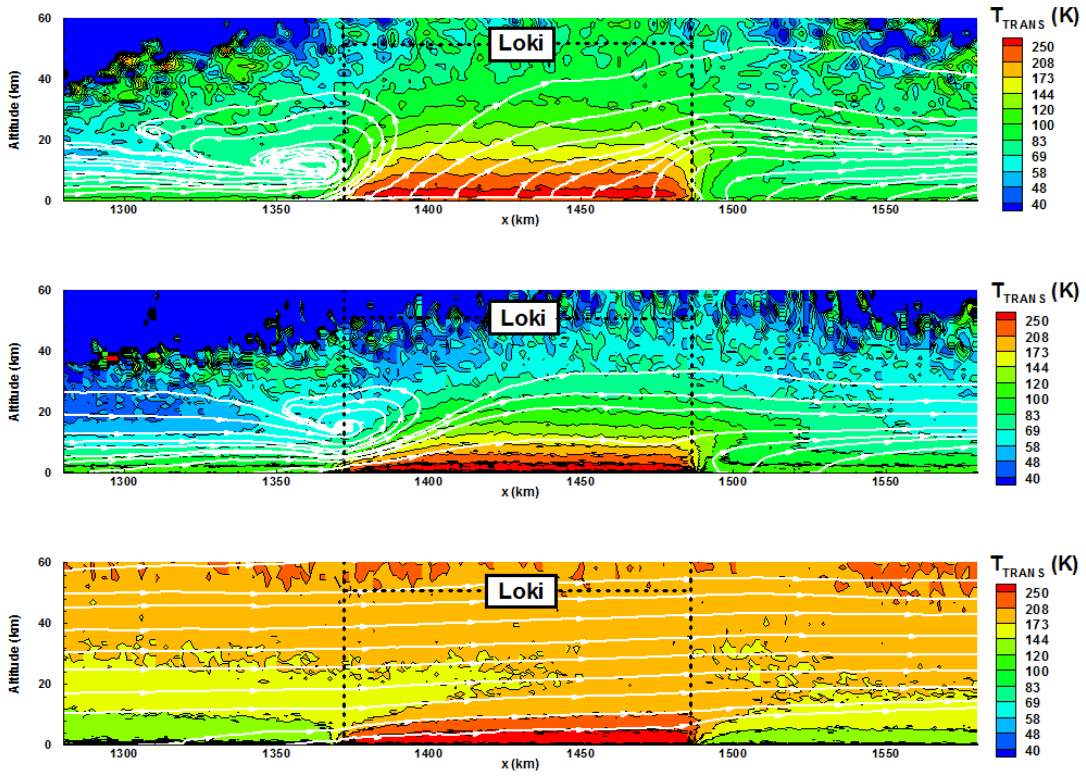

Figure A.6: Contours of translational temperature as a function of altitude and distance away from the peak pressure region along the equator. Streamtraces in white show the circumplanetary flow's interaction with the hot spot, Loki. The rarefied boundary layer flow which had developed separates due to the adverse pressure gradient created by the hot spot in Cases 1 and 2. In Cases 1 and 2, streamtraces continue downstream of the hot spot due to three-dimensional effects as the flow curves around the hot spot. In Case 3, the boundary layer flow remains attached.

The temperature of the local sublimation atmosphere is significantly increased when plasma heating is included (Case 3). The temperature is high immediately above the surface of Loki but then decreases with altitude due to radiation and adiabatic cooling and then rises again above 20 km where the plasma is able to penetrate (Figure A.6c). For all cases, the pressure over the hot spot does not equilibrate with the local sublimation atmospheric pressure because $d_{B\text{-}ATM} < R$. This is in qualitative agreement with Ingersoll (1989) who defined $L = \sqrt{2\pi}H$ (when the sticking coefficient is unity) as a horizontal averaging length scale over which local frost patches control the pressure. In separate zero pressure gradient simulations, we found that as H is increased, the pressure became more uniform over the hot spot. Since H and $d_{B\text{-}ATM}$ are directly proportional, this is the

same as increasing the ballistic length scale. When $d_{B\text{-}ATM} \approx R$, the pressure equilibrates over the hot spot.

REFERENCES

Austin, J.V., Goldstein, D.B., 2000. Rarefied gas model of Io's sublimation-driven atmosphere. *Icarus* **148**, 370-383.

Bagenal, F., Sullivan, J.D., 1980. Spatial distribution of plasma in the Io torus. *Geophys. Res. Letters* **7**, 41-44.

Ballester, G.E., Strobel, D.F., Moos, H.W., Feldman, P.D., 1990. The atmospheric abundance of SO_2 on Io. *Icarus* **88**, 1-23.

Ballester, G.E., McGrath, M.A., Strobel, D.F., Zhu, X., Feldman, P.D., Moos, H.W., 1994. Detection of the SO_2 atmosphere on Io with the Hubble Space Telescope. *Icarus* **111**, 2-17.

Bass, H.F., Winter, T.G., Evans, L.B., 1971. Vibrational and rotational relaxation in sulfur dioxide. *J. of Chem. Phys.* **54**, 644-647.

Bigg, E. K., 1964. Influence of the Satellite Io on Jupiter's Decametric Emission. *Nature* **203** (4949): 1008–1010.

Binder, A.B., Cruikshank, D.P., 1964. Evidence for an atmosphere on Io. *Icarus* **3**, 299-305.

Bird, G.A, *Molecular Gas Dynamics and the Direct Simulation of Gas Flows*. Oxford Univ. Press. Oxford, 1994.

Bridge, H. S., Belcher, J.W., Lazarus, A.J., Sullivan, J.D., McNutt, R.L., Bagenal, F., Scudder, J.D., Sittler, E.C., Siscoe, G.L., Vasyliunas, V.M., Goertz, C.K., Yeates, C.M., 1979a. Plasma observations near Jupiter: Initial results from Voyager 1, *Science* **204**, 987–991.

Bridge, H. S., Belcher, J.W., Lazarus, A.J., Sullivan, J.D., McNutt, R.L., Bagenal, F., Scudder, J.D., Sittler, E.C., Siscoe, G.L., Vasyliunas, V.M., Goertz, C.K., Yeates, C.M., 1979b. Plasma observations near Jupiter: Initial results from Voyager 2, *Science* **206**, 972–976.

Broadfoot, A. L., Belton, M.J.S., Takacs, P.Z., Sandel, B.R., Shemansky, D.E., Holberg, J.B., Ajello, J.M., Atreya, S.K., Donahue, T.M., Bertaux, J.L., Blamont, J.E., Strobel, D.F., McConnel, J.C., Dalgarno, A., Goody, R., McElroy, M.B., Extreme ultraviolet observations from Voyager 1 encounter with Jupiter, *Science* **204**, 979–982.

Carlson, R.W., Smythe, W.D., Lopes-Gautier, R.M.C., Davies, A.G., Kamp, L.W., Mosher, J.A., Soderblom, L.A., Leader, F.E., Mehlman, R., Clark, R.N., Fanale, F.P., 1997. The distribution of sulfur dioxide and other infrared absorbers on the surface of Io. *Geophys. Res. Lett.* **24**, 2479-2482.

Clarke, J.T., Ajello, J., Luhmann, J., Schneider, N., Kanik, I., 1994. Hubble Space Telescope UV spectral observations of Io passing into eclipse. *J. Geophys. Res.* **99**, 8387-8402.

Cruikshank, D.P., Murphy, R.E., 1973. The post-eclipse brightening of Io. *Icarus* **20**, 7-17.

Deng, H., Moore, C.H., Levin, D.A., Goldstein, D.B., and Varghese, P.L., 2011. Analysis of SO_2+O chemistry models for simulations of the atmosphere of Io. *Proceedings of the 27th International Rarefied Gas Dynamics Symposium*. **1033**, 1139–1144.

Douté, S., Schmitt, B., Lopes-Gautier, R., Carlson, R., Soderblom, L., Shirley, J., the Galileo NIMS Team, 2001. Mapping SO_2 frost on Io by the modeling of NIMS hyperspectral images. *Icarus* **149**, 107-132.

Feaga, L.M., McGrath, M.A., Feldman, P.D., 2002. The abundance of atomic sulfur in the atmosphere of Io. *The Astrophysical Journal* **570**, 439-446.

Feaga, L.M., 2005. Hubble Space Telescope Far-Ultraviolet Observations of Io: Determining Atmospheric Abundances, Mapping the SO_2 Distribution, and Correlating the Molecular and Atomic Atmosphere. PhD Dissertation. Johns Hopkins University.

Feaga, L.M, McGrath, M., Feldman, P. D., 2009. Io's dayside SO_2 atmosphere. *Icarus* **201**, 570-584.

Feldman, P.D., Strobel, D.F., Moos, H.W., Retherford, K.D., Wolven, B.C., McGrath, M.A., Roesler, F.L., Woodward, R.C., Oliverson, R.J., Ballester G.L., 2000. Lyman-α imaging of the SO_2 distribution on Io. *Geophys. Res. Lett.* **27**, 1787–1790.

Flaud, J.M., Perrin, A., Salah, L.M., Lafferty, W.J., Gauelachvili, G., 1993. A reanalysis of the (010), (020), (100), and (001) rotational levels of $^{32}S^{16}O^2$. J. Mol. Spectrosc. 160 (1), 272–278.

Frank, L.A., Paterson, W.R., Ackerson, K.L., Vasyliunas, W.M., Corniti, F.V., Bolton, S.J., 1996. Plasma observations at Io with the Galileo spacecraft. *Science* **274**, 394-395.

Franz, O.G., Millis, R.L, 1971. A search for an anomalous brightening of Io after eclipse. *Icarus* **14**, 13-15.

Geissler, P.E., McEwen, A.S., Keszthelyi, L., Lopes-Gautier, R., Granahan, J., Simonelli, D.P., 1999. Global color variations on Io. *Icarus* **140**, 265-282.

Geissler, P., McEwen, A., Philips, C., Keszthelyi, L., Spencer, J., 2004. Surface changes on Io during the Galileo mission. *Icarus* **169**, 29-64.

Gratiy, S.L., Walker, A.C., Levin, D.A., Goldstein, D.B., Varghese, P.L., Trafton, L.M., Moore, C.M., 2009. Multi-wavelength simulations of atmospheric radiation from Io with a 3-D spherical-shell backward Monte Carlo radiative transfer model. *Icarus*, doi:10.1016/j.icarus.2009.11.004.

Hapke, B., 1981. Bidirectional reflectance spectroscopy. I. Theory. J. Geophys. Res. 86, 3039–3054.

Hapke, B., Wells, E., Wagner, J., Partlow, W., 1981. Far-UV, visible, and near-IR reflectance spectra of frosts of H_2O, CO_2, NH_3 and SO_2. Icarus 47 (3), 361–367.

Hapke, B., 1993. Theory of Reflectance and Emittance Spectroscopy, first ed. Cambridge University Press, p. 191.

Hendrix, A.R, Barth, C.A., Hord, C.W., 1999. Io's patchy SO_2 atmosphere as measured by the Galileo ultraviolet spectrometer. *J. Geophys. Res.* **104**, 11,817-11,826.

Houghton, J.T., 2002. The Physics of Atmospheres, third ed. Cambridge University Press, pp. 9–12.

Howell, R.R., Cruikshank, D.P., Fanale, F.P., 1984. Sulfur dioxide on Io: spatial distribution and physical state. *Icarus* **57**, 83-92.

Hou, M., Robinson, M.T., Computer simulation of low-energy sputtering in the binary collision approximation. *Applied Physics* **18**, 381-389.

Huebner, W.F., Keady, J.J., and Lyon, S.P., 1992. Solar photo rates for planetary atmospheres and atmospheric pollutants. *Astrophysics and Space Science*, **195**, 1–294.

Ingersoll, A.P, Summers, M.E., Schlipf, S.G., 1985. Supersonic meteorology of Io: sublimation-driven flow of SO2. *Icarus* **64**, 375-390.

Ingersoll, A.P., 1989. Io meteorology: how atmospheric pressure is controlled locally by volcanos and surface frosts. *Icarus* **81**, 298-313.

Jessup, K.L, Ballester, G.E., Combi, M., Zhu, X., Strobel, D.F., Clarke, J.T., 2002. Io's changing atmosphere. In: The Magnetospheres of the Outer Planets conference abstract book, p. 116.

Jessup, K.L., Spencer, J.R., Ballester, G.E., Howell, R.R., Roesler, F., Vigel, M., Yelle, R., 2004. The atmospheric signature of Io's Prometheus plume and anti-Jovian hemisphere: evidence for a sublimation atmosphere. *Icarus* **169**, 197-215.

Johnson, R.E., 1990. *Energetic charged particle interactions with atmospheres and surfaces*. Springer–Verlag, Berlin.

Johnson, T.V., Matson, D.L., Blaney, D.L., Veeder, G.J., Davies, A., 1995. Stealth plumes on Io. Geophys. Res. Lett. 22, 3293–3296.

Johnson, R.E., 2011. *Private communication.*

Kabin, K., Combi, M.R., Gombosi, T.I., DeZeeuw, D.L., Hansen, K.S., Powell, K.G., 2001. Io's magnetospheric interaction: An MHD model with day–night asymmetry. *Planet. Space Sci.* **49**, 337–344.

Kerton, C.R., Fanale, F.P., Salvail, J.R., 1996. The state of SO_2 on Io's surface. *J. Geophys. Res.* **101**, 7555-7563.

Kivelson, M.G., Khurana, K.K., Walker, R.J., Russel, C.T., Linker, J.A., Southwood, D.J., Polanskey, C., 1996a. A Magnetic Signature at Io: Initial Report from the Galileo Magnetometer. *Science* **273**, 337-340.

Kliore, A.J., Fjeldbo, G., Seidel, B.L., Sweetnam, D.N., Sesplaukis, T.T., Woiceshyn, P.M., 1975. The atmosphere of Io from Pioneer 10 radio occultation measurements. *Icarus* **24**, 407-410.

Laver, C., de Pater, I., 2008. Spatially resolved SO_2 ice on Io, observed in the near IR. *Icarus* **195**, 752-757.

Laver, C., de Pater, I., 2009. The global distribution of sulfur dioxide ice on Io, observed with OSIRIS with the W.M. Keck telescope. *Icarus* **201**, 172-181.

Lellouch, E., Belton, M., de Pater, I., Gulkis, S., Encrenaz, T., 1990. Io's atmosphere from microwave detection of SO_2. *Nature* **369**, 639-641.

Lellouch, E., Belton, M., de Pater, I., Paubert, G., Gulkis, S., Encrenaz, T., 1992. The structure, stability, and global distribution of Io's atmosphere. *Icarus* **98**, 271-295.

Lellouch, E., 1996. Detection of sulfur monoxide in Io's atmosphere. *The Astrophysical Journal* **45**9, 107-110.

Lellouch, E., 1996. Io's atmosphere: not yet understood. *Icarus* **124**, 1-21.

Lellouch, E., Paubert, G., Strobel, D.F., Belton, M., 2000. Millimeter-wave observations of Io's atmosphere: The IRAM 1999 compaign. Bull. Am. Astron. Soc. 32 (1), 3511.

Lellouch, E., McGrath, M.A., Jessup, K.L., 2006. Io's atmosphere. In: Lopes, R.M.C., Spencer, J.R. (Eds.), Io After Galileo. Springer, pp. 231–264.

Linker, J.A., Kivelson, M.G., Walker, R.J., 1988. An MHD simulation of plasma flow past Io: Alfvén and slow mode perturbations. *Geophys. Res. Letters* **15**, 1,311-1314.

Linker, J.A., Kivelson, M.G., Walker, R.J., 1991. A three-dimensional MHD simulation of plasma flow past Io. *J. Geophys. Res*. **96**, 21,037–21,053.

Linker, J.A., Khurana, K.K., Kivelson, M.G., Walker, R.J., 1998. MHD simulation of Io's interaction with the plasma torus. *J. Geophys. Res.* **103**, 19,867–19,877.

Lipatov, A.S., Combi, M.R., 2006. Effects of kinetic processes in shaping Io's global plasma environment: a 3D hybrid model. *Icarus* **180**, 412-427.

Lopes, R.M.C., and 10 colleagues, 2004. Lava lakes on Io: Observations of Io's volcanic activity from Galileo NIMS during the 2001 fly-bys. Icarus 169 (1), 140–174.

Manatt, S.L., Lane, A.L., 1993. A compilation of the absorption cross-sections of SO_2 from 106 to 403 nm. J. Quant. Spectrosc. Radiat. Trans. 50 (3), 267–276.

Marchis F., Le Mignant, D., Chaffee, F.H., Davies, A.G., Kwok, S.H., Prangé, R., de Pater, I., Amico, P., Campbell, R., Fusco, T. Goodrich, R.W., Conrad, A., 2005. Keck AO survey of Io global volcanic activity between 2 and 5 μm. *Icarus* **176**, 96-122.

Matson, D. L., Nash, D. B., 1983. Io's atmosphere: pressure control by regolith cold trapping and surface venting. *J. Geophys. Res.* **88**, 4471-4783.

McEwen, A.S., Johnson, T.V., Matson, D.L., Soderblom, L.A., 1988. The global distribution, abundance, and stability of SO_2 on Io. *Icarus* **75**, 450-478.

McGrath, M.A., Belton, M.J.S., Spencer, J.R., Sartoretti, P., 2000. Spatially resolved spectroscopy of Io's Pele plume and SO_2 atmosphere. *Icarus* **146**, 476-493.

Moore. C. H., Goldstein, D. B., Varghese, P. L., Trafton, L. M., Stewart, B., 2009. 1-D DSMC simulation of Io's atmospheric collapse and reformation during and after eclipse. *Icarus* **201**, 585-597.

Moore. C. H., 2011. Monte Carlo simulation of the Jovian plasma torus interaction with Io's atmosphere and the resultant aurora during eclipse. PhD Dissertation, The University of Texas at Austin.

Moore, C.H., Walker, A.C., Parsons, N., Goldstein, D.B., Varghese, P.L., Trafton, L.M., 2012. DSMC Simulation of the plasma bombardment on Io's sublimated and sputtered atmosphere. *AIAA-2012-0560*.

Moreno, M.A., Schubert, G., Baumgardner, J., Kivelson, M.G., Paige, D.A., 1991. Io's volcanic and sublimation atmospheres. *Icarus* **93**, 63-81.

Moullet, A., Lellouch, E., Moreno, R., Gurwell, M.A., Moore, C., 2008. First disk-resolved millimeter observations of Io's surface and atmosphere. *Astronomy and Astrophysics* **482**, 279-292.

Nash, D.B., Fanale, F.P., Nelson, R.M., 1980. SO_2 frost: UV-visible reflectivity and Io surface coverage. *Geophys. Res. Lett.* **7**, 64-67.

Nash, D.B., 1986. Mid-infrared reflectance spectra (2.3–22 ım) of sulfur, gold, KBr, MgO, and halon. Appl. Opt. 25, 2427–2433.

Nash, D.B., Betts, B.H., 1995. Laboratory infrared spectra (2.3–23 ım) of SO_2 phases: Applications to Io surface analysis. Icarus 117 (2), 402–419.

Nelson, R.M., Lane, A., Matson, D., Fanale, F., Nash, D., Johnson, T., 1980. Io's longitudinal distribution of sulfur dioxide frost. *Science* **210**, 784-786.

O'Leary, B., Veverka, J., 1971. On the anomalous brightening of Io after eclipse. *Icarus* **14**, 265-268.

Parsons, N., Levin, D.A., 2012. Development of a Chemistry Model for DSMC Simulation of the Atmosphere of Io. 50th AIAA Aerospace Sciences Meeting including the New Horizons Forum and Aerospace Exposition. Nashville, TN.

Pearl, J., Hanel, R., Kunde, V., Maguire, W., Fox, K., Gupta, S., Ponnamperuma, C., Raulin, F., 1979. Identification of gaseous SO_2 and new upper limits for other gases on Io. *Nature* **280**, 755-758.

Pospieszalska, M.K., Johnson, R.E., 1996. Monte Carlo calculations of plasma ion-induced sputtering of an atmosphere: SO_2 ejected from Io. *J. Geophys. Res.* **101**, 7565-7573.

Radzig, A.A. and Smirnov, B.M., 1980. Reference data on atoms, molecules, and ions. *Springer-Verlag*.

Rathbun, J.A., Spencer, J.R., Tamppari, L.K., Martin, T.Z., Barnard, L., Travis, L.D., 2004. Mapping of Io's thermal radiation by the Galileo photopolarimeter-radiometer (PPR) instrument. *Icarus* **169**, 127-139.

Roesler, F.L., Moos, H.W., Oliversen, R.J., Woodward Jr., R.C., Retherford, K.D., Scherb, F., McGrath, M.A., Smyth, W.H., Feldman, P.D., Strobel, D.F., 1999. Far-ultraviolet imaging spectroscopy of Io's atmosphere with HST/STIS. *Science* **283**, 353-357.

Rothman, L.S., and 29 colleagues, 2005. The HITRAN 2004 molecular spectroscopic database. J. Quant. Spectrosc. Radiat. Trans. 96 (2), 139–204.

Sandford, S.A., Allamandola, L.J., 1993. The condensation and vaporization behavior of ices containing, SO_2, H_2S, and CO_2: implications for Io. *Icarus* **106**, 478-488.

Sartoretti, P., McGrath, M.A., Paresce, F., 1994. Disk-resolved imaging of Io with the Hubble Space Telescope. *Icarus* **108**, 272-284.

Sartoretti, P., McGrath, M.A., McEwen, A.S., Spencer, J.R., 1995. Post-Voyager brightness variations on Io. J. Geophys. Res. Planets 100 (E4), 7523–7530.

Sartoretti, P., Belton, M.J.S., McGrath, M., 1996. SO_2 distributions on Io. *Icarus* **122**, 273-287.

Saur, J., Neubauer, F.M., Strobel, D.F., Summers, M.E., 1999. Three-dimensional plasma simulation of Io's interaction with the Io plasma torus: Asymmetric plasma flow. *J. Geophys. Res.* **104**, 25,105–25,126.

Saur, J., Neubauer, F.M., Strobel, D.F., Summers, M.E., 2000. Io's ultraviolet aurora: Remote sensing of Io's interaction. *GRL* **27**, 2893-2896.

Saur, J., Neubauer, F.M., Strobel, D.F., Summers, M.E., 2002. Interpretation of Galileo's Io plasma and field observations: The J10, I24, I27 flybys, and close polar passes. *J. Geophys. Res*. **107**, A12, 5-1.

Saur, J., Strobel, D.F., 2004. Relative Contributions of sublimation and volcanoes to Io's atmosphere inferred from its plasma interaction during solar eclipse. *Icarus* **171**, 411-420.

Saur, J., Neubauer, F.M., Connerney, J.E.P., Zarka, P., and Kivelson, M.G., 2004. Plasma interaction of Io with its plasma torus. In: *Jupiter: The planet, Satellites and Magnetosphere* (F. Bagenal, T. Dowling, and W. McKinnon, Eds.). Cambridge University Press, Cambridge, UK, 537–560.

Scarf, F.L., Gurnett, D.A., Kurth, W.S., 1979. Jupiter Plasma Wave Observations: An Initial Voyager 1 Overview. *Science* **204**, 991-995.

Schenk, P., Hargitai, H., Wilson, R., McEwen, A., Thomas, P., 2001. The mountains of Io: Global and geological perspectives from Voyager and Galileo. *J. Geophys. Res.* **106**, 33,201-33,222.

Sigmund, P., 1969. Theory of sputtering. I. Sputtering yield of amorphous and polycrystalline targets. *Physical Review* **184**, 383-416.

Simonelli, D.P., Dodd, C., Veverka, J., 2001. Regolith variations on Io: Implications for bolometric albedos. *J. Geophys. Res.* **106**, 33,241-33,252.

Sinton, W.M., Tokunaga, A.T., Becklin, E.E., Gatley, I., Lee, T.J., Lonsdale, C.J., 1980. Io: ground-based observations of hot spots. *Science* **210**, 1015-1017.

Sinton, W.M., Kaminski, C., 1988. Infrared observations of eclipses of Io, its thermophysical parameters, and the thermal radiation of the Loki volcano and environs. *Icarus* **75**, 207-232.

Smyth, W.H., and Wong, M.C., 2004. Impact of electron chemistry on the structure and composition of Io's atmosphere. *Icarus* **171**, 171-182.

Spencer, J.R., Lebofsky, L.A., Sykes, M.V., 1989. Systematic Biases in Radiometric Diameter Determinations. *Icarus* **78**, 337-354.

Spencer, J.R., Rathbun, J.A., Travis, L.D., Tamppari, L.K., Barnard, L., Martin, T.Z., McEwen, A.S., 2000. Io's thermal emission from the Galileo photopolarimeter-radiometer. *Science* **288**, 1198-1201.

Spencer, J.R., Lellouch, E., Richter, M.J., López-Valverde, M.A., Jessup, K.L, Greathouse, T.K., Flaud, J., 2005. Mid-infrared detection of large longitudinal asymmetries in Io's SO_2 atmosphere. *Icarus* **176**, 283-304.

Spencer, J. R. Jessup K. L. Tsang C. C. C. Cunningham N. Retherford K., 2012. Evidence for volcanic support of Io's Jupiter-facing atmosphere from constraints on post-eclipse atmospheric changes. Abstract #2420. 43rd Lunar and Planetary Science Conference, the Woodlands, Houston, TX.

Stewart, B.D., Pierazzo, E., Goldstein, D.B., Varghese, P.L., Trafton, L.M., Moore, C.H., 2009. Parallel 3D hybrid continuum/DSMC method for unsteady expansions into a vacuum. AIAA Paper 2009-266. 47th AIAA Aerospace Science Meeting, Orlando, FL.

Stewart, B.D., Pierazzo, E., Goldstein, D.B., Varghese, P.L., and Trafton, L.M., 2011. Simulations of a comet impact on the Moon and associated ice depositions in polar cold traps. *Icarus* doi:10.1016/j.icarus.2011.03.014.

Strobel, D.F., Zhu, X., Summers, M.E., 1994. On the vertical structure of Io's atmosphere. *Icarus* **111**, 18-30.

Strobel, D.F., Wolven, B.C., 2001. The atmosphere of Io: abundances and sources of sulfur dioxide and atomic hydrogen. *Astrophysics and Space Science* **277**, 271-287.

Summers, M.E. and Strobel, D.F., 1996. Photochemistry and vertical transport in Io's atmosphere and ionosphere. *Icarus* **120**, 290–316.

Trafton, L.M., Caldwell, J.J., Barnet, C., Cunningham, C.C., 1996. The gaseous sulfur dioxide abundance over Io's leading and trailing hemispheres: HST spectra of Io's C^1B_2-X^1A_1 band of SO_2 near 2100 Å. *The Astrophysical Journal* **456**, 384-392.

Tsang C.C.C., Spencer J.R., Lellouch E., Richter M.J., Lopez-Valverde M.A., Greathouse T.K., 2012. Io's atmosphere: constraints on sublimation support from density variations on seasonal timescales using NASA IRTF/TEXES observations from 2001 to 2010. *Icarus* **217**, 277-296.

Veeder, G.J., Matson, D.L., Johnson, T.V., Blaney, D.L., Goguen, J.D., 1994. Io's heat flow from infrared radiometry: 1983-1993. *J. Geophys. Res*. **99**, 17095-17162.

Warwick, J.W., Pearce, J.B., Riddle, A.C., Alexander, J.K., Desch, M.D., Kaiser, M.L., Thieman, J.R., Carr, T.D., Boischot, A., Leblanc, Y., Pedersen, B.M., Staelin, D.H., 1979. Planetary radio astronomy observations from Voyager 2 near Jupiter. *Science* **206**, 991-995.

Wagman, D., 1979. Sublimation pressure and the enthalpy of SO_2. Chem. Thermodyn. Data Cent., Natl. Bur. of Stand.

Walker, A.C., Gratiy, S.L., Goldstein, D.B., Moore, C.H., Varghese, P.L., Trafton, L.M., Levin, D.A., Stewart, B.D., 2010. A comprehensive numerical simulation of Io's sublimation-driven atmosphere. *Icarus* **207**, 409-432.

Walker, A.C., Goldstein, D.B., Varghese, P.L., Trafton, L.M., Moore, C.H, 2011. "Loki – A lava lake in rarefied circumplanetary cross flow" 27th International Symposium on Rarefied Gas Dynamics, 2010, Levin, D., Wysong, I., Garcia, A., (Eds.), AIP Conf. Proc. Vol. 1333, 1175-1180.

Walker, A.C., Moore, C.H., Goldstein, D.B., Moore, C.H., Varghese, P.L., Trafton, L.M., 2012. A parametric study of Io's thermophysical surface properties and subsequent numerical atmospheric simulations based on the best fit parameters. *Icarus* **submitted**.

Wong, M.C., Johnson, R.E., 1995. The effect of plasma heating on sublimation-driven flow in Io's atmosphere. *Icarus* **115**, 109-118.

Wong, M.C., Johnson, R.E., 1996. A three-dimensional azimuthally symmetric model atmosphere for Io 1, Photochemistry and the accumulation of a nightside atmosphere. *J. of Geophys. Res.* **101**, 23,243-23,254.

Wong, M.C., Smyth, W.H., 2000. Model calculations for Io's atmosphere at eastern and western elongations. *Icarus* **146**, 60-74.

Zhang, J., Goldstein, D.B., Varghese, P.L., Gimelshein, N.E., Gimelshein, S.F., Levin, D.A., 2003. Simulation of gas dynamics and radiation in volcanic plumes on Io. *Icarus* **163**, 182-197.

Zhang, J., Goldstein, D.B., Varghese, P.L., Trafton, L., Moore, C., Miki, K., 2004. Numerical modeling of Ionian volcanic plumes with entrained particulates. *Icarus* **172**, 479-502.